THE UNIVERSITY OF
SYDNEY

Coupled Rigid Body Dynamics with Application to Diving

William Tong

A thesis submitted in fulfilment of
the requirements for the degree of
Doctor of Philosophy

Applied Mathematics
Faculty of Science
University of Sydney

THE UNIVERSITY OF
SYDNEY

March 2016

Acknowledgements

The School of Mathematics and Statistics at the University of Sydney has provided me with the life-changing opportunity to meet very inspiring and talented individuals during my Doctoral candidature who I would like to thank.

Firstly, the most important people who made this thesis possible are my supervisor and associate supervisor, Holger Dullin and Leon Poladian. Professor Holger Dullin has supported me from the very beginning, starting as my supervisor for Honours in my undergraduate degree and kindly agreeing to continue that role for my PhD. Without his guidance, encouragement and expertise, I would not have been able to achieve what I have today. Thank you so much for everything!

My studies enabled close collaboration with various individuals across different research faculties, together forming a group known as the Bodies in Space team. Its members include include Peter Sinclair and Cherie Walker of sports science, Suryah Singh, David Rye and Joanne Mikl of mechanical engineering, Kenneth Graham and Damien O' Meara of New South Wales Institute of Sport (NSWIS). It has been an absolute honour and delight to not only share my research with you all but also to hear yours. We have had many great discussions on the dynamics of diving over the years and have continued to motivate and inspire each other. Your involvement in Bodies in Space is greatly appreciated and I thank you.

I must thank my colleagues, particularly those of Carslaw 807 who made my time at university most pleasant - notably Danya Rose for helping me with the thesis template, and Matthew Chan, Joshua Ching, and Gemie Nitithumbundit for always making it fun and enjoyable around the office. Outside of university my mum and dad have always been there for me providing tremendous moral support, and I could not have completed my studies without them. Finally, I especially want to thank Melissa Chan, who spent an enormous amount of time and effort proofreading my thesis, not many people would have done what you did for me.

I am truly grateful for the financial support received as a recipient of the Australian Postgraduate Award (APA) and the additional contributions from NSWIS and the ARC grant LP100200245.

Abstract

Platform and springboard diving is a sport involving athletes falling or jumping into a pool of water, usually while performing acrobatic manoeuvres. At the highest level it challenges the physical laws of gravity as athletes try to outperform each other by executing more sophisticated dives. With a mathematical model we are able to assist the athletes and coaches by providing some insight into the mechanics of diving, which hopefully gives them an edge during competition.

In this thesis we begin with an introduction to rigid body dynamics and then extend the results to coupled rigid bodies. We generalise Euler's equations of motion and equations of orientation for rigid bodies to be applicable for coupled rigid bodies. The athlete is represented as a mathematical model consisting of ten simple geometric solids, which is used to conduct three projects within this thesis.

In the first project we look at somersaults without twists, which provides a significant reduction as the model becomes planar. The equations of motion and equations of orientation reduce from vector form to a single scalar differential equation for orientation, since angular momentum is conserved. We digitise footage of an elite diver performing 107B (forward 3.5 somersault in pike) from the 3m springboard, and feed that data into our model for comparison between the theoretically predicted and observed result. We show that the overall rotation obtained by the athlete through somersault is composed of two parts, the major contribution coming from the dynamic phase and a small portion from the geometric phase. We note that by modifying the digitised dive slightly we can leave the dynamic phase intact, but change the geometric phase to provide a small boost in overall rotation. The technique involved in doing so is not practical for actual diving though, so we move away from this idea and devise another way of optimising for the overall rotation. We find that by shape changing in a particular way that takes slightly longer than the fastest way of moving into and out of pike, the overall rotation achieved can be improved by utilising the geometric phase.

In the second project we use the model to simulate divers performing forward m somersaults with n twists. The formulas derived are general, but we will specifically look at 5132D, 5134D, 5136D, and 5138D (forward 1.5 somersaults with 1, 2, 3, and 4 twists) dives. To keep the simulation as simple as possible we reduce the segment count to two by restricting the athlete to only using their left arm about the abduction-adduction plane of motion. We show how twisting somersaults can be achieved in this manner using this simple model with predetermined set of motor actions. The dive mechanics consist of the athlete taking off in pure somersaulting motion, executing a shape change mid-flight to get into twist position, perform twisting somersaults in rigid body motion, and then executing

another shape change to revert the motion back into pure somersaulting motion to complete the dive.

In the third and final project we use our model to show how a 513XD dive (forward 1.5 somersaults with 5 twists) is performed. This complicated dive differs from all currently performed dives in that once the diver initiates twist in the somersaulting motion via shape change, they need to perform another appropriately timed shape change to speed up the twist rather than stopping the twist, and only then is five twists obtainable with practical parameters. Such techniques can be found in aerial skiing where the airborne time is longer, but our theory shows that it may also be applicable to platform and springboard diving too. To date, no athlete has ever attempted a 513XD in competition, nor does the International Swimming Federation (FINA) cover dives with five twists in their degree-of-difficulty formula. Our theory shows that 513XD dive is theoretically possible, and with extrapolation we estimate it would have a degree-of-difficulty of 3.9.

Contents

CHAPTER 1

Introduction

1.1 History and Reading

In platform and springboard diving, a diver will jump from either a high stationary surface known as the platform or a springboard, which is a linear cantilever-type flex-spring usually constructed from a single piece extrusion of aircraft grade aluminum. The platform and springboard are set at different heights to provide sufficient airborne time for the diver to perform various acrobatic manoeuvres before entry into the pool. In competition, performances are judged on the following criteria: form, execution, and degree-of-difficulty.

Platform diving debuted in the 1904 Olympic Games in St. Louis, United States, and featured alongside one other diving event for men - the plunge for distance [58]. The plunge for distance event was essentially a diving long jump, in which athletes dove into the pool from a standing position and remained motionless underwater, using only momentum to propel themselves. The distance was measured after either 60 seconds had elapsed or the moment the athlete's head broke the surface of the water - whichever occurred first. The event proved uninteresting and made no further appearances, instead being replaced with springboard diving in the 1908 Olympic Games. The platform and springboard diving events for women were subsequently introduced in the 1912 and 1920 Olympic Games, respectively. At present, the diving heights used in the Olympic Games are set by the International Swimming Federation (FINA), which are currently fixed at 10m for platform and 3m for springboard. Today, with inclusion of the synchronised diving event introduced in the 2000 Olympic Games, there are now a total of eight diving events.

Fairbanks [19] explores the philosophy behind general teaching techniques for diving with a focus on guiding beginner coaches to teach new athletes correct diving techniques, such as head-first entry into the water. For more advanced coaches and divers, Huber [27], Still and Carter [54] cover all aspects of diving, including coaching, conditioning, and competition. Moriarty [46] discusses the body mechanics involved in springboard diving for the main dive groups, and Batterman [5] adds to this by teaching athletes how to correct and therefore save dives, i.e. to rectify faults in mid-air. His book is aimed at the more advanced diver

and dedicates a chapter on the judging aspect of dives. Another book aimed at both athletes and coaches is by O'Brien [47], which includes a chapter on mental preparation for athletes. O'Brien initially trained as a gymnast and transitioned to diving, later becoming a coach when his athletic career ended. Over many years of coaching he has seen divers of all skill levels, including two-time Olympic gold medalist Greg Louganis [37].

1.2 Principles of Diving

Platform and springboard diving is a sport that challenges the physical laws of gravity as the athletes attempt to outperform each other by executing more sophisticated dives. The athletes must appear graceful while performing these acrobatic manoeuvres, which must be completed within a limited airborne time. Although generally not recognised as a dangerous sport, a dive from the 10m platform will result in the athlete reaching speeds in excess of 50 km/hr before hitting the water. This in itself poses considerable danger for the athlete, as the force upon impact is enough to dislocate joints and break bones. Further discussion on safety concerns, diving accidents and common injuries can be found in Appendix A.

At the Olympic Games, men and women perform six and five dives, respectively. For the individual event there is no limit on the degree-of-difficulty (explained in Appendix C) for each dive, but in the synchronised event the first two dives are assigned a degree-of-difficulty of 2.0, while the remaining dives have no limit.

In springboard diving, men and women must perform a dive in each of five dive groups. The sixth dive for men may be performed in any group, but no identical dive can be repeated. The springboard groups are:

1. **Forward group** - starting position facing water and rotating forward.
2. **Backward group** - starting position with back facing water and rotating backward.
3. **Reverse group** - starting position facing water and rotating backward.
4. **Inward group** - starting position with back facing water and rotating forward.
5. **Twisting group** - any of the above that incorporates twists.

The platform groups are the same but with the addition of the

6. **Armstand group** - divers stand on their hands before releasing into the water.

In platform diving, men must perform a dive in each of the six groups, while women have a choice of which group to omit as they are only required to perform five dives. Once airborne, the diver will adopt one of the following four flight positions:

A. **Straight** - no bend in hips or knees, arms can be wherever the diver chooses.
B. **Pike** - body bent at hips while knees are kept straight with no gap between upper body and legs.

C. **Tuck** - body bent at waist and knees, hands clasping shins.
D. **Free** - used exclusively in twisting dives; it is a combination of straight, pike, and/or tuck.

There are two types of pike: open pike, where hands touch the foot or extend out from the body, and closed pike, where hands clasp behind the calves. In all diving positions, the legs and feet must be held together with toes pointed.

With different combinations of somersaults, dive groups and flight positions, the diver has a large variety of acrobatic manoeuvres at their disposal. To keep the dive description as simple and concise as possible, an alphanumeric code of either four or five digits is used, known as the dive number. We explain how to decipher and write down this code in Appendix B.

To earn a podium finish, athletes must achieve among the three highest total scores across the entire diving event. The athlete's total score is the sum of their individual dive scores, which is the product of two elements - the judges score and the degree-of-difficulty, both of which are explained in Appendix C. Essentially in order to achieve a high score, athletes must not only perform dives with a high degree-of-difficulty, but also perform them consistently well.

In dive groups where athletes perform somersaults without twist (i.e. forward, backward, reverse, and inward) the degree-of-difficulty can be increased in two ways - changing the flight position (e.g. from tuck to pike position) or increasing the number of somersaults. On the other hand, twisting somersaults offer greater scope to increase the degree-of-difficulty - athletes can change the dive type (e.g forward twisting, backward twisting), increase the number of somersaults or twists (or both), and also change flight position (where possible). While the majority of twisting somersaults performed in the 'free' position, some are restricted to the pike or tuck option, e.g. forward 2.5 somersault with 3 twist.

The ability to perform high degree-of-difficulty dives begins at take-off. The number of rotations one is able to perform solely depends on the combination of airborne time and angular momentum, which in turn depend on the vertical and angular velocity produced by the athlete at take-off. We know that athletes diving from both the 10m platform and 3m springboard are airborne for approximately 1.6 seconds before making contact with the water. The airborne times are similar because the springboard allows the diver to take off with a much larger vertical velocity, due to the conversion of stored potential energy within the board into kinetic energy. Divers are able to directly control their airborne time and angular momentum to a certain extent by adjusting their initial vertical and angular velocity at take-off. The relationship between the airborne time T_{air} and initial vertical velocity v_0 is given by

$$T_{air} = \frac{v_0}{g} + \sqrt{\left(\frac{v_0}{g}\right)^2 + \frac{2h}{g}}, \tag{1.1}$$

where we define positive v_0 for the upward velocity, g is the standard gravity constant, and h is the height of the springboard or platform. The angular momentum and angular velocity relationship at the instantaneous moment of take-off is given by

$$\boldsymbol{L} = I\boldsymbol{\Omega}, \tag{1.2}$$

where $\boldsymbol{L}$ is the angular momentum, I the tensor of inertia, and $\boldsymbol{\Omega}$ the angular velocity. This indicates that the angular momentum $\boldsymbol{L}$ is directly related to the shape defined by the tensor of inertia I and the angular velocity $\boldsymbol{\Omega}$ of the diver.

1.3 Literature on Diving

We now review some existing literature on platform and springboard diving. Diving is considered a collision sport because of the impact between the athlete and the water upon entry into the pool, and as with all sports it comes with safety concerns. Based on the research by Bailes, Herman, Quigley et al. [4], Kewalramani and Taylor [32], and Steinbruck and Paelslack [53], we learn that 10% to 20% of all spinal admissions to hospital are the result of recreational diving accidents, most of which are preventable, see Appendix A.

Greg Louganis [37] was an elite American Olympic diver (now turned coach) who won gold medals in both the 10m platform and 3m springboard diving events in the 1984 and 1988 Olympic games. After winning his first pair of gold medals, a study by Miller and Munro [40] examining Greg Louganis' forward and reverse 3m springboard take-off revealed the most notable difference distinguishing him from competitors was his greater range of joint motion (particularly at the knees, hips and shoulders) and straighter arm swing. His take-off duration averaged longer than the mean of all other competitors, allowing him more time to complete joint flexion and extension, thereby giving him an edge in technique over his competitors.

Success in performing high degree-of-difficulty dives depends heavily on the athlete's ability to generate and control the vertical velocity and angular velocity at take-off. Sprigings and Miller [52] found the optimal timing in the knee extension and positioning of the legs relative to the torso during the contact phase in the reverse group, which plays a critical role in determining and/or maximising the vertical and angular velocity at take-off.

Research from Miller, George, Yeadon and Zecevic [39] suggests that the vertical velocity and angular momentum requirements in performing 2.5 pike (105B, 205B, 305B or 405B) and 3.5 tuck somersaults (107C, 207C, 307C or 407C) are comparable. If this is the case, then it is always better to perform the 3.5 tuck over the 2.5 pike to take advantage of the higher degree-of-difficulty associated with the dive, assuming the athlete has equal performance for both manoeuvres.

Miller and Sprigings [42] found that keeping the number of somersaults the same but switching between the tuck and pike position led to little difference between the centripetal forces and/or related muscular efforts on the body. However, increasing the number of somersaults resulted in a notable increase in the resulting joint torques and centripetal forces on the body. These additional muscular efforts may pose a challenge for the diver where additional strength training may be needed to hold form while somersaulting.

Angular momentum contributions from the body segments have been investigated in springboard diving by Miller and Munro [41], and in platform diving by Hamill, Richard, and Golden [23]. Both studies found that at least a third of the total angular momentum contribution was due to the arms. Cheng and Hubbard [11] explored the role of arms in springboard diving from a standing dive, compared to the running dive of Miller and Munro [41]. The requirements in angular momentum for different rotation amounts in springboard diving have been examined by Miller and Sprigings [42], and Sanders and Wilson [51]. It is a critical component in diving, and computational techniques and methods to determine angular momentum of a human body in flight have been studied and discussed by Dapena [14], and Hay, Wilson, and Dapena [26].

Koschorreck and Mombaur [33][34] generate dives through numerical optimisation on a mathematical model consisting of coupled rigid bodies, taking into account that the different phases of a dive are governed by different dynamics. They show that without using prior knowledge of the exact execution of the jump, the optimisation leads to very natural looking dives, confirming that athletes at the elite level are already performing near-optimal dives.

Another major contributing author to diving literature is Yeadon, who has not only written about the physics of twisting somersaults in [71], but also has a four part series on the simulation of aerial movement [62], [63], [64] and [65]. The series begins by capturing an athlete performing a forward somersault with 1.5 twists on trampoline using two film cameras placed orthogonally to each other, with one at the front and the other to the side. He then presents a method to determine the shape and orientation angles of the athlete in [62]. The digitised results are curve fitted and later reused as a comparison mechanism between the measured results and his computer simulation model in [65]. Yeadon follows this with another four part series on the biomechanics of twisting somersaults [66], [67], [68] and [69], in which he provides a theoretical understanding of the production and removal of twists in somersaults using both simple and complex mathematical models. He looks at twist induced at take-off, known as contact twist in [67], and aerial twist, which is initiated after take-off in [68]. Yeadon in [69] analysed footage of elite athletes performing twisting somersaults and was able to partition the tilt angle into contributions of contact techniques, symmetrical configuration changes and asymmetrical arm, chest and hip movements. He found that aerial techniques, particularly the asymmetrical movements, were the main contributing factor to

the total tilt angle responsible for twist, and that less than a quarter of the total tilt was a result of contact techniques. Although the footage used by Yeadon was specifically from trampolining, he speculates that the same conclusion would have been reached from twisting somersaults in other sports, such as diving. In fact, in another study Yeadon [61] found that contact contributions accounted for no more than one sixth of the total tilt angle and that the asymmetries in the arm and hip were the main contributors to the tilt angle.

1.4 Mathematical Models

There are many mathematical models of athletes, with each varying in complexity between authors. Hanavan's model [24] is considered one of the most basic because it only uses fifteen geometrical solids to represent the main body segments of the athlete. In his model, he uses a prolate ellipsoid for the head, a sphere for the hands[1], frustum of a right circular cone for the upper arms, forearms, thighs, shanks, feet, and two right elliptical cylinders for the upper and lower torso. Jensen [30] uses the idea first proposed by Weinbach [59] to construct a sixteen segment model using the elliptical zone method. This involves stacking thin elliptical disks (of approximately 20mm thickness) atop each other to allow for better approximation of each segment.

Cross-sections of body segments modelled by Hanavan [24], Jensen [29], and Hatze [25] have all been ellipses, but Yeadon [63] improves upon this by using stadium cross-sections, stacking stadium solids to model the torso, hands, and feet, where the cross-sections of the head, upper arms, forearms, thighs, and shanks are assumed to remain circular. Yeadon's model consists of 40 solids requiring 95 parameters comprising of 34 lengths, 41 perimeters, 17 widths and 3 depths, although he reduced the segment count to eleven by assuming no movement at the neck, wrists or ankles in his simulations ([64] and [65]). Hatze [25] took 242 anthropometric measurements from a subject for his seventeen segment model. Although the geometry of each segment in Hatze's model is complicated, the dynamics are no more complicated than that of a simple geometric model with the same segment count, which applies to all models discussed above. When looking at the dynamics, the only parameters to enter the model are the tensor of inertia, location of the centre of mass, and joint locations for each body segment. The complicated geometries are only used to determine these three parameters, otherwise they play no role in the dynamics and thus are not considered 'true' parameters. For this reason, we can consider a simple model used by Frohlich [20] when discussing different methods of initiating twisting somersaults, in which he

[1]When referring to spheres and other shapes, we always mean the geometric solids and never simply the shell. A solid sphere is technically a ball, but we will continue to use sphere for consistency with other authors.

proposes a fourteen segment model consisting of cylinders, spheres and a cuboid. Starting with Frohlich's model we will assume, like Yeadon, that the wrists and ankles joints are fixed in order to further reduce the segment count to ten. The hands and feet are relatively light compared to the rest of the body, so motion at these joints can be ignored.

A 10-body model consisting of the torso, head, 2× upper arm, 2× forearm with hand attached, 2× thigh, and shank with foot attached is generally the minimum body fragmentation accepted for a realistic simulation. We can use the mass and dimension parameters listed by Frohlich in Table II of [20] directly, and know that the mass parameters were determined by the mass ratios found by Dyson [17], although rounded slightly to yield more aesthetic numbers in the tensors of inertia. The relative masses listed are within the ranges reported by Dempster [15], but with a higher mass percentage concentrated at the limbs and a lower percentage at the torso. This is to be expected because Dempster's data source came from eight cadavers of typical middle aged and old aged men, whereas we are modelling a typical male athlete and not a typical man. The dimension parameters are also chosen so that if the densities were to be computed by assuming uniform density within each segment, they will give similar results to those obtained by Clauser [13].

We code the body segments of our 10-body model as follows: The torso is known as the reference segment and is denoted by B_{ref}, the head is denoted by B_{head}, and the remaining body segments are coded by a three letter subscript. The first two letters together determine the specific limb of the body, the first being

code	body segment	geometric solid	dimensions (cm)			mass (kg)
B_{ref}	torso	rectangular cuboid	18	30	60	32.400
B_{rup}	right upper arm	cylinder	5	30	-	2.356
B_{rud}	right forearm + hand	cylinder + sphere	4.5	28	5	1.781 + 0.523
B_{rlp}	right thigh	cylinder	8	43	-	8.650
B_{rld}	right shank + foot	cylinder + sphere	5.5	43	7	4.086 + 1.436
B_{hd}	head	sphere	-	-	11	5.575
B_{lup}	left upper arm	cylinder	5	30	-	2.356
B_{lud}	left forearm + hand	cylinder + sphere	4.5	28	5	1.781 + 0.523
B_{llp}	left thigh	cylinder	8	43	-	8.650
B_{lld}	left shank + foot	cylinder + sphere	5.5	43	7	4.086 + 1.436

Table 1.1. Body segments, geometric descriptions and masses for our model. The athlete is a male of 75.639 kg and 1.820 metres in height. The torso dimensions are given in order of length, width and height, but for every other segment the columns denote radius of the cylinder, height of cylinder and the radius of sphere, respectively. A hyphen is used for any field not applicable to the solid.

either left (l) or right (r), and the second being the upper limb (u) or lower limb (l). The third letter distinguishes between the proximal (p) (closer to the body, e.g. upper arm) and distal (d) segment (further away from body, e.g. forearm) of that limb. We choose to label the segments with letters instead of numeric values for easier distinction of the body segments. The complete description of each body segment in our model is listed in Table 1.1.

1.5 Summary

In this thesis all parameters introduced take on standard SI units unless explicitly indicated, e.g. tensor of inertia is measured in $kg \cdot m^2$, angular momentum in $kg \cdot m^2/s$, etc. At the start of each chapter we will provide a detailed outline of what is to be covered in each subsection, so only a brief summary is provided here.

In Chapter 2 we provide an overview of the fundamentals of rigid body dynamics, covering aspects including frames of reference, angular velocity, tensor of inertia, and angular momentum. We also derive the equations of motion and equations of orientation for a rigid body, and find explicit solutions for the case when two moments of inertia are equal.

In Chapter 3 we move to a system of n coupled rigid bodies and generalise the equations of motion and equations of orientation. We use Table 1.1 to define the geometry of the athlete, specify how segments are connected, and provide the technical specification of the modelled athlete. The next three chapters form the main focus of this thesis.

In Chapter 4 we look at planar somersaults, derive the scalar variant of the equations of motion, and analyse digitised footage of an elite athlete performing 107B dive off the 3m springboard, where consistency is demonstrated between the model's predicted result and the observed result from the digitised footage.

We then show that the dive with maximal overall rotation does not involve the athlete moving into and out of pike as fast as possible, so that time spent in pike is maximised. Instead, the optimisation shows that the athlete has asymmetrical movement (meaning longer shape change and less time in pike) which utilises the geometric phase to gain the additional rotation.

In Chapter 5 we use the full form of the equations of motion and equations of orientation to simulate twisting somersaults with a 2-body model using the following five stage dive mechanics:

$$\begin{array}{c}\text{pure}\\ \text{somersault}\end{array} \longrightarrow \begin{array}{c}\text{shape}\\ \text{change}\end{array} \longrightarrow \begin{array}{c}\text{twisting}\\ \text{somersault}\end{array} \longrightarrow \begin{array}{c}\text{shape}\\ \text{change}\end{array} \longrightarrow \begin{array}{c}\text{pure}\\ \text{somersault}\end{array}$$

The pure and twisting somersault stages are in rigid body motion and the shape changes are predetermined. We find the parameters needed to make this dive work numerically for realistic shape changes, but an analytical result can be obtained when the shape changes become impulsive. Particular attention is given to dives

consisting of forward 1.5 somersault with different number of twists, i.e. 5132D, 5134D, 5136D, and 5138D.

In Chapter 6 we extend the ideas of Chapter 5 by introducing a nine stage dive, allowing the diver to utilise additional shape changes to enter a faster twisting orbit, where the dive mechanics are:

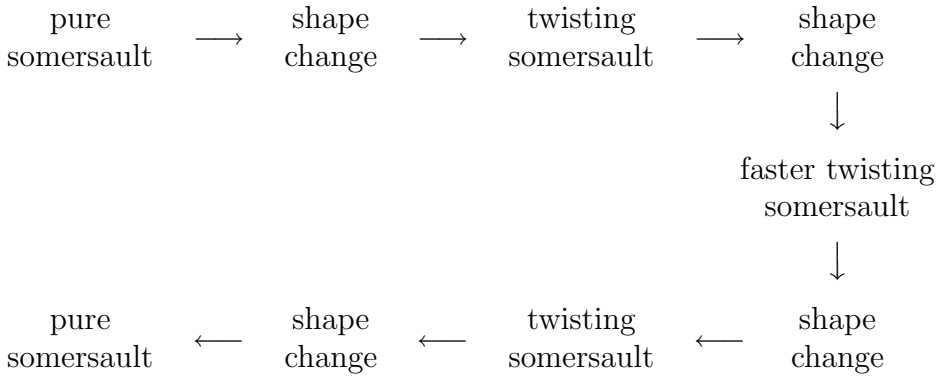

We show with both the 2-body and 3-body models that more twists can be obtained in this manner without any additional cost of angular momentum or airborne time, thus allowing the diver to perform 513XD (forward twisting 1.5 somersault with 5 twists) in reality, where X is used to represent 10 to keep the diving code notation consistent. This new dive is yet to be attempted in competition, and its degree-of-difficulty cannot even be calculated using FINA's degree-of-difficulty formula given in Appendix C. Extrapolating the degree-of-difficulty for 5132D, 5134D, 5136D, and 5138D we estimate the degree-of-difficulty of 513XD to be 3.9. We conclude by demonstrating that it is even possible for an athlete to take-off in pure somersault and transition into pure twist (a state where the rotation is strictly about the twist axis and there is no somersaulting motion at all) given a large enough airborne time, which is achieved through simply using multiple shape changes that are appropriately timed. The theory provides useful insight into the limitations of what athletes can achieve in the twisting somersault.

CHAPTER 2

Rigid Body Dynamics

We start by deriving and setting up the necessary foundations for rigid body dynamics. To describe the motion of a rigid body we need to specify its position and orientation in space as a function of time. We do this by introducing different frames of reference, namely the space and body frame in Chapter 2.1. The velocity of a rigid body can be decomposed into a combination of linear and angular velocity, where the former describes translational motion and the latter rotational motion. The total amount of rotation the body has is described by the angular momentum, which not only takes into account the angular velocity but also the mass and shape defined by the tensor of inertia. In Chapters 2.2 to 2.5 we define these quantities in different frames and write down the relationship connecting the angular momentum, tensor of inertia and angular velocity, which verifies the well known (1.2) in the body frame.

To describe the orientation of a rigid body we review Euler angles in Chapter 2.6, and quaternions in Chapter 2.7, both of which can be used to describe the orientation of the rigid body in 3D space. We then derive the equations of motion and solve it for the case of two moments of inertia being equal in Chapter 2.8. Rotational stability of the equilibrium solutions for angular momentum are examined in Chapter 2.9, and we quote the general solution to the equations of motion as given, e.g. by Landau and Lifshitz [**35**], Gradshteyn and Ryzhik [**22**], Rauch and Lebowitz [**50**]. Magnus series is presented in Chapter 2.10 to provide an exponential representation of the series solution for a n-dimensional first order homogeneous differential equation, which is later needed in Chapter 5 when we look at twisting somersaults. Finally, in Chapter 2.11 we derive the equations of orientation both in terms of Euler angles and quaternions which describe the orientation of the rigid body as a function of time.

2.1 Frames of Reference

There are usually two frames of reference associated with a rigid body B of mass m when looking at the dynamics - a coordinate system attached to the body (referred to as the body-fixed-frame) denoted by $\mathcal{F}_B$, and an inertial spatial frame $\mathcal{F}_{S_F}$. The energy and angular momentum of B can be expressed as a sum of two contributions, the motion of the centre of mass (translation) and the motion about the centre of mass (rotation). We choose the origin of $\mathcal{F}_B$ to coincide with the centre of mass of B, which allows us to completely separate the translational and rotational motions of the rigid body. Now consider a point $\boldsymbol{Q}$ on B viewed from $\mathcal{F}_B$, then that same point observed from $\mathcal{F}_{S_F}$ will be represented as $\boldsymbol{q}$. In general, uppercase letters will be used to denote points and position vectors measured in the body frame, and lowercase letters will be used for the spatial frame equivalent. This allows us to write the relation

$$\boldsymbol{q} = \boldsymbol{c} + R\boldsymbol{Q}. \tag{2.1}$$

Here, R is a rotation matrix that parallelises the coordinate axes of $\mathcal{F}_B$ with $\mathcal{F}_{S_F}$, and $\boldsymbol{c}$ is the translation from the origin of $\mathcal{F}_{S_F}$ to the origin of $\mathcal{F}_B$, which is also the position vector for the centre of mass of B. Now as B moves, we see that

$$\dot{\boldsymbol{q}} = \dot{\boldsymbol{c}} + \dot{R}\boldsymbol{Q}. \tag{2.2}$$

Since $\mathcal{F}_B$ moves with B the point appears motionless in the body frame, which explains why no $\dot{\boldsymbol{Q}}$ term appears in (2.2). In the absence of external forces $\dot{\boldsymbol{c}}$ is a constant vector, so choosing the inertial spatial frame to be the one with $\boldsymbol{c} = \boldsymbol{0}$ eliminates both $\boldsymbol{c}$ and $\dot{\boldsymbol{c}}$. In the presence of a constant force (e.g. gravity) we can still temporarily ignore the centre of mass motion to work out the dynamics without $\boldsymbol{c}$, and then later incorporate $\boldsymbol{c}$ into the final result. The displacement of the centre of mass $\boldsymbol{c}$ of a rigid body in a constant force is fairly simple and is

$$\boldsymbol{c} = \frac{1}{2}\boldsymbol{a}t^2 + \boldsymbol{v}_0 t + \boldsymbol{c}_0, \tag{2.3}$$

where $\boldsymbol{a}$ is the constant acceleration, $\boldsymbol{v}_0$ the initial velocity, and $\boldsymbol{c}_0$ the initial displacement of the rigid body. In the case where we associate the rigid body as a diver taking off the platform or springboard with horizontal velocity v_x and vertical velocity v_z, we get $\boldsymbol{a} = (0, 0, -g)^t$ and $\boldsymbol{v}_0 = (v_x, 0, v_z)^t$, where g is the standard gravity constant. To examine the rotational motion of the rigid body we introduce a new frame called the space-parallel-frame, denoted by $\mathcal{F}_S$. This frame is comoving but not corotating with the body, so the origin of $\mathcal{F}_S$ moves along with the centre of mass, but does not rotate with B, meaning that the origin of $\mathcal{F}_S$ coincides with the origin of $\mathcal{F}_B$ while the coordinate axes of $\mathcal{F}_S$ remain parallel to $\mathcal{F}_{S_F}$. This frame is non-inertial in an environment with external forces, but only in translations and not rotations. For this reason we still refer to $\mathcal{F}_S$ as a spatial frame since the orientation of the coordinate axes do not change, and in

the absence of forces we could in fact choose $\mathcal{F}_S$ to be the same as $\mathcal{F}_{S_F}$. The case we're interested in is for a constant force, so the translational motion we get from (2.3) needs to be incorporated in the final result, thereby requiring the need for all three frames $\mathcal{F}_{S_F}, \mathcal{F}_S$ and $\mathcal{F}_B$. For a vector $\boldsymbol{\mathcal{V}}$ the transformation formulas to allow conversion between frames are

$$\boldsymbol{\mathcal{V}}_{S_F} = \boldsymbol{c} + \boldsymbol{\mathcal{V}}_S \qquad\qquad \boldsymbol{\mathcal{V}}_S = R\boldsymbol{\mathcal{V}}_B, \tag{2.4}$$

where the subscripts denote the frame in which the vector $\boldsymbol{\mathcal{V}}$ is written in. With the use of $\mathcal{F}_S$ and $\mathcal{F}_B$ without $\mathcal{F}_{S_F}$, translational motion is lost within the body, but the rotational motion is maintained. This is fine though as we have (2.3) to describe the translational motion, so we will generally disregard $\mathcal{F}_{S_F}$ and only use it to show animated dives.

2.2 Angular Velocity & Angular Momentum

The velocity of $\boldsymbol{q}$ in $\mathcal{F}_{S_F}$ is often separated into a combination of linear and angular velocity. In many classical mechanics textbooks, e.g. Chow [12], Goldstein [21], Landau and Lifshitz [35], we see the following equation

$$\dot{\boldsymbol{q}} = \dot{\boldsymbol{c}} + \boldsymbol{\omega} \times (\boldsymbol{q} - \boldsymbol{c}) = \dot{\boldsymbol{c}} + \boldsymbol{\omega} \times R\boldsymbol{Q}, \tag{2.5}$$

where $\dot{\boldsymbol{c}}$ is the linear velocity of the centre of mass of B, $\boldsymbol{\omega}$ is the angular velocity vector of the rotating body lying along the axis of rotation, and $R\boldsymbol{Q}$ is the position vector from the centre of mass to the point on B, all of which are viewed in $\mathcal{F}_{S_F}$.

The angular momentum of B about the centre of mass in $\mathcal{F}_S$ is given by

$$\boldsymbol{l} = \int_B \rho(\boldsymbol{q} - \boldsymbol{c}) \times (\dot{\boldsymbol{q}} - \dot{\boldsymbol{c}}) \, \mathrm{d}\boldsymbol{Q}, \tag{2.6}$$

where ρ is the density of B. Substituting (2.1) and (2.5) into the angular momentum equation (2.6) shows that

$$\begin{aligned} \boldsymbol{l} &= \int_B \rho R\boldsymbol{Q} \times (\boldsymbol{\omega} \times R\boldsymbol{Q}) \, \mathrm{d}\boldsymbol{Q} \\ &= \int_B \rho \left((R\boldsymbol{Q} \cdot R\boldsymbol{Q})\boldsymbol{\omega} - (R\boldsymbol{Q} \cdot \boldsymbol{\omega}) R\boldsymbol{Q} \right) \mathrm{d}\boldsymbol{Q} \\ &= \int_B \rho (|\boldsymbol{Q}|^2 \mathbb{1} - R\boldsymbol{Q}\boldsymbol{Q}^t R^t)\boldsymbol{\omega} \, \mathrm{d}\boldsymbol{Q} \\ &= R \int_B \rho (|\boldsymbol{Q}|^2 \mathbb{1} - \boldsymbol{Q}\boldsymbol{Q}^t) \, \mathrm{d}\boldsymbol{Q} \; R^{-1}\boldsymbol{\omega}, \end{aligned} \tag{2.7}$$

where the vector identity

$$\boldsymbol{a} \times (\boldsymbol{b} \times \boldsymbol{c}) = (\boldsymbol{a} \cdot \boldsymbol{c})\boldsymbol{b} - (\boldsymbol{a} \cdot \boldsymbol{b})\boldsymbol{c} \tag{2.8}$$

and $RR^{-1} = RR^t = \mathbb{1}$ were used in the simplification of (2.7).

2.3 Tensor of Inertia

The integral that appears in (2.7) is known as the tensor of inertia of B, which is a quantity expressing the rigid body's tendency to resist angular acceleration, and can be used to determine the torque needed for a desired angular acceleration about an arbitrary axis of rotation. Specifically it is

$$J = \int_B \rho \left(|\boldsymbol{Q}|^2 \mathbb{1} - \boldsymbol{Q}\boldsymbol{Q}^t \right) \, \mathrm{d}\boldsymbol{Q} \tag{2.9}$$

when viewed in $\mathcal{F}_B$ and written about the centre of mass of B. If we write out the components explicitly as

$$\boldsymbol{Q} = \begin{pmatrix} Q_x \\ Q_y \\ Q_z \end{pmatrix} \text{ and} \tag{2.10}$$

$$J = \begin{pmatrix} J_{xx} & J_{xy} & J_{xz} \\ J_{yx} & J_{yy} & J_{yz} \\ J_{zx} & J_{zy} & J_{zz} \end{pmatrix}, \tag{2.11}$$

we see that the diagonal entries of the tensor give

$$\begin{aligned} J_{xx} &= \int_B \rho(Q_y^2 + Q_z^2) \, \mathrm{d}\boldsymbol{Q} \\ J_{yy} &= \int_B \rho(Q_x^2 + Q_z^2) \, \mathrm{d}\boldsymbol{Q} \\ J_{zz} &= \int_B \rho(Q_x^2 + Q_y^2) \, \mathrm{d}\boldsymbol{Q}. \end{aligned}$$

These quantities are called the moments of inertia with respect to the x, y and z-axis, respectively. Each integrand contains the distance square to one of the axes, so the moments of inertia are always positive. Now the non-diagonal entries are

$$\begin{aligned} -J_{xy} = -J_{yx} &= \int_B \rho \, Q_x Q_y \, \mathrm{d}\boldsymbol{Q} \\ -J_{xz} = -J_{zx} &= \int_B \rho \, Q_x Q_z \, \mathrm{d}\boldsymbol{Q} \\ -J_{yz} = -J_{zy} &= \int_B \rho \, Q_y Q_z \, \mathrm{d}\boldsymbol{Q}, \end{aligned}$$

and these quantities are called the products of inertia. Unlike the moments of inertia, these terms can be positive, negative or zero, and are a measure of the imbalance in the mass distribution relative to $\mathcal{F}_B$. It follows from the definition of the products of inertia that the tensor of inertia is always symmetric, and it is always possible to find a set of coordinate axes in which the products of inertia

are all zero, even when there is no symmetry in the body. This means the tensor of inertia can be made diagonal when we choose an appropriate body-fixed-frame that results in the coordinate axes of $\mathcal{F}_B$ being aligned with the principal axes of inertia.

Suppose that I is a non-diagonal tensor of inertia in some other body-fixed-frame $\mathcal{F}_C$ (which will play an important role in coupled rigid bodies), then there is always a transformation

$$J = R_\xi^{-1} I R_\xi \tag{2.12}$$

with some rotation matrix R_ξ that makes J diagonal in $\mathcal{F}_B$. Finding this frame is a characteristic value problem, where the eigenvectors of I give the direction of the principal axes, the eigenvalues are the moments of inertia for J, and the rotation matrix R has the orthonormalised eigenvectors of I as columns. Consider a simpler case where

$$I = \begin{pmatrix} I_{xx} & 0 & 0 \\ 0 & I_{yy} & I_{yz} \\ 0 & I_{yz} & I_{zz} \end{pmatrix} \quad \text{in } \mathcal{F}_C. \tag{2.13}$$

We wish to find a rotation matrix R_ξ so that J in $\mathcal{F}_B$ is diagonal with $J = \text{diag}(J_x, J_y, J_z)$. This can be achieved by a rotation about the x-axis, so if we let ξ be the angle of rotation and multiply out the transformation, this gives

$$\begin{aligned} J_x &= I_{xx} \\ J_y &= I_{yy}\cos^2\xi + I_{zz}\sin^2\xi + I_{yz}\sin 2\xi \\ J_z &= I_{yy}\sin^2\xi + I_{zz}\cos^2\xi - I_{yz}\sin 2\xi, \end{aligned} \tag{2.14}$$

and for the non-diagonal entries to be zero we need

$$\frac{1}{2}(I_{zz} - I_{yy})\sin 2\xi + I_{yz}\cos 2\xi = 0. \tag{2.15}$$

Choosing the smallest ξ that satisfies this equation, we find that

$$\xi = \frac{1}{2}\arctan\left(\frac{2I_{yz}}{I_{yy} - I_{zz}}\right). \tag{2.16}$$

In this example the transformation leaves the x-component of the moment of inertia intact because both R_ξ and R_ξ^{-1} are rotations about the x-axis.

If at times we want to the know the tensor of inertia $\tilde{J}$ about an arbitrary point instead of its centre of mass, it is often easiest to use the parallel axis theorem. The theorem decomposes $\tilde{J}$ into the sum of two tensors, the tensor of inertia J about the centre of mass, and a tensor in terms of the displacement vector $\boldsymbol{C}$ from the point of interest to the centre of mass. Any point on B from the point of

interest is now given by $\boldsymbol{C}+\boldsymbol{Q}$, so the tensor of inertia $\tilde{J}$ can be written as

$$\begin{aligned}\tilde{J} &= \int_B \rho\left(|\boldsymbol{C}+\boldsymbol{Q}|^2\mathbb{1} - (\boldsymbol{C}+\boldsymbol{Q})(\boldsymbol{C}+\boldsymbol{Q})^t\right)\,\mathrm{d}\boldsymbol{Q}\\ &= J + \int_B \rho\big(2(\boldsymbol{C}\cdot\boldsymbol{Q})\mathbb{1} - \boldsymbol{C}\boldsymbol{Q}^t - \boldsymbol{Q}\boldsymbol{C}^t\big)\,\mathrm{d}\boldsymbol{Q} + \int_B \rho\,\mathrm{d}\boldsymbol{Q}\Big(|\boldsymbol{C}|^2\mathbb{1} - \boldsymbol{C}\boldsymbol{C}^t\Big)\\ &= J + m\left(|\boldsymbol{C}|^2\mathbb{1} - \boldsymbol{C}\boldsymbol{C}^t\right),\end{aligned} \tag{2.17}$$

where to simplify the result we used

$$\int_B \rho\,\mathrm{d}\boldsymbol{Q} = m \qquad\qquad \int_B \rho\,\boldsymbol{Q}\,\mathrm{d}\boldsymbol{Q} = \mathbf{0}. \tag{2.18}$$

The left integral states that integrating the density over B gives the mass m, while the right integral gives the weighted position of the body times mass which is simply $\mathbf{0}$ in $\mathcal{F}_B$, since we picked the centre of mass to be at the origin.

2.4 Body Segment Inertias

The complete description of each body segment in our model is listed in Table 1.1. The torso B_{ref} is modelled as a rectangular cuboid, B_{hd} as a sphere, $B_{rup}, B_{rlp}, B_{lup}$, and B_{llp} as cylinders, and $B_{rud}, B_{rld}, B_{lud}$, and B_{lld} as cylinders with spheres attached, see Figure 2.1 for illustrations. We now use (2.9) to compute the tensor of inertia in the principal axes frame $\mathcal{F}_B$ for

- a rectangular cuboid of mass m, length l, width w and height h
- a cylinder of mass m, radius p and height h
- a sphere of mass m and radius r,

and if we assume uniform density for these solids we get

- $J_{cub} = \frac{m}{12}\,\mathrm{diag}\,(w^2+h^2, l^2+h^2, l^2+w^2)$
- $J_{cyl} = \frac{m}{12}\,\mathrm{diag}\,(3p^2+h^2, 3p^2+h^2, 6p^2)$
- $J_{sph} = \frac{2mr^2}{5}\mathbb{1}$.

The tensor of inertia for the cylinder with sphere attached (Figure 2.1D) is computed using the parallel axis theorem (2.17). Note that the while density of the combined solid may not be uniform, the individual cylinder and sphere components by themselves are. Now let the position vectors $\boldsymbol{C}_c$ and $\boldsymbol{C}_s$ denote the position vectors from the centre of mass (origin) to the centre of cylinder and to the centre of sphere, respectively. Then clearly both the x and y components of $\boldsymbol{C}_c$ and $\boldsymbol{C}_s$ are zero, and we can write $\boldsymbol{C}_c = (0,0,C_c)^t, \boldsymbol{C}_s = (0,0,C_s)^t$. The z components are then obtained by solving

$$\begin{aligned} m_c C_c + m_s C_s &= 0 \qquad \text{and}\\ C_c - C_s &= \frac{h}{2} + r \qquad \text{simultaneously,}\end{aligned}$$

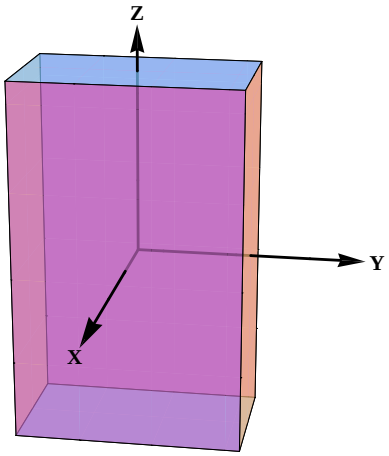

(A) Rectangular cuboid.

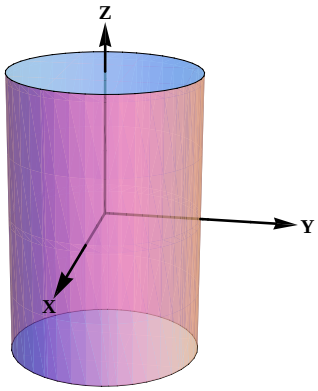

(B) Cylinder.

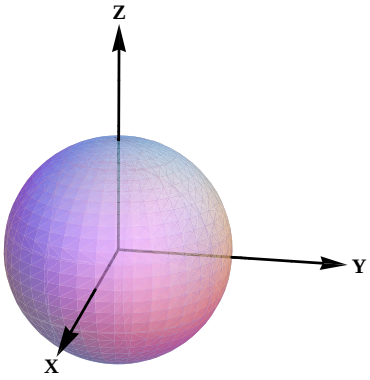

(C) Sphere.

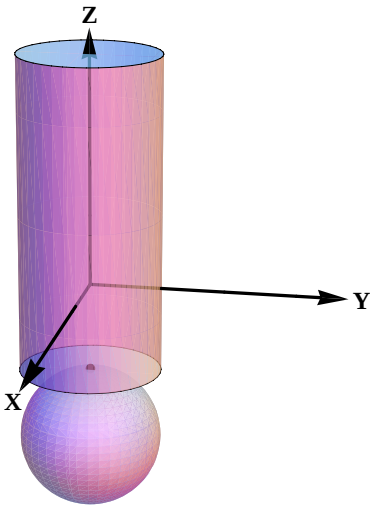

(D) Cylinder with sphere.

Figure 2.1. The different geometric solids used in our model. The local coordinate system $\mathcal{F}_{B_i}$ attached to each solid has its origin coinciding with the centre of mass and its axes aligned with the principal axes of inertia as shown.

where m_c is the mass component of the cylinder, m_s the mass of sphere, h the height of cylinder, and r the radius of sphere. These two equations appear from the centre of mass constraint, with the distance between the cylinder and sphere centres being constant. Solving for the centres yields

$$C_c = \frac{m_s}{m_c + m_s}\left(\frac{h}{2} + r\right) \qquad C_s = -\frac{m_c}{m_c + m_s}\left(\frac{h}{2} + r\right). \tag{2.19}$$

Using the parallel axis theorem (2.17) to add the tensor of inertia together about the overall centre of mass, we get

$$J_{cyl+sph} = J_{cyl} + J_{sph} + m_c[(\boldsymbol{C}_c \cdot \boldsymbol{C}_c)\mathbb{1} - \boldsymbol{C}_c\boldsymbol{C}_c^t] + m_s[(\boldsymbol{C}_s \cdot \boldsymbol{C}_s)\mathbb{1} - \boldsymbol{C}_s\boldsymbol{C}_s^t].$$

Specifically for our model, using the dimension parameters from Table 1.1, we find the tensor of inertia to be:

- $J_{ref} = \text{diag}\,(1.215, 1.059, 0.330)$
- $J_{rup} = J_{lup} = \text{diag}\,(0.019, 0.019, 0.003)$
- $J_{rud} = J_{lud} = \text{diag}\,(0.028, 0.028, 0.002)$
- $J_{rlp} = J_{llp} = \text{diag}\,(0.147, 0.147, 0.028)$
- $J_{rld} = J_{lld} = \text{diag}\,(0.155, 0.155, 0.009)$
- $J_{hd} = \text{diag}\,(0.027, 0.027, 0.027)$.

Due to the high symmetry of the body segments, a total of twelve parameters are needed to describe the tensors of inertia for our mathematical model.

2.5 Angular Velocity & Angular Momentum 2

The symbols used for angular momentum, tensor of inertia, and angular velocity in different frames are shown in Table 2.1. The concepts of angular momentum and angular velocity viewed in $\mathcal{F}_S$ are well understood, but in other frames there may be confusion as to what these quantities actually mean, e.g. in body frames there are no rotations observed since the frame itself is attached to the body. As such, we want to emphasise that vectors are actually obtained from $\mathcal{F}_S$ and simply rewritten in the appropriate frame.

We now show the equation (1.2) which relates the angular momentum, tensor of inertia, and angular velocity, is true in all frames provided all quantities are

	Frame		
	$\mathcal{F}_S$	$\mathcal{F}_B$	$\mathcal{F}_C$
angular momentum	$\boldsymbol{l}$	$\boldsymbol{M}$	$\boldsymbol{L}$
tensor of inertia	I_S	J	I
angular velocity	$\boldsymbol{\omega}$	$\boldsymbol{\mathcal{W}}$	$\boldsymbol{\Omega}$

Table 2.1. Symbols for different quantities in different frames.

written in the same frame. Substituting the tensor of inertia (2.9) into (2.7) we find

$$\boldsymbol{l} = RJR^{-1}\boldsymbol{\omega}, \tag{2.20}$$

so for (1.2) to be true in $\mathcal{F}_S$ we need

$$I_S = RJR^{-1}, \tag{2.21}$$

which is the same transformation seen in (2.12) for converting tensors between frames, thus we know for a fact that I_S is the tensor of inertia in $\mathcal{F}_S$, hence (1.2) holds in $\mathcal{F}_S$.

Let R be the rotation matrix that transforms quantities from $\mathcal{F}_B$ to $\mathcal{F}_S$, where the transformation is given by (2.4). We can rewrite all quantities of (2.7) to $\mathcal{F}_B$ and get

$$R\boldsymbol{M} = RJR^{-1}R\boldsymbol{\mathcal{W}} \implies \boldsymbol{M} = J\boldsymbol{\mathcal{W}}, \tag{2.22}$$

which shows (1.2) holds in $\mathcal{F}_B$. Finally, let R_ξ transform quantities from $\mathcal{F}_B$ to $\mathcal{F}_C$, then converting all quantities in (2.22) to $\mathcal{F}_C$ shows (1.2). To summarise the different transformations we have:

$\mathcal{F}_S \to \mathcal{F}_B$	$\mathcal{F}_S \to \mathcal{F}_C$	$\mathcal{F}_C \to \mathcal{F}_B$
$R^{-1}\boldsymbol{l} = \boldsymbol{M}$	$R_\xi R^{-1}\boldsymbol{l} = \boldsymbol{L}$	$R_\xi^{-1}\boldsymbol{L} = \boldsymbol{M}$
$R^{-1}\boldsymbol{\omega} = \boldsymbol{\mathcal{W}}$	$R_\xi R^{-1}\boldsymbol{\omega} = \boldsymbol{\Omega}$	$R_\xi^{-1}\boldsymbol{\Omega} = \boldsymbol{\mathcal{W}}$
$R^{-1}I_sR = J$	$R_\xi R^{-1}I_sRR_\xi^{-1} = I$	$R_\xi^{-1}IR_\xi = J$

$\mathcal{F}_B \to \mathcal{F}_S$	$\mathcal{F}_C \to \mathcal{F}_S$	$\mathcal{F}_B \to \mathcal{F}_C$
$R\boldsymbol{M} = \boldsymbol{l}$	$RR_\xi^{-1}\boldsymbol{L} = \boldsymbol{l}$	$R_\xi\boldsymbol{M} = \boldsymbol{L}$
$R\boldsymbol{\mathcal{W}} = \boldsymbol{\omega}$	$RR_\xi^{-1}\boldsymbol{\Omega} = \boldsymbol{\omega}$	$R_\xi\boldsymbol{\mathcal{W}} = \boldsymbol{\Omega}$
$RJR^{-1} = I_s$	$RR_\xi^{-1}IR_\xi R^{-1} = I_s$	$R_\xi JR_\xi^{-1} = I.$

(2.23)

From the angular velocity vector $\boldsymbol{\omega} = \begin{pmatrix} \omega_x \\ \omega_y \\ \omega_z \end{pmatrix}$, we can introduce the angular velocity tensor $\hat{\boldsymbol{\omega}} = \begin{pmatrix} 0 & -\omega_z & \omega_y \\ \omega_z & 0 & -\omega_x \\ -\omega_y & \omega_x & 0 \end{pmatrix}$. As the cross product is a linear transformation, it can be represented as a matrix. The tensor $\hat{\boldsymbol{\omega}}$ acts as if it were a $\boldsymbol{\omega}\times$ operator. Comparing (2.5) with (2.2) we see that
$\boldsymbol{\omega} \times R\boldsymbol{Q} = \dot{R}\boldsymbol{Q} \implies \boldsymbol{\omega}\times = \dot{R}R^{-1}$, i.e.

$$\hat{\boldsymbol{\omega}} = \dot{R}R^t. \tag{2.24}$$

This shows that $\hat{\boldsymbol{\omega}}$ can in fact be written in terms of rotation matrices. The equivalent of (2.24) in $\mathcal{F}_B$ is found with the transformation (2.23) and shows

$$\hat{\boldsymbol{\mathcal{W}}} = R^{-1}\hat{\boldsymbol{\omega}}R = R^{-1}\dot{R}R^tR = R^t\dot{R}, \tag{2.25}$$

which can be rearranged to get

$$\dot{R} = R\hat{\boldsymbol{\mathcal{W}}}. \tag{2.26}$$

The tensor $\hat{\boldsymbol{\mathcal{W}}}$ is a skew symmetric matrix just like $\hat{\boldsymbol{\omega}}$, which can be proved simply by considering $R^tR = \mathbb{1}$. Differentiating both sides gives

$$\begin{aligned} \dot{R}^tR + R^t\dot{R} &= \mathbf{0} \\ (R^t\dot{R})^t + R^t\dot{R} = \mathbf{0} \implies \hat{\boldsymbol{\mathcal{W}}} &= -\hat{\boldsymbol{\mathcal{W}}}^t. \end{aligned}$$

The result in (2.20) can be written as

$$\boldsymbol{l} = RJ\boldsymbol{\mathcal{W}} = R\boldsymbol{M}, \tag{2.27}$$

which can alternatively be derived from substituting (2.1) and (2.2) into (2.6), and then eliminating $\dot{R}$ with (2.26). With this approach we get

$$\begin{aligned} \boldsymbol{l} &= \int_B \rho R\boldsymbol{Q} \times \dot{R}\boldsymbol{Q}\,\mathrm{d}\boldsymbol{Q} \\ &= R\int_B \rho\,\boldsymbol{Q} \times \hat{\boldsymbol{\mathcal{W}}}\boldsymbol{Q}\,\mathrm{d}\boldsymbol{Q} \\ &= R\int_B \rho\,\boldsymbol{Q} \times (\boldsymbol{\mathcal{W}} \times \boldsymbol{Q})\,\mathrm{d}\boldsymbol{Q} \\ &= R\int_B \rho\,[(\boldsymbol{Q}\cdot\boldsymbol{Q})\boldsymbol{\mathcal{W}} - (\boldsymbol{Q}\cdot\boldsymbol{\mathcal{W}})\boldsymbol{Q}]\,\mathrm{d}\boldsymbol{Q} \\ &= R\int_B \rho\left(|\boldsymbol{Q}|^2\mathbb{1} - \boldsymbol{Q}\boldsymbol{Q}^t\right)\mathrm{d}\boldsymbol{Q}\;\boldsymbol{\mathcal{W}} \\ &= RJ\boldsymbol{\mathcal{W}} = R\boldsymbol{M} \text{ as expected.} \end{aligned} \tag{2.28}$$

2.6 Euler Angles

A total of six independent coordinates are needed to fully describe the motion of a rigid body. Three generalised coordinates are used to describe translation, i.e. $\boldsymbol{c}$ in (2.1), and three for orientation, i.e. R in (2.1). There are different methods of obtaining the rotation matrix R, but two common conventions are with Euler angles or with unit quaternions. We will generally use quaternions in our study, but under certain circumstances it may be useful to express the orientation in terms of Euler angles instead.

To describe an arbitrary orientation of a body in space, three elemental rotations can be used. An elemental rotation is one of

$$R_x(\xi) = \begin{pmatrix} 1 & 0 & 0 \\ 0 & \cos\xi & -\sin\xi \\ 0 & \sin\xi & \cos\xi \end{pmatrix} \qquad R_y(\xi) = \begin{pmatrix} \cos\xi & 0 & \sin\xi \\ 0 & 1 & 0 \\ -\sin\xi & 0 & \cos\xi \end{pmatrix}$$

$$R_z(\xi) = \begin{pmatrix} \cos\xi & -\sin\xi & 0 \\ \sin\xi & \cos\xi & 0 \\ 0 & 0 & 1 \end{pmatrix}.$$

Euler angles use three parameters (ϕ, θ, ψ) to form a sequence of these elemental rotations. We may write

$$R = R_a(\phi) R_b(\theta) R_c(\psi), \tag{2.29}$$

where each subscript denotes an axis of rotation about a coordinate axis that is yet to be specified, but is either the x-axis, y-axis or z-axis. For the rotation sequence to be non-degenerate, we also require $a \neq b$ and $b \neq c$. With Euler angles the ordering of the rotation axis is not unique, but can be subdivided into two groups, classic-Euler angles and Tait-Bryan angles.[1] There are six possible sequences for each of the two groups, which are:

classic-Euler angles: $R_z R_y R_z, R_y R_x R_y, R_x R_z R_x, R_z R_x R_z, R_y R_z R_y, R_x R_y R_x$

Tait-Bryan angles: $R_z R_y R_x, R_y R_x R_z, R_x R_z R_y, R_z R_x R_y, R_x R_y R_z, R_y R_z R_x$

Classic-Euler angles have a rotation sequence of $R_a R_b R_a$ where the first and last elemental rotations are about the same axis, which exploit the fact that rotations in 3D space are not commutative (unless $\theta = 0$). These angles can be interpreted as precession, nutation and spin, respectively. On the other hand, Tait-Bryan angles use all distinct axes of rotation (a convention more commonly associated with aeronautical engineering), where the angles represent yaw, pitch, and roll, or sometimes called heading, elevation, and bank instead.

The rotation sequence given in (2.29) has two interpretations, i.e., the three elemental rotations can be executed *extrinsically* or *intrinsically*. Extrinsic rotations are performed in order of ψ, θ, then ϕ, resulting in rotations corresponding to c-b-a of the fixed spatial axes of $\mathcal{F}_S$. Intrinsic rotations, however, are performed in inverted order of the Euler angles (i.e. ϕ, θ, then ψ), meaning the order of the rotations are about a-b'-c'' of the body frame $\mathcal{F}_B$, in which $'$ and $''$ denote intermediate body frames. In both instances, the final orientation of the body remains the same. The ordering of extrinsic rotations is clear and given directly by (2.29), but for intrinsic rotations we have

$$R = R_{c''}(\psi) R_{b'}(\theta) R_a(\phi). \tag{2.30}$$

[1] Classic-Euler angles are sometimes referred to as proper-Euler angles, and Tait-Bryan angles are also known as Cardan angles or nautical angles.

However, for the rotation to be performed about the b'-axis we require a coordinate transformation given by $R_{b'}(\theta) = R_a(\phi)R_b(\theta)R_a^{-1}(\phi)$, and similarly for the rotation about the c''-axis we need $R_{c''}(\psi) = R_a(\phi)R_b(\theta)R_c(\psi)R_b^{-1}(\theta)R_a^{-1}(\phi)$. This results in (2.30) simplifying to (2.29), and hence extrinsic and intrinsic rotations represent the same orientation in space, provided the Euler angles are given in inverted order.

Euler angles are more intuitive to visualise than quaternions, which explains why they are often preferred when describing rotations and orientations of rigid bodies in space. However, coordinate singularities occur when multiple solutions exist for Euler angles that represent the same orientation in space, which pose a problem as the Euler angles cannot be uniquely recovered. The singularities also correspond to orientations in space where infinite rotational rates are required in order to produce finite angular velocity and acceleration of the rigid body, but this is not a physical singularity as there is no actual limitation on the rigid body itself. For specific rotations where we encounter coordinate singularities, the problem may be solved by switching to an alternate sequence of three elementary rotations. E.g. using the 'z-x-z' convention instead of 'y-z-y' moves the singularities elsewhere where they may not be encountered but will always exist. This is because Euler angles do not provide a complete coordinate system for $SO(3)$. The coordinate singularities specifically occur when $\theta = 0$ or π for classic-Euler angles, and $\theta = \pm\frac{\pi}{2}$ for Tait-Bryan angles.

We now demonstrate how Euler angles work in 'z-x-z' convention (where the subscripts a and c denote the z-axis and b the x-axis in (2.29)) by initially aligning the body frame $\mathcal{F}_B$ with XYZ-axes to the spatial frame $\mathcal{F}_S$ with xyz-axes, before performing three elemental rotations to arrive at the actual orientation of the body. We denote $X'Y'Z'$ as the intermediate body axes after the first elemental rotation and $X''Y''Z''$ after the second, while the third elemental rotation yields the final orientation of the body and will take the standard XYZ-axes. We note that the rotations we perform are active, i.e. we are physically rotating the body, and not passive in which only the coordinate system changes. We show the extrinsic sequence of elemental rotations in Figure 2.2, followed by the intrinsic sequence in Figure 2.3. In both cases the rotations are performed in the clockwise direction when viewed in the direction of the positive axis.

Let $\boldsymbol{X} = \begin{pmatrix} X \\ Y \\ Z \end{pmatrix}$ be a vector viewed in $\mathcal{F}_B$, then that same vector $\boldsymbol{x} = \begin{pmatrix} x \\ y \\ z \end{pmatrix}$ written in $\mathcal{F}_S$ is given by

$$\boldsymbol{x} = R_z(\phi)R_x(\theta)R_z(\psi)\boldsymbol{X} = R\boldsymbol{X}, \tag{2.31}$$

where in 'z-x-z' convention we have

$$R = \begin{pmatrix} c_\phi c_\psi - s_\phi c_\theta s_\psi & -s_\phi c_\theta c_\psi - c_\phi s_\psi & s_\phi s_\theta \\ c_\phi c_\theta s_\psi + s_\phi c_\psi & c_\phi c_\theta c_\psi - s_\phi s_\psi & -c_\phi s_\theta \\ s_\theta s_\psi & s_\theta c_\psi & c_\theta \end{pmatrix}. \tag{2.32}$$

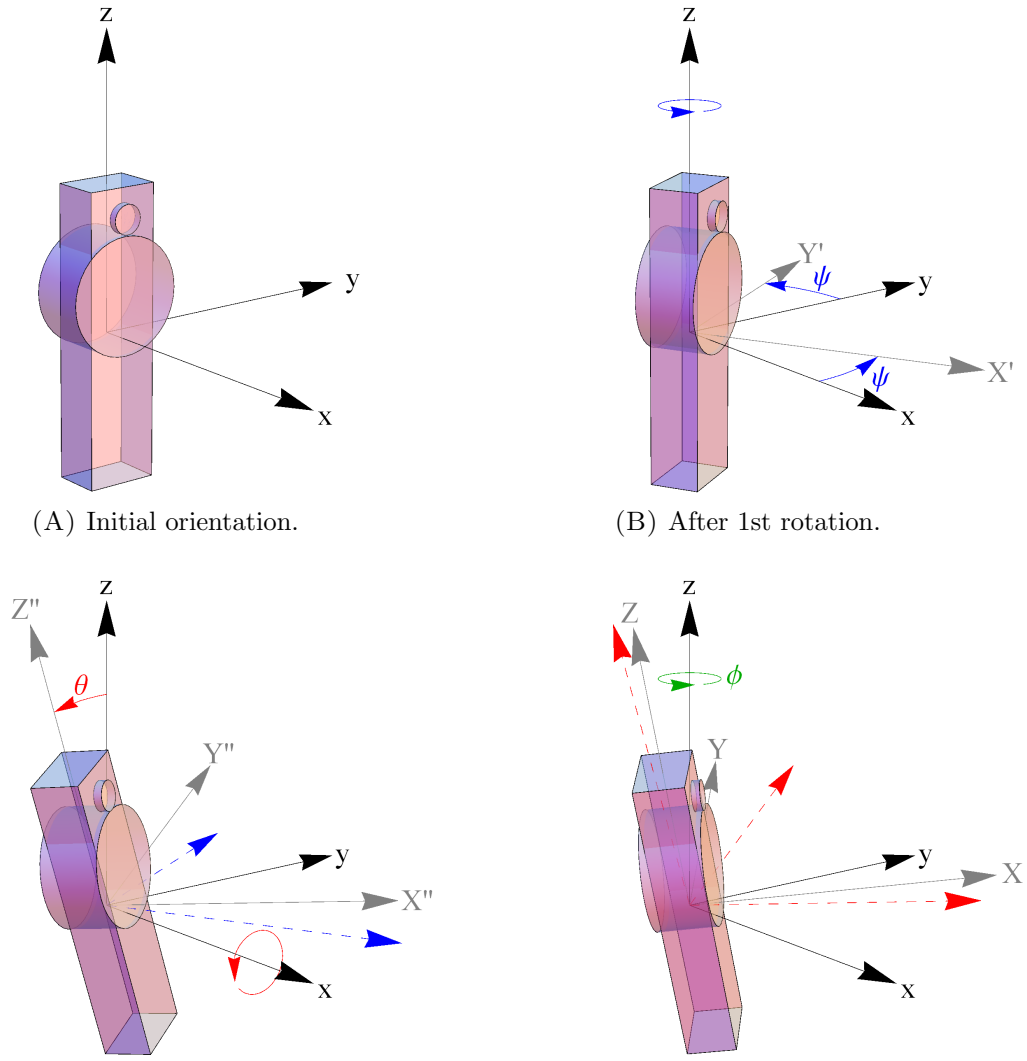

(A) Initial orientation.

(B) After 1st rotation.

(C) After 2nd rotation.

(D) Final orientation.

Figure 2.2. The sequence of extrinsic rotations.

To conserve space we abbreviated the sines and cosines as s and c and expressed their arguments as subscripts.

We now consider the inverse transformation from R to the Euler angles (ϕ, θ, ψ). Start by letting

$$R = \begin{pmatrix} R_{1,1} & R_{1,2} & R_{1,3} \\ R_{2,1} & R_{2,2} & R_{2,3} \\ R_{3,1} & R_{3,2} & R_{3,3} \end{pmatrix}, \tag{2.33}$$

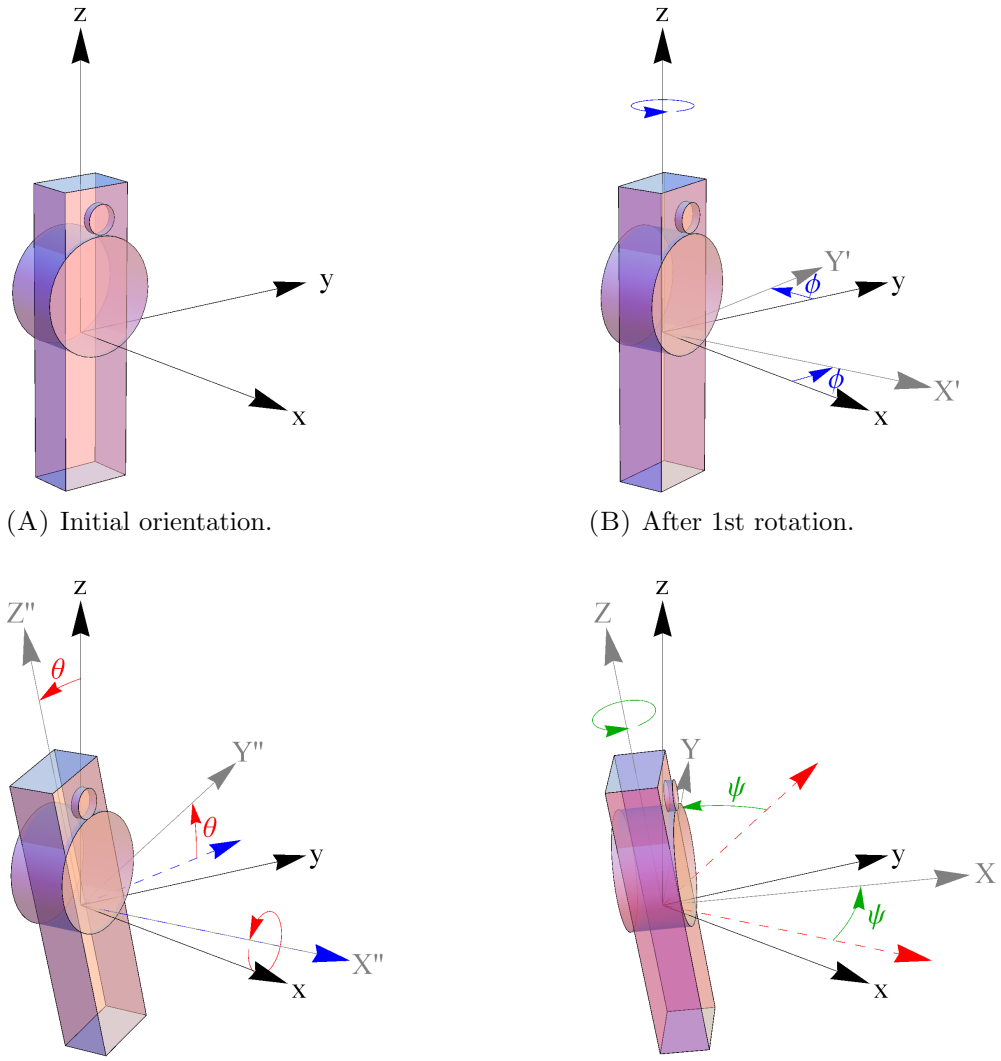

(A) Initial orientation.

(B) After 1st rotation.

(C) After 2nd rotation.

(D) Final orientation.

Figure 2.3. The sequence of intrinsic rotations. In Figure 2.3C the rotation is about the X'-axis which is also known as the line-of-nodes, it arises from the intersection between the xy and XY-plane.

if $\theta \neq 0$ or π, then the third column and row of (2.32) tells us that

$$\begin{pmatrix} \phi \\ \theta \\ \psi \end{pmatrix} = \begin{pmatrix} \operatorname{Arg}(-R_{2,3} + iR_{1,3}) \\ \arccos R_{3,3} \\ \operatorname{Arg}(R_{3,2} + iR_{3,1}) \end{pmatrix}. \tag{2.34}$$

It is important that $\theta \in [0, \pi]$, otherwise there would be two sets of Euler angles for each rotation matrix. Now the problem arises when $\theta = 0$ or π, where there is no

information to be extracted from the third column or row, meaning the remaining entries say

$$\begin{aligned}\theta &= 0\\ \phi+\psi &= \arccos R_{1,1} = \arccos R_{2,2}\\ &= \arcsin\left(-R_{2,1}\right) = \arcsin R_{2,1}\end{aligned}$$

or

$$\begin{aligned}\theta &= \pi\\ \phi-\psi &= \arccos R_{1,1} = \arccos\left(-R_{2,2}\right)\\ &= \arcsin R_{2,1} = \arcsin R_{2,1}.\end{aligned}$$

As we can see, there are infinitely many solutions for ϕ and ψ here, which is why the coordinate singularities occur.

2.7 Quaternions

Coordinate singularities can be avoided by using a covering map from $\mathcal{S}^3 \to SO(3)$, which results in a double cover. This means that there are precisely two unit quaternions for every orientation in 3D space, and the two quaternions are in fact negatives of each other. According to Euler's rotation theorem, for every rotation R there is a vector $\boldsymbol{u}$ for which $R\boldsymbol{u} = \boldsymbol{u}$. This means the line $a\boldsymbol{u}$ is the rotation axis of R and we can specify the rotation in terms of an angle and axis, where the axis is known as the Euler axis and is typically represented by a unit vector. Quaternions provide an elegant way to encode this angle-vector information. Consider a clockwise rotation of ξ about the unit vector $\boldsymbol{u} = (u_x, u_y, u_z)^t$ so that $u_x^2 + u_y^2 + u_z^2 = 1$, then this can be represented with the unit quaternion

$$\boldsymbol{q} = \cos(\xi/2) + u_x \sin(\xi/2)\boldsymbol{i} + u_y \sin(\xi/2)\boldsymbol{j} + u_z \sin(\xi/2)\boldsymbol{k},$$

where $\boldsymbol{i} = (1,0,0)^t$, $\boldsymbol{j} = (0,1,0)^t$ and $\boldsymbol{k} = (0,0,1)^t$ are treated as the standard unit vectors. Associating the real part of this quaternion as a scalar $q_0 = \cos(\xi/2)$ and the imaginary parts as a vector $\vec{\boldsymbol{q}} = u_x \sin(\xi/2)\boldsymbol{i} + u_y \sin(\xi/2)\boldsymbol{j} + u_z \sin(\xi/2)\boldsymbol{k}$, we may write

$$\boldsymbol{q} = \begin{pmatrix} \cos(\xi/2) \\ \boldsymbol{u}\sin(\xi/2) \end{pmatrix} = \begin{pmatrix} q_0 \\ \vec{\boldsymbol{q}} \end{pmatrix}. \tag{2.35}$$

The conjugate of a quaternion is defined as $\bar{\boldsymbol{q}} = \begin{pmatrix} q_0 \\ -\vec{\boldsymbol{q}} \end{pmatrix}$, and for the special case of unit quaternions the conjugate is also equal to the inverse, but in general the quaternion inverse is defined as $\boldsymbol{q}^{-1} = \dfrac{\bar{\boldsymbol{q}}}{|\boldsymbol{q}|^2}$, where the denominator is the norm square, i.e. the sum of squares of the components of $\boldsymbol{q}$. Now let us introduce a

second quaternion $\boldsymbol{p} = \begin{pmatrix} p_0 \\ \vec{\boldsymbol{p}} \end{pmatrix}$, quaternion addition and multiplication is then defined as

$$\boldsymbol{p} + \boldsymbol{q} = \begin{pmatrix} p_0 + q_0 \\ \vec{\boldsymbol{p}} + \vec{\boldsymbol{q}} \end{pmatrix} \qquad \text{and} \qquad \boldsymbol{pq} = \begin{pmatrix} p_0 q_0 - \vec{\boldsymbol{p}} \cdot \vec{\boldsymbol{q}} \\ p_0 \vec{\boldsymbol{q}} + q_0 \vec{\boldsymbol{p}} + \vec{\boldsymbol{p}} \times \vec{\boldsymbol{q}} \end{pmatrix}. \tag{2.36}$$

Due to the cross product term, quaternion multiplication is not commutative. A quaternion with zero scalar component, e.g. $\boldsymbol{p} = \begin{pmatrix} 0 \\ \vec{\boldsymbol{p}} \end{pmatrix}$ is known as a *pure* quaternion, which was first termed a *vector* by Hamilton in 1846 [1].

To rotate an arbitrary vector $\vec{\boldsymbol{p}}$ by amount ξ about $\boldsymbol{u}$, we write $\vec{\boldsymbol{p}}$ as a pure quaternion $\boldsymbol{p}$ and simply apply the operation $\boldsymbol{qp\bar{q}}$, where $\boldsymbol{q}$ is given in (2.35). The result is a pure quaternion where

$$\begin{pmatrix} 0 \\ \vec{\boldsymbol{r}} \end{pmatrix} = \begin{pmatrix} q_0 \\ \vec{\boldsymbol{q}} \end{pmatrix} \begin{pmatrix} 0 \\ \vec{\boldsymbol{p}} \end{pmatrix} \begin{pmatrix} q_0 \\ -\vec{\boldsymbol{q}} \end{pmatrix} = \begin{pmatrix} 0 \\ 2(\vec{\boldsymbol{p}} \cdot \vec{\boldsymbol{q}})\vec{\boldsymbol{q}} + (q_0^2 - \vec{\boldsymbol{q}} \cdot \vec{\boldsymbol{q}})\vec{\boldsymbol{p}} - 2q_0 \vec{\boldsymbol{p}} \times \vec{\boldsymbol{q}} \end{pmatrix}.$$

This result is linear in $\vec{\boldsymbol{p}}$, so we can factorise it out to obtain

$$\vec{\boldsymbol{r}} = \underbrace{\left[2(\vec{\boldsymbol{q}}\vec{\boldsymbol{q}}^t + q_0 \hat{\vec{\boldsymbol{q}}}) + (q_0^2 - \vec{\boldsymbol{q}} \cdot \vec{\boldsymbol{q}})\mathbb{1}\right]}_{R} \vec{\boldsymbol{p}}. \tag{2.37}$$

If we let $\vec{\boldsymbol{q}} = (q_1, q_2, q_3)^t$, we can write the rotation matrix R explicitly as

$$R = \begin{pmatrix} q_0^2 + q_1^2 - q_2^2 - q_3^2 & 2q_1q_2 - 2q_0q_3 & 2q_1q_3 + 2q_0q_2 \\ 2q_1q_2 + 2q_0q_3 & q_0^2 - q_1^2 + q_2^2 - q_3^2 & 2q_2q_3 - 2q_0q_1 \\ 2q_1q_3 - 2q_0q_2 & 2q_2q_3 + 2q_0q_1 & q_0^2 - q_1^2 - q_2^2 + q_3^2 \end{pmatrix}. \tag{2.38}$$

In general, Ebbinghaus [18] states and proves that for every quadruple $(\kappa, \lambda, \mu, \nu) \in \mathbb{R}^4 \setminus \{0\}$ the 3×3 matrix

$$\frac{1}{\kappa^2 + \lambda^2 + \mu^2 + \nu^2} \begin{pmatrix} \kappa^2 + \lambda^2 - \mu^2 - \nu^2 & 2\lambda\mu - 2\kappa\nu & 2\lambda\nu + 2\kappa\mu \\ 2\lambda\mu + 2\kappa\nu & \kappa^2 - \lambda^2 + \mu^2 - \nu^2 & 2\mu\nu - 2\kappa\lambda \\ 2\lambda\nu - 2\kappa\mu & 2\mu\nu + 2\kappa\lambda & \kappa^2 - \lambda^2 - \mu^2 + \nu^2 \end{pmatrix}$$

is properly orthogonal, and all properly orthogonal 3×3 matrices can be expressed in this form. The result found in (2.38) is the simpler case of this for unit quaternions and reveals how to construct the rotation matrix R given the unit quaternion $\boldsymbol{q}$.

The inverse transformation from the rotation matrix R to the quaternion $\boldsymbol{q}$ is obtained by comparing (2.33) with (2.38). Adding

$$q_0^2 + q_1^2 + q_2^2 + q_3^2 = 1$$

to the trace of R allows us to solve for q_0^2 in terms of $R_{i,j}$, yielding two solutions for q_0. The remaining components of the quaternion are then obtained by taking

differences in the skew-symmetric part of the off-diagonal entries. When we solve for $\boldsymbol{q}$ we obtain

$$\begin{pmatrix} q_0 \\ q_1 \\ q_2 \\ q_3 \end{pmatrix} = \frac{1}{2r} \begin{pmatrix} r^2 \\ R_{3,2} - R_{2,3} \\ R_{1,3} - R_{3,1} \\ R_{2,1} - R_{1,2} \end{pmatrix}, \tag{2.39}$$

where $r = \pm\sqrt{1 + R_{1,1} + R_{2,2} + R_{3,3}}$. The $\pm$ sign shows that there are exactly two opposite quaternions that correspond to the same rotation matrix R, which explains why the double cover occurs.

In theory we could remove the double cover by simply disposing half of $\mathcal{S}^3$, such as taking only the positive sign (or negative sign) of r in (2.39). The reasoning against this is that whenever $r = 0$ we have $q_0 = 0$, $R_{j+1,j} - R_{j,j+1} = 0$, and the remaining q_i's for $i \in \{1, 2, 3\}$ need to be evaluated using limits. If $q_i \neq 0$ for $i \in \{1, 2, 3\}$ we get one sided limits that are equal in magnitude but opposite in sign for the two directions of approach, meaning a discontinuity occurs. So if we want a continuous curve for the quaternion $\boldsymbol{q}$ on our chosen hemisphere of $\mathcal{S}^3$ we need to consider both solutions of (2.39), and switch solutions whenever we cross $r = 0$ in the trajectory $\boldsymbol{q}$. The orientation of the body itself is of course always continuous, and it is only the quaternion representation of the orientation that may contain jumps if only half of $\mathcal{S}^3$ is used. We illustrate this with a simple example of a rigid body rotating once about its x-axis. This is a steady rotation represented by the rotation matrix $R_x(t)$, where t runs from 0 to 2π. Applying

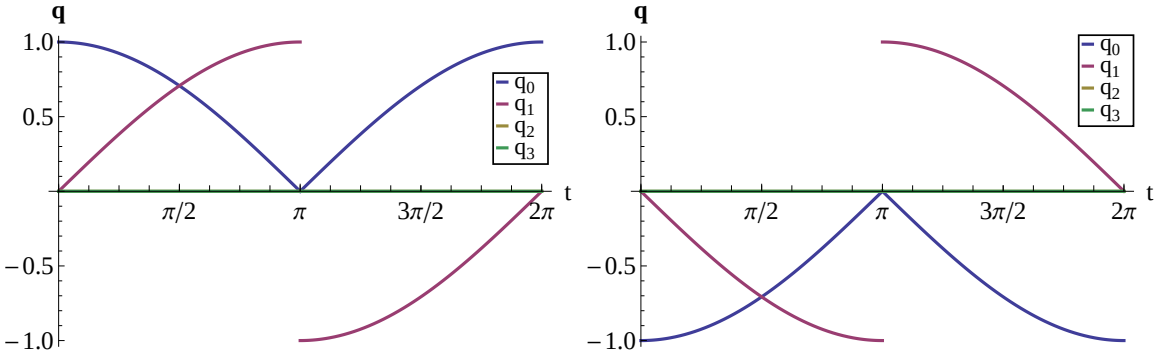

(A) With + sign of (2.40). (B) With − sign of (2.40).

Figure 2.4. We see that there is a discontinuity for q_1 at $t = \pi$ because $q_1 \neq 0$ when $q_0 = 0$. The curve can be made continuous by switching solutions whenever $q_0 = 0$, as shown in Figure 2.5. Note that in these diagrams $q_2 = q_3 = 0$ for all t.

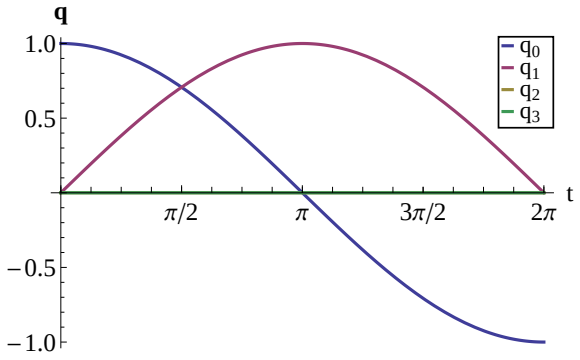

Figure 2.5. We take the + sign of (2.40) for $t \in [0, \pi]$ and the − sign for $t \in (\pi, 2\pi]$ to produce a continuous $\boldsymbol{q}$ in $\mathcal{S}^3$.

(2.39) to $R_x(t)$ we get

$$\boldsymbol{q} = \pm \left(\frac{1}{2}\sqrt{2 + 2\cos t}, \frac{\sin t}{\sqrt{2 + 2\cos t}}, 0, 0 \right)^t, \tag{2.40}$$

which we plot in Figure 2.4. The smooth $\boldsymbol{q}$ corresponding to $R_x(t)$ is shown in Figure 2.5.

2.8 Equations of Motion

Angular momentum in $\mathcal{F}_S$ and $\mathcal{F}_B$ are connected with the rotation matrix R as seen in 2.23, and differentiating $\boldsymbol{l} = R\boldsymbol{M}$ gives

$$\dot{\boldsymbol{l}} = \dot{R}\boldsymbol{M} + R\dot{\boldsymbol{M}} = \boldsymbol{0}. \tag{2.41}$$

The result is $\boldsymbol{0}$ because of the conservation of angular momentum in $\mathcal{F}_S$. Rearranging this result gives

$$\begin{aligned} \dot{\boldsymbol{M}} &= -R^t \dot{R}\boldsymbol{M} = -\hat{\boldsymbol{\mathcal{W}}}\boldsymbol{M} \quad \text{from (2.26)} \\ &= \boldsymbol{M} \times \boldsymbol{\mathcal{W}}, \end{aligned} \tag{2.42}$$

which are the equations of motion. Since we know

$$\boldsymbol{\mathcal{W}} = J^{-1}\boldsymbol{M}, \tag{2.43}$$

we can also rewrite (2.42) as

$$\dot{\boldsymbol{M}} = \boldsymbol{M} \times J^{-1}\boldsymbol{M} \tag{2.44}$$

for the rigid body case. The differential equation (2.44) has an analytical solution, but because it is not in terms of elementary functions we will first look at a simpler

case where two moments of inertia are equal. Let $\boldsymbol{M} = (M_x, M_y, M_z)^t$ and suppose we have

$$J = \operatorname{diag}(J_y, J_y, J_z), \tag{2.45}$$

then writing out the components explicitly we see that

$$\begin{pmatrix} \dot{M}_x \\ \dot{M}_y \\ \dot{M}_z \end{pmatrix} = \begin{pmatrix} (J_z^{-1} - J_y^{-1}) M_z M_y \\ -(J_z^{-1} - J_y^{-1}) M_z M_x \\ 0 \end{pmatrix}.$$

The third equation clearly tells us that M_z is constant, and we can think of

$$W = -(J_z^{-1} - J_y^{-1}) M_z \tag{2.46}$$

appearing in the first two parts as an angular velocity, which is constant because M_z is constant. The first two differential equations are associated with the simple harmonic oscillator, where the solutions are well known in terms of trigonometry functions. We may write

$$\begin{pmatrix} \dot{M}_x \\ \dot{M}_y \\ \dot{M}_z \end{pmatrix} = \begin{pmatrix} 0 & -W & 0 \\ W & 0 & 0 \\ 0 & 0 & 0 \end{pmatrix} \begin{pmatrix} M_x \\ M_y \\ M_z \end{pmatrix}, \tag{2.47}$$

and since this is linear, it can be solved with the matrix exponential to give

$$\begin{aligned} \begin{pmatrix} M_x \\ M_y \\ M_z \end{pmatrix} &= \exp \begin{pmatrix} 0 & -Wt & 0 \\ Wt & 0 & 0 \\ 0 & 0 & 0 \end{pmatrix} \begin{pmatrix} M_x(0) \\ M_y(0) \\ M_z(0) \end{pmatrix} \\ &= \begin{pmatrix} \cos(Wt) & -\sin(Wt) & 0 \\ \sin(Wt) & \cos(Wt) & 0 \\ 0 & 0 & 1 \end{pmatrix} \begin{pmatrix} M_x(0) \\ M_y(0) \\ M_z(0) \end{pmatrix}. \end{aligned} \tag{2.48}$$

In vector notation this corresponds to

$$\boldsymbol{M} = R_z(Wt)\boldsymbol{M}(0), \tag{2.49}$$

where $\boldsymbol{M}(0)$ is the initial condition. Using the formulas

$$\begin{aligned} \sin(Wt + \alpha) &= \sin\alpha \cos(Wt) + \cos\alpha \sin(Wt) \\ \text{and} \quad \sin\alpha &= \cos(\alpha - \pi/2), \end{aligned}$$

we can simplify (2.48) to

$$\begin{pmatrix} M_x \\ M_y \\ M_z \end{pmatrix} = \begin{pmatrix} A_0 \cos(Wt + \alpha_0) \\ A_0 \sin(Wt + \alpha_0) \\ M_z(0) \end{pmatrix}, \tag{2.50}$$

where $A_0 = \sqrt{M_x^2(0) + M_y^2(0)}$ and $\alpha_0 = \operatorname{Arg}\big(M_x(0) + iM_y(0)\big)$. The solution is a circle parallel to the M_xM_y-plane with radius A_0 and height $M_z(0)$.

2.9 Rotational Stability

Expressing the equations of motion (2.44) in terms of angular velocity $\boldsymbol{\mathcal{W}} = \begin{pmatrix} \mathcal{W}_x \\ \mathcal{W}_y \\ \mathcal{W}_z \end{pmatrix}$, we get

$$\begin{pmatrix} \dot{\mathcal{W}}_x \\ \dot{\mathcal{W}}_y \\ \dot{\mathcal{W}}_z \end{pmatrix} = \begin{pmatrix} (J_y - J_z)J_x^{-1}\mathcal{W}_y\mathcal{W}_z \\ (J_z - J_x)J_y^{-1}\mathcal{W}_z\mathcal{W}_x \\ (J_x - J_y)J_z^{-1}\mathcal{W}_x\mathcal{W}_y \end{pmatrix}. \tag{2.51}$$

If we have a rotation about any of the principal axes of inertia, we clearly get steady rotations about that axis since we are at an equilibrium. This means $\dot{\boldsymbol{\mathcal{W}}} = \mathbf{0}$ and only one of the components of $\boldsymbol{\mathcal{W}}$, say $\mathcal{W}_i$, is non-zero. So from the $\mathcal{F}_B$ form of (1.2) we may write $l = J_i\mathcal{W}_i$, since the angular momentum between $\mathcal{F}_S$ and $\mathcal{F}_B$ are equal during steady rotations. We have J_i corresponding to the moment of inertia of the axis of rotation, and is the (i,i)-component in the diagonal tensor of inertia J. The rigid body B will therefore rotate uniformly about a principal axis with period

$$T = \frac{2\pi}{\mathcal{W}_i} = \frac{2\pi J_i}{l}, \tag{2.52}$$

where the subscript i indicates the axis of steady rotation.

Now suppose $J_x > J_y > J_z$ and consider a rotation about the x-axis with a small perturbation so that $\boldsymbol{\mathcal{W}} = \begin{pmatrix} \mathcal{W}_x + \epsilon_x \\ \epsilon_y \\ \epsilon_z \end{pmatrix}$, where ϵ_x, ϵ_y, and ϵ_z are small. Then (2.51) becomes

$$\begin{pmatrix} \dot{\mathcal{W}}_x + \dot{\epsilon}_x \\ \dot{\epsilon}_y \\ \dot{\epsilon}_z \end{pmatrix} = \begin{pmatrix} \mathcal{O}(\epsilon_y\epsilon_z) \\ (J_z - J_x)J_y^{-1}\mathcal{W}_x\epsilon_z + \mathcal{O}(\epsilon_x\epsilon_z) \\ (J_x - J_y)J_z^{-1}\mathcal{W}_x\epsilon_y + \mathcal{O}(\epsilon_x\epsilon_y) \end{pmatrix}, \tag{2.53}$$

and if we neglect the second order perturbation terms then $\mathcal{W}_x + \epsilon_x$ is constant. Differentiating $\dot{\epsilon}_y$ and substituting in $\dot{\epsilon}_z$, we find

$$\ddot{\epsilon}_y = \frac{(J_z - J_x)(J_x - J_y)}{J_yJ_z}\mathcal{W}_x^2\epsilon_y,$$

and similarly

$$\ddot{\epsilon}_z = \frac{(J_z - J_x)(J_x - J_y)}{J_yJ_z}\mathcal{W}_x^2\epsilon_z.$$

As $\mathcal{W}_x^2 > 0$ the sign of

$$\frac{(J_z - J_x)(J_x - J_y)}{J_yJ_z}$$

determines the stability of the rotation, and since $J_z - J_x < 0$ the whole expression is negative. This corresponds to a linearly stable rotation because we get oscillatory solutions for both ϵ_y and ϵ_z. Repeating the same calculation with $\boldsymbol{\mathcal{W}} = \begin{pmatrix} \epsilon_x \\ \epsilon_y \\ \mathcal{W}_z + \epsilon_z \end{pmatrix}$ for rotations about the z-axis with a small perturbation, we find the term of interest becomes

$$\frac{(J_y - J_z)(J_z - J_x)}{J_x J_y},$$

which again is negative because $J_z - J_x < 0$, and this results in stable rotations. For rotations about the y-axis we get

$$\frac{(J_x - J_y)(J_y - J_z)}{J_z J_x},$$

and is now positive resulting in exponential solutions for ϵ_x and ϵ_z, which leads to an unstable rotation because both ϵ_x and ϵ_z grow exponentially without bound. This shows that rotations about the x-axis and z-axis with the largest and smallest moments of inertia are stable, while rotations about the y-axis with the intermediate moment of inertia are unstable - a phenomena known as the intermediate axis theorem.

Another way to examine this is to consider the conservation laws, where we have conservation of energy and total angular momentum:

$$E = \frac{1}{2}\boldsymbol{\mathcal{W}}^t J \boldsymbol{\mathcal{W}} = \frac{1}{2}J_x \mathcal{W}_x^2 + \frac{1}{2}J_y \mathcal{W}_y^2 + \frac{1}{2}J_z \mathcal{W}_z^2 \tag{2.54}$$

$$l^2 = \boldsymbol{M} \cdot \boldsymbol{M} = M_x^2 + M_y^2 + M_z^2. \tag{2.55}$$

Rewriting the energy E in terms of angular momentum gives

$$E = \frac{1}{2}\boldsymbol{M}^t J^{-1} \boldsymbol{M} = \frac{M_x^2}{2J_x} + \frac{M_y^2}{2J_y} + \frac{M_z^2}{2J_z}. \tag{2.56}$$

Notice how (2.55) defines a sphere with coordinate axes M_x, M_y and M_z, and (2.56) an ellipsoid. The sphere in (2.55) only depends on l so we refer to it as the L-sphere[2], while the ellipsoid (2.56) depends on both the energy E and principal moments of inertia J, and is therefore referred to as the energy-inertia ellipsoid. This ellipsoid, or more commonly the one given by (2.54), is also known as Poinsot's ellipsoid, named after Louis Poinsot. As the energy E is homogeneous of degree 2 in $\boldsymbol{M}$ (or $\boldsymbol{L}$) it is useful to introduce the scaled energy

$$\mathcal{E} = E/l^2, \tag{2.57}$$

[2]We capitalise the l for aesthetic reasons, but it could be interpreted as $L = |\boldsymbol{L}|$, which is the same as l. In rigid bodies there is no reason not to align $\mathcal{F}_C$ with $\mathcal{F}_B$, hence $\boldsymbol{L} = \boldsymbol{M}$.

and scaled angular momentum

$$\boldsymbol{\mathcal{M}}(t;\mathcal{E},J)=\boldsymbol{M}(t;\mathcal{E},J)/l. \tag{2.58}$$

In general if the energy E, tensor of inertia J, and initial angular momentum $\boldsymbol{M}(0)$ are known, then the entire (scaled) orbit $\boldsymbol{\mathcal{M}}(t;\mathcal{E},J)$ is known in terms of Jacobi elliptic functions, which we will soon see.

As both (2.55) and (2.56) must be satisfied by the rotating body, the orbit must lay on the intersection of the L-sphere and energy-inertia ellipsoid, which is only possible when $J_x^{-1}\leq 2\mathcal{E}\leq J_z^{-1}$. The boundary cases are simple and correspond to steady rotations that are stable, since the intersection only produces two singular points on opposite ends. When

$$J_x^{-1}<2\mathcal{E}<J_y^{-1} \tag{2.59}$$

the intersection forms two small closed curves around the $\mathcal{M}_x$-axis shown in Figure 2.6A, and if

$$J_y^{-1}<2\mathcal{E}<J_z^{-1} \tag{2.60}$$

then the two closed curves are instead around the $\mathcal{M}_z$-axis as shown in Figure 2.6C. As the second inequality is almost always true in the case of the diver (and is always true when the diver is in twisting somersaulting motion) we shall write down the formulas for the second inequality (2.60), but note that for the first inequality (2.59) the formulas can be manipulated to work by simply interchanging the x and z indices of J and $\mathcal{M}$.

We begin by finding the curves of intersection between the two surfaces, which is done by rearranging (2.55) for M_z^2, substituting in (2.56), and obtaining the expression in terms of M_x^2 and M_y^2. Realising that this expression is an ellipse in M_x and M_y, we can parametrise the scaled angular momentum as

$$\begin{aligned}
\mathcal{M}_x &= \sqrt{\frac{J_x}{J_x-J_z}\Big(1-2\mathcal{E}J_z\Big)}\cos a\\
\mathcal{M}_y &= \sqrt{\frac{J_y}{J_y-J_z}\Big(1-2\mathcal{E}J_z\Big)}\sin a\\
\mathcal{M}_z &= \pm\sqrt{1-\frac{1-2\mathcal{E}J_z}{(J_y-J_z)(J_x-J_z)}S(a)},
\end{aligned} \tag{2.61}$$

where $S(a)=J_x(J_y-J_z)\cos^2\phi+J_y(J_x-J_z)\sin^2\phi$, and the $\pm$ sign of $\mathcal{M}_z$ shows that there are in fact two disjoint closed curves on the sphere at opposite ends. It is important to stress that these parametric equations only give the curves of intersection between the two surfaces, and do not give the time parametrisation of the actual solutions, which are much more complicated and must be written in terms of Jacobi elliptic functions as Landau and Lifshitz [**35**] show. We will

not provide this derivation but take their result, convert it to our notation for the scaled angular momentum, and suppress the arguments shown in (2.58) to get

$$\begin{aligned}\mathcal{M}_x &= s\sqrt{\frac{J_x(1-2\mathcal{E}J_z)}{J_x-J_z}}\,\mathrm{cn}\,(\tau,k)\\ \mathcal{M}_y &= \sqrt{\frac{J_y(1-2\mathcal{E}J_z)}{J_y-J_z}}\,\mathrm{sn}\,(\tau,k)\\ \mathcal{M}_z &= -s\sqrt{\frac{J_z(2\mathcal{E}J_x-1)}{J_x-J_z}}\,\mathrm{dn}\,(\tau,k),\end{aligned} \tag{2.62}$$

where

$$\begin{aligned}\tau &= l\sqrt{\frac{(J_y-J_z)(2\mathcal{E}J_x-1)}{J_xJ_yJ_z}}\,(t+c)\\ k &= \frac{(J_x-J_y)(1-2\mathcal{E}J_z)}{(J_y-J_z)(2\mathcal{E}J_x-1)}\end{aligned} \tag{2.63}$$

and the two constants s (direction that is either ± 1) and c (phase shift) that appear are chosen to satisfy the initial condition. It is important to note that the minus sign in front of $\mathcal{M}_z$ appears because we assumed $J_x > J_y > J_z$, which is the case of the diver, but had we instead assumed $J_x < J_y < J_z$ then no minus sign would appear. Now in (2.62) the only place l appears is in τ, so while the frequency of $\boldsymbol{\mathcal{M}}(t;\mathcal{E},J)$ changes as we vary l, the trajectory itself does not because $\mathcal{M}$ and $\mathcal{E}$ are scaled with l. Due to the Jacobi elliptic functions being periodic with period $4K(k)$ in τ, where

$$K(k) = \int_0^{\frac{\pi}{2}} \frac{du}{\sqrt{1-k\sin^2 u}} \tag{2.64}$$

is the complete elliptic integral of the first kind, we find that the period is

$$T(\mathcal{E},J) = \frac{4K\big(k(\mathcal{E},J)\big)}{l}\sqrt{\frac{J_xJ_yJ_z}{(J_y-J_z)(2\mathcal{E}J_x-1)}}. \tag{2.65}$$

Note that the formulas given by (2.61), (2.62), and (2.65) only hold true when (2.60) is satisfied, and in the case of (2.59) the x and z indices of J and $\mathcal{M}$ need to be swapped. Looking at the limiting case of (2.61), when $\mathcal{E} \to 1/(2J_z)$ the coefficient of the trigonometric functions in $\mathcal{M}_x$ and $\mathcal{M}_y$ begin to vanish, which corresponds to the curves shrinking to points at the poles of the ellipsoid. When $\mathcal{E} = 1/(2J_z)$ the scaled energy is maximal, the angular velocity vector is precisely parallel to the smallest principal axis of inertia, and we have the scaled angular momentum being $(0,0,\pm 1)^t$, where the $\pm$ sign corresponds to the rotation being either clockwise or counterclockwise. As the scaled energy $\mathcal{E}$ decreases, the points

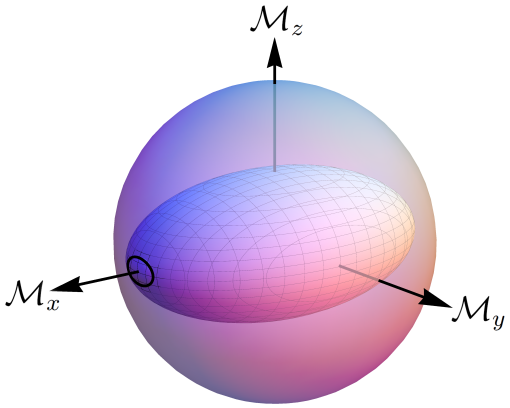

(A) $\mathcal{E}$ slightly $> 1/(2J_x)$

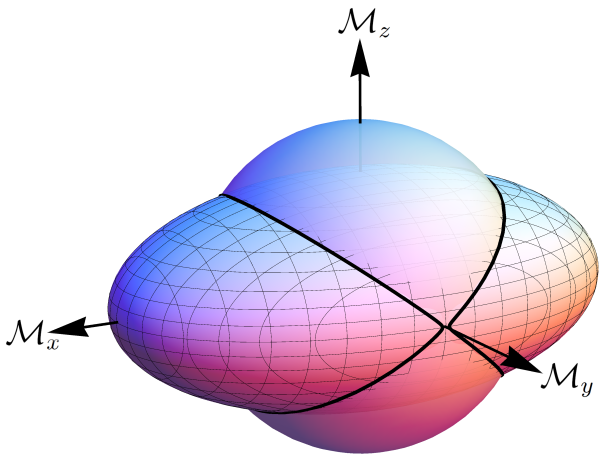

(B) $\mathcal{E} = 1/(2J_y)$

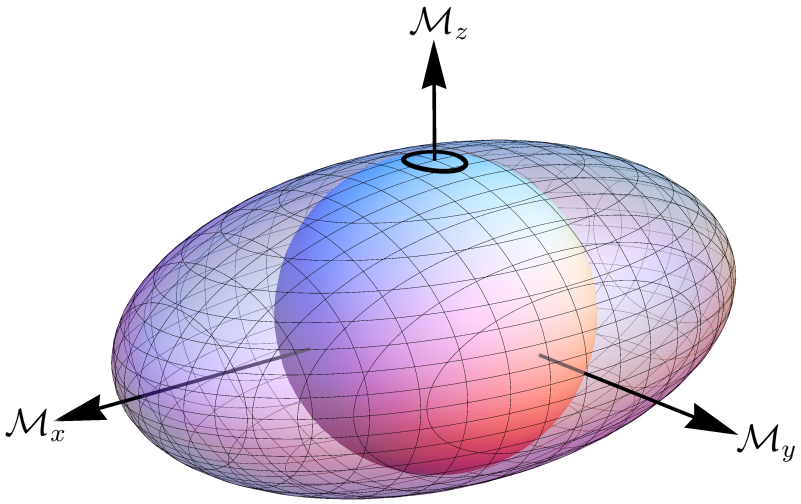

(C) $\mathcal{E}$ slightly $< 1/(2J_z)$

FIGURE 2.6. Intersection between the L-sphere and tri-axial energy-inertia ellipsoid with different energy states. There are two closed curves at opposite ends (although only one can be seen in the figures) in Figure 2.6A and Figure 2.6C corresponding to orbits near the stable equilibriums $(\pm l, 0, 0)^t$ and $(0, 0, \pm l)^t$, respectively. We show the separatrices given by (2.67) in Figure 2.6B, meaning orbits near the unstable equilibriums $(0, \pm l, 0)^t$ produce exponentially unstable rotations.

become two closed curves around the $\mathcal{M}_z$-axis shown in Figure 2.6C which grow in size according to (2.61). The growing continues until $\mathcal{E} = 1/(2J_y)$, which results in two plane curves that cross the poles of the ellipsoid on the $\mathcal{M}_y$-axis shown in Figure 2.6B. The curves seen in Figure 2.6B are rotated great circles, which represent the separatrices with parametric vector equation

$$\begin{pmatrix} \mathcal{M}_x \\ \mathcal{M}_y \\ \mathcal{M}_z \end{pmatrix} = R_y \left(\pm \arctan \sqrt{\frac{J_x(J_y - J_z)}{J_z(J_x - J_y)}} \right) \begin{pmatrix} 0 \\ \cos a \\ \sin a \end{pmatrix}. \tag{2.66}$$

For this specific case the time parametrised Jacobi elliptic functions reduce to hyperbolic functions which can be found, e.g. in Ashbaugh, Chicone and Cushman [2]. The solution becomes

$$\begin{aligned} \mathcal{M}_x &= s_1 \sqrt{\frac{J_x(J_y - J_z)}{J_y(J_x - J_z)}} \operatorname{sech} \tau \\ \mathcal{M}_y &= s_2 \tanh \tau \\ \mathcal{M}_z &= -s_1 s_2 \sqrt{\frac{J_z(J_x - J_y)}{J_y(J_x - J_z)}} \operatorname{sech} \tau, \end{aligned} \tag{2.67}$$

where τ given by (2.63) simplifies to

$$\tau = \frac{l}{J_y} \sqrt{\frac{(J_x - J_y)(J_y - J_z)}{J_x J_z}} (t + c).$$

There are two signs s_1 and s_2 which correspond to the four trajectories resulting from the intersection of the L-sphere and energy-inertia ellipsoid. The sign s_2 determines whether we are on the stable or unstable manifold of the unstable equilibrium points, and s_1 determines which of the two branches of the manifold we are on. As the scaled energy $\mathcal{E}$ continues to decrease, two closed curves form around the $\mathcal{M}_x$-axis as shown in Figure 2.6A. These curves then begin to shrink until $\mathcal{E} = 1/(2J_x)$, at which point the curves reduce to two points laying on the $\mathcal{M}_x$-axis, where the steady rotations are about the maximal moment of inertia axis. The formulas (2.61), (2.62), (2.66), and (2.67) have all been scaled using (2.58), but the scaling can be undone if desired by multiplying with l.

By examining the nature of the paths near the poles of the ellipsoid we can determine stability of the rotation. We see that closed paths near the $\mathcal{M}_x$ and $\mathcal{M}_z$ axes lie entirely in a neighbourhood of the corresponding poles and thus these rotations are stable. On the other hand, paths near the $\mathcal{M}_y$-axis travel all the way to the other side before coming back, so these rotations are clearly unstable.

In the case where two moments of inertia are equal and in the form shown in (2.45), we have the solution given by (2.50). A steady rotation is obtained if $\boldsymbol{\mathcal{M}} = (0, 0, \pm 1)^t$ or $\boldsymbol{\mathcal{M}} = (\cos a, \sin a, 0)^t$ for $a \in \mathbb{R}$. In the first case a small perturbation results in $A_0 \neq 0$ (but still small), so the oscillatory solution of

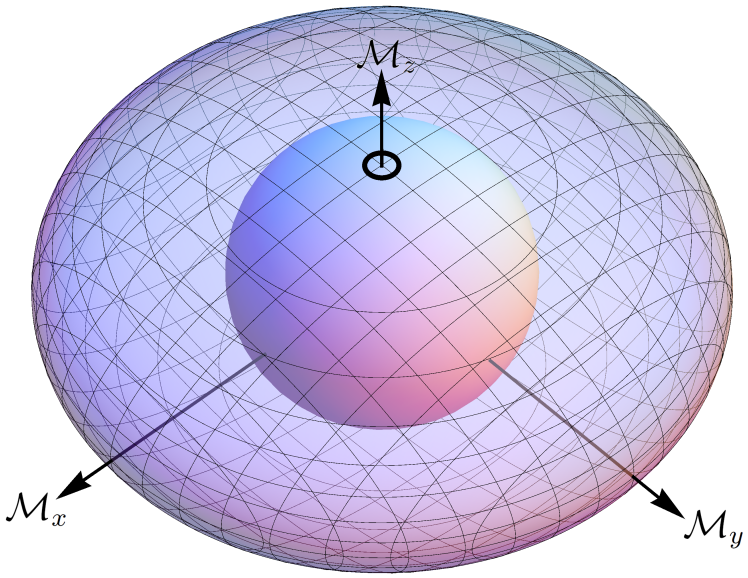

(A) Stable rotation.

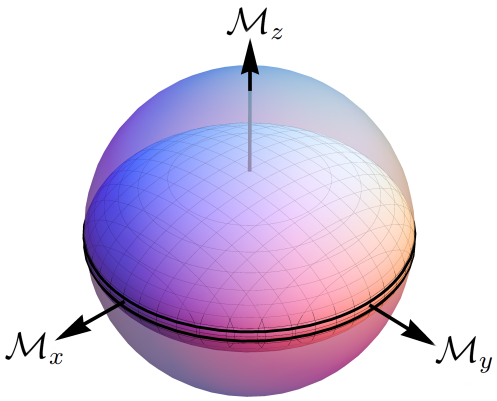

(B) Algebraically unstable rotation.

Figure 2.7. Intersection of the L-sphere with energy-inertia ellipsoid when $J_x = J_y > J_z$. For the case $J_x = J_z > J_y$ or $J_y = J_z > J_x$, appropriately relabelling the coordinate axes can accommodate this change and the diagram otherwise remains the same. However, if the inequality sign is reversed, then the oblate ellipsoid appearing in the diagram needs to be swapped for a prolate ellipsoid.

(2.50) produces a small circle around the stable equilibrium point as shown in Figure 2.7A. In the second case a small perturbation means $W \neq 0$, so again the solutions are oscillatory but this time A_0 is large, resulting in an algebraically unstable equilibrium due to the oscillatory (and not hyperbolic) nature, which can be seen in Figure 2.7B.

2.10 Magnus Series

The solution to a system of linear differential equations of the form

$$\dot{\boldsymbol{X}} = M\boldsymbol{X}$$

where M is a constant matrix is

$$\boldsymbol{X} = e^{Mt}\boldsymbol{X}(0).$$

If M is no longer a constant but a time dependent matrix $M(t)$ then the above solution in general no longer holds. The approach by Magnus [38] is to solve this initial value problem by expressing the solution in terms of the matrix exponential of a certain matrix function $\Omega(t)$ so that

$$\boldsymbol{X} = e^{\Omega(t)}\boldsymbol{X}(0), \tag{2.68}$$

where

$$\Omega(t) = \sum_{n=1}^{\infty} \Omega_n(t) \tag{2.69}$$

is an infinite series, now called the *Magnus series*. Care must be taken not to confuse the Magnus series $\Omega(t)$ with the angular velocity $\boldsymbol{\Omega}$.

The Magnus terms $\Omega_n(t)$ can be obtained explicitly in multiple ways. Explicit expressions for $\Omega_n(t)$ are given by Bialynicki-Birula, Mielnik, and Plebański [7], Chacon and Fomenko [10], and Iserles and Nørsett [28], although they are quite complicated. The simplest way to obtain these terms is by computing them recursively using a procedure given by Blanes et al. [8]. The recurrence relation is

$$\begin{aligned} \Omega_1(t) &= \int_0^t M(\tau)\,\mathrm{d}\tau \\ \Omega_n(t) &= \sum_{j=1}^{n-1} \frac{B_j}{j!} \int_0^t S_n^j(\tau)\,\mathrm{d}\tau \quad \text{for } n \geq 2, \end{aligned} \tag{2.70}$$

where B_j is the jth Bernoulli number and

$$S_n^j(\tau) = \sum_{i_1+\cdots+i_j=n-1} [\Omega_{i_1}(\tau), [\ldots[\Omega_{i_j}(\tau), M(\tau)]\ldots]] \tag{2.71}$$

for $i_k \in \mathbb{N} \setminus \{0\}$ with $k \in \{1, \ldots, j\}$. The $[.,.]$ operator that appears in (2.71) is the matrix commutator $[A, B] = AB - BA$. Now $S_n^j(\tau)$ can also be computed recursively using

$$
\begin{aligned}
S_n^1(\tau) &= [\Omega_{n-1}(\tau), M(\tau)] \\
S_n^j(\tau) &= \sum_{m=1}^{n-j} [\Omega_m(\tau), S_{n-m}^{j-1}(\tau)] \quad \text{for } 2 \leq j \leq n-1.
\end{aligned} \tag{2.72}
$$

If we take S_n^j from (2.71) and substitute it in (2.70) we get

$$
\Omega_n(t) = \sum_{j=1}^{n-1} \frac{B_j}{j!} \sum_{i_1 + \cdots + i_j = n-1} \int_0^t \operatorname{ad}_{\Omega_{i_1}(\tau)} \operatorname{ad}_{\Omega_{i_2}(\tau)} \ldots \operatorname{ad}_{\Omega_{i_j}(\tau)} M(\tau)\, \mathrm{d}\tau \quad n \geq 2,
$$

where the commutator $[\Omega, M]$ is written as the adjoint action $\operatorname{ad}_\Omega(M) = [\Omega, M]$. This is a sum of n-fold integrals of $n-1$ nested commutators, an expression that becomes more intricate as n increases. If $M(t)$ belongs to some Lie algebra $\mathfrak{g}$, then $\Omega(t)$ or any truncation of $\Omega(t)$ from the Magnus expansion also stays in $\mathfrak{g}$, thus $\exp(\Omega(t)) \in G$ where G denotes the Lie group whose corresponding Lie algebra is $\mathfrak{g}$. We are interested in the case where $\mathfrak{g}$ is the set of anti-symmetric 3×3 matrices and G is the set of 3×3 rotation matrices in $SO(3)$.

Magnus [**38**] gave no convergence estimate for the Magnus series but did state that the series converges for sufficiently small t. A sufficient condition for convergence is given by Moan and Niesen [**43**], who state that the series converges for

$$
\int_0^t \|M(\tau)\|_2 \, \mathrm{d}\tau < \pi, \tag{2.73}
$$

where $\|.\|_2$ denotes the 2-norm. Writing out the first four terms of $\Omega_n(t)$ explicitly using (2.70) and (2.72), along with the formula

$$
\int_0^\alpha \int_y^\alpha f(x, y)\, \mathrm{d}x\, \mathrm{d}y = \int_0^\alpha \int_0^x f(x, y)\, \mathrm{d}y\, \mathrm{d}x, \tag{2.74}
$$

we find that

$$\begin{aligned}
\Omega_1(t) &= \int_0^t M_1 \,\mathrm{d}t_1 \\
\Omega_2(t) &= \frac{1}{2}\int_0^t\int_0^{t_1} [M_1, M_2] \,\mathrm{d}t_2 \,\mathrm{d}t_1 \\
\Omega_3(t) &= \frac{1}{6}\int_0^t\int_0^{t_1}\int_0^{t_2} \Big([M_1, [M_2, M_3]] + [M_3, [M_2, M_1]]\Big) \,\mathrm{d}t_3 \,\mathrm{d}t_2 \,\mathrm{d}t_1 \\
\Omega_4(t) &= \frac{1}{12}\int_0^t\int_0^{t_1}\int_0^{t_2}\int_0^{t_3} \Big([[[M_1, M_2], M_3], M_4] + [M_1, [[M_2, M_3], M_4]] \\
&\qquad + [M_1, [M_2, [M_3, M_4]]] + [M_2, [M_3, [M_4, M_1]]]\Big) \,\mathrm{d}t_4 \,\mathrm{d}t_3 \,\mathrm{d}t_2 \,\mathrm{d}t_1,
\end{aligned}$$

where we abbreviated $M_i = M(t_i)$. The fifth order term is simply too long to list here, but can be found in Prato and Lamberti [48]. For the full derivation of the first three terms, see Appendix D. The symmetry that appears in the first three terms is misleading, because higher order terms require repeated use of (2.74) the series becomes complicated quickly, and there is no actual symmetry.

In the scalar case $\Omega_1(t)$ is the exact exponent that appears in the exponential, but for higher dimensions this term cannot give the whole solution. If we insist on having an exponential representation of the solution then the exponent needs to be corrected, and the remaining terms of the Magnus series provide this correction systematically, i.e. Ω or parts of it are in the Lie algebra of the Lie group of evolution.

In the special case where the time dependent square matrix $M(t)$ commutes with itself, all the commutators that appear in each $\Omega_n(t)$ for $n \geq 2$ vanish and the Magnus series reduces to $\Omega(t) = \Omega_1(t)$. As a consequence we get the following result:

If $M(t)$ is a time dependent square matrix where $[M(t_1), M(t_2)] = 0$ for any pair of t_1 and t_2, then the general solution for a system of differential equations of the form

$$\dot{\boldsymbol{X}} = M(t)\boldsymbol{X} \tag{2.75}$$

is precisely given by

$$\boldsymbol{X} = \exp\left(\int_{t_0}^t M(\tau)\,\mathrm{d}\tau\right)\boldsymbol{X}(0), \tag{2.76}$$

where $\boldsymbol{X}(0)$ is the initial condition.

2.11 Equations of Orientation

2.11.1 In Euler Angles

The differential equation for rotations given in (2.26) can be written in terms of Euler angles or in quaternions. We start with Euler angles and choose the z-x-z convention, so that

$$R = R_z(\phi)R_x(\theta)R_z(\psi) \qquad \text{and}$$
$$\dot{R} = R_z'(\phi)R_x(\theta)R_z(\psi)\dot{\phi} + R_z(\phi)R_x'(\theta)R_z(\psi)\dot{\theta} + R_z(\phi)R_x(\theta)R_z'(\psi)\dot{\psi}.$$

Substituting these results in (2.25) yields the angular velocity tensor in $\mathcal{F}_B$, which is an antisymmetric matrix, and the non-diagonal entries tell us that the angular velocity is

$$\boldsymbol{\mathcal{W}} = \begin{pmatrix} \dot{\phi}\sin(\theta)\sin(\psi) + \dot{\theta}\cos(\psi) \\ \dot{\phi}\sin(\theta)\cos(\psi) - \dot{\theta}\sin(\psi) \\ \dot{\phi}\cos(\theta) + \dot{\psi} \end{pmatrix}. \tag{2.77}$$

As this is linear in the velocities, it can be rewritten as

$$\boldsymbol{\mathcal{W}} = \underbrace{\begin{pmatrix} \sin(\theta)\sin(\psi) & \cos(\psi) & 0 \\ \cos(\psi)\sin(\theta) & -\sin(\psi) & 0 \\ \cos(\theta) & 0 & 1 \end{pmatrix}}_{\mathcal{A}} \begin{pmatrix} \dot{\phi} \\ \dot{\theta} \\ \dot{\psi} \end{pmatrix}. \tag{2.78}$$

Now $\mathcal{A}$ is almost everywhere invertible, except for the singularities which occur at

$$\theta = n\pi \ \forall n \in \mathbb{Z}.$$

These points correspond to the coordinate singularities discussed earlier and as they are not physical singularities, they can be removed by switching to an alternate Euler convention. If we let $\dot{\boldsymbol{\phi}} = \begin{pmatrix} \dot{\phi} \\ \dot{\theta} \\ \dot{\psi} \end{pmatrix}$ we may write

$$\dot{\boldsymbol{\phi}} = \mathcal{A}^{-1}\boldsymbol{\mathcal{W}}, \tag{2.79}$$

where $\mathcal{A}^{-1} = \begin{pmatrix} \csc\theta\sin\psi & \csc\theta\cos\psi & 0 \\ \cos\psi & -\sin\psi & 0 \\ -\cot\theta\sin\psi & -\cot\theta\cos\psi & 1 \end{pmatrix}$ and $\boldsymbol{\mathcal{W}}$ is a known function of time. This gives the equations of orientation in terms of Euler angles and for a rigid body we may use (2.43) to write (2.79) as

$$\dot{\boldsymbol{\phi}} = \mathcal{A}^{-1}J^{-1}\boldsymbol{M}, \tag{2.80}$$

where $\boldsymbol{M}$ is determined by the equations of motion (2.44).

Consider the case where two moments of inertia are the same as in (2.45). If we let the z-axis of $\mathcal{F}_S$ point in the direction of the angular momentum vector and initially align the x-axis of $\mathcal{F}_S$ with X-axis of $\mathcal{F}_B$ so that they coincide with the line-of-nodes, then the initial condition of $\boldsymbol{\phi}$ is

$$\begin{pmatrix} \phi(0) \\ \theta(0) \\ \psi(0) \end{pmatrix} = \begin{pmatrix} 0 \\ \theta_0 \\ 0 \end{pmatrix}. \tag{2.81}$$

With this setup the initial condition for the angular momentum $\boldsymbol{M}$ with magnitude l becomes

$$\begin{pmatrix} M_x(0) \\ M_y(0) \\ M_z(0) \end{pmatrix} = l \begin{pmatrix} 0 \\ \sin\theta_0 \\ \cos\theta_0 \end{pmatrix}, \tag{2.82}$$

which simplifies the solution given in (2.50) to

$$\begin{pmatrix} M_x \\ M_y \\ M_z \end{pmatrix} = l \begin{pmatrix} -\sin\theta_0 \sin(Wt) \\ \sin\theta_0 \cos(Wt) \\ \cos\theta_0 \end{pmatrix}. \tag{2.83}$$

The angular velocity is then

$$\boldsymbol{\mathcal{W}} = \begin{pmatrix} \mathcal{W}_x \\ \mathcal{W}_y \\ \mathcal{W}_z \end{pmatrix} = l \begin{pmatrix} -J_y^{-1} \sin\theta_0 \sin(Wt) \\ J_y^{-1} \sin\theta_0 \cos(Wt) \\ J_z^{-1} \cos\theta_0 \end{pmatrix}, \tag{2.84}$$

which shows that the component of the angular velocity perpendicular to the Z-axis is of constant amplitude $lJ_y^{-1}\sin\theta_0$ and that it must rotate uniformly with angular speed W. This means the spin $\dot{\psi}$ can only be either W or $-W$, which in turn implies $\psi = Wt$ or $\psi = -Wt$, both of which have zero as the constant term in order to satisfy the initial condition $\psi(0)$ of (2.81). Plugging (2.84) into (2.79) with $\psi = Wt$ we find that $\dot{\psi}$ is time t dependent, which is inconsistent with our earlier statement of uniform spin so this is not a valid solution. Trying again with $\psi = -Wt$ we get

$$\begin{pmatrix} \dot{\phi} \\ \dot{\theta} \\ \dot{\psi} \end{pmatrix} = l \begin{pmatrix} J_y^{-1} \sin\theta_0 \csc\theta \\ 0 \\ J_z^{-1}\cos\theta_0 - J_y^{-1}\sin\theta_0 \cot\theta \end{pmatrix}, \tag{2.85}$$

indicating there is no nutation meaning θ is constant and that both $\dot{\phi}$ and $\dot{\psi}$ are constants, which can be integrated to obtain linear functions of time. So $\psi = -Wt$ is the only valid solution and using the initial condition (2.81) to determine the constants we find that the solution to (2.85) is

$$\begin{pmatrix} \phi \\ \theta \\ \psi \end{pmatrix} = \begin{pmatrix} lJ_y^{-1}t \\ \theta_0 \\ l(J_z^{-1} - J_y^{-1})\cos(\theta_0)t \end{pmatrix}. \tag{2.86}$$

If we associate $\dot{\phi}$ as the somersault rate and $\dot{\psi}$ as the twist rate like Yeadon in [66] (though he labelled these quantities as Ω and p respectively), we get the relation

$$\dot{\psi} = \dot{\phi}\left(\frac{J_y}{J_z} - 1\right)\cos\theta_0. \tag{2.87}$$

Now the way Yeadon defined the tilt α in [66] is equivalent to $\theta_0 = \pi/2 - \alpha$ for us, so $\cos\theta_0$ in (2.87) becomes $\sin\alpha$ and this is equivalent to Yeadon's (25) in [66], which he later used in the study of [67], [68], and [72].

2.11.2 In Quaternions

We now derive the equations of orientation in quaternions. Starting with R from (2.38) and computing $\dot{R}$ with the chain rule we can obtain the angular velocity tensor $\hat{\boldsymbol{\mathcal{W}}}$ using (2.25), giving

$$\hat{\boldsymbol{\mathcal{W}}} = 2\begin{pmatrix} q_0\dot{q}_0 + q_1\dot{q}_1 + q_2\dot{q}_2 + q_3\dot{q}_3 & q_3\dot{q}_0 - q_2\dot{q}_1 + q_1\dot{q}_2 - q_0\dot{q}_3 & -q_2\dot{q}_0 - q_3\dot{q}_1 + q_0\dot{q}_2 + q_1\dot{q}_3 \\ -q_3\dot{q}_0 + q_2\dot{q}_1 - q_1\dot{q}_2 + q_0\dot{q}_3 & q_0\dot{q}_0 + q_1\dot{q}_1 + q_2\dot{q}_2 + q_3\dot{q}_3 & q_1\dot{q}_0 - q_0\dot{q}_1 - q_3\dot{q}_2 + q_2\dot{q}_3 \\ q_2\dot{q}_0 + q_3\dot{q}_1 - q_0\dot{q}_2 - q_1\dot{q}_3 & -q_1\dot{q}_0 + q_0\dot{q}_1 + q_3\dot{q}_2 - q_2\dot{q}_3 & q_0\dot{q}_0 + q_1\dot{q}_1 + q_2\dot{q}_2 + q_3\dot{q}_3 \end{pmatrix}$$

which is an antisymmetric matrix because in vector form $\boldsymbol{q}\cdot\boldsymbol{q} = 1 \implies 2\boldsymbol{q}\cdot\dot{\boldsymbol{q}} = 0$, making the diagonal entries vanish. Removing the hat operator and adding the condition for unit quaternions we get

$$2\begin{pmatrix} -q_1\dot{q}_0 + q_0\dot{q}_1 + q_3\dot{q}_2 - q_2\dot{q}_3 \\ -q_2\dot{q}_0 - q_3\dot{q}_1 + q_0\dot{q}_2 + q_1\dot{q}_3 \\ -q_3\dot{q}_0 + q_2\dot{q}_1 - q_1\dot{q}_2 + q_0\dot{q}_3 \\ q_0\dot{q}_0 + q_1\dot{q}_1 + q_2\dot{q}_2 + q_3\dot{q}_3 \end{pmatrix} = \begin{pmatrix} \mathcal{W}_x \\ \mathcal{W}_y \\ \mathcal{W}_z \\ 0 \end{pmatrix},$$

and since this is linear in the velocities we can rewrite it as

$$\begin{aligned} \begin{pmatrix} \dot{q}_0 \\ \dot{q}_1 \\ \dot{q}_2 \\ \dot{q}_3 \end{pmatrix} &= \frac{1}{2}\begin{pmatrix} -q_1 & -q_2 & -q_3 & q_0 \\ q_0 & -q_3 & q_2 & q_1 \\ q_3 & q_0 & -q_1 & q_2 \\ -q_2 & q_1 & q_0 & q_3 \end{pmatrix}\begin{pmatrix} \mathcal{W}_x \\ \mathcal{W}_y \\ \mathcal{W}_z \\ 0 \end{pmatrix} \\ &= \frac{1}{2}\begin{pmatrix} 0 & -\mathcal{W}_x & -\mathcal{W}_y & -\mathcal{W}_z \\ \mathcal{W}_x & 0 & \mathcal{W}_z & -\mathcal{W}_y \\ \mathcal{W}_y & -\mathcal{W}_z & 0 & \mathcal{W}_x \\ \mathcal{W}_z & \mathcal{W}_y & -\mathcal{W}_x & 0 \end{pmatrix}\begin{pmatrix} q_0 \\ q_1 \\ q_2 \\ q_3 \end{pmatrix}, \end{aligned} \tag{2.88}$$

where these are the equations of orientation in terms of quaternions.

If we interpret the quaternion $\boldsymbol{q}$ as the angle-vector information with rotation ξ about the unit vector $\boldsymbol{u}$ as done in (2.35), then the equations of orientation (3.2) transform to

$$\begin{pmatrix} -\frac{1}{2}\sin\left(\frac{\xi}{2}\right) & \mathbf{0}^t \\ \frac{1}{2}\boldsymbol{u}\cos\left(\frac{\xi}{2}\right) & \sin\left(\frac{\xi}{2}\right)\mathbb{1} \end{pmatrix}\begin{pmatrix} \dot{\xi} \\ \dot{\boldsymbol{u}} \end{pmatrix} = \frac{1}{2}\begin{pmatrix} -\boldsymbol{\mathcal{W}}^t\boldsymbol{u}\sin\left(\frac{\xi}{2}\right) \\ \boldsymbol{\mathcal{W}}\cos\left(\frac{\xi}{2}\right) - \hat{\boldsymbol{\mathcal{W}}}\boldsymbol{u}\sin\left(\frac{\xi}{2}\right) \end{pmatrix}.$$

The matrix on the LHS has determinant $-\frac{1}{2}\sin^4\left(\frac{\xi}{2}\right)$, which is almost everywhere invertible except when $\xi = 2k\pi$ for $k \in \mathbb{Z}$. These situations correspond to the case of no net rotation, and for every other ξ we can invert the matrix on the LHS to obtain

$$\begin{pmatrix} \dot{\xi} \\ \dot{\boldsymbol{u}} \end{pmatrix} = \begin{pmatrix} \boldsymbol{u}^t \\ \frac{1}{2}\Big(\cot\left(\frac{\xi}{2}\right)(\mathbb{1} - \boldsymbol{u}\boldsymbol{u}^t) + \hat{\boldsymbol{u}}\Big) \end{pmatrix} \boldsymbol{\mathcal{W}}. \tag{2.89}$$

By converting the equations of orientation written in terms of quaternions into the angle-vector representation we have once again introduced singularities, as can be seen in (2.89) when $\xi = 2k\pi$ for $k \in \mathbb{Z}$. These are mild singularities like those encountered from using spherical polar coordinates, but are singularities nonetheless, and their appearance bears some resemblance to those encountered with the use of Euler angles.

Any result obtained in Euler angles can of course be converted into quaternions and vice versa. For our standard Euler convention z-x-z, the transformation from Euler angles to quaternions is given by

$$\begin{aligned} \begin{pmatrix} q_0 \\ q_1 \\ q_2 \\ q_3 \end{pmatrix} &= \begin{pmatrix} \cos\left(\frac{\phi}{2}\right) \\ 0 \\ 0 \\ \sin\left(\frac{\phi}{2}\right) \end{pmatrix} \begin{pmatrix} \cos\left(\frac{\theta}{2}\right) \\ \sin\left(\frac{\theta}{2}\right) \\ 0 \\ 0 \end{pmatrix} \begin{pmatrix} \cos\left(\frac{\psi}{2}\right) \\ 0 \\ 0 \\ \sin\left(\frac{\psi}{2}\right) \end{pmatrix} \\ &= \begin{pmatrix} \cos\left(\frac{\theta}{2}\right)\cos\left(\frac{\phi+\psi}{2}\right) \\ \sin\left(\frac{\theta}{2}\right)\cos\left(\frac{\phi-\psi}{2}\right) \\ \sin\left(\frac{\theta}{2}\right)\sin\left(\frac{\phi-\psi}{2}\right) \\ \cos\left(\frac{\theta}{2}\right)\sin\left(\frac{\phi+\psi}{2}\right) \end{pmatrix}, \end{aligned} \tag{2.90}$$

where quaternion multiplication is used to yield the final result. The inverse is then obtained by solving these equations to get

$$\begin{pmatrix} \phi \\ \theta \\ \psi \end{pmatrix} = \begin{pmatrix} \operatorname{Arg}\Big[(q_0 + iq_3)(q_1 + iq_2)\Big] \\ 2\arcsin\sqrt{q_1^2 + q_2^2} \\ \operatorname{Arg}\Big[(q_0 + iq_3)/(q_1 + iq_2)\Big] \end{pmatrix}. \tag{2.91}$$

We provide a diagram showing the relationship between rotation matrices, Euler angles, and quaternions with their respective transformation formulas listed.

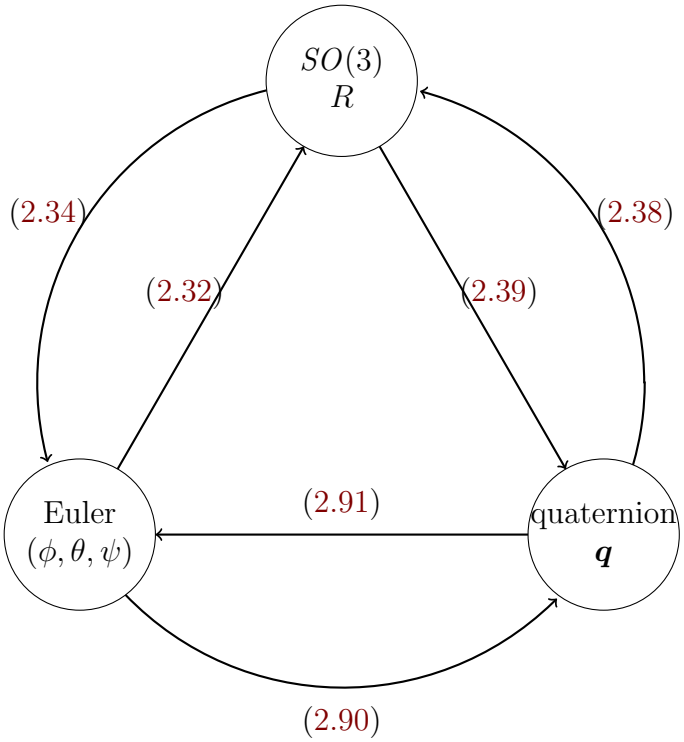

CHAPTER 3

Coupled Rigid Bodies

In this chapter we move to a system of n coupled rigid bodies, where the orientation is defined by the orientation of a reference segment. We begin by discussing angular velocities, joint locations, and centre of mass in Chapter 3.1. We use Table 1.1 to define the geometry of the athlete, specify how segments are connected together with position vectors, and present the technical specifications of the general 10-body model in Chapter 3.2. The equation for angular momentum is derived for n coupled rigid bodies in Chapter 3.3, where in generalising (1.2) we find that an additional term $\boldsymbol{A}$ appears during shape change, which we define this to be the angular momentum shift. The equations of motion (2.42) and equations of orientation (2.88) are then extended in Chapter 3.4, where in $\mathcal{F}_C$ we find

$$\dot{\boldsymbol{L}} = \boldsymbol{L} \times \boldsymbol{\Omega} \qquad \text{equations of motion} \tag{3.1}$$

$$\dot{\boldsymbol{q}} = \frac{1}{2} \begin{pmatrix} 0 & -\boldsymbol{\Omega}^t \\ \boldsymbol{\Omega} & -\hat{\boldsymbol{\Omega}} \end{pmatrix} \boldsymbol{q} \qquad \text{equations of orientation} \tag{3.2}$$

hold true if the angular velocity vector $\boldsymbol{\Omega}$ is modified to (3.24). Unlike the angular momentum and angular velocity, we will not be referring again to the quaternion in $\mathcal{F}_B$, and have therefore kept $\boldsymbol{q}$ as the symbol to represent the quaternion in $\mathcal{F}_C$.

In Chapter 3.5 we fix most shape angles to obtain a 2-body model, which has simpler formulas for the geometry (given by the centre of mass vectors $\boldsymbol{C}_1$ and $\boldsymbol{C}_2$), tensor of inertia I, and angular momentum shift $\boldsymbol{A}$. The reduction is then repeated for the 3-body model, and these models will be used later in Chapter 5 and Chapter 6.

3.1 Velocities, Joints & Centre of Mass

The previous chapter provided the complete description of the dynamics of a single rigid body, and this will now be extended for n coupled rigid bodies. The goal of the next three sections is to derive the equation $\boldsymbol{L} = I\boldsymbol{\Omega} + \boldsymbol{A}$ which generalises $\boldsymbol{L} = I\boldsymbol{\Omega}$ to the case of a shape changing body. Let each rigid body B_i of mass m_i have its own local coordinate system denoted by $\mathcal{F}_{B_i}$, for each $i \in \{1, 2, ..., n\}$. The natural choice for each $\mathcal{F}_{B_i}$ is to position its origin at the centre of mass of B_i, and to align its coordinate axes with the principle axes of inertia of B_i so that the tensor of inertia I_i is diagonal. It therefore seems clear to define $\mathcal{F}_B$ as the frame with the origin located at the overall centre of mass of the coupled rigid bodies and its coordinate axes pointing in the direction of the in general changing principal axes of inertia of the system. However, as this is not an intuitive body frame, we introduce the central-body-frame $\mathcal{F}_C$ that has its origin positioned at the overall centre of mass, but its coordinate axes aligned parallel to a reference body segment $\mathcal{F}_{B_{ref}}$ for some $ref \in \{1, 2, ..., n\}$, which we pick to be the torso of the diver. Lastly there is $\mathcal{F}_S$ that moves with the overall centre of mass, but as the directions of the coordinate axes are fixed we treat this as a spatial frame (one under no external torque). The overall orientation of the coupled rigid body is then determined by the difference in direction of the coordinate axes of $\mathcal{F}_C$ and $\mathcal{F}_S$.

Let R_i be the rotation matrix that describes the orientation of B_i in $\mathcal{F}_S$. We now want to decompose R_i into two rotation matrices, such that

$$R_i = R_\upsilon R_{\alpha_i}. \tag{3.3}$$

The rotation matrix R_υ specifies the orientation of B_{ref} in $\mathcal{F}_C$ with respect to $\mathcal{F}_S$ while each R_{α_i} measures the relative orientation between B_i and B_{ref} (note for convenience we allow the index i to run through ref as well and simply set $R_{\alpha_{ref}}$ to be the identity matrix). This decomposition allows us to specify the orientation of the system by R_υ, and the shape with the collection of R_{α_i}. The geometric meaning of using R_υ and R_{α_i} instead of R_i directly means we first orient $\mathcal{F}_{B_i}$ to $\mathcal{F}_C$ with R_{α_i}, then use R_υ to align $\mathcal{F}_C$ with $\mathcal{F}_S$. Now the orientation R_υ is determined by B_{ref}, and a natural choice for B_{ref} is the torso, but mathematically we could have chosen any other body segment (e.g. the head), since no choice is superior to any other. Different choices of B_{ref} lead to different values of R_υ (and also R_i), but if the athlete performs a sequence of shape changes that forms a closed curve on shape space, i.e. the athlete starts and finishes with the same shape, then the orientation change ΔR_υ is well-defined and cannot be different for different ways of measuring R_υ and ΔR_υ. However, if the sequence of shape change leads to the athlete having different initial and final shapes, i.e. a non-closed curve on shape space, then ΔR_υ is not well-defined as it depends on the way R_υ is measured. Thus we see there is freedom on how we decide to measure R_υ, which is known

as the 'gauge freedom'. We pick the torso to be the reference segment so that R_v is defined, allowing the gauge to be fixed. Quantities with physical meaning will have to be gauge invariant, as it is not logical for a physical quantity to change with the choice of B_{ref}. Thus we should only look at the orientation change when the athlete begins and ends with the same shape, i.e. only closed curves on shape space are considered. Gauge theory is discussed further in Montgomery [45] where it is applied to the Kane-Scher [31] cat, Littlejohn and Reinsch [36] applies gauge theory in the n-body problem, and Putterman and Raz [49] uses it to demonstrate gauge transformations for a simple model cat that can rotate itself under zero angular momentum.

Going back to (3.3), if we take the time derivative we get

$$\dot{R}_i = \dot{R}_v R_{\alpha_i} + R_v \dot{R}_{\alpha_i}. \tag{3.4}$$

Substituting this result along with (3.3) into (2.25) produces

$$\begin{aligned} \hat{\boldsymbol{\mathcal{W}}}_i &= (R_v R_{\alpha_i})^t (R_v R_{\alpha_i})' \\ &= R^t_{\alpha_i} R^t_v (\dot{R}_v R_{\alpha_i} + R_v \dot{R}_{\alpha_i}) \\ &= R^t_{\alpha_i} \hat{\boldsymbol{\Omega}}_v R_{\alpha_i} + \hat{\boldsymbol{\Omega}}_{\alpha_i}, \end{aligned} \tag{3.5}$$

where we can interpret $\hat{\boldsymbol{\Omega}}_v$ as the angular velocity tensor of B_{ref} in $\mathcal{F}_C$, and $\hat{\boldsymbol{\Omega}}_{\alpha_i}$ as the angular velocity tensor of B_i relative to B_{ref}, also measured in $\mathcal{F}_C$. To extract the angular velocity vector $\boldsymbol{\mathcal{W}}_i$ in terms of $\boldsymbol{\Omega}_v$ and $\boldsymbol{\Omega}_{\alpha_i}$ from (3.5), we use the fact that

$$\begin{aligned} \hat{\boldsymbol{\mathcal{W}}}_i \boldsymbol{v} &= (R^t_{\alpha_i} \hat{\boldsymbol{\Omega}}_v R_{\alpha_i} + \hat{\boldsymbol{\Omega}}_{\alpha_i}) \boldsymbol{v} \\ &= R^t_{\alpha_i} (\boldsymbol{\Omega}_v \times R_{\alpha_i} \boldsymbol{v}) + \boldsymbol{\Omega}_{\alpha_i} \times \boldsymbol{v} \\ &= R^t_{\alpha_i} (R_{\alpha_i} R^t_{\alpha_i} \boldsymbol{\Omega}_v \times R_{\alpha_i} \boldsymbol{v}) + \boldsymbol{\Omega}_{\alpha_i} \times \boldsymbol{v} \\ &= R^t_{\alpha_i} R_{\alpha_i} (R^t_{\alpha_i} \boldsymbol{\Omega}_v \times \boldsymbol{v}) + \boldsymbol{\Omega}_{\alpha_i} \times \boldsymbol{v} \\ &= (R^t_{\alpha_i} \boldsymbol{\Omega}_v + \boldsymbol{\Omega}_{\alpha_i}) \times \boldsymbol{v} \end{aligned}$$

for any vector $\boldsymbol{v}$, allowing us to see

$$\boldsymbol{\mathcal{W}}_i = R^t_{\alpha_i} \boldsymbol{\Omega}_v + \boldsymbol{\Omega}_{\alpha_i}. \tag{3.6}$$

Now if we let $\boldsymbol{C}_i$ be the position vector in $\mathcal{F}_C$ that goes from the overall centre of mass to the centre of mass of B_i, then the relationships of a vector $\boldsymbol{\mathcal{V}}$ in each of the frames are

$$\boldsymbol{\mathcal{V}}_S = R_v \boldsymbol{\mathcal{V}}_C \qquad\qquad \boldsymbol{\mathcal{V}}_C = \boldsymbol{C}_i + R_{\alpha_i} \boldsymbol{\mathcal{V}}_{B_i},$$

where the subscripts of $\boldsymbol{\mathcal{V}}$ denote the frame the vector is written in. The $\boldsymbol{C}_i$'s are not independent variables but depend on the shape and geometry of the system. The shape of the system is determined by the collection of R_{α_i}, and geometry refers to how the n bodies are connected together, i.e. with a set of vectors $\boldsymbol{E}^j_i$

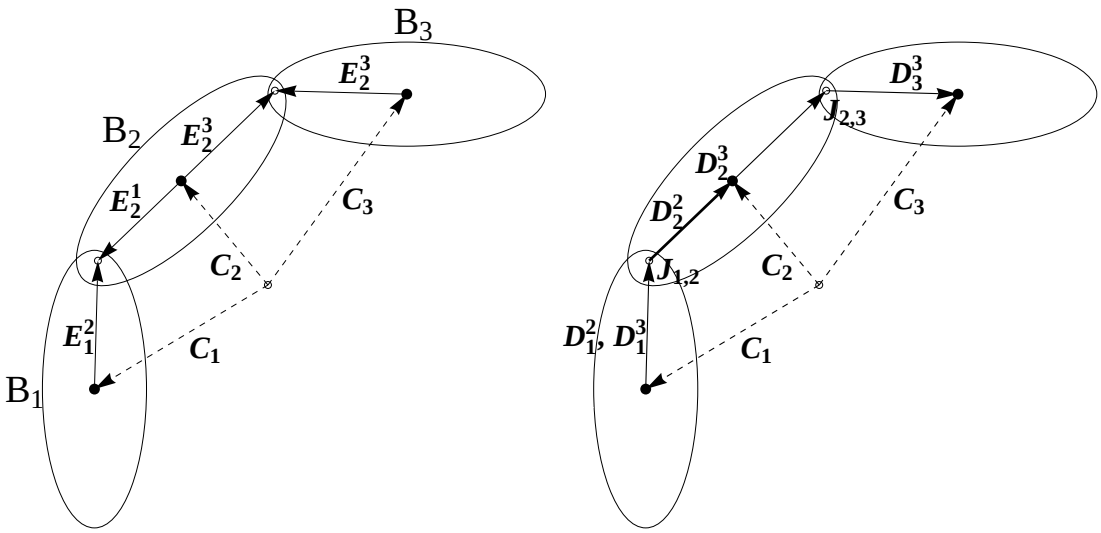

(A) Three bodies with $\boldsymbol{C}_i, B_i$, and $\boldsymbol{E}_j^i$ labelled.

(B) Three bodies with $\boldsymbol{C}_i, \boldsymbol{J}_{i,j}$, and $\boldsymbol{D}_j^i$ labelled.

Figure 3.1. Illustration of coupled rigid bodies with three body segments given by B_i for $i \in \{1, 2, 3\}$. The position vectors $\boldsymbol{C}_i$ measured in $\mathcal{F}_C$ are from the overall centre of mass to the centre of mass of B_i. The point where B_i connects with B_j in $\mathcal{F}_C$ is given by the joint position $\boldsymbol{J}_{i,j}$. The constant vectors $\boldsymbol{E}_j^i$ and $\boldsymbol{D}_j^i$ are written in $\mathcal{F}_{B_j}$ to determine the joint locations of the coupled rigid body.

written in $\mathcal{F}_{B_i}$ so that they are constant, which can then be used to determine the set of joint locations $\boldsymbol{J}_{i,j}$ specified in the overall body frame $\mathcal{F}_C$.

Consider a simple example with three bodies as shown in Figure 3.1. We have the following relations

$$\begin{aligned} \boldsymbol{C}_1 + R_{\alpha_1} \boldsymbol{E}_1^2 &= \boldsymbol{C}_2 + R_{\alpha_2} \boldsymbol{E}_2^1 \\ \boldsymbol{C}_2 + R_{\alpha_2} \boldsymbol{E}_2^3 &= \boldsymbol{C}_3 + R_{\alpha_3} \boldsymbol{E}_3^2, \end{aligned}$$

which can be rewritten as

$$\begin{aligned} \boldsymbol{C}_2 &= \boldsymbol{C}_1 + R_{\alpha_1} \boldsymbol{E}_1^2 - R_{\alpha_2} \boldsymbol{E}_2^1 \\ \boldsymbol{C}_3 &= \boldsymbol{C}_1 + R_{\alpha_1} \boldsymbol{E}_1^2 + R_{\alpha_2} (\boldsymbol{E}_2^3 - \boldsymbol{E}_2^1) - R_{\alpha_3} \boldsymbol{E}_3^2. \end{aligned} \tag{3.7}$$

Without loss of generality, we set $\boldsymbol{C}_{ref} = \boldsymbol{C}_1$ and express $\boldsymbol{C}_2$ and $\boldsymbol{C}_3$ in terms of $\boldsymbol{C}_{ref}$, the shape with R_{α_2} and R_{α_3}, and geometry with the collection of $\boldsymbol{E}_i^j$. To enable formulas to be written concisely we introduce the constant vectors $\boldsymbol{D}_j^i$,

which are only geometry dependent thereby allowing us to compactly write

$$\boldsymbol{C}_i = \boldsymbol{C}_{ref} + \sum_{j=1}^{n} R_{\alpha_j} \boldsymbol{D}_j^i, \tag{3.8}$$

and thus the collection of $\boldsymbol{D}_j^i$ relates every $\boldsymbol{C}_i$ to $\boldsymbol{C}_{ref}$. In this example

$$\begin{aligned} \boldsymbol{D}_1^2 &= \boldsymbol{D}_1^3 = \boldsymbol{E}_1^2 & \boldsymbol{D}_2^2 &= -\boldsymbol{E}_2^1 \\ \boldsymbol{D}_2^3 &= \boldsymbol{E}_2^3 - \boldsymbol{E}_2^1 & \boldsymbol{D}_3^3 &= -\boldsymbol{E}_3^2, \end{aligned}$$

and every other unspecified vector it is $\boldsymbol{D}_j^i = \boldsymbol{0}$.

In general, we allow any number of joints on B_i for each of the n bodies, and constrain each joint on B_i to connect with exactly one other adjacent body. So if B_i is joined to B_j at the joint $\boldsymbol{J}_{i,j}$, then $\boldsymbol{E}_i^j$ is the constant vector in $\mathcal{F}_{B_i}$ that connects the centre of mass of B_i (origin of $\mathcal{F}_{B_i}$) to the point $\boldsymbol{J}_{i,j}$. The superscript j in $\boldsymbol{E}_i^j$ also informs us that the adjacent body being attached to B_i at $\boldsymbol{J}_{i,j}$ is in fact B_j. So clearly there must be a corresponding vector $\boldsymbol{E}_j^i$ in $\mathcal{F}_{B_j}$ that connects the centre of mass of B_j to $\boldsymbol{J}_{j,i} = \boldsymbol{J}_{i,j}$. These $\boldsymbol{E}_i^j$ vectors must always occur in pairs, i.e. every $\boldsymbol{E}_i^j$ will have a corresponding $\boldsymbol{E}_j^i$ vector and together they create the link between B_i and B_j at $\boldsymbol{J}_{i,j}$ (or $\boldsymbol{J}_{j,i}$). Since the joint location can be thought of as a position vector written in $\mathcal{F}_C$ at any instantaneous moment in time, we may write the identity

$$\boldsymbol{J}_{i,j} := \boldsymbol{C}_i + R_{\alpha_i} \boldsymbol{E}_i^j = \boldsymbol{C}_j + R_{\alpha_j} \boldsymbol{E}_j^i. \tag{3.9}$$

Consider a rooted tree where each B_i is treated as a node with B_{ref} being the root (top most node). Let $B_{p(j)}$ denote the node who is the parent of B_j in the tree, and $B_{c(j,i)}$ be the child of B_j who is either B_i or is the node with the direct line to B_i, i.e. an ancestor of B_i. An ancestor of B_i is any node reachable by repeated proceedings from child to parent, e.g. the root of the tree B_{ref} is an ancestor to every other node. We can now give the general definition of the constant vectors $\boldsymbol{D}_j^i$ using the idea of trees. We have $\boldsymbol{D}_j^i = \boldsymbol{0}$ for $1 \leq i \leq n$ and $1 \leq j \leq n$, unless either $j = i$ and $j \neq ref$, or if B_j is an ancestor of B_i in the tree. When this occurs we have

$$\boldsymbol{D}_j^i = \begin{cases} -\boldsymbol{E}_j^{p(j)} & \text{if } j = i \text{ and } j \neq ref \\ \boldsymbol{E}_{j=ref}^{c(j,i)} & \text{if } j \neq i \text{ and } j = ref \\ -\boldsymbol{E}_j^{p(j)} + \boldsymbol{E}_j^{c(j,i)} & \text{if } j \neq i \text{ and } j \neq ref. \end{cases} \tag{3.10}$$

Now

$$\sum_{i=1}^{n} m_i \boldsymbol{C}_i = \sum_{i=1}^{n} m_i \boldsymbol{C}_{ref} + \sum_{i=1}^{n} \left(m_i \sum_{j=1}^{n} R_{\alpha_j} \boldsymbol{D}_j^i \right) \tag{3.11}$$
$$= \boldsymbol{C}_{ref} \sum_{i=1}^{n} m_i + \sum_{j=1}^{n} \left(R_{\alpha_j} \sum_{i=1}^{n} m_i \boldsymbol{D}_j^i \right) = \mathbf{0},$$

the last line gives $\mathbf{0}$ because the overall centre of mass is located at the origin in $\mathcal{F}_C$ by definition, allowing us to rearrange (3.11) to yield

$$\boldsymbol{C}_{ref} = -\sum_{j=1}^{n} \left(R_{\alpha_j} \bar{\boldsymbol{D}}_j \right), \tag{3.12}$$

where

$$\bar{\boldsymbol{D}}_j = \frac{1}{M} \sum_{i=1}^{n} m_i \boldsymbol{D}_j^i \qquad \text{and} \qquad \sum_{i=1}^{n} m_i = M.$$

The $\bar{\boldsymbol{D}}_j$'s are interpreted as the weighted mean of the $\boldsymbol{D}_j^i$'s. Substituting (3.12) back in (3.8) produces

$$\boldsymbol{C}_i = \sum_{j=1}^{n} R_{\alpha_j} (\boldsymbol{D}_j^i - \bar{\boldsymbol{D}}_j), \tag{3.13}$$

and in $\mathcal{F}_S$ this is

$$\boldsymbol{c}_i = R_v \boldsymbol{C}_i = R_v \sum_{j=1}^{n} R_{\alpha_j} (\boldsymbol{D}_j^i - \bar{\boldsymbol{D}}_j). \tag{3.14}$$

The time derivative of this gives the velocities of the centre of mass of B_i relative to the overall centre of mass, and is

$$\dot{\boldsymbol{c}}_i = \dot{R}_v \boldsymbol{C}_i + R_v \dot{\boldsymbol{C}}_i = R_v (\hat{\boldsymbol{\Omega}}_v \boldsymbol{C}_i + \dot{\boldsymbol{C}}_i), \tag{3.15}$$

where

$$\dot{\boldsymbol{C}}_i = \sum_{j=1}^{n} R_{\alpha_j} \hat{\boldsymbol{\Omega}}_{\alpha_j} (\boldsymbol{D}_j^i - \bar{\boldsymbol{D}}_j). \tag{3.16}$$

3.2 Geometry of the Model

We can associate a rooted tree to the model by imagining each body segment as a node, and the edges being $\boldsymbol{C}_j - \boldsymbol{C}_i$, i.e. the centre of mass of B_i to the centre of mass of B_j for connected segments. Then the tree for the model with 10 bodies

has the following structure:

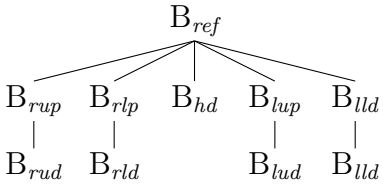

The directed edges are given by $R_{v_i}\boldsymbol{E}_i^j - R_{v_j}\boldsymbol{E}_j^i$ found from (3.9), and we can interpret this as the edge starting at the centre of mass of B_i, traverses to the joint $\boldsymbol{J}_{i,j}$, which then continues on to the centre of mass of B_j. The $\boldsymbol{E}_i^j$ vector is written in $\mathcal{F}_{B_i}$ and it gives the centre of mass of B_i to the joint $\boldsymbol{J}_{i,j}$. For our model we define:

$$
\begin{aligned}
\boldsymbol{E}_{ref}^{rup} &= (0,-0.2,0.25)^t & \boldsymbol{E}_{rup}^{ref} &= (0,0,0.2)^t \\
\boldsymbol{E}_{rup}^{rud} &= (0,0,-0.15)^t & \boldsymbol{E}_{rud}^{rup} &= (0,0,0.183)^t \\
\boldsymbol{E}_{ref}^{rlp} &= (0.08,-0.08,-0.3)^t & \boldsymbol{E}_{rlp}^{ref} &= (0.08,0,0.215)^t \\
\boldsymbol{E}_{rlp}^{rld} &= (0,0,-0.215)^t & \boldsymbol{E}_{rld}^{rlp} &= (0,0,0.289)^t \\
\boldsymbol{E}_{ref}^{hd} &= (0,0,0.3)^t & \boldsymbol{E}_{hd}^{ref} &= (0,0,-0.11)^t \\
\boldsymbol{E}_{ref}^{lup} &= (0,0.2,0.25)^t & \boldsymbol{E}_{lup}^{ref} &= (0,0,0.2)^t \\
\boldsymbol{E}_{lup}^{lud} &= (0,0,-0.15)^t & \boldsymbol{E}_{lud}^{lup} &= (0,0,0.183)^t \\
\boldsymbol{E}_{ref}^{llp} &= (0.08,0.08,-0.3)^t & \boldsymbol{E}_{llp}^{ref} &= (0.08,0,0.215)^t \\
\boldsymbol{E}_{llp}^{lld} &= (0,0,-0.215)^t & \boldsymbol{E}_{lld}^{llp} &= (0,0,0.289)^t.
\end{aligned}
$$

These parameters are chosen based on the dimensions listed in Table 1.1, but written in the SI unit metres instead of centimetres. The shoulder joints are chosen to lay outside of both the torso and the upper arm segment by a small amount determined by the radius of the upper arm. This is for aesthetic reasons only to make the arm motions appear more pleasing and only makes a minute difference in the dynamical behavior of the model. For the segments modelled by a cylinder with sphere attached (i.e. the forearm with hand and shank with foot segments) we need to first compute C_c with (2.19) before we can write down $\boldsymbol{E}_i^j$. This is needed because the displacement between the centre of mass of the combined segment to the joint location is determined by C_c.

A schematic diagram specifying all the $\boldsymbol{E}_i^j$ vectors is shown in Figure 3.2 to help us visualise the model. With the set of $\boldsymbol{E}_i^j$ vectors defined, we can compute $\boldsymbol{D}_j^i$ with (3.10), $\bar{\boldsymbol{D}}_j$ follows from (3.12), and this leads to $\boldsymbol{C}_i$ now determined as a function of shape governed by (3.13).

3.3 Angular Momentum

We now write down the angular momentum $\boldsymbol{l}_i$ of B_i in $\mathcal{F}_S$ with respect to the overall centre of mass $\boldsymbol{c}$ for coupled rigid bodies. Let

$$\boldsymbol{q}_i = \boldsymbol{c}_i + R_i\boldsymbol{Q}_i \tag{3.17}$$

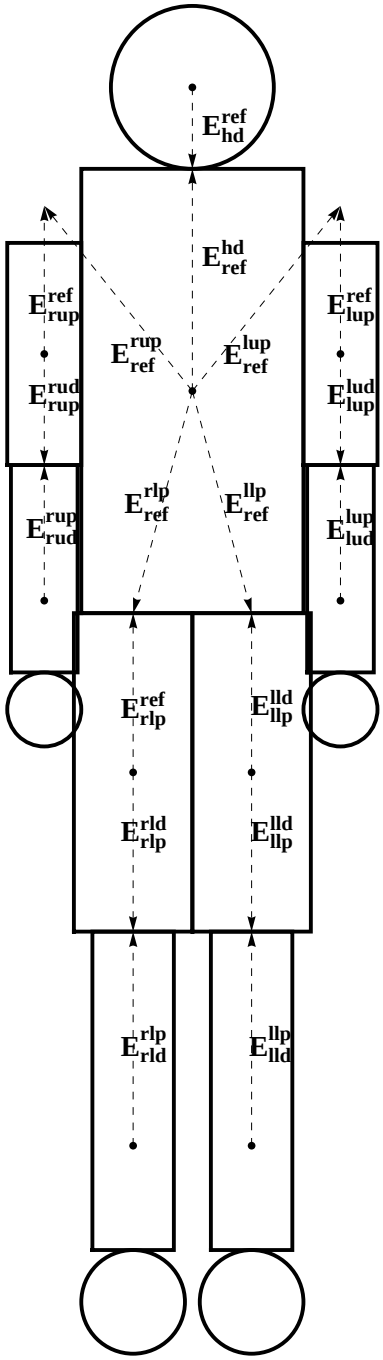

FIGURE 3.2. A planar diagram of the anatomical neutral position (identity shape), which is the shape when all relative rotation matrices are the identity matrix. To help distinguish between the front and back of the athlete, we designate the colour white to represent the front of the torso, and black for the back of the torso. In this diagram the athlete is facing towards us.

be a point on B_i viewed from $\mathcal{F}_S$, where $\boldsymbol{c}_i$ is the position vector from the overall centre of mass to the centre of mass of B_i written in $\mathcal{F}_S$, R_i is the rotation matrix that parallelises the coordinate axes of $\mathcal{F}_{B_i}$ with $\mathcal{F}_S$, and $\boldsymbol{Q}_i$ is the position vector written in $\mathcal{F}_{B_i}$ that denotes the same instantaneous point in space as $\boldsymbol{q}_i$. The velocity of $\boldsymbol{q}$ is then

$$\dot{\boldsymbol{q}}_i = \dot{\boldsymbol{c}}_i + \dot{R}_i \boldsymbol{Q}_i. \tag{3.18}$$

The angular momentum $\boldsymbol{l}_i$ of B_i in $\mathcal{F}_S$ is given by

$$\begin{aligned}
\boldsymbol{l}_i &= \int_{B_i} \rho_i \boldsymbol{q}_i \times \dot{\boldsymbol{q}}_i \,\mathrm{d}\boldsymbol{Q}_i \\
&= \int_{B_i} \rho_i (\boldsymbol{c}_i + R_i \boldsymbol{Q}_i) \times (\dot{\boldsymbol{c}}_i + \dot{R}_i \boldsymbol{Q}_i) \,\mathrm{d}\boldsymbol{Q}_i \\
&= \int_{B_i} \rho_i \,\mathrm{d}\boldsymbol{Q}_i (\boldsymbol{c}_i \times \dot{\boldsymbol{c}}_i) + \boldsymbol{c}_i \times \dot{R}_i \int_{B_i} \rho_i \boldsymbol{Q}_i \,\mathrm{d}\boldsymbol{Q}_i \\
&\qquad + R_i \int_{B_i} \rho_i \boldsymbol{Q}_i \,\mathrm{d}\boldsymbol{Q}_i \times \dot{\boldsymbol{c}}_i + \int_{B_i} \rho_i R_i \boldsymbol{Q}_i \times \dot{R}_i \boldsymbol{Q}_i \,\mathrm{d}\boldsymbol{Q}_i \\
&= m_i \boldsymbol{c}_i \times \dot{\boldsymbol{c}}_i + \int_{B_i} \rho_i R_i \boldsymbol{Q}_i \times \dot{R}_i \boldsymbol{Q}_i \,\mathrm{d}\boldsymbol{Q}_i \qquad \text{from (2.18)} \\
&= m_i \boldsymbol{c}_i \times \dot{\boldsymbol{c}}_i + R_i J_i \boldsymbol{\mathcal{W}}_i \qquad \text{from (2.28)}.
\end{aligned}$$

where ρ_i is the density of B_i. Using the results of (3.3), (3.6), (3.14), (3.15) along with the vector identity (2.8), we can write $\boldsymbol{l}_i$ in terms of $R_v, R_{\alpha_i}, \boldsymbol{\Omega}_v$ and $\boldsymbol{\Omega}_{\alpha_i}$, giving

$$\boldsymbol{l}_i = R_v \left[\left(R_{\alpha_i} J_i R_{\alpha_i}^t + m_i \left[|\boldsymbol{C}_i|^2 \mathbb{1} - \boldsymbol{C}_i \boldsymbol{C}_i^t \right] \right) \boldsymbol{\Omega}_v + (m_i \boldsymbol{C}_i \times \dot{\boldsymbol{C}}_i + R_{\alpha_i} J_i \boldsymbol{\Omega}_{\alpha_i}) \right]. \tag{3.19}$$

This result now solely depends on the orientation R_v, shape R_{α_i} and combination of shape and geometry that determines $\boldsymbol{C}_i$ for each $i \in \{1, 2, ..., n\}$. The total angular momentum $\boldsymbol{l}$ of the system is the sum of all $\boldsymbol{l}_i$, i.e.

$$\boldsymbol{l} = \sum_{i=1}^{n} \boldsymbol{l}_i = R_v \Big(I \boldsymbol{\Omega}_v + \boldsymbol{A} \Big), \tag{3.20}$$

where the two essential terms are the tensor of inertia of the system I and the angular momentum shift $\boldsymbol{A}$ generated by the shape change. They are defined as

$$I = \sum_{i=1}^{n} \left(R_{\alpha_i} J_i R_{\alpha_i}^t + m_i \left[|\boldsymbol{C}_i|^2 \mathbb{1} - \boldsymbol{C}_i \boldsymbol{C}_i^t \right] \right) \tag{3.21}$$

$$\boldsymbol{A} = \sum_{i=1}^{n} \Big(m_i \boldsymbol{C}_i \times \dot{\boldsymbol{C}}_i + R_{\alpha_i} J_i \boldsymbol{\Omega}_{\alpha_i} \Big). \tag{3.22}$$

For I in (3.21) we use the parallel axis theorem (2.17) to sum up the tensors J_i of each individual body segment. Since each J_i is written in $\mathcal{F}_{B_i}$ instead of $\mathcal{F}_C$, there are additional rotation matrices R_{α_i} and $R^t_{\alpha_i}$ used to first align the coordinate axes of $\mathcal{F}_{B_i}$ with $\mathcal{F}_C$ before the parallel axis theorem (2.17) is applied. The vector $\boldsymbol{A}$ only appears during shape change, and as $\dot{\boldsymbol{C}}_i$ and $\boldsymbol{\Omega}_{\alpha_i}$ are linear in the shape change velocities, $\boldsymbol{A}$ is therefore also linear in the velocities.

The total angular momentum relating $\mathcal{F}_C$ and $\mathcal{F}_S$ is given by the transformation (2.4) where R refers here to R_v, so comparing with (3.20) we have

$$\boldsymbol{L} = I\boldsymbol{\Omega}_v + \boldsymbol{A}. \tag{3.23}$$

Since $\boldsymbol{A}$ is linear in the velocities, it vanishes when there is no shape change. In this situation the equation reduces back to the standard angular momentum equation for a rigid body given by (1.2) as expected. From (3.23) we see that $\boldsymbol{A}$ can be interpreted as internal angular momentum generated by the shape change. Assuming that the geometry and masses of the model are constant, then I depends solely on the collection of rotation matrices R_{α_i} (which determines the shape), while $\boldsymbol{A}$ depends on both R_{α_i} and its derivatives.

3.4 Equations of Motion and Orientation

The angular velocity $\boldsymbol{\Omega}$ in (2.43) no longer holds for coupled rigid bodies, hence we rearrange (3.23) to get

$$\boldsymbol{\Omega} = I^{-1}(\boldsymbol{L} - \boldsymbol{A}), \tag{3.24}$$

which is the new angular velocity for coupled rigid bodies, where the subscript v will be omitted from now on. It is important to note that the old derivation of the equations of motion (3.1) and equations of orientation (3.2) from Chapter 2 are still valid here, even though we now have time dependent terms. Substituting $\boldsymbol{\Omega}$ from (3.24) into the equations of motion (3.1) and equations of orientation (3.2) now produces the correct results. We may write the equations of motion (3.1) as

$$\dot{\boldsymbol{L}} = \boldsymbol{L} \times I^{-1}(\boldsymbol{L} - \boldsymbol{A}), \tag{3.25}$$

where both I and $\boldsymbol{A}$ are now time dependent. This is the extension to Euler's equations of motion (2.44), which is now applicable to coupled rigid body dynamics where shape change can occur. Montgomery in principal wrote down the equations we derived, but they are hard to recognise, see his equation (2) in [**45**].

Since the nonlinear differential equations of (3.25) in general has no analytic solution, we resort to numerical solutions and/or approximation methods; however, under special assumptions the equations can be sufficiently simplified to obtain an exact solution for $\boldsymbol{L}$. Once obtained we can compute $\boldsymbol{\Omega}$ using (3.24), substitute it in the equations of orientation (3.2) and solve for $\boldsymbol{q}$, which gives the spatial orientation of the coupled rigid body as a function of time. The solution to $\boldsymbol{q}$ may

be expressed as a Magnus series if desired, but usually this is unnecessary as we will not have an exact $\boldsymbol{L}$ to begin with.

Treating an athlete as coupled rigid bodies in space allows the inertial parameters such as the mass, dimensions, geometry and joint locations of body segments to be measured. Since the shape is controllable by the athlete, all $\boldsymbol{C}_i$'s (determined by the combination of shape and geometry) and R_{α_i}'s (governed by shape) are known functions of time, and if given the initial orientation $R_v(0)$ of the athlete, we can compute the orientation of the athlete R_v as a function of time by solving the equations of motion (3.1) and equations of orientation (3.2).

3.5 Segment Reduction

In order to simplify the model we reduce the segment count by fixing body segments. The general 10-body model is reduced to the 2-body model (which will be used in Chapter 5 and Chapter 6) and the 3-body model (to be used in Chapter 6). Here, we find the new collection of centre of mass vectors $\boldsymbol{C}_i$, tensor of inertia I, and angular momentum shift $\boldsymbol{A}$ for the various reductions.

3.5.1 The 2-Body Model

To keep the twisting somersault simulation as simple as possible while still being able to achieve the desired effect, it is enough to consider a 2-body model with a single hinge joint, see Figure 3.3. With this setup the body segments are fixed relative to the torso, except for one segment which we will choose to be the left

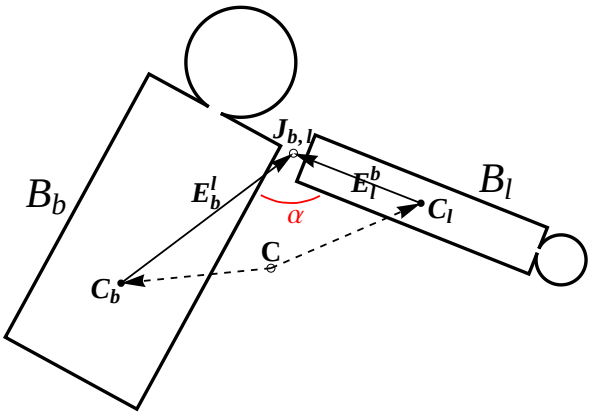

Figure 3.3. 2-body model with bodies B_b and B_l, centre of mass at $\boldsymbol{C}_b$ and $\boldsymbol{C}_l$, and overall centre of mass at $\boldsymbol{C}$. Taking B_b as the reference segment we find that the joint $\boldsymbol{J}_{b,l}$ given by (3.9) shows the relation $\boldsymbol{C}_b + \boldsymbol{E}_b^l = \boldsymbol{C}_l + R_x(\alpha)\boldsymbol{E}_l^b$, where α is the shape angle.

arm. The left elbow is fully extended at all times, and we further restrict the shoulder joint to only allow motion along the abduction-adduction plane. This means only a single angle α is required to fully describe the shape of the athlete, and the shape space is simply a circle for the reduced 2-body model. The relative rotation matrices are then:

$$\tilde{R}_{\alpha_i} = \begin{pmatrix} 1 & 0 & 0 \\ 0 & 1 & 0 \\ 0 & 0 & 1 \end{pmatrix} \text{ for } i \in \{ref, rlp, rld, llp, lld, hd\}$$

$$\tilde{R}_{\alpha_{rup}} = \tilde{R}_{\alpha_{rud}} = \begin{pmatrix} -1 & 0 & 0 \\ 0 & 1 & 0 \\ 0 & 0 & -1 \end{pmatrix}$$

$$\tilde{R}_{\alpha_{lup}} = \tilde{R}_{\alpha_{lud}} = \begin{pmatrix} 1 & 0 & 0 \\ 0 & \cos\alpha & -\sin\alpha \\ 0 & \sin\alpha & \cos\alpha \end{pmatrix}.$$

Besides the arms, every other segment has identity orientation corresponding to the anatomical neutral position shown in Figure 3.2. Since divers typically take off in the layout position, we choose to fix the right arm pointing straight up, and allow the left arm free to move along the abduction-adduction range of motion. We do not want any medial/lateral rotation of the arms in this model, so we fix $\xi \in \mathbb{R}$ in

$$\tilde{R}_{\alpha_{rup}} = \tilde{R}_{\alpha_{rud}} = R_y(\pi)R_z(\xi) = \begin{pmatrix} -\cos\xi & \sin\xi & 0 \\ \sin\xi & \cos\xi & 0 \\ 0 & 0 & -1 \end{pmatrix}$$

$$\tilde{R}_{\alpha_{lup}} = \tilde{R}_{\alpha_{lud}} = R_x(\alpha)R_z(\xi) = \begin{pmatrix} \cos\xi & -\sin\xi & 0 \\ \cos\alpha\sin\xi & \cos\alpha\cos\xi & -\sin\alpha \\ \sin\alpha\sin\xi & \cos\xi\sin\alpha & \cos\alpha \end{pmatrix}.$$

As long as ξ is constant then the value itself is irrelevant. Due to the rotation symmetry of the arm we will arrive at the same differential equations since both J_i and $\boldsymbol{C}_i$ are independent of the parameter ξ. For simplicity we choose to set $\xi = 0$ to obtain the rotation matrices initially shown.

As there is no shape change between the segments except for the left arm, we may group the appropriate body segments together as

$$g_b = \{ref, rup, rud, rlp, rld, llp, lld, hd\}$$
$$g_l = \{lup, lud\},$$

which allows us to relabel the body segments as

$$B_j = \bigcup_{i \in g_j} \tilde{B}_i$$

for $j \in \{b, l\}$, where B_l denotes the entire left arm and B_b is the remainder of the body. For this section we use tilde to refer to quantities in the original 10-body model, and no tilde for the reduced two segment model. Writing down the masses in our new notation we get

$$m_b = \sum_{i \in g_b} \tilde{m}_i = 70.979 \qquad m_l = \sum_{i \in g_l} \tilde{m}_i = 4.660 \tag{3.26}$$
$$M = m_b + m_l = 75.639,$$

where m_b and m_l are the masses of B_b and B_l respectively, and M is the total mass. The position vectors for the centre of mass measured in $\mathcal{F}_C$ are

$$\boldsymbol{C}_j = \frac{1}{m_j} \sum_{i \in g_j} \tilde{m}_i \tilde{\boldsymbol{C}}_i. \tag{3.27}$$

Alternately, writing $\boldsymbol{C}_j$ using (3.13) shows that

$$\boldsymbol{C}_b = -\frac{m_l}{M} \left(\boldsymbol{E}_b^l - R_\alpha \boldsymbol{E}_l^b \right) \qquad \boldsymbol{C}_l = \frac{m_b}{M} \left(\boldsymbol{E}_b^l - R_\alpha \boldsymbol{E}_l^b \right), \tag{3.28}$$

where we will write R_α as $R_x(\alpha)$ from here on. The vector $\boldsymbol{E}_b^l$ is the vector from the centre of mass of B_b to the left shoulder joint, and $-R_\alpha \boldsymbol{E}_l^b$ is the vector from the shoulder joint to the centre of mass of B_l, where the rotation matrix R_α is needed transform the vector to $\mathcal{F}_C$. We introduce

$$\boldsymbol{V} := \boldsymbol{E}_b^l - R_\alpha \boldsymbol{E}_l^b \tag{3.29}$$

as an intermediate vector to simplify our equations, meaning

$$\boldsymbol{C}_b = -\frac{m_l}{M} \boldsymbol{V} \qquad \boldsymbol{C}_l = \frac{m_b}{M} \boldsymbol{V}. \tag{3.30}$$

Taking the difference of these vectors shows that

$$\boldsymbol{C}_l - \boldsymbol{C}_b = \frac{m_b + m_l}{M} \boldsymbol{V} = \boldsymbol{V}, \tag{3.31}$$

and thus $\boldsymbol{V}$ is precisely the vector from the centre of mass of B_b to the centre of mass of B_l. Using basic geometry we see that

$$\boldsymbol{E}_b^l = (\tilde{\boldsymbol{C}}_{ref} - \boldsymbol{C}_b) + \tilde{\boldsymbol{E}}_{ref}^{lup} \qquad \boldsymbol{E}_l^b = R_\alpha^{-1}(\tilde{\boldsymbol{C}}_{lup} - \boldsymbol{C}_l) + \tilde{\boldsymbol{E}}_{lup}^{ref}, \tag{3.32}$$

which gives the relationship between the geometry vectors in our original 10-body model with the vectors in the reduced two segment model.

The tensor of inertia I_j in $\mathcal{F}_C$ for $j \in \{b, l\}$ is found with (3.21), and having $\boldsymbol{C}_j$ as the new centre of mass of B_j we end up with

$$I_j = \sum_{i \in g_j} \left[\tilde{R}_{\alpha_i} \tilde{J}_i \tilde{R}_{\alpha_i}^t + \tilde{m}_i \Big(|\tilde{\boldsymbol{C}}_i - \boldsymbol{C}_j|^2 \mathbb{1} - (\tilde{\boldsymbol{C}}_i - \boldsymbol{C}_j)(\tilde{\boldsymbol{C}}_i - \boldsymbol{C}_j)^t \Big) \right]. \tag{3.33}$$

Evaluating the calculation in (3.33) shows that both I_b and I_l are of the form $\begin{pmatrix} * & 0 & 0 \\ 0 & * & * \\ 0 & * & * \end{pmatrix}$, where in particular I_b is a constant tensor, and I_l is a function of α. Now B_b is not fixed in $\mathcal{F}_C$ but does rotate with the frame, which explains why I_b is a constant tensor. To obtain a diagonal tensor J_j in $\mathcal{F}_{B_j}$ from I_j in $\mathcal{F}_C$, we use (2.12) to find the principal axes frame. This may be performed for J_l to obtain a constant tensor, but it is actually more convenient to leave I_b alone in the non principal frame as it is already constant. We proceed to write down the total tensor of inertia $I(\alpha)$ and angular momentum shift $\boldsymbol{A}(\alpha, \dot{\alpha})$ for the 2-body system using (3.21) and (3.22), respectively. Remembering that the inertia tensor I_b is written in $\mathcal{F}_C$, and J_l is in $\mathcal{F}_{B_l}$, we have

$$
\begin{aligned}
I(\alpha) &= (m_b|\boldsymbol{C}_b|^2 + m_l|\boldsymbol{C}_l|^2)\mathbb{1} - (m_b\boldsymbol{C}_b\boldsymbol{C}_b^t + m_l\boldsymbol{C}_l\boldsymbol{C}_l^t) + I_b + R_\alpha J_l R_\alpha^{-1} \qquad (3.34)\\
&= \frac{m_b m_l}{M}\left(|\boldsymbol{V}|^2\,\mathbb{1} - \boldsymbol{V}\boldsymbol{V}^t\right) + I_b + R_\alpha J_l R_\alpha^{-1}\\
\boldsymbol{A}(\alpha, \dot{\alpha}) &= m_b\boldsymbol{C}_b \times \dot{\boldsymbol{C}}_b + m_l\boldsymbol{C}_l \times \dot{\boldsymbol{C}}_l + R_\alpha J_l \boldsymbol{\Omega}_\alpha \qquad (3.35)\\
&= \frac{m_b m_l}{M}\boldsymbol{V} \times \dot{\boldsymbol{V}} + R_\alpha J_l \boldsymbol{\Omega}_\alpha,
\end{aligned}
$$

where (3.26) and (3.29) are used to simplify the equations. Now by differentiating (3.29) we see that

$$\dot{\boldsymbol{V}} = -\dot{R}_\alpha \boldsymbol{E}_l^b = -R_\alpha \hat{\boldsymbol{\Omega}}_\alpha \boldsymbol{E}_l^b,$$

and so

$$
\begin{aligned}
\boldsymbol{V} \times \dot{\boldsymbol{V}} &= \boldsymbol{V} \times (-R_\alpha \hat{\boldsymbol{\Omega}}_\alpha \boldsymbol{E}_l^b) \qquad (3.36)\\
&= R_\alpha(-R_\alpha^t \boldsymbol{V} \times (\boldsymbol{\Omega}_\alpha \times \boldsymbol{E}_l^b))\\
&= R_\alpha((-R_\alpha^t \boldsymbol{V} \cdot \boldsymbol{E}_l^b)\boldsymbol{\Omega}_\alpha + (R_\alpha^t \boldsymbol{V} \cdot \boldsymbol{\Omega}_\alpha)\boldsymbol{E}_l^b) \quad \text{using (2.8)}\\
&= R_\alpha((-R_\alpha^t \boldsymbol{V} \cdot \boldsymbol{E}_l^b)\mathbb{1} + \boldsymbol{E}_l^b (R_\alpha^t \boldsymbol{V})^t)\boldsymbol{\Omega}_\alpha\\
&= R_\alpha(\boldsymbol{E}_l^b \boldsymbol{V}^t R_\alpha - (\boldsymbol{V}^t R_\alpha \boldsymbol{E}_l^b)\mathbb{1})\boldsymbol{\Omega}_\alpha.
\end{aligned}
$$

As $\hat{\boldsymbol{\Omega}}_\alpha = R_\alpha^t \dot{R}_\alpha = \begin{pmatrix} 0 & 0 & 0 \\ 0 & 0 & -\dot{\alpha} \\ 0 & \dot{\alpha} & 0 \end{pmatrix}$, we conclude that $\boldsymbol{\Omega}_\alpha = \begin{pmatrix} \dot{\alpha} \\ 0 \\ 0 \end{pmatrix}$.
Using this result for $\boldsymbol{\Omega}_\alpha$ and (3.36), we may write (3.35) as

$$\boldsymbol{A}(\alpha, \dot{\alpha}) = R_\alpha \left(\frac{m_b m_l}{M}\left(\boldsymbol{E}_l^b \boldsymbol{V}^t R_\alpha - (\boldsymbol{V}^t R_\alpha \boldsymbol{E}_l^b)\mathbb{1}\right) + J_l\right) \begin{pmatrix} \dot{\alpha} \\ 0 \\ 0 \end{pmatrix}. \qquad (3.37)$$

Let $\boldsymbol{E}_b^l = \begin{pmatrix} 0 \\ \mathcal{E}_2 \\ \mathcal{E}_3 \end{pmatrix}$ and $\boldsymbol{E}_l^b = \begin{pmatrix} 0 \\ 0 \\ \mathcal{F} \end{pmatrix}$, where the form is known through explicit computation using (3.32). It follows that $\boldsymbol{V}$ is of the form $\begin{pmatrix} 0 \\ * \\ * \end{pmatrix}$ from (3.29), thus it can be shown that

$$\frac{m_b m_l}{M} R_\alpha \boldsymbol{E}_l^b \boldsymbol{V}^t R_\alpha \boldsymbol{\Omega}_\alpha = \mathbf{0},$$

which means (3.37) can be simplified. Furthermore, it is clear that

$$-\frac{m_b m_l}{M} \boldsymbol{V}^t R_\alpha \boldsymbol{E}_l^b \mathbb{1} + J_l$$

is diagonal, so multiplying by R_α on the left leaves the first column and row invariant (as R_α is just a rotation about the x-axis), and then multiplying by $\boldsymbol{\Omega}_\alpha$ on the right simply picks up the first column of that matrix with an extra factor of $\dot{\alpha}$. Furthermore, since only the first entry of that column is non-zero, we can write

$$\boldsymbol{A}(\alpha, \dot{\alpha}) = \begin{pmatrix} A_x \\ 0 \\ 0 \end{pmatrix} \dot{\alpha}, \tag{3.38}$$

where

$$A_x = -\frac{m_b m_l}{M} \boldsymbol{V}^t R_\alpha \boldsymbol{E}_l^b + J_{l_x}, \tag{3.39}$$

and J_{l_x} is the $(1,1)$ entry of J_l. Now eliminating $\boldsymbol{V}$ with (3.29) we see that

$$\begin{aligned} A_x &= -\frac{m_b m_l}{M} (\boldsymbol{E}_b^l)^t R_\alpha \boldsymbol{E}_l^b + \frac{m_b m_l}{M} \boldsymbol{E}_l^b \cdot \boldsymbol{E}_l^b + J_{l_x} \\ &= -\frac{m_b m_l}{M} \mathcal{E}_3 \mathcal{F} \cos\alpha + \frac{m_b m_l}{M} \mathcal{E}_2 \mathcal{F} \sin\alpha + \frac{m_b m_l}{M} \mathcal{F}^2 + J_{l_x} \\ &= -2\mathcal{M}\mathcal{E}_3 \mathcal{F} \cos\alpha + 2\mathcal{M}\mathcal{E}_2 \mathcal{F} \sin\alpha + 2\mathcal{M}\mathcal{F}^2 + J_{l_x}, \end{aligned} \tag{3.40}$$

where $\mathcal{M} = \dfrac{m_b m_l}{2M}$. We will now take a closer look at $I(\alpha)$ in (3.34). First let

$$\frac{m_b m_l}{M} \left(|\boldsymbol{V}|^2 \mathbb{1} - \boldsymbol{V}\boldsymbol{V}^t \right) = \begin{pmatrix} \mathcal{V}_{1,1} & 0 & 0 \\ 0 & \mathcal{V}_{2,2} & \mathcal{V}_{2,3} \\ 0 & \mathcal{V}_{2,3} & \mathcal{V}_{3,3} \end{pmatrix}, \tag{3.41}$$

so that direct substitution into (3.29) shows

$$\begin{aligned}
\mathcal{V}_{1,1} &= \frac{m_b m_l}{M}\Big(\mathcal{E}_2^2 + \mathcal{E}_3^2 + \mathcal{F}^2 - 2\mathcal{E}_3\mathcal{F}\cos\alpha + 2\mathcal{E}_2\mathcal{F}\sin\alpha\Big) \\
&= 2\mathcal{M}(\mathcal{E}_2^2 + \mathcal{E}_3^2 + \mathcal{F}^2) - 4\mathcal{M}\mathcal{E}_3\mathcal{F}\cos\alpha + 4\mathcal{M}\mathcal{E}_2\mathcal{F}\sin\alpha \\
\mathcal{V}_{2,2} &= \frac{m_b m_l}{M}\Big(\mathcal{E}_3 - \mathcal{F}\cos\alpha\Big)^2 \\
&= 2\mathcal{M}\mathcal{E}_3^2 - 4\mathcal{M}\mathcal{E}_3\mathcal{F}\cos\alpha + 2\mathcal{M}\mathcal{F}^2\cos^2\alpha \\
&= \mathcal{M}(2\mathcal{E}_3^2 + \mathcal{F}^2) - 4\mathcal{M}\mathcal{E}_3\mathcal{F}\cos\alpha + \mathcal{M}\mathcal{F}^2\cos 2\alpha \\
\mathcal{V}_{3,3} &= \frac{m_b m_l}{M}\Big(\mathcal{E}_2 + \mathcal{F}\sin\alpha\Big)^2 \\
&= 2\mathcal{M}\mathcal{E}_2^2 + 4\mathcal{M}\mathcal{E}_2\mathcal{F}\sin\alpha + 2\mathcal{M}\mathcal{F}^2\sin^2\alpha \\
&= \mathcal{M}(2\mathcal{E}_2^2 + \mathcal{F}^2) + 4\mathcal{M}\mathcal{E}_2\mathcal{F}\sin\alpha - \mathcal{M}\mathcal{F}^2\cos 2\alpha \\
\mathcal{V}_{2,3} &= -\frac{m_b m_l}{M}\Big(\mathcal{E}_3 - \mathcal{F}\cos\alpha\Big)\Big(\mathcal{E}_2 + \mathcal{F}\sin\alpha\Big) \\
&= -2\mathcal{M}\mathcal{E}_2\mathcal{E}_3 + 2\mathcal{M}\mathcal{E}_2\mathcal{F}\cos\alpha - 2\mathcal{M}\mathcal{E}_3\mathcal{F}\sin\alpha + \mathcal{M}\mathcal{F}^2\sin 2\alpha.
\end{aligned}$$

We will keep

$$I_b = \begin{pmatrix} I_{b_{xx}} & 0 & 0 \\ 0 & I_{b_{yy}} & I_{b_{yz}} \\ 0 & I_{b_{yz}} & I_{b_{zz}} \end{pmatrix} \tag{3.42}$$

since computing it from (3.33) already yields a constant tensor, but

$$I_l = \begin{pmatrix} I_{l_{xx}} & 0 & 0 \\ 0 & I_{l_{yy}} & I_{l_{yz}} \\ 0 & I_{l_{yz}} & I_{l_{zz}} \end{pmatrix} \tag{3.43}$$

is a function of α, which is why we use

$$J_l = \operatorname{diag}\left(J_{l_x}, J_{l_y}, J_{l_z}\right) \tag{3.44}$$

written in $\mathcal{F}_{B_l}$, where J_l and I_l are related via (2.12), i.e. $I_l = R_\alpha J_l R_\alpha^{-1}$. Abbreviating

$$\mathcal{I}_+ = \frac{1}{2}\Big(J_{l_y} + J_{l_z}\Big) \qquad\qquad \mathcal{I}_- = \frac{1}{2}\Big(J_{l_y} - J_{l_z}\Big)$$

we find that

$$\begin{aligned}
I_{l_{xx}} &= J_{l_x} & I_{l_{yy}} &= \mathcal{I}_+ + \mathcal{I}_-\cos 2\alpha \\
I_{l_{yz}} &= \mathcal{I}_-\sin 2\alpha & I_{l_{zz}} &= \mathcal{I}_+ - \mathcal{I}_-\cos 2\alpha.
\end{aligned}$$

So summing (3.41), (3.42) and (3.44) together gives (3.34), which is in the form of

$$I(\alpha) = \begin{pmatrix} I_{xx} & 0 & 0 \\ 0 & I_{yy} & I_{yz} \\ 0 & I_{yz} & I_{zz} \end{pmatrix}, \tag{3.45}$$

where the components are

$$\begin{aligned}
I_{xx} &= -4\mathcal{M}\mathcal{E}_3\mathcal{F}\cos\alpha + 4\mathcal{M}\mathcal{E}_2\mathcal{F}\sin\alpha + \left[2\mathcal{M}(\mathcal{E}_2^2+\mathcal{E}_3^2+\mathcal{F}^2) + I_{b_{xx}} + J_{l_x}\right] \\
I_{yy} &= -4\mathcal{M}\mathcal{E}_3\mathcal{F}\cos\alpha + \left[\mathcal{M}\mathcal{F}^2 + \mathcal{I}_-\right]\cos 2\alpha + \left[\mathcal{M}(2\mathcal{E}_3^2+\mathcal{F}^2) + I_{b_{yy}} + \mathcal{I}_+\right] \\
I_{zz} &= 4\mathcal{M}\mathcal{E}_2\mathcal{F}\sin\alpha - [\mathcal{M}\mathcal{F}^2 + \mathcal{I}_-]\cos 2\alpha + \left[\mathcal{M}(2\mathcal{E}_2^2+\mathcal{F}^2) + I_{b_{zz}} + \mathcal{I}_+\right] \\
I_{yz} &= 2\mathcal{M}\mathcal{E}_2\mathcal{F}\cos\alpha - 2\mathcal{M}\mathcal{E}_3\mathcal{F}\sin\alpha + \left[\mathcal{M}\mathcal{F}^2 + \mathcal{I}_-\right]\sin 2\alpha + \left[I_{b_{yz}} - 2\mathcal{M}\mathcal{E}_2\mathcal{E}_3\right].
\end{aligned}$$

Numerically the corresponding values for (3.40) and (3.45) are

$$\begin{aligned}
A_x &= -0.736\cos\alpha + 0.340\sin\alpha + 0.758 \\
&\quad \text{and} \\
I_{xx} &= -1.472\cos\alpha + 0.680\sin\alpha + 19.847 \\
I_{yy} &= -1.472\cos\alpha + 0.376\cos 2\alpha + 18.761 \\
I_{zz} &= 0.680\sin\alpha - 0.376\cos 2\alpha + 1.372 \\
I_{yz} &= 0.340\cos\alpha - 0.736\sin\alpha + 0.376\sin 2\alpha + 0.340.
\end{aligned}$$

For completeness we include the numerical values of $\boldsymbol{C}_b$, $\boldsymbol{C}_l$ obtained with (3.27), $\boldsymbol{E}_b^l$, $\boldsymbol{E}_l^b$ obtained with (3.32), and the constant tensors of inertia I_b and $J_l = R_\alpha^{-1} I_l R_\alpha$, which are

$$\boldsymbol{C}_b = \begin{pmatrix} 0 \\ -0.022\sin\alpha - 0.013 \\ 0.022\cos\alpha - 0.028 \end{pmatrix} \qquad \boldsymbol{E}_b^l = \begin{pmatrix} 0 \\ 0.213 \\ 0.462 \end{pmatrix}$$

$$\boldsymbol{C}_l = \begin{pmatrix} 0 \\ 0.342\sin\alpha + 0.200 \\ -0.342\cos\alpha + 0.433 \end{pmatrix} \qquad \boldsymbol{E}_l^b = \begin{pmatrix} 0 \\ 0 \\ 0.365 \end{pmatrix}$$

$$I_b = \begin{pmatrix} 17.959 & 0 & 0 \\ 0 & 17.448 & 0.770 \\ 0 & 0.770 & 0.792 \end{pmatrix} \qquad J_l = \begin{pmatrix} 0.176 & 0 & 0 \\ 0 & 0.176 & 0 \\ 0 & 0 & 0.005 \end{pmatrix}.$$

3.5.2 The 3-Body Model

The 3-body model is used in Chapter 6 to allow both arms to move simultaneously during the dive. We derive the tensor of inertia I and angular momentum shift $\boldsymbol{A}$

for this model, but since the derivation is very similar to the 2-body model, not all details will be presented. We begin by grouping the body segments as follows:

$$g_l = \{lup, lud\} \qquad g_b = \{ref, rlp, rld, llp, lld, hd\}$$
$$g_r = \{rup, rud\},$$

and label the groups B_b, B_l, and B_r for body (including legs and head), left arm, and right arm, respectively. A diagram illustrating the segments, centre of mass, and geometry vectors of the 3-body model is provided in Figure 3.4.

The shape corresponding to the angle of the left and right arm about the abduction-adduction plane of motion is written as $\boldsymbol{\alpha} = (\bar{\alpha}_l, \bar{\alpha}_r)^t$, where $\bar{\alpha}_l \in [0, \pi]$ and $\bar{\alpha}_r \in [\pi, 2\pi]$ for our shape change of interest. When the arms are pointing straight up in the layout position we have $\bar{\alpha}_l = \bar{\alpha}_r = \pi$, but in order to position the arms down by the side, the left arm must move counterclockwise while the right arm moves clockwise, hence the different intervals of shape change. From a

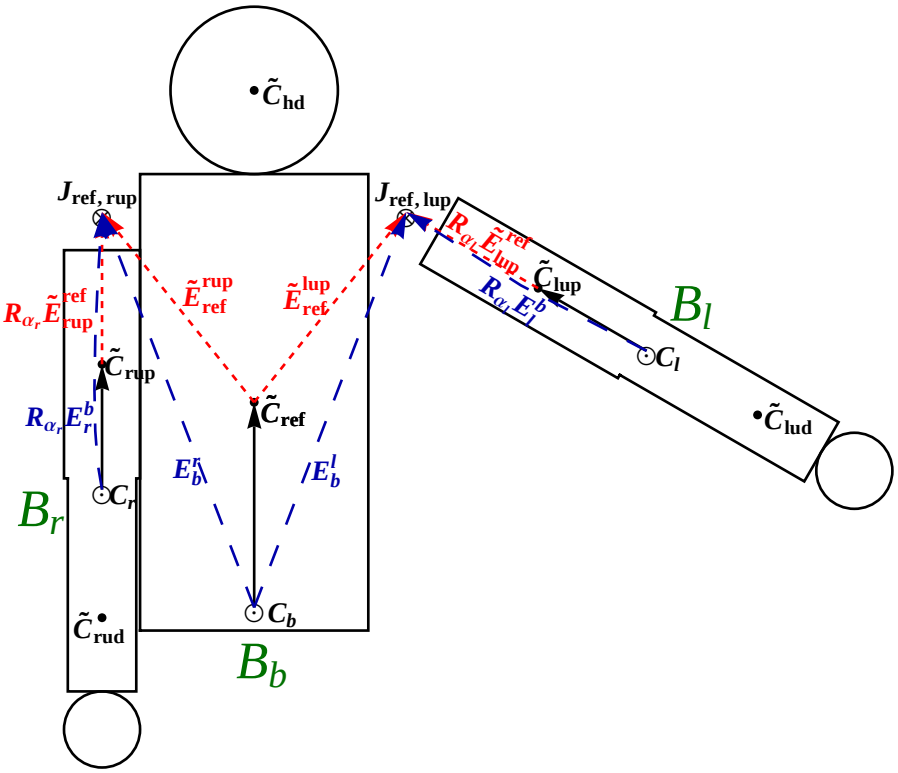

Figure 3.4. The 3-body model with legs not shown. Quantities with tilde are from the general 10-body model of Chapter 3.2 and are included to illustrate the relationship between the two models.

symmetry perspective it may be better to measure the right arm in the counter-clockwise direction starting from the arm by the side, which is achieved by setting $\alpha_l = \bar{\alpha}_l$ and $\alpha_r = 2\pi - \bar{\alpha}_r$ so that both intervals are in the same range, meaning $\boldsymbol{\alpha}(\alpha_l, \alpha_r) \in [0, \pi]^2$. The mass of the bodies B_b, B_l, and B_r are respectively

$$m_b = \sum_{i \in g_b} \tilde{m}_i = 66.319 \qquad m_l = \sum_{i \in g_l} \tilde{m}_i = 4.660 \tag{3.46}$$
$$m_r = \sum_{i \in g_r} \tilde{m}_i = 4.660 \qquad M = m_b + m_l + m_r = 75.639.$$

We keep the notion of using tilde when referring to quantities in the original 10-body model, and no tilde for the reduced three segment model. The position vector from the origin of $\mathcal{F}_C$ to the centre of mass of B_j is given by

$$\boldsymbol{C}_j = \frac{1}{m_j} \sum_{i \in g_j} \tilde{m}_i \tilde{\boldsymbol{C}}_i \qquad \text{for } j \in \{b, l, r\}, \tag{3.47}$$

and numerically evaluating gives

$$\boldsymbol{C}_b = \begin{pmatrix} 0 \\ -0.022 \sin \alpha_l + 0.022 \sin \alpha_r \\ 0.022 \cos \alpha_l + 0.022 \cos \alpha_r - 0.064 \end{pmatrix}$$
$$\boldsymbol{C}_l = \begin{pmatrix} 0 \\ 0.342 \sin \alpha_l + 0.022 \sin \alpha_r + 0.200 \\ -0.342 \cos \alpha_l + 0.022 \cos \alpha_r + 0.456 \end{pmatrix}$$
$$\boldsymbol{C}_r = \begin{pmatrix} 0 \\ -0.022 \sin \alpha_l - 0.342 \sin \alpha_r - 0.200 \\ 0.022 \cos \alpha_l - 0.342 \cos \alpha_r + 0.456 \end{pmatrix}.$$

We can write down the $\boldsymbol{E}_i^j$ vectors in $\mathcal{F}_{B_i}$ using existing known quantities, and looking at Figure 3.4 we see that

$$\boldsymbol{E}_b^l = (\tilde{\boldsymbol{C}}_{ref} - \boldsymbol{C}_b) + \tilde{\boldsymbol{E}}_{ref}^{lup} \qquad \boldsymbol{E}_l^b = R_{\alpha_l}^{-1}(\tilde{\boldsymbol{C}}_{lup} - \boldsymbol{C}_l) + \tilde{\boldsymbol{E}}_{lup}^{ref} \tag{3.48}$$
$$\boldsymbol{E}_b^r = (\tilde{\boldsymbol{C}}_{ref} - \boldsymbol{C}_b) + \tilde{\boldsymbol{E}}_{ref}^{rup} \qquad \boldsymbol{E}_r^b = R_{\alpha_r}^{-1}(\tilde{\boldsymbol{C}}_{rup} - \boldsymbol{C}_r) + \tilde{\boldsymbol{E}}_{rup}^{ref}.$$

We introduce

$$\boldsymbol{V}_l := \boldsymbol{E}_b^l - R_{\alpha_l} \boldsymbol{E}_l^b \qquad \boldsymbol{V}_r := \boldsymbol{E}_b^r - R_{\alpha_r} \boldsymbol{E}_r^b, \tag{3.49}$$

so by traversing along the blue dashed vectors from $\boldsymbol{C}_b$ in Figure 3.4 we see that

$$\boldsymbol{C}_l = \boldsymbol{C}_b + \boldsymbol{V}_l \qquad \boldsymbol{C}_r = \boldsymbol{C}_b + \boldsymbol{V}_r. \tag{3.50}$$

The overall centre of mass of the three body system is defined to be at the origin of $\mathcal{F}_C$ like in (3.11), hence

$$m_b \boldsymbol{C}_b + m_l \boldsymbol{C}_l + m_r \boldsymbol{C}_r = \boldsymbol{0}. \tag{3.51}$$

Using (3.50), (3.51), and M we find that

$$\boldsymbol{C}_l = \frac{1}{M}\Big[(m_b + m_r)\boldsymbol{V}_l - m_r\boldsymbol{V}_r\Big] \qquad \boldsymbol{C}_b = -\frac{1}{M}\Big[m_l\boldsymbol{V}_l + m_r\boldsymbol{V}_r\Big] \tag{3.52}$$
$$\boldsymbol{C}_r = \frac{1}{M}\Big[-m_l\boldsymbol{V}_l + (m_b + m_l)\boldsymbol{V}_r\Big].$$

The tensor of inertia I_j for B_j written in $\mathcal{F}_C$ is the same as (3.33), but with the new $\boldsymbol{C}_j$ given by (3.47). The parallel axis theorem (2.17) can then be used to find the overall tensor of inertia I of the system. As I_j is not constant in $\mathcal{F}_C$, we switch to J_j in $\mathcal{F}_{B_j}$ giving

$$\begin{aligned} I(\alpha_l, \alpha_r) &= (m_b|\boldsymbol{C}_b|^2 + m_l|\boldsymbol{C}_l|^2 + m_r|\boldsymbol{C}_r|^2)\mathbb{1} \\ &\quad - (m_b\boldsymbol{C}_b\boldsymbol{C}_b^t + m_l\boldsymbol{C}_l\boldsymbol{C}_l^t + m_r\boldsymbol{C}_r\boldsymbol{C}_r^t) \\ &\quad + J_b + R_{\alpha_l}J_lR_{\alpha_l}^{-1} + R_{\alpha_r}J_rR_{\alpha_r}^{-1}. \end{aligned} \tag{3.53}$$

The angular momentum shift $\boldsymbol{A}$ follows from (3.22), and writing it out explicitly gives

$$\begin{aligned} \boldsymbol{A}(\alpha_l, \alpha_r, \dot\alpha_l, \dot\alpha_r) &= m_b\boldsymbol{C}_b \times \dot{\boldsymbol{C}}_b + m_l\boldsymbol{C}_l \times \dot{\boldsymbol{C}}_l + m_r\boldsymbol{C}_r \times \dot{\boldsymbol{C}}_r \\ &\quad + R_{\alpha_l}J_l\boldsymbol{\Omega}_{\alpha_l} + R_{\alpha_r}J_r\boldsymbol{\Omega}_{\alpha_r}. \end{aligned} \tag{3.54}$$

The numerical values of J_j for $j \in \{b, l, r\}$ are

$$\begin{aligned} J_b &= \operatorname{diag}(14.204, 13.867, 0.612) \\ J_l = J_r &= \operatorname{diag}(0.176, 0.176, 0.005). \end{aligned}$$

Since $\boldsymbol{C}_i$ for $i \in \{b, l, r\}$ have a zero x-component (due to the arms moving in the abduction-adduction plane of motion) the cross product $\boldsymbol{C}_i \times \dot{\boldsymbol{C}}_i$ is non-zero only in the x-component. As both angular velocities $\boldsymbol{\Omega}_{\alpha_l}$ and $\boldsymbol{\Omega}_{\alpha_r}$ are also only non-zero in the x-component, then for the same reason we can write the x-component of $\boldsymbol{A}$ from (3.54) as

$$A_x(\alpha_l, \alpha_r, \dot\alpha_l, \dot\alpha_r) = \boldsymbol{A}_x(\alpha_l, \alpha_r) \cdot \dot{\boldsymbol{\alpha}} = A_l(\alpha_l, \alpha_r)\dot\alpha_l + A_r(\alpha_l, \alpha_r)\dot\alpha_r, \tag{3.55}$$

where

$$\begin{aligned} A_l(\alpha_l, \alpha_r) &= b_0 - b_1\cos\alpha_l + b_2\sin\alpha_l - b_3\cos(\alpha_l + \alpha_r) \\ A_r(\alpha_l, \alpha_r) &= b_0 - b_1\cos\alpha_r + b_2\sin\alpha_r - b_3\cos(\alpha_l + \alpha_r), \end{aligned} \tag{3.56}$$

and the constants are

$$\begin{aligned} b_0 &= 0.758 & b_1 &= 0.774 & b_2 &= 0.340 \\ b_3 &= 0.038 & b_4 &= 18.298. \end{aligned}$$

CHAPTER 4

Planar Somersaults

The equations of motion (3.1) and equations of orientation (3.2) derived so far describe the 3D motion of the athlete during flight, and are needed when analysing the twisting somersault. However, before we do that we first want to look at the simpler planar somersaults, i.e. somersaults without twists.

We begin by performing a planar reduction of the 3D model in Chapter 4.1, which confines movement to lie within a 2D subspace. To ensure all motion remains in the somersault plane, the limbs are restricted to move together so that the body is always symmetric about the midsagittal plane, which bisects the body vertically into equal left and right halves. This reduces the segment count of the athlete from ten to six while also reducing the tensor of inertia I given by (3.21) and angular momentum shift $\boldsymbol{A}$ given by (3.22) to their scalar equivalents. The resultant is a scalar differential equation describing the orientation of the athlete.

In Chapter 4.2 we import data taken from digitised footage of an elite athlete performing a 107B dive off the 3m springboard, use the data to determine the angular momentum L of the dive, feed the initial orientation and shape angles from the data into the differential equation and solve to obtain the orientation as a function of time. Comparing the orientation of the athlete (determined by the differential equation) to the observed results reveals a close match, providing confidence in using the model to perform further computations.

Some additional assumptions are made in Chapter 4.3 to reduce the segment count of the planar model from six to three. The dynamics are then computed both with and without these extra assumptions for the digitised dive to establish the difference is minimal. Next, we compute the geometric phase of the digitised dive and demonstrate how it can be improved without affecting the dynamic phase by simply reordering and reversing certain sections of the dive.

Finally, in Chapter 4.4 we propose a theoretical planar dive which we can optimise for overall rotation achieved by the athlete.

A preliminary version of this chapter was presented at the 1st Symposium for Researchers in Diving at Leipzig, Germany in 2013. The conference proceedings can be found in [**56**], although the final optimisation procedure for maximising overall rotation using the geometric phase differs to what is presented here.

4.1 Planar Reduction

In the 10-body model there are 27 degrees-of-freedom specifying the shape of the athlete. The translational degrees of freedom can be removed by choosing the spatial frame whose origin moves with the centre of mass. As there are no external forces in this frame, the orientation is determined by shape change under conservation of angular momentum, thus leaving only degrees-of-freedom specifying the shape of the athlete. Now, if the shape change is restricted about the somersault axis and we enforce the limbs to move together so that the body is always symmetric about the midsagittal plane, then no tilt can ever be induced, thus the somersaulting motion is strictly planar. This suggests we can perform a planar reduction to obtain a simpler 2D model. As the limbs must move together, the segment count can be reduced by combining left and right limb segments, resulting with a six segment model consisting of: B_{ref}, B_{hd}, and the new combined segments

$$\begin{aligned} B_{up} &= B_{rup} \cup B_{lup} & B_{lp} &= B_{rlp} \cup B_{llp} \\ B_{ud} &= B_{rud} \cup B_{lud} & B_{ld} &= B_{rld} \cup B_{lld}, \end{aligned}$$

see Figure 4.2. The planar model only requires five shape angles α_i for $i \in \{up, ud, lp, ld, hd\}$ to specify the shape of the athlete, which is significantly less than the original 27 of the full 3D model. The angles are measured with respect to the anatomical neutral position, which means

$$R_{\alpha_i} = R_y(\alpha_i). \tag{4.1}$$

Let m_i be the mass of B_i, and J_i the tensor of inertia of B_i aligned with the principal axes of inertia. As the athlete is symmetric about the midsagittal plane for the planar model, it is clear from construction that the centres of mass for each of the six segments take the form

$$\boldsymbol{C}_i = \begin{pmatrix} C_{i_x} \\ 0 \\ C_{i_z} \end{pmatrix}. \tag{4.2}$$

The limbs are made up of the corresponding left and right segment of the original 10-body model. The centre of mass for each half is located at $(C_{i_x}, \pm C_{i_y}, C_{i_z})^t$, where $+$ refers to the left half and $-$ the right half. If we denote the left and right half by subscript l and r, respectively, then the tensor of inertia can be computed in terms of the original parameters (m_i from Table 1.1, J_i given at the end of Chapter 2.4, and $\boldsymbol{C}_i$ given by (3.13)) using the parallel axis theorem (2.17) to obtain

$$\begin{aligned} J_i = J_{l\cup r} &= J_l + J_r + m_l C_{l_y}^2 \operatorname{diag}(1,0,1) + m_r C_{r_y}^2 \operatorname{diag}(1,0,1) \\ &= 2\big(J_l + m_l C_{l_y}^2 \operatorname{diag}(1,0,1)\big), \end{aligned} \tag{4.3}$$

since $m_l = m_r$, $J_l = J_r$, and $C_{i_y} = C_{l_y} = -C_{r_y}$. We now look at the components which make up the tensor of inertia I given by (3.21) and angular momentum shift $\boldsymbol{A}$ given by (3.22). Writing out the components of the tensor of inertia J_i as $\operatorname{diag}(J_{i_x}, J_{i_y}, J_{i_z})$ we have in the central-body-frame $\mathcal{F}_C$ that

$$
\begin{aligned}
I_i &= R_{\alpha_i} J_i R_{\alpha_i}^t \\
&= \begin{pmatrix} J_{i_x}\cos^2\alpha_i + J_{i_z}\sin^2\alpha_i & 0 & (J_{i_z} - J_{i_x})\cos\alpha_i \sin\alpha_i \\ 0 & J_{i_y} & 0 \\ (J_{i_z} - J_{i_x})\cos\alpha_i \sin\alpha_i & 0 & J_{i_z}\cos^2\alpha_i + J_{i_x}\sin^2\alpha_i \end{pmatrix},
\end{aligned} \tag{4.4}
$$

and starting with $\boldsymbol{C}_i$ given by (4.2) we find that

$$
m_i \left[|\boldsymbol{C}_i|^2 \mathbb{1} - \boldsymbol{C}_i \boldsymbol{C}_i^t \right] = m_i \begin{pmatrix} C_{i_z}^2 & 0 & -C_{i_x} C_{i_z} \\ 0 & C_{i_x}^2 + C_{i_z}^2 & 0 \\ -C_{i_x} C_{i_z} & 0 & C_{i_x}^2 \end{pmatrix}. \tag{4.5}
$$

So summing (4.4) and (4.5) over the six segments yields the tensor of inertia I, which is in the form of

$$
I = \begin{pmatrix} I_{xx} & 0 & I_{xz} \\ 0 & I_{yy} & 0 \\ I_{xz} & 0 & I_{zz} \end{pmatrix}. \tag{4.6}
$$

We will later see that the $(2,2)$ entry of I is the particular term of interest, and it is

$$
I_{yy} = \sum_i J_{i_y} + m_i (C_{i_x}^2 + C_{i_z}^2). \tag{4.7}
$$

Differentiating $\boldsymbol{C}_i$ in (4.2) gives $\dot{\boldsymbol{C}}_i$, and we can show that

$$
m_i \boldsymbol{C}_i \times \dot{\boldsymbol{C}}_i = \begin{pmatrix} 0 \\ m_i (C_{i_z} \dot{C}_{i_x} - C_{i_x} \dot{C}_{i_z}) \\ 0 \end{pmatrix}. \tag{4.8}
$$

For planar somersaults all angular velocities are orthogonal to the midsagittal plane, i.e.

$$
\boldsymbol{\Omega}_v = \begin{pmatrix} 0 \\ \dot{v} \\ 0 \end{pmatrix} \text{ and } \boldsymbol{\Omega}_{\alpha_i} = \begin{pmatrix} 0 \\ \dot{\alpha}_i \\ 0 \end{pmatrix}, \tag{4.9}
$$

which means

$$
R_{\alpha_i} J_i \boldsymbol{\Omega}_{\alpha_i} = \begin{pmatrix} 0 \\ J_{i_y} \dot{\alpha}_i \\ 0 \end{pmatrix}, \tag{4.10}
$$

and summing (4.8) and (4.10) over the six body segments gives the angular momentum shift

$$\boldsymbol{A} = \begin{pmatrix} A_x \\ A_y \\ A_z \end{pmatrix} = \begin{pmatrix} 0 \\ \sum_i \left[m_i (C_{i_z} \dot{C}_{i_x} - C_{i_x} \dot{C}_{i_z}) + J_{i_y} \dot{\alpha}_i \right] \\ 0 \end{pmatrix}. \tag{4.11}$$

From (3.13) and (3.16) we see that $C_{i_z}\dot{C}_{i_x} - C_{i_x}\dot{C}_{i_z}$ can be written in combinations involving the joint location vector $\boldsymbol{D}_i^j$, shape angle α_i, and shape velocity $\dot{\alpha}_i$. More specifically this quantity is linear in the shape velocities, so we can write the y-component of (4.11) as

$$A_y = \boldsymbol{A}_y(\boldsymbol{\alpha}) \cdot \dot{\boldsymbol{\alpha}}, \tag{4.12}$$

where $\boldsymbol{\alpha}$ denotes the collection of shape angles $(\alpha_{up}, \dots)^t$. We emphasise that $\boldsymbol{\alpha}$, $\dot{\boldsymbol{\alpha}}$, $\boldsymbol{A}_y(\boldsymbol{\alpha})$, and soon $\boldsymbol{F}(\boldsymbol{\alpha})$ defined in (4.14) all have dimension 5 (corresponding to the number of shape angles). Due to the form of I given by (4.6), $\boldsymbol{A}$ in (4.11), and $\boldsymbol{L}$ we have $\dot{\boldsymbol{L}} = \boldsymbol{0}$ in the equations of motion (3.25), hence $\boldsymbol{L} = (0, L, 0)^t$ is constant with L being the angular momentum at take-off. Substituting (4.6), (4.9), and (4.11) into $\boldsymbol{L}$ given by (3.23) we find that only the y-component is non-zero, and it is

$$L_y = I_{yy}(\boldsymbol{\alpha})\dot{\upsilon} + \boldsymbol{A}_y(\boldsymbol{\alpha}) \cdot \dot{\boldsymbol{\alpha}}. \tag{4.13}$$

Defining

$$\boldsymbol{F}(\boldsymbol{\alpha}) = -I_{yy}^{-1}(\boldsymbol{\alpha})\boldsymbol{A}_y(\boldsymbol{\alpha}) \tag{4.14}$$

and dropping the subscripts we can rearrange this to get

$$\dot{\upsilon} = I^{-1}(\boldsymbol{\alpha})L + \boldsymbol{F}(\boldsymbol{\alpha}) \cdot \dot{\boldsymbol{\alpha}}, \tag{4.15}$$

which is similar to the differential equation Tong and Dullin [**55**] used in the study of the equilateral pentagon at zero angular momentum. However, a key difference is that we now want $L \neq 0$ for the diver to perform planar somersaults (unlike the previous study where $L = 0$). The differential equation (4.15) is composed of two parts - the dynamic phase given by $I^{-1}(\boldsymbol{\alpha})L$ which is proportional to L, and the geometric phase $\boldsymbol{F}(\boldsymbol{\alpha}) \cdot \dot{\boldsymbol{\alpha}}$ which is independent of L. Solving (4.15) with the initial condition $\upsilon(0) = \upsilon_0$ gives the orientation of the athlete as a function of time.

During a dive the athlete goes through a sequence of shape changes that can be represented by a curve on shape space, and provided the take-off and final shape of the athlete are the same then this curve closes into a loop. While both the dynamic phase and geometric phase depend on the path of the loop, the dynamic phase also depends on the velocity with which the loop is traversed, whereas the geometric phase is independent of the velocity. As such, traversing through the same loop with different velocities yields different contributions to the dynamic phase, but the same contribution in the geometric phase. In general, we expect the dynamic

phase to be the dominating term for planar somersaults as it is proportional to L, which is large, and the geometric phase to play a smaller role.

4.2 Digitised Data

Footage of a professional male athlete performing 107B (forward 3.5 somersaults in pike) off the 3m springboard was captured at the New South Wales Institute of Sport (NSWIS) using a 120 FPS camera. SkillSpector [57] was used to manually digitise the footage, creating a total of 187 frames starting from the moment of take-off and ending when the athlete's hand first makes contact with the water upon entry, spanning a total airborne time of 1.55 seconds. The digitisation of the dive is shown in Figure 4.1. For convenience we shall refer to the initial frame as the zeroth frame, and write $\boldsymbol{\alpha}[j] = \{\alpha_{up}[j], \dots\}$ to denote the collection of shape angles of the jth frame, where $0 \leq j \leq 186$.

In each frame we locate the joint positions of the ankle, knee, hip, shoulder, elbow, wrist, and ear (which serves as a decent approximation for the centre of mass of the head). To reduce digitisation errors a discrete Fourier cosine transform is applied to the data in Mathematica (FourierDCT type II), so by keeping the first fifteen Fourier coefficients the data is smoothed when inverting the transformation. We then compute the absolute orientation υ_i for each B_i in every frame by looking at the appropriate joint positions, e.g. to determine $\upsilon_{ref}[0]$ we look at the hip to shoulder vector at the zeroth (initial) frame and compare it to the corresponding vector obtained from the anatomical neutral position when standing upright in

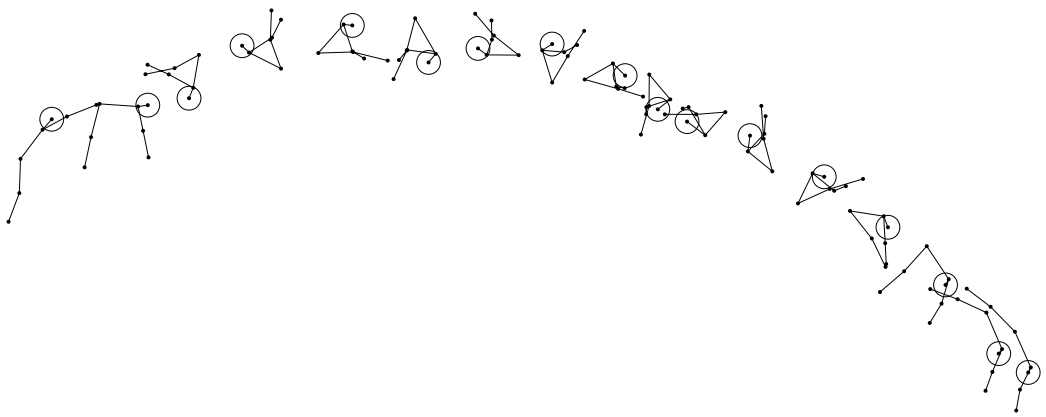

Figure 4.1. Illustration of the digitised dive for frames: 0, 15, 30, 45, 60, 75, 90, 100, 110, 120, 130, 140, 150, 160, 170, 180 and 186 from left to right. To avoid clutter, each illustrated frame is shifted to the right by a small constant amount to provide better visualisation of the dive sequence.

the spatial frame. The spatial frame has a planar view of the xz-plane with y-axis pointing into the page, so that clockwise is the positive direction of rotation. The computation of υ_i for each $i \in \{ref, \dots\}$ in each frame is provided in Appendix E, and with this we can compute the shape angles using

$$\alpha_i = \upsilon_i - \upsilon_{ref} \text{ for } i \in \{up, ud, lp, ld, hd\}, \tag{4.16}$$

which are orientation independent. We plot the diver at take-off and entry into the water in Figure 4.2, and the orientation and shape angles for the complete dive are shown in Figure 4.3. We choose to define the orientation of the athlete by looking at the orientation of the torso, which from the digitised dive is given by υ_{ref}. A method to ascertain validity of our model is to compute υ theoretically

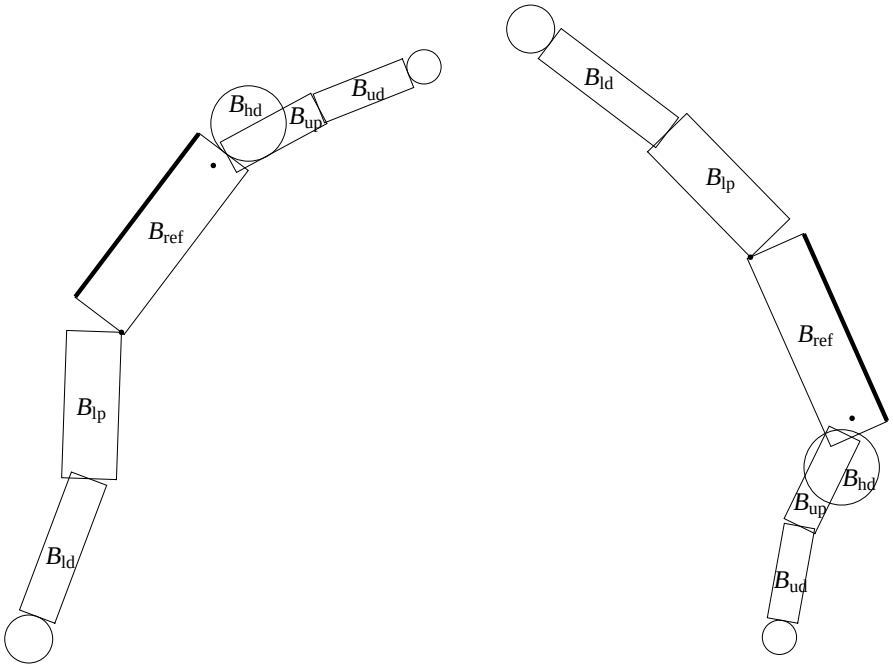

(A) Take-off. (B) Entry.

Figure 4.2. The orientation and shape angles of the athlete at take-off (Figure 4.2A) and entry into the water (Figure 4.2B) for the digitised dive. To help distinguish the anterior and posterior ends, a thick line is used to depict the posterior side of the torso. The values for take-off are: $\upsilon_{ref}[0] = 0.648$, $\boldsymbol{\alpha}[0] = \{-2.714, -2.595, -0.618, -0.288, 0.073\}$, and the values for entry are: $\upsilon_{ref}[186] = 21.573 \equiv 2.723$, $\boldsymbol{\alpha}[186] = \{-2.269, -2.545, -0.355, -0.503, 0.898\}$. The shape angles follow the same ordering specified in (4.16).

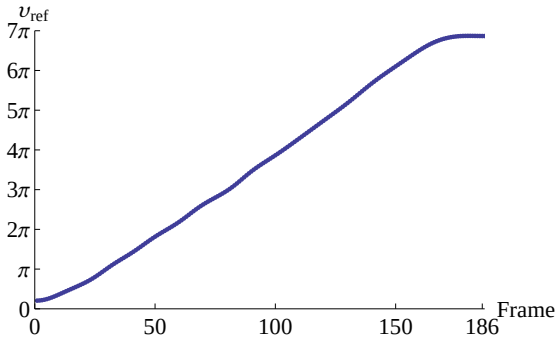

(A) Orientation of the athlete.

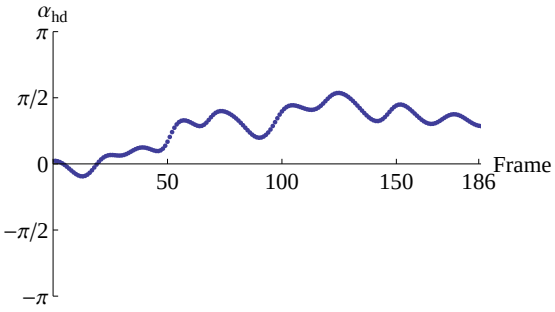

(B) Shape angle of head.

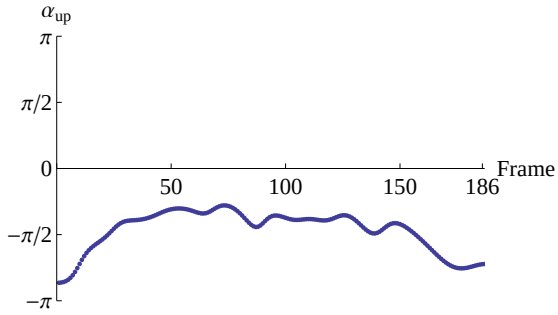

(C) Shape angle of upper arm.

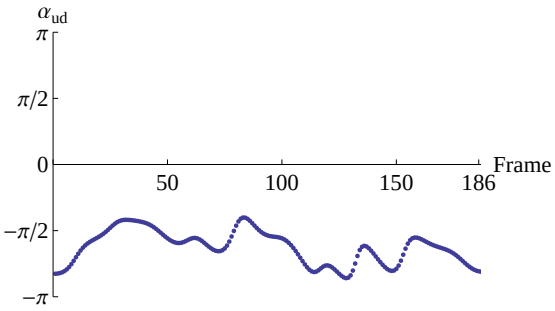

(D) Shape angle of forearm and hand.

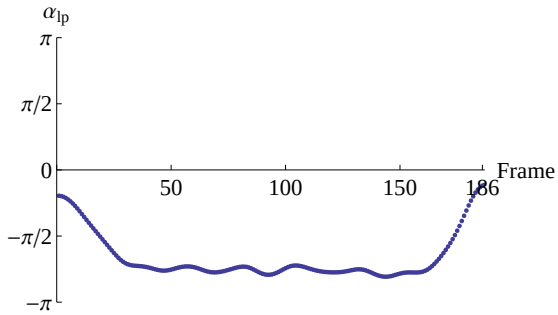

(E) Shape angle of thigh.

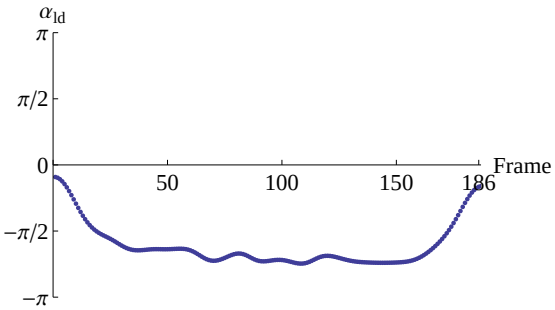

(F) Shape angle of lower leg and foot.

Figure 4.3. We have υ_{ref} specifying the orientation of the athlete given by the torso, and the collection of α_i specifying the shape.

using (4.15) and compare the result to the observed υ_{ref} from the data. If the differences are small then this confirms our model is valid. Slight variation is expected as the parameters used in the computation of (4.15) have been taken from Table 1.1, and not the particular athlete captured in the footage. To complete the comparison we need the initial orientation $\upsilon_{ref}[0]$, and the shape angles $\boldsymbol{\alpha}$ from the digitised dataset which we can interpolate to obtain a continuous curve

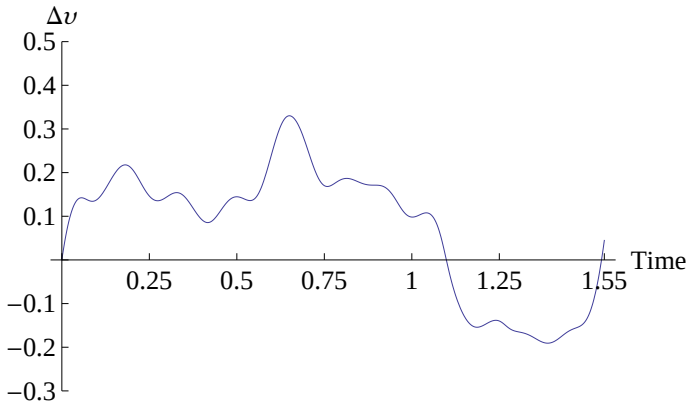

FIGURE 4.4. Plot of $\Delta\upsilon = \upsilon - \upsilon_{ref}$ as a function of time with $L = 122.756$. From the moment of take-off until the diver hits the water, the difference between the computed υ and observed υ_{ref} is < 0.331 radians throughout the dive with the maximum difference occurring at $t = 0.650$. This peak difference appears isolated, which is possibly due to digitisation errors in addition to discrepancies between inertia parameters used in the model and the actual athlete. At the moment of entry into the pool the difference $\Delta\upsilon$ is 0.045 radians, demonstrating good comparison between the computed and observed final orientation.

before substituting in (4.15). The angular momentum L is found by minimising the integrated difference squared of the theoretically computed υ and observed υ_{ref}. The result is $L = 122.756$, which produces the minimum difference shown in Figure 4.4. The maximal difference is 0.331 radians and the final difference is 0.045 radians, and therefore adds confidence in the model.

4.3 Geometric Phase and Segment Reduction

The discrete collection of $\boldsymbol{\alpha}[i]$ is interpolated to produce a continuous curve $\boldsymbol{\alpha}(t)$, where round brackets are used to denote the interpolated result as a function of time, and square brackets are reserved for the discrete frames. Since the take-off and entry shapes are not identical as shown in Figure 4.2, the overall rotation obtained depends on the choice of the reference segment. To eliminate this ambiguity we add one additional frame where $\boldsymbol{\alpha}[187] = \boldsymbol{\alpha}[0]$, so $\boldsymbol{\alpha}(t)$ closes and the overall rotation is well-defined. In $\boldsymbol{\alpha}(t)$ we keep the interpolation order cubic (default in Mathematica) for the digitised points, but use linear interpolation for the final two points to close the curve. The additional frame adds 1/120th of a second to the

airborne time and it is now

$$T_{air} = 187/120, \tag{4.17}$$

as we have 188 frames at 120 FPS. Solving (4.15) with initial condition

$$\upsilon(0) = \upsilon_{ref}[0] = 0.6478$$

we find that at the end of the dive the orientation is

$$\upsilon(T_{air}) = \upsilon_{dyn} + \upsilon_{geo} + \upsilon_{ref}[0], \tag{4.18}$$

where the dynamic phase is given by

$$\upsilon_{dyn} = L\int_0^{T_{air}} I^{-1}\big(\boldsymbol{\alpha}(t)\big)\,\mathrm{d}t = (0.1713 + 0.0004)L = 0.1718L, \tag{4.19}$$

and geometric phase given by

$$\upsilon_{geo} = \int_0^{T_{air}} \boldsymbol{F}\big(\boldsymbol{\alpha}(t)\big)\cdot\dot{\boldsymbol{\alpha}}(t)\,\mathrm{d}t = -0.0532 + 0.0970 = 0.0437. \tag{4.20}$$

As the shape velocities are discontinuous at $t = 186/120$ we split the region into $t \in [0, 186/120]$ and $(186/120, T_{air}]$ in order to evaluate the integrals. As $L \approx 120$ in the digitised dive, this means the dynamic phase is the dominant term and the geometric phase only plays a minute role in contributing towards the overall rotation.

Looking at the graphs in Figure 4.3 we notice that the upper arms and forearms move similarly relative to the torso, and the same is also observed for the thighs and lower legs. Therefore it is not too unreasonable to assume that the elbows and knees remain straight throughout the dive, particularly the knees during pike somersaults. The head does not make a significant contribution to the dynamics and can therefore also be set to zero for simplicity. Using the assumptions

$$\alpha_{up} = \alpha_{ud} \qquad \alpha_{lp} = \alpha_{ld} \qquad \alpha_{hd} = 0 \tag{4.21}$$

therefore allows us to reduce the segment count of the athlete and subsequently reduce the shape space from some subset of a five dimensional torus to some subset of a two dimensional torus. We say subset as there are shapes deemed impossible or unrealistic for diving, e.g. the shape shown in Figure 4.5. In the reduced model there are two shape angles that specify the shape of the athlete, which we denote as α_u for the arms and α_l for the legs, and the constraint on shape space that we impose is $\{\alpha_u, \alpha_l\} \in [-\pi, 0]^2$ for the set of all possible shapes obtainable by the athlete. One point to note is that the general theory is not dependent on the final assumptions (4.21) used to reduce the segment count. While reverting to the more complicated model is possible, these assumptions make it easier to grasp the main principles behind the theory. The reduced model does possess slightly different numerical values for the dynamic and geometric phases though, which are now

$$\upsilon_{dyn} = 0.1705L \qquad \upsilon_{geo} = 0.0721, \tag{4.22}$$

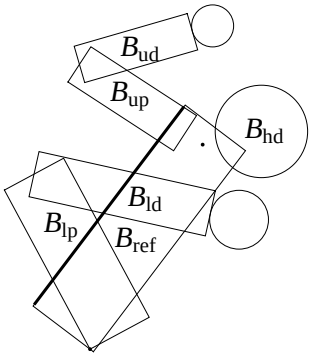

FIGURE 4.5. An impossible shape configuration of the athlete. The parameters are $\upsilon = 0.648$ and $\boldsymbol{\alpha} = \{1.5, -2.5, 2, -2, 1\}$.

where the details are given in Appendix F. While the difference in υ_{geo} may appear large, it does not change the fundamental principles behind the theory.

From here on, we will use the reduced model for any further computations unless otherwise indicated. We plot the moment of inertia for each individual frame in Figure 4.6, and the shape curve on shape space in Figure 4.7.

As the geometric phase is related to the area enclosed by the loop $\boldsymbol{C}$, it is useful to convert the line integral

$$\int_{\boldsymbol{C}} F_1(\boldsymbol{\alpha})\, d\alpha_u + F_2(\boldsymbol{\alpha})\, d\alpha_l \tag{4.23}$$

(where $\boldsymbol{F}(\boldsymbol{\alpha}) = F_1(\boldsymbol{\alpha})\boldsymbol{i} + F_2(\boldsymbol{\alpha})\boldsymbol{j}$) into a double integral using Green's theorem.

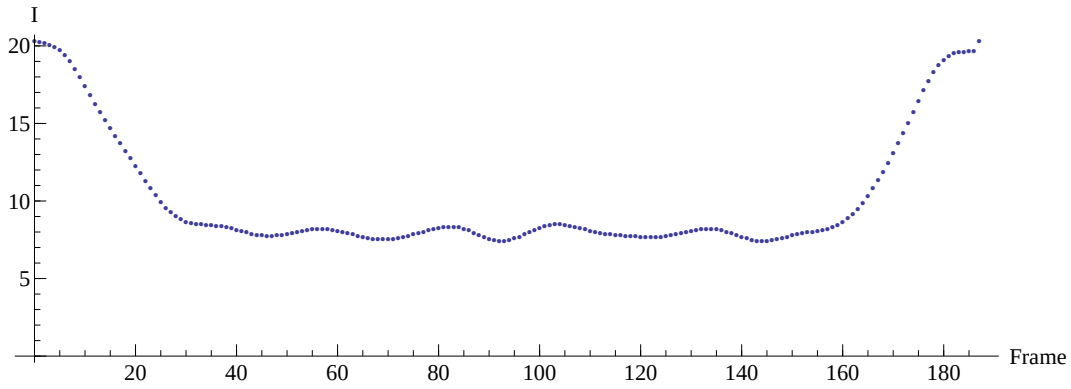

FIGURE 4.6. The maximum I occurs at $\boldsymbol{\alpha}[0] = \boldsymbol{\alpha}[187]$ with value 20.302, and the minimum occurs at $\boldsymbol{\alpha}[144]$ with value 7.4427. The last point is a jump because it is the additional frame we added to allow $\boldsymbol{\alpha}(t)$ to close on shape space.

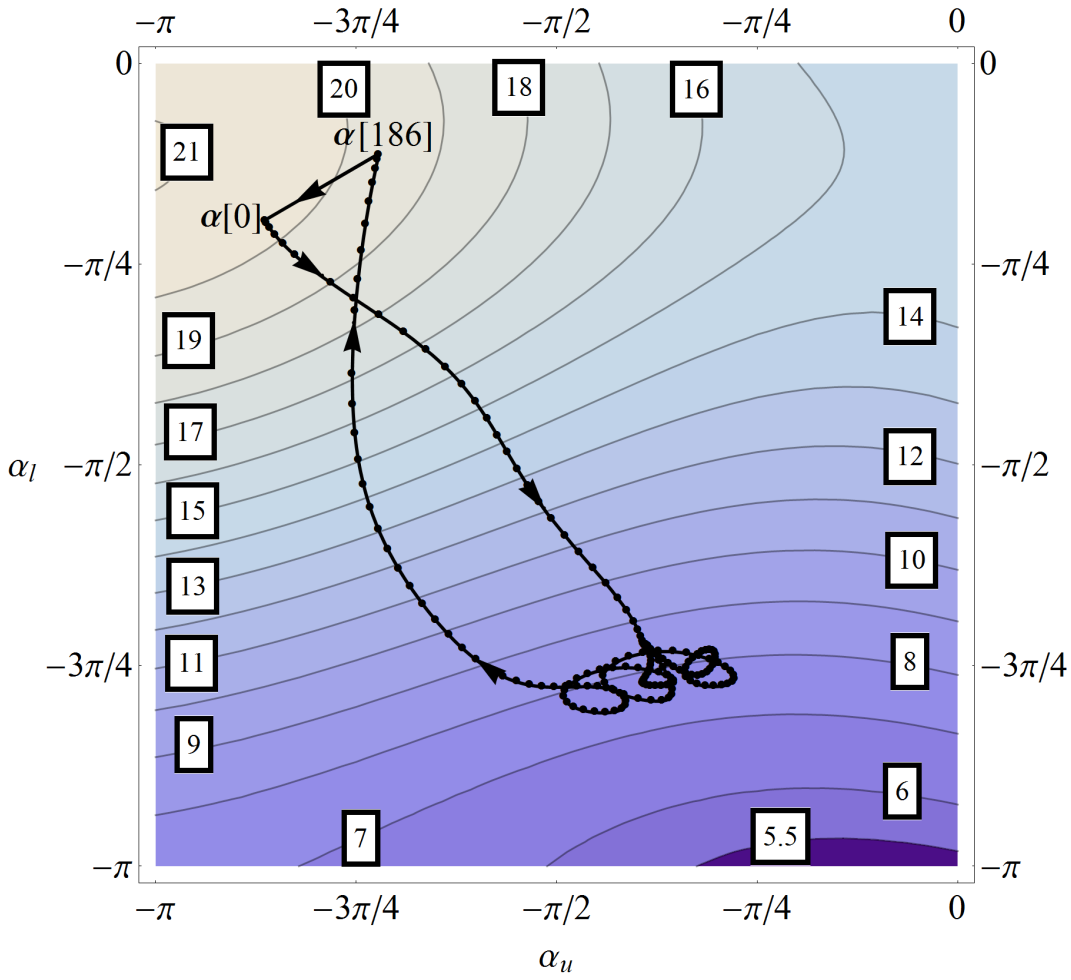

FIGURE 4.7. The black points are the collection of $\boldsymbol{\alpha}[i]$, and the black curve is $\boldsymbol{\alpha}(t)$ interpolated from that collection of points. The curve is shown along with the constant $I(\boldsymbol{\alpha})$ contours on shape space.

This gives

$$\iint_A \frac{\partial F_2(\boldsymbol{\alpha})}{\partial \alpha_u} - \frac{\partial F_1(\boldsymbol{\alpha})}{\partial \alpha_l}\, d\alpha_u d\alpha_l = \iint_A B(\boldsymbol{\alpha})\, d\alpha_u\, d\alpha_l \tag{4.24}$$

where we refer to $B(\boldsymbol{\alpha})$ as the magnetic field, and the region A is enclosed by the loop $\boldsymbol{C}$. We show the loop $\boldsymbol{C}$ (which in our case is $\boldsymbol{\alpha}(t)$ when t runs from 0 to T_{air}) on shape space for the digitised dive along with constant $B(\boldsymbol{\alpha})$ contours in Figure 4.8. As the loop $\boldsymbol{C}$ is self-intersecting we partition it into ten pieces denoted by $\boldsymbol{C}_i$ for $i \in \{1, \ldots, 10\}$, take the appropriate pieces that make up smaller loops, e.g. the $\boldsymbol{C}_1$, $\boldsymbol{C}_9$ and $\boldsymbol{C}_{10}$ pieces that make up the red loop in Figure 4.8, compute the

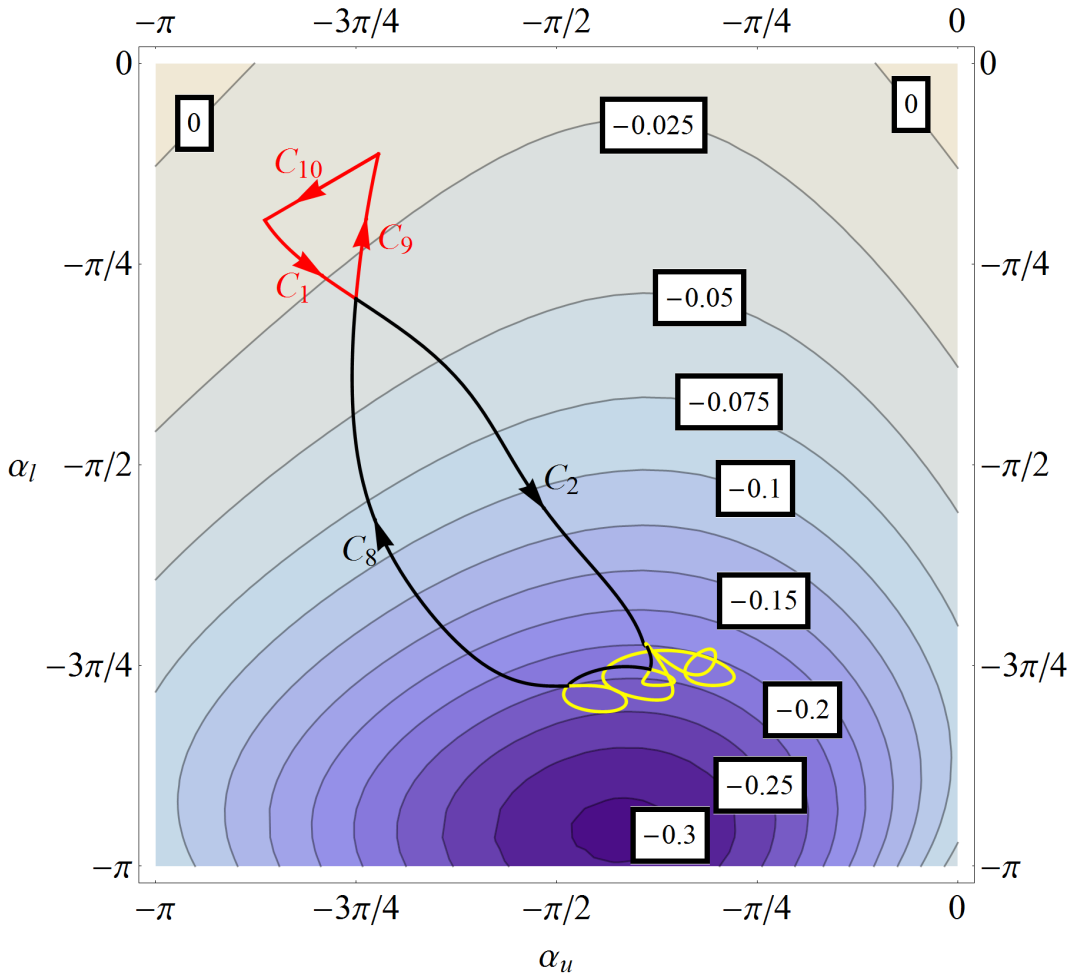

FIGURE 4.8. Loop $\boldsymbol{C}$ consisting of the partition pieces $\boldsymbol{C}_1$, $\boldsymbol{C}_2$, etc shown along with constant $B(\boldsymbol{\alpha})$ contours.

geometric phase contribution in each loop, and finally sum up all the contributions to get the total geometric phase.

As $B(\boldsymbol{\alpha}) < 0$ throughout the dive, loops orientated clockwise will provide a positive contribution towards the geometric phase (and hence the overall rotation), while loops oriented counterclockwise will provide a negative contribution. By reversing the orientation of the red and yellow loops in Figure 4.8, we can improve the overall rotation achieved by increasing the geometric phase to $\upsilon_{geo} = 0.1186$ (c.f. υ_{geo} in (4.22)) without affecting the dynamic phase υ_{dyn}. While the effect from the geometric phase is small, it is an improvement of 64.39% compared to the original υ_{geo}. As the changes needed for this improvement are neither realistic nor practical in an actual dive, the details are included in Appendix G. It is

worthwhile to note that by simply reordering and reversing certain parts of the loop $\boldsymbol{C}$, an increase in overall rotation can be achieved.

4.4 Optimisation of Planar Dive

From the digitised footage and moment of inertia plot shown in Figure 4.6 we observe the following structure in the dive:

1. The athlete takes off with large moment of inertia.
2. The athlete quickly moves into pike position.
3. The athlete (roughly) holds pike where moment of inertia is small.
4. The athlete completes the dive with (roughly) the same take-off shape.

The shape changing velocities are shown in Figure 4.9, and from there we see that the transition into and out of pike takes about a quarter second or slightly longer.

Let $\boldsymbol{\alpha}_{max}$ correspond to the shape with maximum moment of inertia I_{max}, and $\boldsymbol{\alpha}_{min}$ correspond to the shape with minimum moment of inertia I_{min}. Then for $\boldsymbol{\alpha} = (\alpha_u, \alpha_l) \in [-\pi, 0]^2$ we find that

$$\begin{aligned} \boldsymbol{\alpha}_{max} &= (-\pi, -0.3608) \longrightarrow I_{max} = 21.0647 \\ \boldsymbol{\alpha}_{min} &= (-0.3867, -\pi) \longrightarrow I_{min} = 5.2888, \end{aligned}$$

and these shapes are illustrated in Figure 4.10. The figure shows that the shape for I_{max} has a hip flexion, which is a consequence of the hip joint being placed at the front of the two segments. If the joint were centred, like in the case of the shoulders, then the body would be straight. However, this poses the problem of the athlete's legs lying within their torso while in pike. Besides being unphysical, the moment of inertia may also be too small to accurately model the dive. We see in Figure 4.2 that divers in reality do exhibit some hip flexion angle during take-off and entry into the water, making the front (as opposed to the centre) a more suitable location for the hip joint.

From Figure 4.3C it appears the arms do not move into position until at least frame 50, however we see from Figure 4.9 that this is not the case. Instead, the arm movement finishes at frame 32 and is supported by the forearm movement in Figure 4.3D. Any additional movement beyond this is undesired wobble, which happens to be in the same direction as the arm movement, thus making it appear longer. The structure observed in the digitised dive will serve as a guideline for the theoretical dive that we will now propose. In the ideal dive we want the athlete to take off with shape $\boldsymbol{\alpha}_{max}$ and immediately start moving into pike position specified by shape $\boldsymbol{\alpha}_{min}$. The athlete holds pike steadily without wobble, and then transitions back into the original shape $\boldsymbol{\alpha}_{max}$ where the dive is completed. If the limbs are moving at maximum speed, we want $|\dot{\alpha}_u| = 11.0194$ and $|\dot{\alpha}_l| = 11.1230$ so the transition from $\boldsymbol{\alpha}_{max}$ to $\boldsymbol{\alpha}_{min}$ and vice versa takes precisely a quarter second;

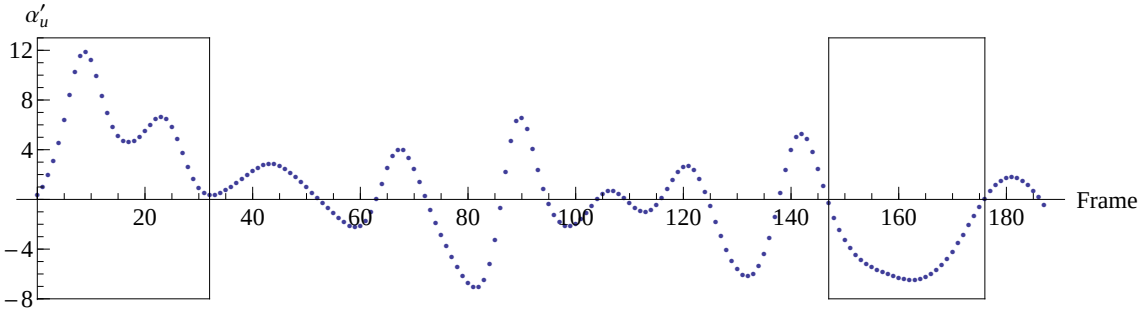

(A) Shape changing velocity of arms.

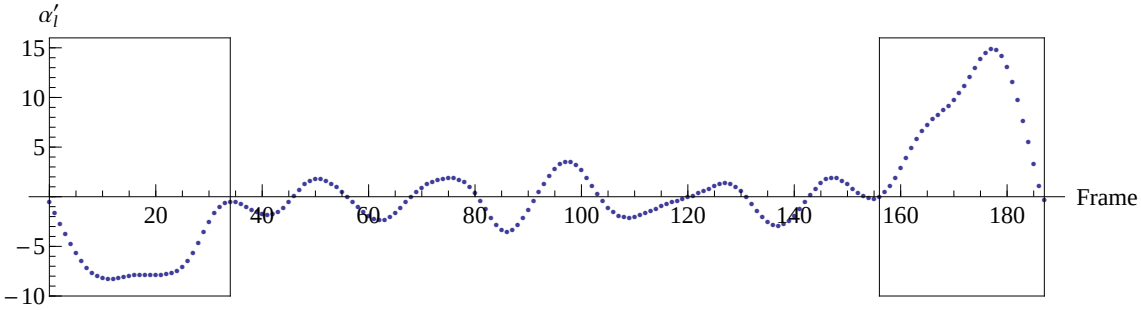

(B) Shape changing velocity of legs.

Figure 4.9. Following take-off, the athlete quickly moves into pike position. The above plots of the digitised dive indicate that the athlete's arms and legs reached their necessary positions at frames 32 and 34, respectively. When leaving pike, the arms moved first during frames 147 to 176, followed by the legs between frames 156 and 187. The transitions in and out of pike position are highlighted by the black boxes. Between these two stages, we observe some wobble with the limbs while the pike is held by the athlete.

this is represented by the curve shown in Figure 4.11. When the limbs move at maximum speed into and out of pike, the time spent in pike is maximised but without geometric phase.

The construction in Figure 4.12 involves slower leg movement when moving into pike. After a quarter second the arms are in place while the legs are not, corresponding to the shape $\boldsymbol{\alpha}_f$. The legs require some additional time to move into place, as shown by the black vertical curve. When moving out of pike the arms move first (shown by the black horizontal line) to get into shape $\boldsymbol{\alpha}_b$. This is followed by subsequent arm movements at a slower speed while the legs move at maximum speed in order to reach $\boldsymbol{\alpha}_{max}$ a quarter second later to complete the dive. This dive requires additional time in shape change indicated by the vertical and horizontal black curve, which could have alternatively been spent in pike position.

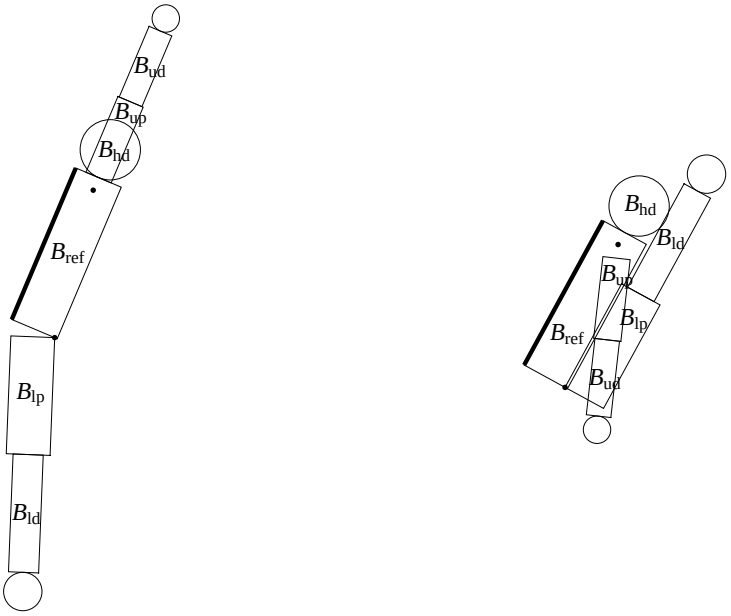

(A) $I_{max} = 21.0647$. (B) $I_{min} = 5.2888$.

FIGURE 4.10. The shapes with extremums of I in the domain $[-\pi, 0]^2$. Note there is also a saddle point located at $\boldsymbol{\alpha}_{sad} = (-0.1376, -0.4037)$ which gives $I_{sad} = 14.8431$, see Figure 4.7, but this point is not important and thus the shape is not shown.

Although some extra time was needed in shape change and thus not spent in pike, the gain is a positive contribution from the geometric phase due to a clockwise oriented loop on shape space. As the geometric phase given by (4.24) involves integrating $B(\boldsymbol{\alpha})$ over the region enclosed by the loop $\boldsymbol{C}$, having the region contain the absolute maximum of $B(\boldsymbol{\alpha})$ and its neighbourhood of large absolute values provides a more efficient (in terms of geometric phase per arc length) contribution towards the geometric phase. We now perform the optimisation to determine how fast the arms and legs should move to maximise the overall rotation obtained. This is done by finding the balance between the dynamic and geometric phase contributions.

To be concise, we define $s_l \in [0, 1]$ to be a percentage of max speed for the legs when moving into pike, and $s_u \in [0, 1]$ to be a percentage of max speed for the arms when moving out of pike. These potentially slower speeds will only be used when moving from $\boldsymbol{\alpha}_{max}$ to $\boldsymbol{\alpha}_f$ and $\boldsymbol{\alpha}_b$ to $\boldsymbol{\alpha}_{max}$, as the transition from $\boldsymbol{\alpha}_f$ to $\boldsymbol{\alpha}_{min}$ and $\boldsymbol{\alpha}_{min}$ to $\boldsymbol{\alpha}_b$ will have the appropriate limb moving at max speed in order to minimise the extra time needed in shape change. With this construction, the

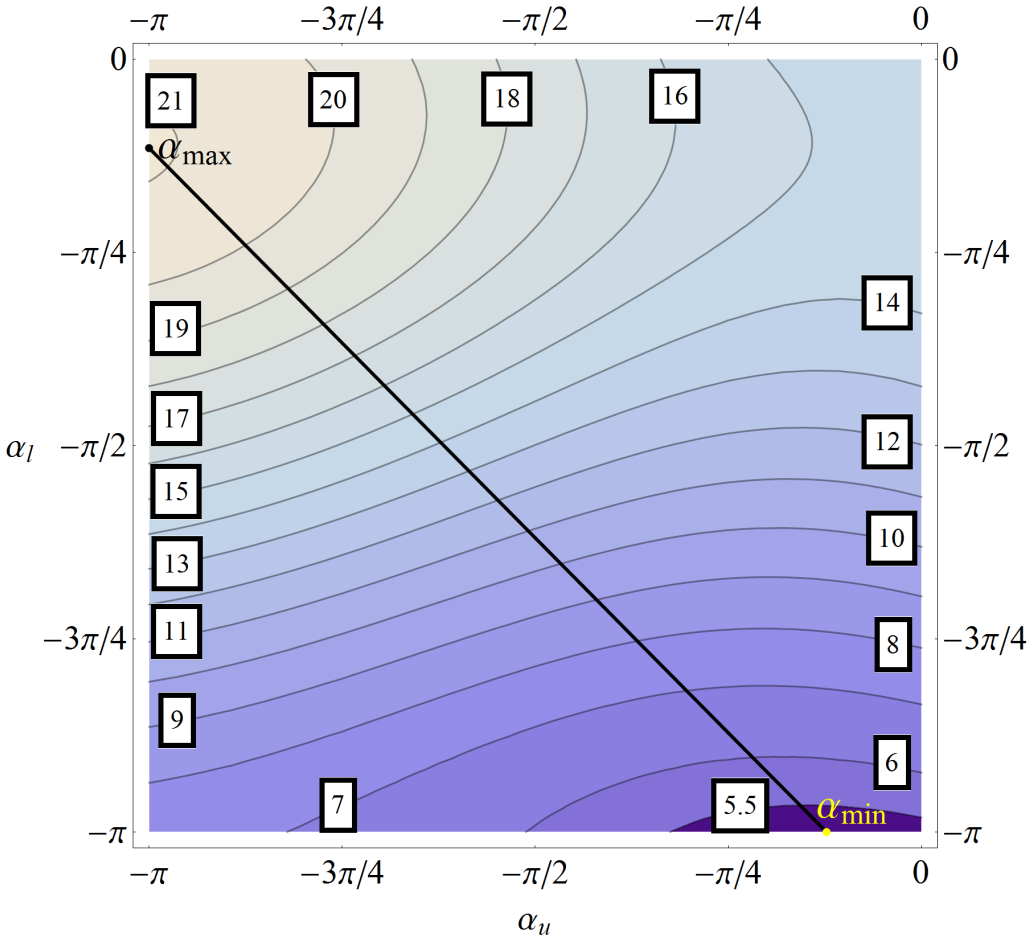

FIGURE 4.11. The black curve shows the fastest way to move into and out of pike so that the transition time is a quarter second. Constant $I(\boldsymbol{\alpha})$ contours are plotted which show at $\boldsymbol{\alpha}_{max}$ the moment of inertia is I_{max} and at $\boldsymbol{\alpha}_{min}$ the moment of inertia is I_{min}.

extra time needed to move into pike is $\tau_E(s_l)$, and when moving out of pike it is $\tau_E(s_u)$, where we define the extra time as

$$\tau_E(s) = (1-s)/4. \tag{4.25}$$

In the dive shown in Figure 4.11 we have $\{s_l, s_u\} = \{1, 1\}$, so both $\tau_E(s_l) = \tau_E(s_u) = 0$. We define

$$\boldsymbol{v}(s_l, s_u) = 4\,\mathrm{diag}\,(s_u, s_l)(\boldsymbol{\alpha}_{min} - \boldsymbol{\alpha}_{max}) \tag{4.26}$$

to correspond with the shape velocities written in vector form. Let $\boldsymbol{C}_i(t)$ for $i \in \{1, 2, 3, 4\}$ be the curve on shape space from $\boldsymbol{\alpha}_{max} \to \boldsymbol{\alpha}_f$, $\boldsymbol{\alpha}_f \to \boldsymbol{\alpha}_{min}$, $\boldsymbol{\alpha}_{min} \to$

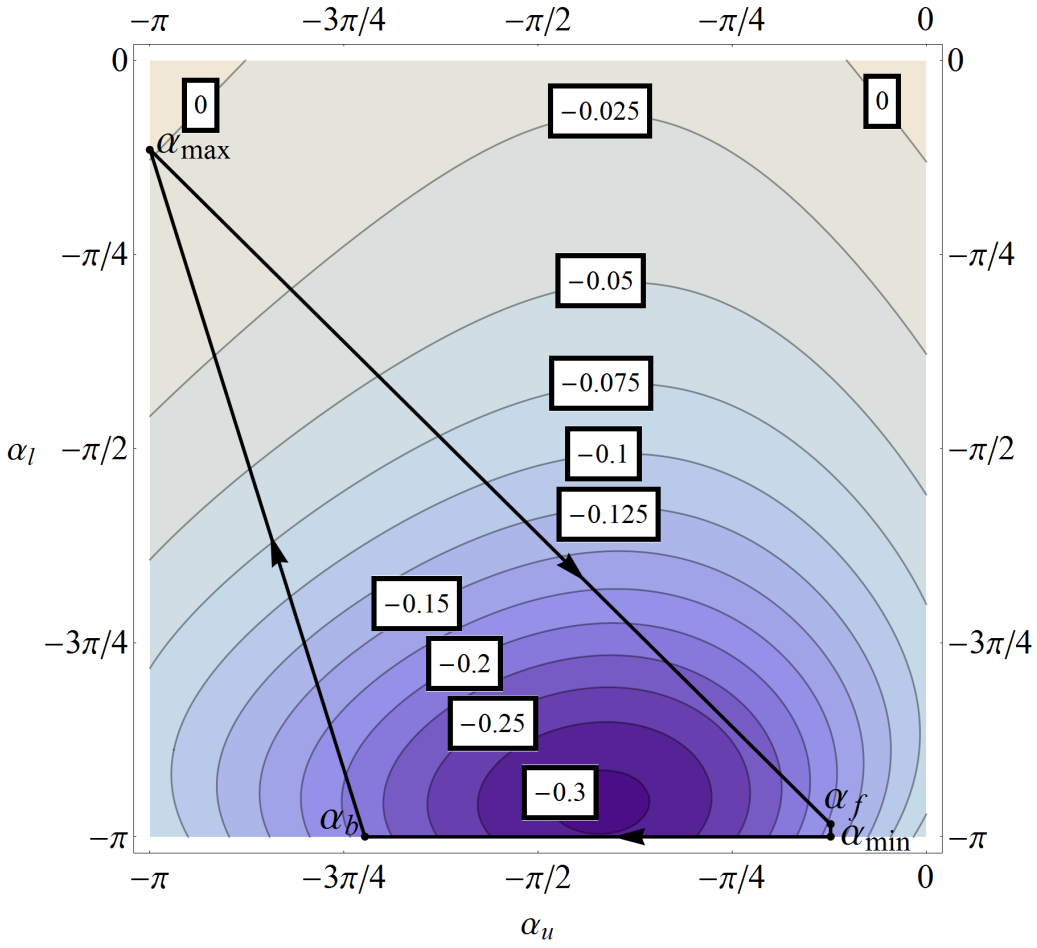

FIGURE 4.12. In this dive we have $\{s_l, s_u\} = \{0.9818, 0.3158\}$, so the transition from $\boldsymbol{\alpha}_f = (-0.3867, -3.0910)$ to $\boldsymbol{\alpha}_{min}$ is 0.0046 seconds, and from $\boldsymbol{\alpha}_{min}$ to $\boldsymbol{\alpha}_b = (-2.2717, -\pi)$ is 0.1711 seconds. The loop is shown with constant $B(\boldsymbol{\alpha})$ contours, so the region enclosed gives an idea of the geometric phase contribution we should expect.

$\boldsymbol{\alpha}_b$, and $\boldsymbol{\alpha}_b \to \boldsymbol{\alpha}_{max}$ in that order, then for each $\boldsymbol{C}_i(t)$ where $t \in [0, \tau_i]$ we have $\tau_1 = \tau_4 = 1/4$, $\tau_2 = \tau_E(s_l)$, $\tau_3 = \tau_E(s_u)$, and the total accumulated shape change time is

$$\tau_\Sigma = 1/2 + \tau_E(s_l) + \tau_E(s_u). \tag{4.27}$$

The curves themselves are defined by:

$$\boldsymbol{C}_1(t) = \boldsymbol{v}(s_l, s_u)t + \boldsymbol{\alpha}_{max} \qquad \boldsymbol{C}_3(t) = \boldsymbol{\alpha}_{min} - \boldsymbol{v}(0,1)t$$
$$\boldsymbol{C}_2(t) = \boldsymbol{C}_1(t_1) + \boldsymbol{v}(1,0)t \qquad \boldsymbol{C}_4(t) = \boldsymbol{C}_3(t_3) - \boldsymbol{v}(s_l, s_u)t,$$

and we sometimes write $\boldsymbol{C}_i(t; s_l, s_u)$ to explicitly denote the percentages of max speed. The overall rotation obtained by traversing along the loop $\boldsymbol{C} = \boldsymbol{C}_1 \cup \boldsymbol{C}_2 \cup \boldsymbol{C}_3 \cup \boldsymbol{C}_4$ is then

$$\upsilon(s_l, s_u) = \upsilon_{dyn}(s_l, s_u) + \upsilon_{geo}(s_l, s_u), \tag{4.28}$$

where we solve (4.15) to find

$$\upsilon_{dyn}(s_l, s_u) = L \sum_{i=1}^{4} \int_0^{\tau_i} I^{-1}\big(\boldsymbol{C}_i(t; s_l, s_u)\big)\, \mathrm{d}t$$

$$\upsilon_{geo}(s_l, s_u) = \sum_{i=1}^{4} \int_0^{\tau_i} \boldsymbol{F}\big(\boldsymbol{C}_i(t; s_l, s_u)\big) \cdot \dot{\boldsymbol{C}}_i(t; s_l, s_u)\, \mathrm{d}t.$$

To judge how good the overall rotation obtained is, we compare $\upsilon(s_l, s_u)$ in (4.28) to the overall rotation

$$\upsilon_\Sigma(s_l, s_u) = L I^{-1}(\boldsymbol{\alpha}_{min}) \tau_\Sigma \tag{4.29}$$

obtained by holding the pike for τ_Σ, the amount of time required to traverse along the loop $\boldsymbol{C}$. Although different loops defined by the choice of $\{s_l, s_u\}$ require different times to complete, using a fixed airborne time T_{air} (so that shorter loops needing less shape changing time can spend more time τ_{pike} in pike) makes the comparison fair. The overall rotation obtained is compared for the constant airborne time $T_{air} = \tau_\Sigma + \tau_{pike}$, so the result which minimises

$$\upsilon_\Sigma(s_l, s_u) - \upsilon(s_l, s_u) \tag{4.30}$$

is the dive that yields maximal rotation. In the optimisation for $L = 120$ we find that $\{s_l, s_u\} = \{1, 0.8593\}$ minimises (4.30), which is the loop shown in Figure 4.13.

When compared to the dive $\{s_l, s_u\} = \{1, 1\}$ shown in Figure 4.11 (where the diver moves into and out of pike the fastest) the gain in overall rotation is 0.0189 radians or 1.0836°. We see that in the optimal dive the limbs move at max speed into pike, but when exiting the arms move slower, thus providing a geometric phase contribution that exceeds the lost contribution from the dynamic phase by 1.0836°. This behaviour is due to the take-off and pike shapes being $\boldsymbol{\alpha}_{max}$ and $\boldsymbol{\alpha}_{min}$, but had we chosen different shapes then the observed result may differ. The dynamic phase benefits from being at (or close to) the minimum moment of inertia I_{min} located at $\boldsymbol{\alpha}_{min}$, whereas the geometric phase prefers to enclose a region with large magnitudes of the magnetic field B, where the absolute maximum is 0.3058 occurring at $(-1.3148, -3.0043)$. In order to obtain maximal rotation there is competition between B and I, and L also plays an important role due to its proportionality to the dynamic phase. By making L smaller, the dynamic phase is reduced while the geometric phase is unchanged, hence allowing the latter to have a bigger impact on the overall rotation obtained by the diver. We find that for $L = 30$, repeating the same optimisation yields $\{s_l, s_u\} = \{0.9818, 0.3158\}$,

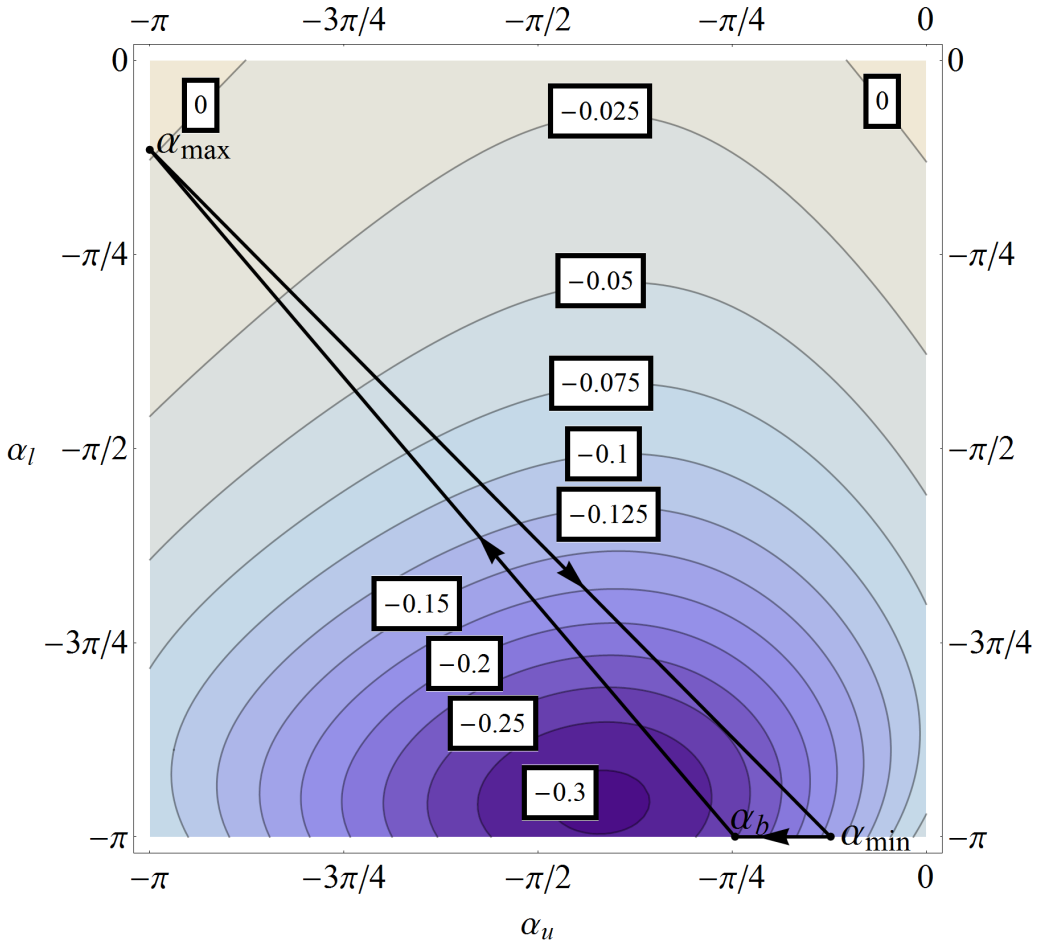

FIGURE 4.13. Loop with $\{s_l, s_u\} = \{1, 0.8593\}$ shown with constant $B(\boldsymbol{\alpha})$ contours, and the point $\boldsymbol{\alpha}_b = (-0.7743, -\pi)$.

which is the loop shown in Figure 4.12. The gain in overall rotation over the $\{s_l, s_u\} = \{1, 1\}$ dive shown in Figure 4.11 is an additional 0.2327 radians or 13.3354°, which is more significant than the 1.0836° found for $L = 120$. This result should be considered a proof of principle. Clearly the addition of 1° is irrelevant, but the model is extremely simple, and one can hope that for more realistic models similar ideas using an asymmetry of movement into and out of pike may make a small but important contribution.

CHAPTER 5

m Somersaults with n Twists

In this chapter we are going to simulate divers performing m somersaults with n twists. In real dives, m is typically a half integer and n an integer in forward/inward dives, or a half integer in backward/reverse dives. The exception is when $m = \frac{1}{2}$ (a dive) or $m = 1$ (somersault), where n could also take the values of $\frac{1}{2}$ or 1. We will specifically look at forward twisting somersaults, in particular, 5132D, 5134D, 5136D, and 5138D, but the results can be extended to backward, inward and reverse twisting somersaults by including an overall minus sign in the rotational dynamics, reversing the horizontal direction of translational motion, or a combination of the two. We use the 2-body model described in Chapter 3.5.1, where the reduced tensor of inertia I and angular momentum shift $\boldsymbol{A}$ are respectively found in (3.45) and (3.38).

In Chapter 5.1 we describe how forward twisting somersaults are performed using a predetermined set of motor actions. In Chapter 5.2 we find numerical results for twisting somersaults using realistic arm motions, where the parameters needed to make the dive work are found numerically by brute force. In Chapter 5.3 we take the limiting case where the shape changes become impulsive, resorting to fast-kicks that simplify the motor actions. This enables us to obtain analytical results in the twisting somersault. The numerical and analytical approximation are compared in Chapter 5.4, where we show how the generalisation of Montogomery's geometric phase formula due to Cabrera [**9**] links the two.

Every differential equation that needs to be solved numerically is computed with Mathematica 8 using 'NDSolve' with 'WorkingPrecision' set to 25, as opposed to standard machine precision which is ∼16. We use a slower but higher precision because the athlete completes the dive with pure somersault in our simulation, which is an unstable steady rotation. The use of the higher precision minimises the emergence of errors due to the instability.

The results of this chapter have been published in 'Twisting Somersault' [**16**], and provided inspiration for 'The Diver With A Rotor' [**6**], where the arms are replaced with a rotor that can be switched on and off. This simplifies the dynamics by making I constant and $\boldsymbol{A}$ piecewise constant, so that explicit analytical formulas can be found.

5.1 Dive Proposal

We begin by describing the dive procedure for the athlete performing m forward somersaults with n twists, which is done by using a predetermined set of motor actions. We use the reduced 2-body model described in Chapter 3.5.1 to keep the simulation as simple as possible whilst still being able to achieve the desired effect. The motor action is the lowering and raising of the left arm about the abduction-adduction plane of motion as shown in Figure 5.1. The simulation consists of five stages denoted by $\mathcal{S}_k$ for $k \in \{1, \dots, 5\}$, where the odd numbered stages are rigid body dynamics with no shape change, and the even numbered stages are the transition stages with shape change (i.e. the left arm moves). The procedure is as follows:

$\mathcal{S}_1$ - rigid body - layout position, Figure 5.1A
$\mathcal{S}_2$ - transition - left arm moves down
$\mathcal{S}_3$ - rigid body - twist position, Figure 5.1F
$\mathcal{S}_4$ - transition - left arm moves up
$\mathcal{S}_5$ - rigid body - layout position, Figure 5.1A.

Let τ_k denote the time spent in stage $\mathcal{S}_k$. For convenience we use a relative time t in each individual stage that measures the time elapsed from the beginning of $\mathcal{S}_k$, and not the absolute time from the moment of take-off. A quick reminder: The symbols denoting tensor of inertia, angular momentum, and angular velocity in the central-body-frame $\mathcal{F}_C$ are given by I, $\boldsymbol{L}$, and $\boldsymbol{\Omega}$, respectively, and in the principal-axes-frame $\mathcal{F}_B$ they are given by J, $\boldsymbol{M}$, and $\boldsymbol{\mathcal{W}}$, respectively. The angular momentum and angular velocity in either frame are always assumed to be functions of t, but unless specifically evaluating at a certain time we will always suppress the argument. In our notation we use subscript $k \in \{1, \dots, 5\}$ to denote vector quantities in $\mathcal{S}_k$, but when writing out the components explicitly, e.g. $\boldsymbol{L}_1 = (L_x, L_y, L_z)^t$ we use subscript $\{x, y, z\}$ to distinguish the components and omit the stage number to prevent clutter. In order to avoid confusion, we will cover each stage separately in different subsections.

The diver uses two key shapes to perform pure and twisting somersaults, given by the layout and twist positions, respectively. To distinguish between quantities written in these two shapes, the superscripts s and t will be used to represent somersault and twisting somersault. We denote the period of pure somersault as ${}^sT$, and the period of twist in the twisting somersault as ${}^tT$. The tensor of inertia $I(\alpha)$ given by (3.45) is a function of shape, and in the layout position we write

$$\begin{aligned} {}^sI &= \operatorname{diag}({}^sI_x, {}^sI_y, {}^sI_z) = I(\pi) \\ &= \operatorname{diag}(21.3188, 20.6091, 0.9956). \end{aligned} \tag{5.1}$$

During shape change the tensor of inertia $I(\alpha)$ is non-diagonal (because the axes of central-body-frame $\mathcal{F}_C$ are always aligned with the torso), so we move to the principal-axes-frame $\mathcal{F}_B$ where it is diagonal and denoted by $J(\alpha)$, see (2.12). The

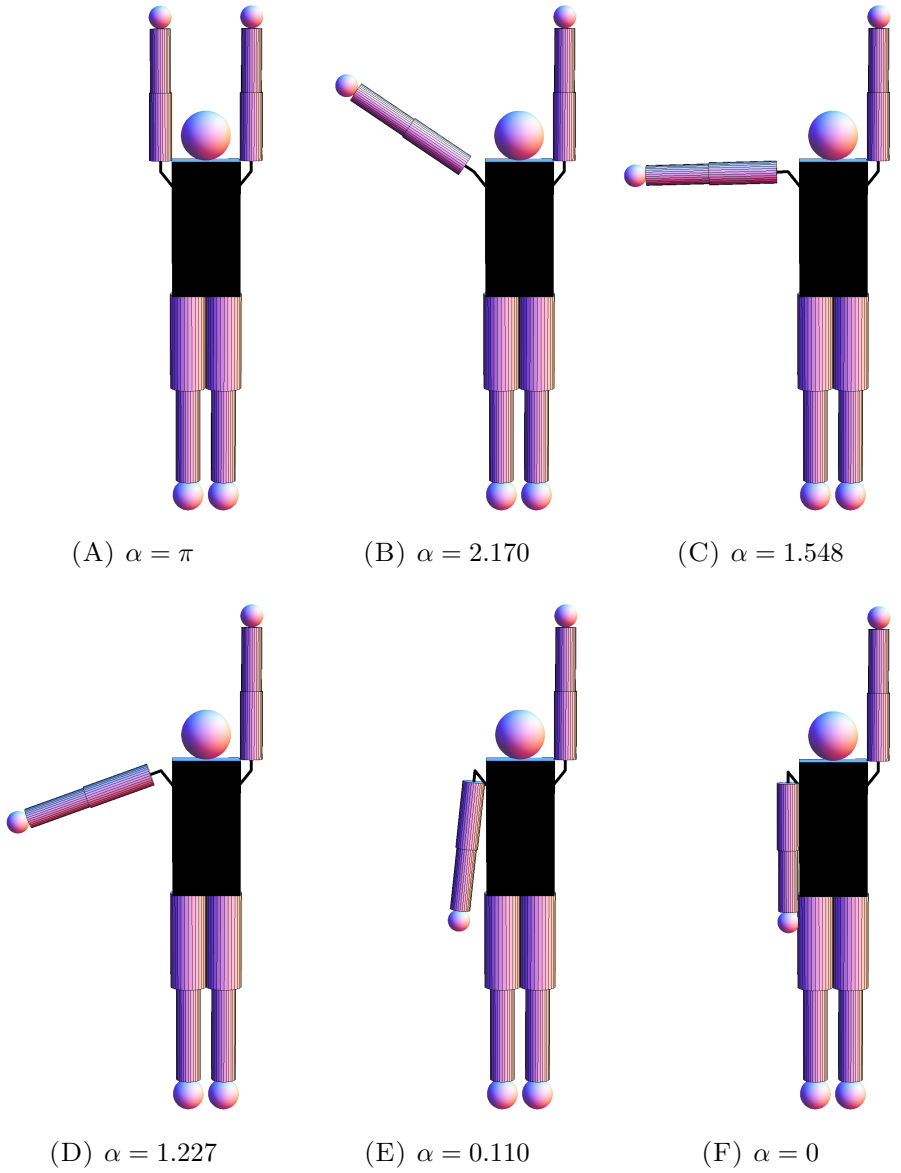

(A) $\alpha = \pi$ (B) $\alpha = 2.170$ (C) $\alpha = 1.548$

(D) $\alpha = 1.227$ (E) $\alpha = 0.110$ (F) $\alpha = 0$

Figure 5.1. The athlete lowers ($\alpha : \pi \to 0$) or raises ($\alpha : 0 \to \pi$) the left arm. A single angle $\alpha \in [0, \pi]$ determines the shape of the athlete and we illustrate some examples here.

two frames can be aligned by a rotation through ξ about the x-axis. The angle ξ given by (2.16) is shape dependent, and we plot the angle ξ as a function of α in Figure 5.2. When the diver is in the twist position the angle $\xi(0)$ is needed to convert between the two frames, and since this angle is important we will for

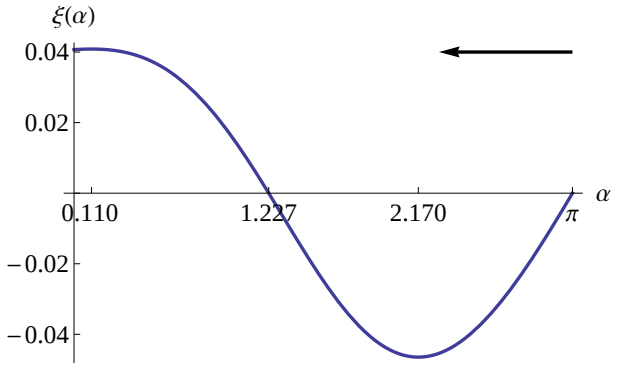

FIGURE 5.2. The difference between $\mathcal{F}_B$ and $\mathcal{F}_C$ is given by a rotation about the x-axis by amount $\xi(\alpha)$ (the transformation formula along with others is shown in (2.23)). From layout position to twist position the shape change is $\alpha = \pi \to 0$. The critical points of ξ occur at $(0.110, 0.0409)$ and $(2.170, -0.0465)$, and the roots of ξ are at $\alpha = 1.227$ and $\alpha = \pi$. These four points correspond to shapes shown in Figure 5.1E, Figure 5.1B, Figure 5.1D and Figure 5.1A, respectively.

simplicity define

$$\mathcal{P} = \xi(0) = 0.0407. \tag{5.2}$$

This enables us to write

$$\begin{aligned} {}^tJ &= \operatorname{diag}({}^tJ_x, {}^tJ_y, {}^tJ_z) = R_x^{-1}(\mathcal{P}) I(0) R_x(\mathcal{P}) \\ &= \operatorname{diag}(18.3745, 17.6925, 0.9679) \end{aligned} \tag{5.3}$$

as the tensor of inertia in $\mathcal{F}_B$ for the twist position.

We now describe the stages in more detail. The athlete takes off the platform or springboard in $\mathcal{S}_1$ with a prescribed vertical velocity v_0 and angular velocity $\boldsymbol{\Omega}_1(0)$ in the layout position, see Figure 5.1A. Since the angular velocity $\boldsymbol{\Omega}_1$ is about a principal axis of inertia, this corresponds to a steady rotation with constant angular momentum $\boldsymbol{L}_1$, and so the athlete simply somersaults without twist. The angular momentum vector in $\mathcal{F}_S$ is determined at take-off and remains constant throughout the dive, so we write $\boldsymbol{l} = (0, l, 0)^t$.

The athlete performs a shape change in $\mathcal{S}_2$ to move into twist position, as shown by the sequence of diagrams in Figure 5.1. The arm movement induces a counter rotation of the rest of the body causing tilt, which initiates the twisting somersault phase of the dive.

In $\mathcal{S}_3$ the athlete is in rigid body motion performing twisting somersaults. To make the twisting somersault easier to analyse we work in $\mathcal{F}_B$ where the tensor of inertia ${}^tJ$ given by (5.3) is diagonal. The precise amount of time τ_3 that the athlete

stays in $\mathcal{S}_3$ plays a critical role in the entire dive, as it ensures the correct number of twists is achieved before the athlete reverts back into pure somersaulting motion.

The athlete performs another shape change in $\mathcal{S}_4$ to get back into layout position, and with the correct choice of τ_3 in $\mathcal{S}_3$ the twisting motion terminates. Finally, in $\mathcal{S}_5$ the athlete is back in pure somersaulting motion and the time τ_5 is determined to ensure the athlete enters the pool correctly with head-first entry into water. In summary, we use τ_3 to control the twist quantity, and $\tau_1 + \tau_5$ to control the somersault quantity.

The airborne time T_{air} of the dive comprises the sum of the time spent in each of the five stages, i.e.

$$T_{air} = \tau_1 + \tau_2 + \tau_3 + \tau_4 + \tau_5, \tag{5.4}$$

where the athlete is able to control the airborne time to a certain extent by adjusting their vertical velocity at take-off. Suppose we are interested in divers performing off the 10m platform, then by estimating the appropriate limits for the take-off vertical velocity v_0 we are able to find bounds so that $T_{min} \leq T_{air} \leq T_{max}$. To get T_{min} we can safely assume $v_0 = 0$, and substituting in (1.1) gives $T_{min} \approx 1.4$. The maximum v_0 is more difficult to determine, so we estimate v_0 in the high jump world record instead (which is 2.45 metres set by Javier Sotomayor of Cuba on 27 July 1993 in Salamanca, Spain) and take it as the maximum for the diver. With our model, an athlete standing in the anatomical neutral position has centre of mass located approximately 57.66% of their natural height, so applying this percentage to Sotomayor (who is 1.95 metres tall) yields 1.12 metres off the ground. Taking a rough estimate of $h = 2.45 - 1.12 = 1.33$, where h represents the difference in height Sotomayor needs to produce in order to clear the bar successfully, we find using standard projectile motion that $v_0 = \sqrt{2gh} \approx 5.1$. Plugging this in (1.1) shows that $T_{max} \approx 2$, so we get the bounds

$$1.4 \leq T_{air} \leq 2. \tag{5.5}$$

Typically we expect $T_{air} \approx 1.6$ as observed from past Olympic Games for the 10m platform, but by adjusting v_0 the athlete is actually able to alter the airborne time T_{air} slightly, up to the bounds provided.

5.2 Numerical Simulation

We begin with the numerical simulation of the dive proposed. The equations of motion (3.1) and equations of orientation (3.2) are non-linear, and as there are no known analytical solutions when I and $\boldsymbol{A}$ are not constant we resort to numerical solutions. To compute the numerics we first set the angular momentum to a reasonable

$$l = 100, \tag{5.6}$$

and find the necessary parameters τ_k for $k \in \{1, \ldots, 5\}$ by brute force to ensure the dive works. The computation is then repeated for every other integer $l \in [80, 140]$, and using the tabulated results we find a curve of best fit for each τ_k in terms of l in order to obtain empirical formulas.

5.2.1 $\mathcal{S}_1$: Initiate Somersault

For simplicity we shall remove $\mathcal{S}_1$ altogether in the numerical simulation by setting

$$\tau_1 = 0. \tag{5.7}$$

As the dynamics of $\mathcal{S}_1$ and $\mathcal{S}_5$ are the same, we concentrate on the athlete performing pure somersaults without twist in $\mathcal{S}_5$. Later on in the analytical approximation using fast-kicks, we show that provided $\tau_1 + \tau_5$ is constant, we can distribute τ_1 and τ_5 however way we like and still obtain a dive with m somersaults and n twists.

As nothing occurs in $\mathcal{S}_1$, the initial condition defined for $\mathcal{S}_1$ corresponds to the initial condition of $\mathcal{S}_2$. The athlete takes off the platform or springboard vertically in the layout position, and with our choice of $\mathcal{F}_C$ we set

$$\begin{aligned} \boldsymbol{L}_2(0) &= \boldsymbol{L}_1(0) = (0, 100, 0)^t \\ \boldsymbol{q}_2(0) &= \boldsymbol{q}_1(0) = (1, 0, 0, 0)^t. \end{aligned} \tag{5.8}$$

5.2.2 $\mathcal{S}_2$: Initiate Twist

In $\mathcal{S}_2$ the athlete makes a transition from the layout position to twist position, see the sequence of diagrams from Figure 5.1A to Figure 5.1F. We want the angular velocity of the arm to be C^1 (once differentiable) for the arm movement to appear smooth. This can be achieved through the use of a cubic spline, where the velocities at the endpoints of the time interval are zero. The shape change is then

$$\alpha_2(t) = \frac{\pi}{\tau_2^3} (\tau_2 - t)^2 (\tau_2 + 2t), \tag{5.9}$$

where we select the transition time for our numerical study to be

$$\tau_2 = 0.25, \tag{5.10}$$

as athletes cannot be expected to perform this arm motion any faster.

To obtain the angular momentum $\boldsymbol{L}_2$ and quaternion $\boldsymbol{q}_2$, we solve the equations of motion (3.1) and equations of orientation (3.2) numerically by substituting $\alpha_2(t)$ given by (5.9) and its derivative, l given by (5.6), τ_2 given by (5.10), and use the initial conditions given by (5.8). The results are shown in Figure 5.3.

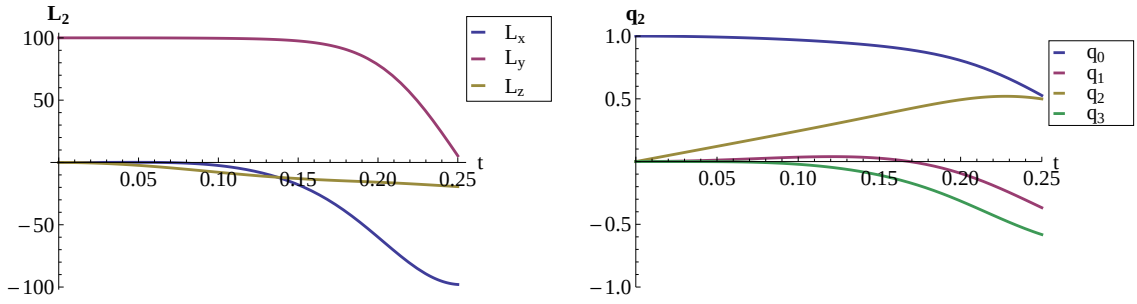

(A) $\boldsymbol{L}_2 = (L_x, L_y, L_z)^t$. (B) $\boldsymbol{q}_2 = (q_0, q_1, q_2, q_3)^t$.

FIGURE 5.3. Angular momentum $\boldsymbol{L}_2$ and quaternion $\boldsymbol{q}_2$ in $\mathcal{S}_2$.

To obtain the kinetic energy E_2 we use (2.54), and since the energy is frame invariant we do the calculation in $\mathcal{F}_C$, giving

$$E_2 = \frac{1}{2}\boldsymbol{\Omega}_2^t I(\alpha_2)\boldsymbol{\Omega}_2 = \frac{1}{2}\big(\boldsymbol{L}_2 - \boldsymbol{A}(\alpha_2, \dot{\alpha}_2)\big)^t I^{-1}(\alpha_2)\big(\boldsymbol{L}_2 - \boldsymbol{A}(\alpha_2, \dot{\alpha}_2)\big). \tag{5.11}$$

The energy E_2 is different from the rigid body case because $\boldsymbol{\Omega}_2$ is given by (3.24). Using the traditonal (2.56) instead gives

$$\tilde{E}_2 = \frac{1}{2}\boldsymbol{L}_2^t I^{-1}(\alpha_2)\boldsymbol{L}_2, \tag{5.12}$$

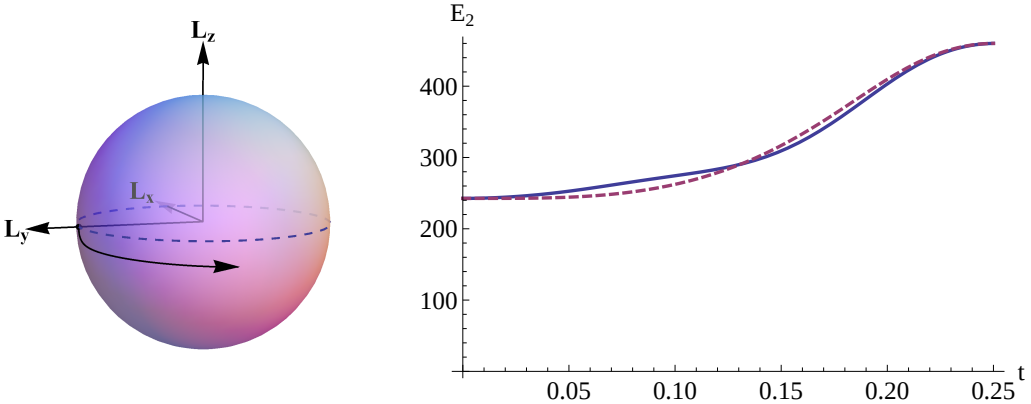

(A) $\boldsymbol{L}_2$ on L-sphere. (B) E_2 given by the solid curve and $\tilde{E}_2$ by the dashed curve.

FIGURE 5.4. The left pane shows the trajectory of $\boldsymbol{L}_2$, and the right pane shows E_2 and $\tilde{E}_2$ during the shape change.

which can be interpreted as the energy ignoring the contributions from the shape change. Although E_2 and $\tilde{E}_2$ are different during shape change, they are equal at the end points, i.e.

$$E_1 = E_2(0) = \tilde{E}_2(0) = 242.612$$
$$E_3 = E_2(\tau_2) = \tilde{E}_2(\tau_2) = 460.012 \tag{5.13}$$

because $\boldsymbol{A}(\alpha_2, \dot{\alpha}_2)$ vanishes as $\dot{\alpha}_2 \to 0$.

5.2.3 $\mathcal{S}_3$: Twisting Somersault

The athlete holds twist position to remain in twisting somersaulting motion. The initial conditions with $l = 100$ set in (5.6) are

$$\boldsymbol{L}_3(0) = \boldsymbol{L}_2(\tau_2) = (-97.957, 5.328, -19.393)^t \tag{5.14}$$
$$\boldsymbol{q}_3(0) = \boldsymbol{q}_2(\tau_2) = (0.527, -0.367, 0.499, -0.582)^t.$$

Solving the equations of motion (3.1) and equations of orientation (3.2) numerically gives the orbit $\boldsymbol{L}_3$ and $\boldsymbol{q}_3$, which are plotted in Figure 5.5. The intersection of the L-sphere and energy-inertia ellipsoid is shown in Figure 5.6, where the energy-inertia ellipsoid in $\mathcal{S}_3$ is different from the one in $\mathcal{S}_1$ because the moments of inertia, principal axes of inertia, and energy have all changed.

The period of twist ${}^tT$ in the twisting somersault is determined by (2.65), so substituting in the parameters (5.3), (5.6), and (5.13), we find

$${}^tT = T\big(E_3/l^2, {}^tJ\big) = 0.3325. \tag{5.15}$$

In principle there is an analytical solution for $\boldsymbol{L}_3$ given by

$$\boldsymbol{L}_3 = l R_x(\mathcal{P}) \boldsymbol{\mathcal{M}}(t; E_3/l^2, {}^tJ) \tag{5.16}$$

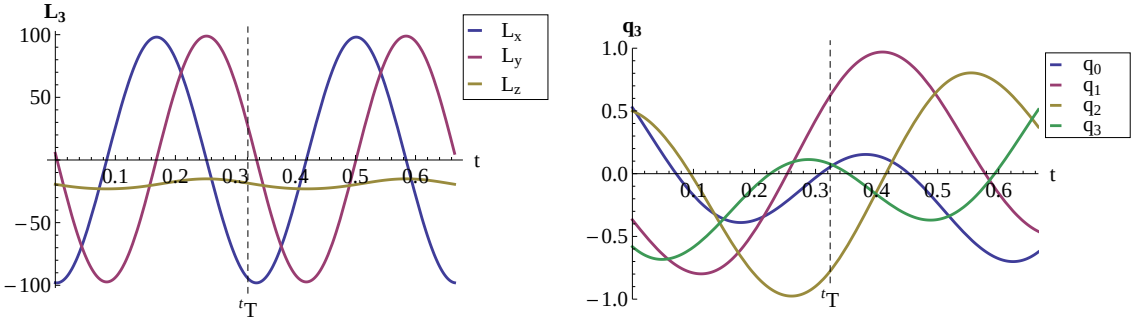

(A) $\boldsymbol{L}_3 = (L_x, L_y, L_z)^t$. (B) $\boldsymbol{q}_3 = (q_0, q_1, q_2, q_3)^t$.

FIGURE 5.5. We only show the solution curves for $n = 2$ periods of twist to avoid clutter.

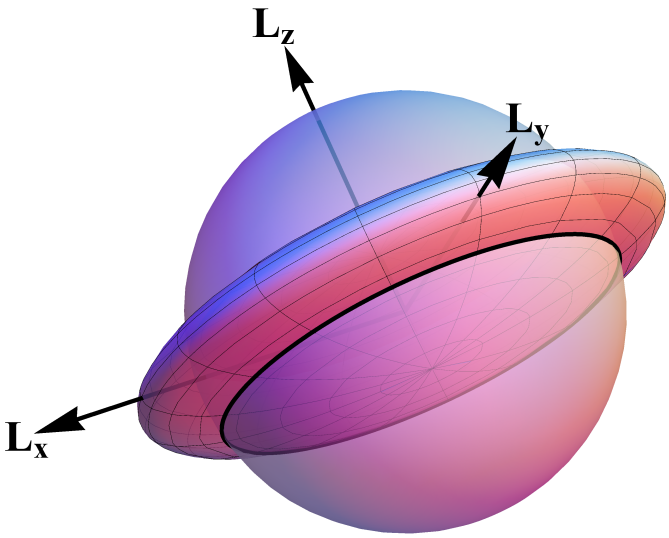

Figure 5.6. L-sphere and energy-inertia ellipsoid intersection. The closed bold black curve is the orbit $\boldsymbol{L}_3$.

with direction $s = 1$ and phase shift $c = 0.1638$, where $\mathcal{M}(t; \mathcal{E}, J)$ is defined in (2.62). However, since the phase shift c has to be determined numerically anyways, there is little to gain by using this analytical solution.

5.2.4 $\mathcal{S}_4$: Terminate Twist

The athlete now transitions back into the layout position by performing another shape change. Because of symmetry we may set

$$\tau_4 = \tau_2 \qquad \alpha_4(t) = \alpha_2(\tau_2 - t), \tag{5.17}$$

where $\alpha_2(t)$ is given by (5.9) back in $\mathcal{S}_2$.

The amount of time τ_3 spent in $\mathcal{S}_3$ needs to be just right in order for the athlete to get back into pure somersaulting motion for $\mathcal{S}_5$. If the athlete executes the shape change at the incorrect time the twisting motion will not stop because the L_x and L_z components remain non-zero as shown in Figure 5.7A and 5.7B; the athlete will only somersault without twist if the shape change is performed at the right time as shown in Figure 5.7C. We find by brute force that $\tau_3 = 0.1711$ for $n = 1$ twist stops the twisting motion in $\mathcal{S}_5$, and because $\boldsymbol{L}_3$ is periodic with time ${}^tT$ we can generalise the result to

$$\begin{aligned} \tau_3 &= (n-1)\,{}^tT + 0.1711 \\ &= n\,{}^tT - 0.1614 \quad \text{for } n \in \mathbb{N} \setminus \{0\}. \end{aligned} \tag{5.18}$$

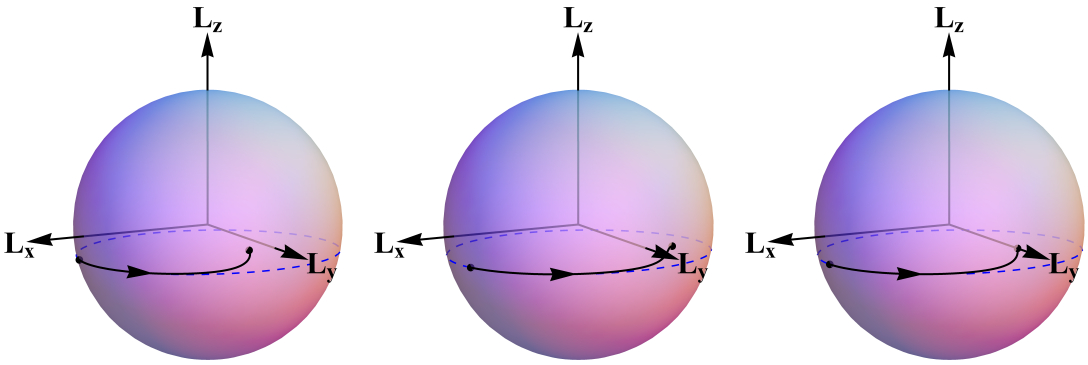

(A) Too early. (B) Too late. (C) Just right.

FIGURE 5.7. Performing the shape change in $\mathcal{S}_4$ after different τ_3 time spent in $\mathcal{S}_3$.

The choice of n does not affect the initial angular momentum as $\boldsymbol{L}_3$ is periodic, but after each twist the athlete somersaults by

$$\phi_s = 1.8448 \text{ radians}, \tag{5.19}$$

so the orientation given by $\boldsymbol{q}_4(0;n)$ will depend on the number of twists. The initial conditions in $\mathcal{S}_4$ are then

$$\begin{aligned} \boldsymbol{L}_4(0) &= \boldsymbol{L}_3(\tau_3) = (97.957, 5.328, -19.393)^t \\ \boldsymbol{q}_4(0;n) &= \boldsymbol{q}_3(\tau_3) = \boldsymbol{p}^n \boldsymbol{q}_4(0;1), \end{aligned} \tag{5.20}$$

where $\boldsymbol{q}_4(0;n)$ is computed with quaternion multiplication, see (2.36). Using (2.90) to convert (5.19) into the quaternion equivalent gives

$$\boldsymbol{p} = (0.604, 0, 0.797, 0)^t, \tag{5.21}$$

and $\boldsymbol{q}_4(0;1) = (-0.388, -0.642, -0.613, -0.248)^t$. The numerical solutions for $\boldsymbol{L}_4$ and $\boldsymbol{q}_4(t;n)$ can then be found as usual by solving the equations of motion (3.1) and equations of orientation (3.2), respectively, and we plot the results in Figure 5.8. For $n = 1$ and $n = 2$ the initial condition can be read off Figure 5.5B by looking at the values when $t = {}^tT$ and $t = 2\,{}^tT$, respectively. By direct comparison of Figure 5.8A and Figure 5.3A we see that

$$\boldsymbol{L}_4(t) = \operatorname{diag}(-1, 1, 1)\boldsymbol{L}_2(\tau_2 - t), \tag{5.22}$$

which we numerically checked to be accurate up to $\mathcal{O}(10^{-6})$. Since $\boldsymbol{A}$ is linear in the shape velocity and non-zero only in the first component, we can write

$$\boldsymbol{A}(\alpha_4(t), \dot{\alpha}_4(t)) = \operatorname{diag}(-1, 1, 1)\boldsymbol{A}(\alpha_2(\tau_2 - t), \dot{\alpha}_2(\tau_2 - t)). \tag{5.23}$$

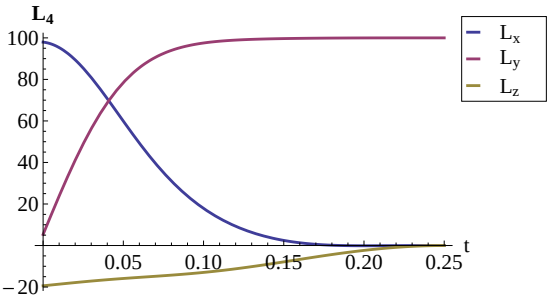

(A) Initial condition $\boldsymbol{L}_4(0) = (97.957, 5.328, -19.393)^t$ is independent of n.

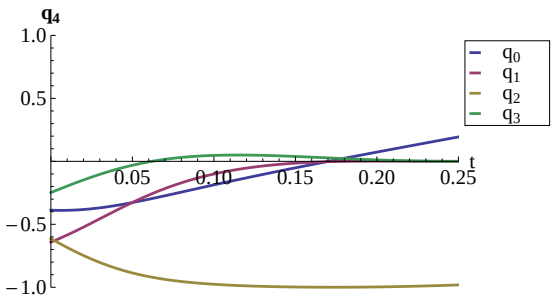

(B) Initial condition $\boldsymbol{q}_4(0;1) = (-0.388, -0.642, -0.613, -0.248)^t$.

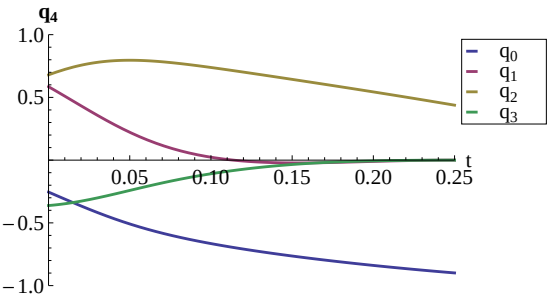

(C) Initial condition $\boldsymbol{q}_4(0;2) = (-0.255, 0.585, 0.680, -0.362)^t$.

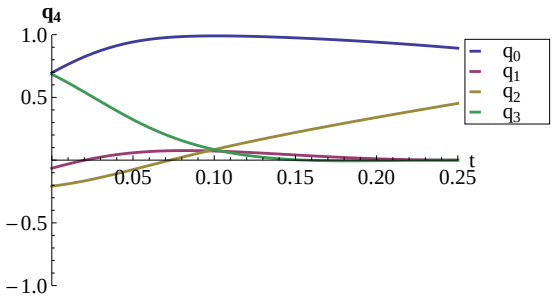

(D) Initial condition $\boldsymbol{q}_4(0;3) = (0.695, -0.065, -0.207, 0.685)^t$.

FIGURE 5.8. The solution curves for $\boldsymbol{L}_4$ and $\boldsymbol{q}_4(t;n)$ for $n = 1, 2, 3$.

Due to the form of I^{-1} (which is the same as I shown in (3.45)), the -1 appearing in the argument of diag cancels when substituting in (5.11), so we get

$$E_4(t) = E_2(\tau_2 - t) \tag{5.24}$$

meaning the energy $E_4(t)$ is just the reverse of $E_2(t)$ shown in Figure 5.4B.

5.2.5 $\mathcal{S}_5$: Terminate Somersault

Due to the correct timing of the shape change in (5.18), we get a steady rotation about the somersault axis for the athlete to complete the dive up to numerical error. The L_x and L_z components never completely vanish in the numerical computation though, and because this equilibrium is unstable the solution will eventually escape from the neighbourhood of the steady rotation as shown in Figure 5.9. From the

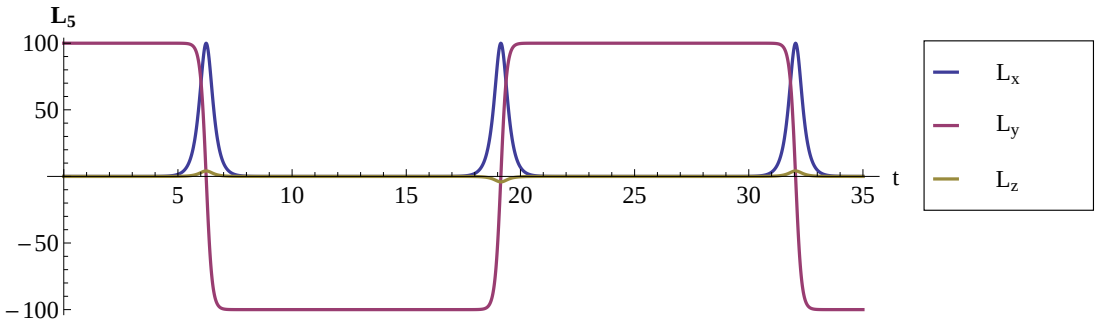

FIGURE 5.9. Eventual escape from the unstable somersaulting. The athlete alternates between the forward and backward somersault with a quick half-twist transition in between. The duration the athlete remains in each motion depends on the accuracy and perturbation of $\boldsymbol{L}_5(0)$, and we find that with our precision ('WorkingPrecision' set to 25 in Mathematica 8) the duration in steady somersault before the first half-twist far exceeds and the total time of any realistic dive.

numerical computation the initial conditions in $\mathcal{S}_5$ have structure

$$\begin{aligned}\boldsymbol{L}_5(0) &= \left(\mathcal{O}(10^{-9}), 100 - \mathcal{O}(10^{-11}), \mathcal{O}(10^{-10})\right)^t \\ \boldsymbol{q}_5(0;n) &= \left(\ *\ , \mathcal{O}(10^{-11}),\ *\ , \mathcal{O}(10^{-12})\right)^t,\end{aligned}$$

where such small terms are due to numerical errors. Nevertheless, taking the results and dropping the small terms give

$$\boldsymbol{L}_5(0) = (0, 100, 0)^t \qquad\qquad \boldsymbol{q}_5(0;n) = \boldsymbol{p}^n \boldsymbol{q}_5(0;1), \tag{5.25}$$

where $\boldsymbol{q}_5(0;1) = (0.194, 0, -0.981, 0)^t$ and $\boldsymbol{p}$ is given by (5.21). To ensure the diver finishes the dive with head-first entry into the pool, we need to find τ_5 so that

$$\boldsymbol{q}_5(\tau_5;n) = (0, 0, \pm 1, 0)^t, \tag{5.26}$$

where there are two possible quaternions due to the double covering of quaternions to $SO(3)$. In the case of m somersaults with n twists, we find

$$\begin{aligned}\tau_5 &= -n\mathcal{T}\,{}^tT + 1.5947 + (m - 1.5)\,{}^sT \\ &= m\,{}^sT - n\mathcal{T}\,{}^tT - 0.3476,\end{aligned} \tag{5.27}$$

where

$$\mathcal{T} = 1.14339 \tag{5.28}$$

with ${}^sT$ and ${}^tT$ given by (5.34) and (5.15), respectively. For it to be a valid dive m and n have to be chosen so that $\tau_5 > 0$. In the case of $m = 1.5$ somersaults only $n = 1, 2, 3, 4$ twists are valid, and we plot the results in Figure 5.10.

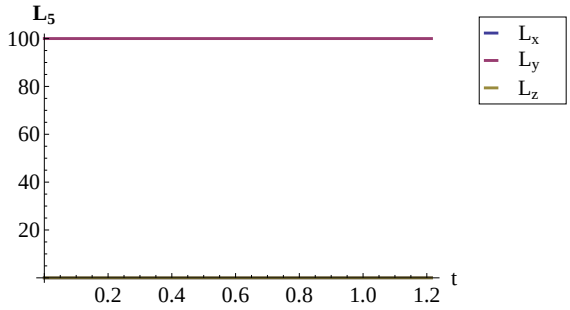

(A) Solution curves for $\boldsymbol{L}_5(t)$.

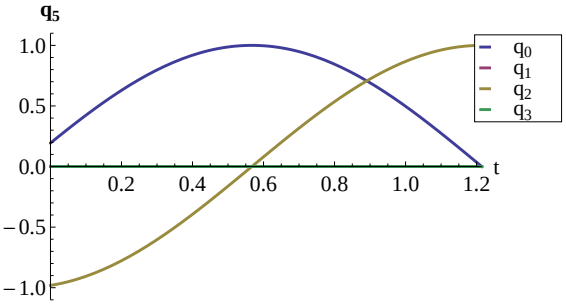

(B) Solution curves for $\boldsymbol{q}_5(t;1)$.

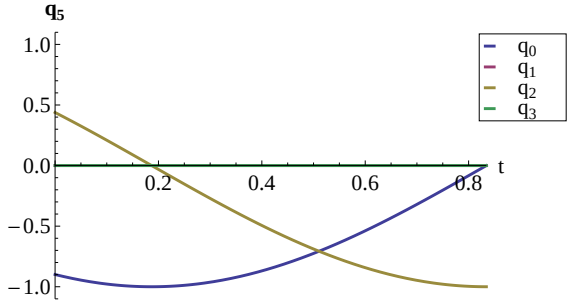

(C) Solution curves for $\boldsymbol{q}_5(t;2)$.

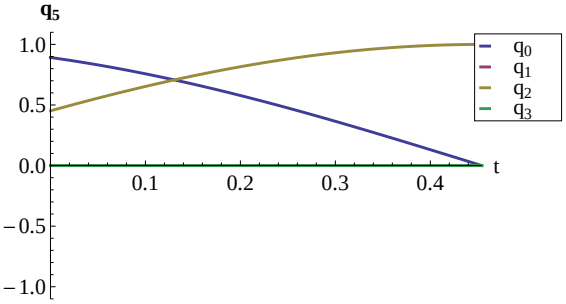

(D) Solution curves for $\boldsymbol{q}_5(t;3)$.

FIGURE 5.10. The solution curves of $\boldsymbol{q}_5(t;n)$ are shown for the case of $m = 1.5$ somersaults with $n = 1$, $n = 2$, and $n = 3$ twists.

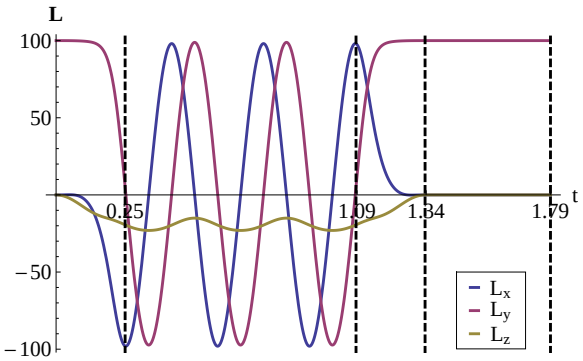

(A) Trajectory of $\boldsymbol{L}$.

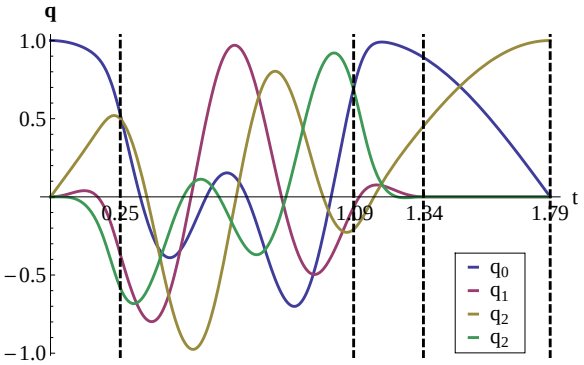

(B) Trajectory of $\boldsymbol{q}$.

FIGURE 5.11. Time evolution of the 5136D dive. The stages $\mathcal{S}_2$ to $\mathcal{S}_5$ are separated by vertical dashed lines.

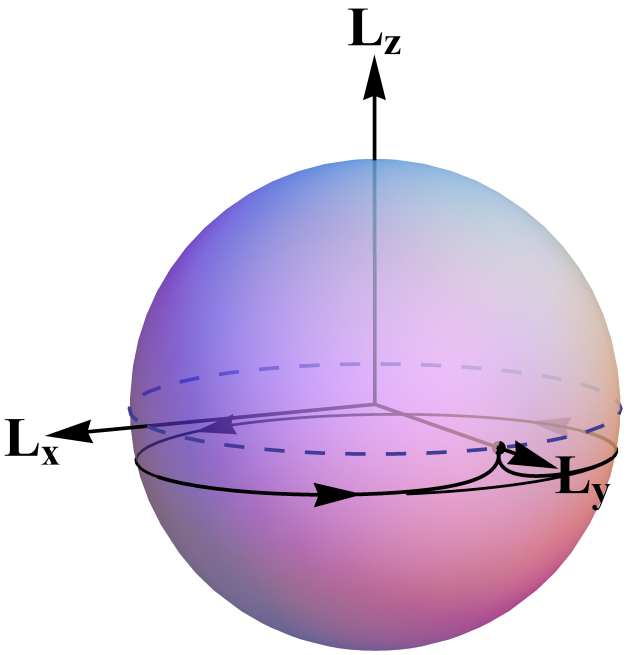

Figure 5.12. The 5136D dive on the L-sphere. The equator is represented by the dashed line. Three revolutions are made around the L-sphere corresponding to the three twists.

Combining all the stages together, we show the components of $\boldsymbol{L}$ and $\boldsymbol{q}$ for a 5136D dive (forward $m = 1.5$ somersaults with $n = 3$ twists) in Figure 5.11, and the complete trajectory of $\boldsymbol{L}$ on the L-sphere in Figure 5.12. Based on the shape changing time of 0.25 seconds and segmental inertias chosen in the model, we were able to obtain up to $n = 4$ twists. However, with different parameters (e.g. the moments of inertia taken from an individual athlete) the $n = 4$ case may not be achievable. Nevertheless, the principles and relationships derived are independent of such particular values, which only limit the range of n.

5.2.6 Changing the Angular Momentum

So far the results for τ_3 given by (5.18) and τ_5 given by (5.27) have specific values for the case $l = 100$. Generalising to arbitrary l they become

$$\tau_3 = n\,{}^tT - T_\psi \qquad\qquad \tau_5 = m\,{}^sT - n\mathcal{T}\,{}^tT - T_\phi, \tag{5.29}$$

where T_ψ and T_ϕ are functions of l, and $\mathcal{T}$ given by (5.28) appears to be constant. We devise the terms 'twist transition' for T_ψ and 'somersault transition' for T_ϕ, as they represent the time needed to be subtracted from $\mathcal{S}_3$ and $\mathcal{S}_5$ due to the twist and somersault obtained during the transition stages $\mathcal{S}_2$ and $\mathcal{S}_4$. The values

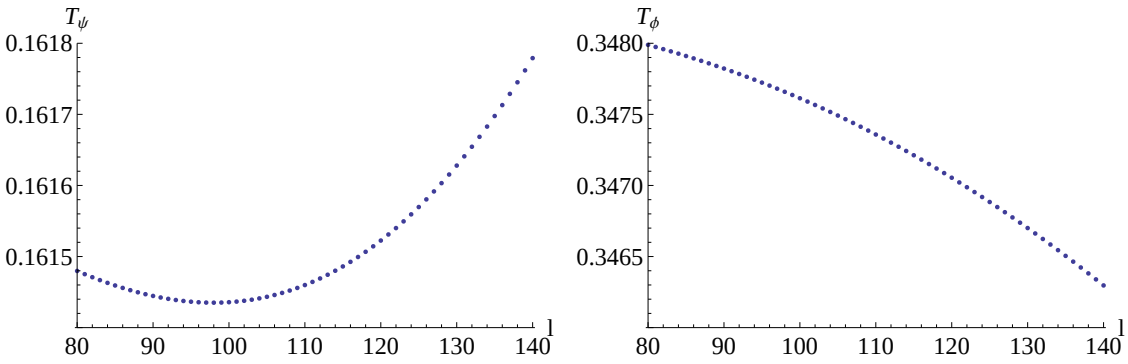

(A) Twist transition. (B) Somersault transition.

FIGURE 5.13. Plot of the tabulated results for T_ψ and T_ϕ.

for each integer $l \in [80, 140]$ are found by repeating the computation in Chapter 5.2 by brute force, and we show the tabulated results in Figure 5.13. These quantities are nearly constant as the dependence on l is small for T_ϕ and T_ψ, so a crude approximation is to set them equal to their mean values (specified by $\bar{T}_\psi$ and $\bar{T}_\phi$, respectively) for integer $l \in [80, 140]$, which in doing so we find

$$T_\psi \approx \bar{T}_\psi = 0.1615 \qquad T_\phi \approx \bar{T}_\phi = 0.3473. \tag{5.30}$$

The actual sum of $T_\psi + T_\phi$ is shown in Figure 5.14, but we see that

$$T_\psi + T_\phi \approx \bar{T}_\psi + \bar{T}_\phi = 0.5088, \tag{5.31}$$

so another approximation we can make is

$$T_\psi + T_\phi \approx \tau_2 + \tau_4 = 0.5. \tag{5.32}$$

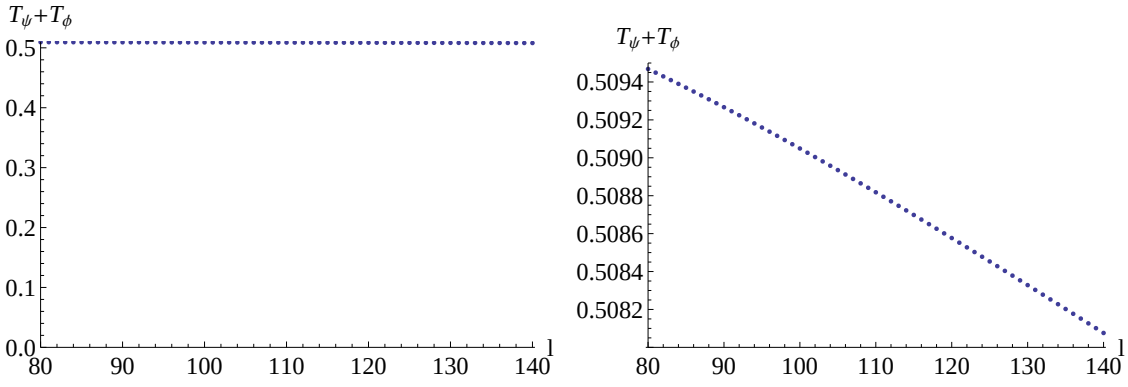

(A) Plot of $T_\psi + T_\phi$. (B) Zoom in of $T_\psi + T_\phi$.

FIGURE 5.14. The sum $T_\psi + T_\phi$ evaluated directly from the tabulated results shown in Figure 5.13.

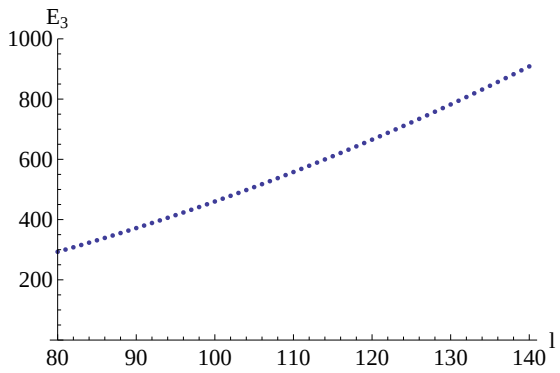

(A) The tabulated kinetic energy E_3.

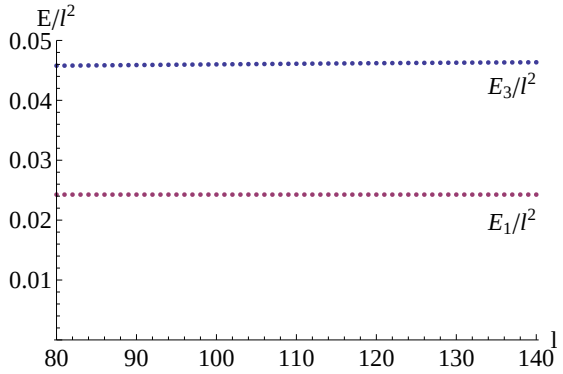

(B) Plot of E_3/l^2 and E_1/l^2 as a function of l.

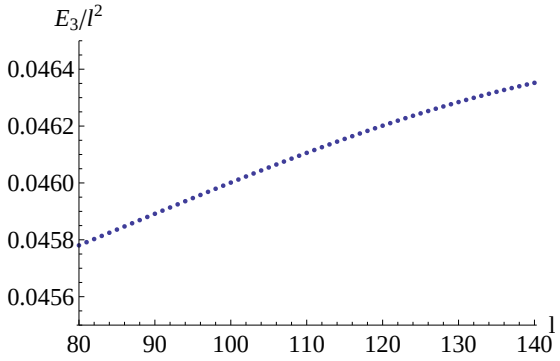

(C) Zoomed in version of E_3/l^2.

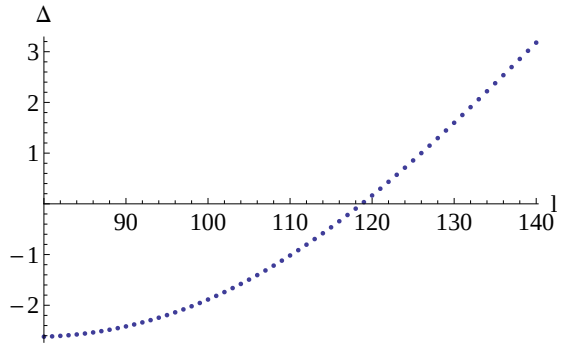

(D) Tabulated $E_3 - 0.04619l^2$ fit.

FIGURE 5.15. As both $\boldsymbol{L}_1$ and ${}^sI$ are analytically known we can use (2.56) to show $E_1/l^2 = \frac{1}{2}{}^sI_y^{-1}$ is constant. To obtain E_3/l^2 we use the numerically found $\boldsymbol{L}_2(\tau_2)$, and substitute $\boldsymbol{M}_2(\tau_2) = R_x^{-1}(\mathcal{P})\boldsymbol{L}_2(\tau_2)$ and ${}^tJ$ into (2.56). We see in Figure 5.15C that E_3/l^2 is nearly constant but not quite, so enforcing a l^2 fit for E_3 reveals a small difference given by Δ, which is shown in Figure 5.15D.

The analytical formula for ${}^tT$ given by (2.65) is precise, but sometimes a simpler approximation that is inversely proportional to l will suffice, especially if the energy cannot be obtained analytically to begin with (we numerically tabulate and show the energy E_3 in Figure 5.15), so forcing such a fit for ${}^tT$ gives

$$ {}^tT \approx \frac{33.2218}{l}. \tag{5.33}$$

This approximate formula is accurate to $\mathcal{O}(10^{-3})$ for any $l \in [80, 140]$, which is usually sufficient. The period of pure somersault ${}^sT$ in $\mathcal{S}_5$ is simple since it is a steady rotation, so using (2.52) without resorting to any approximations we can

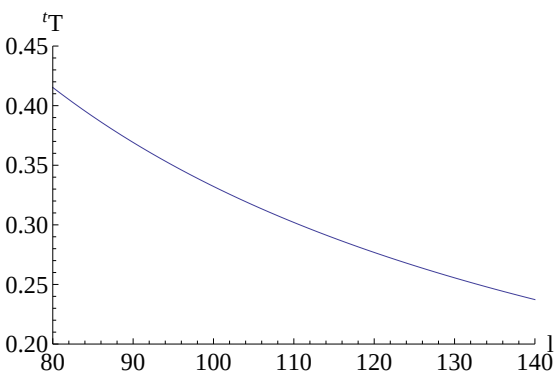

(A) Approximate ${}^tT$ when fitted to be inversely proportional to l.

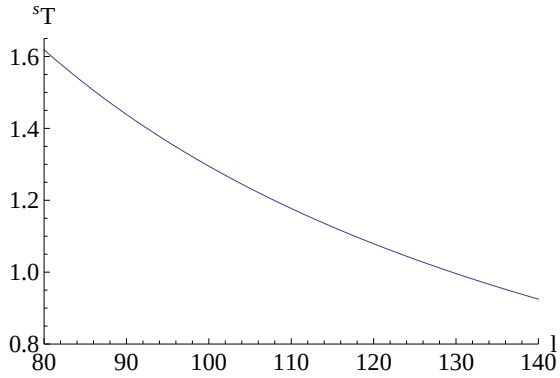

(B) The period of pure somersault ${}^sT$ as a function of l.

FIGURE 5.16. The approximate period of twist ${}^tT$ in the twisting somersault and period of pure somersault ${}^sT$.

show

$$ {}^sT = \frac{2\pi\, {}^sI_y}{l} = \frac{129.490}{l}. \tag{5.34}$$

We plot the approximate ${}^tT$ given by (5.33) in Figure 5.16A, and ${}^sT$ given by (5.34) in Figure 5.16B. The formulas for τ_3 and τ_5 given by (5.29) require T_ψ and T_ϕ, which can be taken directly from the tabulated results for each integer

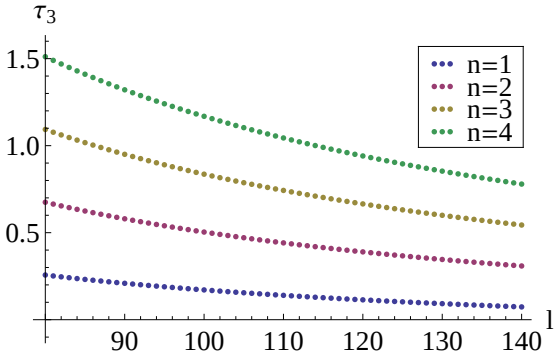

(A) Time τ_3 spent in $\mathcal{S}_3$.

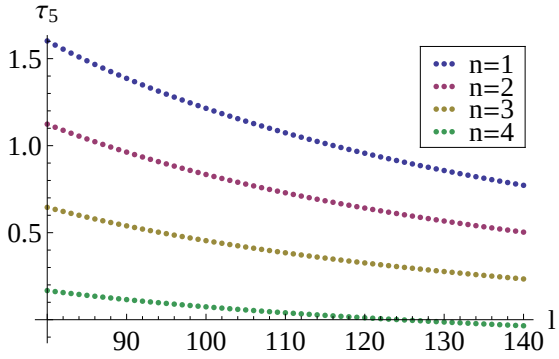

(B) Time τ_5 spent in $\mathcal{S}_5$.

FIGURE 5.17. With $m = 1.5$ somersaults the number of n twists cannot exceed 4 as that corresponds to a negative τ_5, and in the case of $n = 4$ twists the angular momentum l cannot exceed 124 for the very same reason.

τ_3	tabulated T_i/analytic ${}^tT$	mean T_i/approximate ${}^tT$
$n=1$	$34.2082/l-0.1710$	$33.2218/l-0.1615$
$n=2$	$68.3680/l-0.1800$	$66.4436/l-0.1615$
$n=3$	$102.5278/l-0.1890$	$99.6654/l-0.1615$
$n=4$	$136.6876/l-0.1980$	$132.8872/l-0.1615$
τ_5	tabulated T_i/analytic ${}^tT$	mean T_i/approximate ${}^tT$
$n=1$	$154.8671/l-0.3341$	$156.2503/l-0.3473$
$n=2$	$115.8091/l-0.3238$	$118.2648/l-0.3473$
$n=3$	$76.7511/l-0.3135$	$80.2794/l-0.3473$
$n=4$	$37.6932/l-0.3032$	$42.2940/l-0.3473$

TABLE 5.1. The curves listed are in the form of $a/l+b$ with coefficients a and b chosen for best fit.

$l\in[80,140]$ shown in Figure 5.13. In order to minimise any errors we may as well also use the analytical formula for ${}^tT$ given by (2.65). For $m=1.5$ somersaults with arbitrary n twists, the tabulated results for τ_3 and τ_5 are shown in Figure 5.17. The discrete points are then fitted with a curve in the form of $a/l+b$, where the fits are given in Table 5.1 under the 'tabulated T_i/analytic ${}^tT$' column. For comparison we repeat the calculation using mean $\bar{T}_\psi$ and $\bar{T}_\phi$ given by (5.30), use the simpler approximate formula for ${}^tT$ given by (5.33), and list the results under the 'mean T_i/approximate ${}^tT$' column in Table 5.1. The difference between the 'mean T_i/approximate ${}^tT$' and 'tabulated T_i/analytic ${}^tT$' fitted curve is shown in Figure 5.18.

For this dive we have $\tau_1=0$ set in (5.7), $\tau_2=\tau_4=1/4$ from construction shown in (5.10), (5.17), and τ_3, τ_5 given by (5.29). So we can now find the airborne time T_{air} given by (5.4), using the approximation given by (5.32) we get

$$\begin{aligned} T_{air} &= m\,{}^sT-n(\mathfrak{T}-1)\,{}^tT-(T_\psi+T_\phi)+0.5 \\ &\approx m\,{}^sT-n(\mathfrak{T}-1)\,{}^tT, \end{aligned} \tag{5.35}$$

T_{air}	using (5.36) with $m=1.5$	using directly tabulated τ_3 and τ_5
$n=1$	$189.4721/l$	$188.5473/l$
$n=2$	$184.7085/l$	$183.7836/l$
$n=3$	$179.9448/l$	$179.0200/l$
$n=4$	$175.1812/l$	$174.2563/l$

TABLE 5.2. The differences between the two curves are about $0.925/l$, but since l is large the difference is minute.

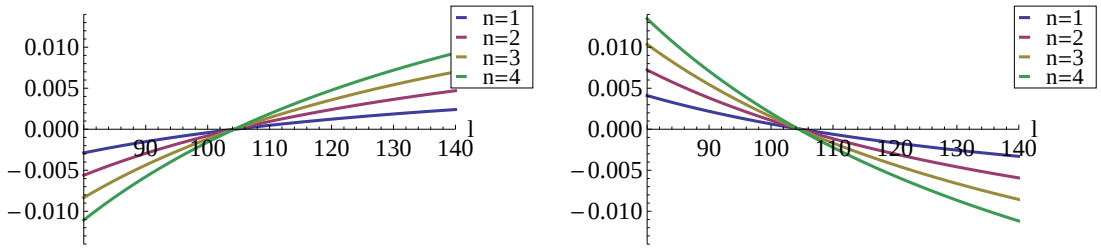

(A) Difference in T_ψ.

(B) Difference in T_ϕ.

FIGURE 5.18. The plots of 'mean T_i/approximate ${}^tT$' minus 'tabulated T_i/analytic ${}^tT$' fitted curves, we see that the difference is mainly $\mathcal{O}(10^{-3})$ except for $n = 4$, where the difference grows to $\mathcal{O}(10^{-2})$.

and substituting ${}^sT$ given by (5.34) and approximate ${}^tT$ given by (5.33) we produce the nice formula

$$T_{air}(l) = \frac{1}{l}\,(129.4905m - 4.7636n) \tag{5.36}$$

which is inversely proportional to l that links the airborne time to the number of somersaults and twists. Alternatively, to be more precise we can use the tabulated results for τ_3 and τ_5 shown in Figure 5.17 for $m = 1.5$ somersaults with n twists, obtain T_{air} directly for each integer $l \in [80, 140]$ without any fitting (as shown in Figure 5.19), and then do an inversely proportional to l fitting afterwards. Doing it this way leads to slightly different fitted curves highlighted in Table 5.2, but the results do not differ by much, meaning the approximations given by (5.32) and (5.33) were decent when used to find T_{air} in (5.36).

5.3 Analytical Approximation: Fast-kick Model

Suppose we have a theoretical athlete who can perform impulsive shape changes in no time, so that $\tau_2 = \tau_4 \to 0^+$, then the angular velocity $\boldsymbol{\Omega}$ given by (3.24) becomes

$$\boldsymbol{\Omega}(\alpha, \dot{\alpha}) = -I^{-1}(\alpha)\boldsymbol{A}(\alpha, \dot{\alpha}) \tag{5.37}$$

during shape change, which we will refer to as a fast-kick. The reduction occurs because $\dot{\alpha} \to \infty$, and since the angular momentum shift $\boldsymbol{A}(\alpha, \dot{\alpha})$ is linear in $\dot{\alpha}$, this makes the contribution from $\boldsymbol{L}$ negligible. The equations of motion (3.25) reduce to a system of linear differential equations where

$$\dot{\boldsymbol{L}} = I^{-1}(\alpha)\boldsymbol{A}(\alpha, \dot{\alpha}) \times \boldsymbol{L}, \tag{5.38}$$

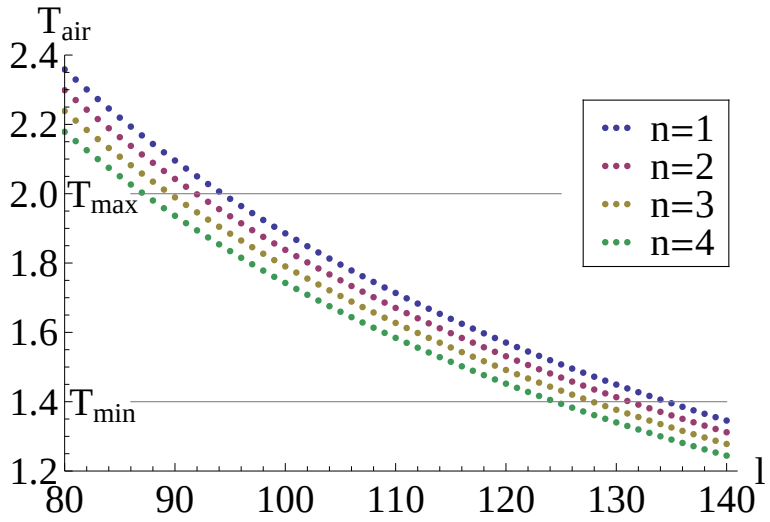

FIGURE 5.19. The tabulated results of T_{air} for $m = 1.5$ somersaults with n twists. The bounds for T_{air} are found in (5.5).

and similarly, the equations of orientation (3.2) also reduce with (5.37). Both of these differential equations can now be solved using Magnus series (see Chapter 2.10). For the one- and two-armed diver we find that only the leading term is non-zero in the series, thus explicit analytical formulas in $\mathcal{S}_2$ and $\mathcal{S}_4$ can be obtained. The pure somersault stages $\mathcal{S}_1$ and $\mathcal{S}_5$ are steady rotations and have simple analytical solutions, which leaves only the twisting somersault stage $\mathcal{S}_3$. Although an analytical solution can be obtained for distinct moments of inertia, they involve non-elementary functions and are complicated (especially for the equations of orientation (3.2)). By making the assumption that two moments of inertia are equal we can utilise the solution provided in (2.50) for the equations of motion, and (2.86) for the equations of orientation, meaning the entire dive can be solved analytically in terms of elementary functions.

5.3.1 $\mathcal{S}_1$: Initiate Somersault

The athlete begins by pure somersaulting in layout position with angular momentum l, and throughout the dive we have $|\boldsymbol{L}_k|^2 = l^2$ for any $k \in \{1, \dots, 5\}$ due to conservation of angular momentum. The initial conditions in $\mathcal{F}_C$ are

$$\boldsymbol{L}_1(0) = (0, l, 0)^t \qquad \boldsymbol{q}_1(0) = (1, 0, 0, 0)^t, \tag{5.39}$$

and since $\mathcal{S}_1$ is a steady rotation they can be easily solved to give

$$\boldsymbol{L}_1 = (0, l, 0)^t \qquad \boldsymbol{q}_1 = \Big(\cos(\Omega_1 t/2), 0, \sin(\Omega_1 t/2), 0\Big)^t, \tag{5.40}$$

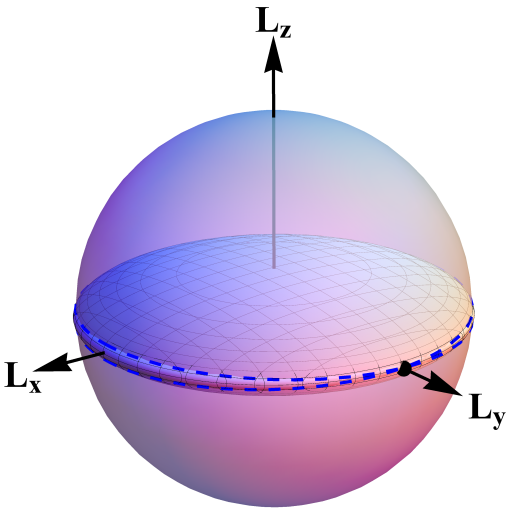

FIGURE 5.20. The steady rotation of $\boldsymbol{L}_1$ corresponds to the point shown on the L_y-axis. We show the L-sphere, energy-inertia ellipsoid, and separatrices given by the blue dashed curves.

where $\Omega_1 = l/{}^sI_y$ is the angular velocity about the somersault axis. During pure somersault the angular velocity vector $\boldsymbol{\Omega}_1 = (0, \Omega_1, 0)^t$ points in the same direction as the middle principal axis of inertia, hence $\boldsymbol{\Omega}_1$ is constant and we only have a single point on the L-sphere shown in Figure 5.20. The quaternion $\boldsymbol{q}_1$ corresponds to a great circle on a three dimensional sphere with period $2\,{}^sT$, where the period of somersault ${}^sT$ is given by (5.34). The period of the great circle is twice that of ${}^sT$ due to the double covering of orientations with quaternions. However, since $\boldsymbol{q}$ and $-\boldsymbol{q}$ represent the same orientation in space, this means in reality the athlete returns to the same orientation in space after every half period.

5.3.2 $\mathcal{S}_2$: Initiate Twist

After τ_1 time is spent in $\mathcal{S}_1$ the athlete performs a fast-kick in $\mathcal{S}_2$ to move into twist position, inducing a tilt of the body which we will now determine. Writing out the components of (5.37) explicitly using I given by (3.45) and $\boldsymbol{A}$ given by (3.38), we obtain

$$\begin{pmatrix} \Omega_x \\ \Omega_y \\ \Omega_z \end{pmatrix} = \begin{pmatrix} -\frac{I_{yy}I_{zz}-I_{yz}^2}{I_{xx}I_{yy}I_{zz}-I_{xx}I_{yz}^2} A_x\dot{\alpha} \\ 0 \\ 0 \end{pmatrix} = \begin{pmatrix} -I_{xx}^{-1} A_x\dot{\alpha} \\ 0 \\ 0 \end{pmatrix}, \tag{5.41}$$

which shows that only the first component Ω_x is non-zero. Using the hat operator denoted by $\widehat{\ }$, we can write

$$\widehat{I^{-1}\boldsymbol{A}} = \Omega_x \begin{pmatrix} 0 & 0 & 0 \\ 0 & 0 & 1 \\ 0 & -1 & 0 \end{pmatrix} \tag{5.42}$$

due to the cross product being a linear transformation, which can be represented as a matrix. The only time dependent component on the RHS of (5.42) is the scalar function Ω_x, where without suppressing the arguments is $\Omega_x\big(\alpha(t), \dot{\alpha}(t)\big)$. The matrix (5.42) commutes with itself for different values of Ω_x, so to solve the reduced equations of motion (5.38) we can use the solution given by (2.76) to write

$$\boldsymbol{L}_2 = \exp\left[\int_0^t \Omega_x\big(\alpha(\tilde{t}), \dot{\alpha}(\tilde{t})\big)\,\mathrm{d}\tilde{t} \begin{pmatrix} 0 & 0 & 0 \\ 0 & 0 & 1 \\ 0 & -1 & 0 \end{pmatrix}\right] \begin{pmatrix} 0 \\ l \\ 0 \end{pmatrix}. \tag{5.43}$$

Performing a substitution enables us to evaluate the integral over the shape angle α rather than time t. Although the shape α is not well-defined for $t \in (0, \tau_2)$, it is defined at the boundary with $\alpha(0) = \pi$ and $\alpha(\tau_2) = 0$. As the dependence on t is completely eliminated the effect of the fast-kick is only α dependent, so for the fast-kick we have

$$\begin{aligned} \mathcal{X} &= \int_0^{\tau_2} \Omega_x\big(\alpha(\tilde{t}), \dot{\alpha}(\tilde{t})\big)\,\mathrm{d}\tilde{t} = -\int_0^{\tau_2} I_{xx}^{-1}(\alpha(\tilde{t}))A_x(\alpha(\tilde{t}))\dot{\alpha}(\tilde{t})\,\mathrm{d}\tilde{t} \\ &= -\int_{\alpha(0)}^{\alpha(\tau_2)} I_{xx}^{-1}(\alpha)A_x(\alpha)\,\mathrm{d}\alpha = -\int_{\pi}^{0} I_{xx}^{-1}(\alpha)A_x(\alpha)\,\mathrm{d}\alpha \\ &= \int_0^{\pi} I_{xx}^{-1}(\alpha)A_x(\alpha)\,\mathrm{d}\alpha. \end{aligned} \tag{5.44}$$

This integral is of the form

$$\int_0^{\pi} \frac{1}{2} - \frac{a_0}{a_1 - a_2\cos\alpha + a_3\sin\alpha}\,\mathrm{d}\alpha, \tag{5.45}$$

where specifically the constants are

$$\begin{aligned} a_0 &= \mathcal{M}(\mathcal{E}_2^2 + \mathcal{E}_3^2 - \mathcal{F}^2) + \frac{1}{2}\left(I_{1_{xx}} - J_{2_x}\right) & a_2 &= 4\mathcal{M}\mathcal{E}_3\mathcal{F} \\ a_1 &= 2\mathcal{M}(\mathcal{E}_2^2 + \mathcal{E}_3^2 + \mathcal{F}^2) + I_{1_{xx}} + J_{2_x} & a_3 &= 4\mathcal{M}\mathcal{E}_2\mathcal{F}. \end{aligned}$$

The numerical values for these symbolic constants are found in (3.45), and evaluating gives

$$a_0 = 9.166 \qquad a_1 = 19.847 \qquad a_2 = 1.472 \qquad a_3 = 0.680.$$

The integral (5.45) can then be integrated using Weierstrass' substitution to obtain

$$\mathcal{X} = \frac{\pi}{2} - \frac{2a_0}{\sqrt{a_1^2 - a_2^2 - a_3^2}} \arctan\left(\frac{\sqrt{a_1^2 - a_2^2 - a_3^2}}{a_3}\right) = 0.1469, \tag{5.46}$$

where the derivation is shown in Appendix H. The change in angular momentum as a result of the fast-kick is

$$\boldsymbol{L}_3(0) = \exp\begin{pmatrix} 0 & 0 & 0 \\ 0 & 0 & \mathcal{X} \\ 0 & -\mathcal{X} & 0 \end{pmatrix} \boldsymbol{L}_2(0) = R_x(-\mathcal{X})\boldsymbol{L}_2(0), \tag{5.47}$$

where $\boldsymbol{L}_2(0)$ and $\boldsymbol{L}_3(0)$ are the angular momentums before and after the fast-kick, respectively. The equations of orientation (3.2) become

$$\dot{\boldsymbol{q}}_2 = \frac{1}{2}\Omega_x\big(\alpha(t), \dot{\alpha}(t)\big) \begin{pmatrix} R_2\left(\pi/2\right) & 0 \\ 0 & R_2\left(-\pi/2\right) \end{pmatrix} \boldsymbol{q}_2, \tag{5.48}$$

where $R_2(\zeta) = \begin{pmatrix} \cos\zeta & -\sin\zeta \\ \sin\zeta & \cos\zeta \end{pmatrix}$ corresponds to the standard 2D rotation matrix. Again, the 4×4 matrix is constant so the solution is

$$\boldsymbol{q}_2 = \exp\left[\frac{1}{2}\int_0^t \Omega_x\big(\alpha(\tilde{t}), \dot{\alpha}(\tilde{t})\big)\,\mathrm{d}\tilde{t} \begin{pmatrix} R_2\left(\pi/2\right) & 0 \\ 0 & R_2\left(-\pi/2\right) \end{pmatrix}\right] \boldsymbol{q}_2(0),$$

and after the fast-kick we have

$$\begin{aligned} \boldsymbol{q}_3(0) &= \exp\left[\frac{1}{2}\mathcal{X} \begin{pmatrix} R_2\left(\pi/2\right) & 0 \\ 0 & R_2\left(-\pi/2\right) \end{pmatrix}\right] \boldsymbol{q}_2(0) \\ &= \begin{pmatrix} R_2\left(\mathcal{X}/2\right) & 0 \\ 0 & R_2\left(-\mathcal{X}/2\right) \end{pmatrix} \boldsymbol{q}_2(0), \end{aligned} \tag{5.49}$$

where

$$\boldsymbol{q}_2(0) = \boldsymbol{q}_1(\tau_1) = \Big(\cos\left(\Omega_1\tau_1/2\right), 0, \sin\left(\Omega_1\tau_1/2\right), 0\Big)^t. \tag{5.50}$$

Previously in Chapter 5.2 we set $\tau_1 = 0$ in order to run the numerical computation, but as this simplification is not required here we will keep τ_1 arbitrary.

The quaternion $\boldsymbol{q}_3(0)$ in (5.49) is expressed as a transformation of the quaternion $\boldsymbol{q}_2(0)$, but if we instead express it as a product of two quaternions then

$$\boldsymbol{q}_3(0) = \underbrace{\begin{pmatrix} \cos\left(\Omega_1\tau_1/2\right) \\ 0 \\ \sin\left(\Omega_1\tau_1/2\right) \\ 0 \end{pmatrix}}_{\boldsymbol{q}_2(0)} \begin{pmatrix} \cos\left(\mathcal{X}/2\right) \\ \sin\left(\mathcal{X}/2\right) \\ 0 \\ 0 \end{pmatrix}.$$

Using (2.38) to rewrite this in terms of rotation matrices, we have

$$R_{\boldsymbol{q}_3}(0) = R_y(\Omega_1\tau_1)R_x(\mathcal{X}), \tag{5.51}$$

which can be interpreted as the athlete somersaulting by $\Omega_1\tau_1$ in $\mathcal{S}_1$ followed by tilting their body by $\mathcal{X}$ in $\mathcal{S}_2$. The rotation matrices are written from left to right, as the rotations are intrinsic as explained in Chapter 2.6.

5.3.3 $\mathcal{S}_3$: Twisting Somersault

The athlete holds twist position in $\mathcal{S}_3$ to perform twisting somersaults, and due to the asymmetry of the body we want to work in $\mathcal{F}_B$ where the tensor of inertia ${}^tJ$ given by (5.3) is diagonal. In the components we see ${}^tJ_x$ is larger than ${}^tJ_y$ by less than 4% and ${}^tJ_y$ is over 18 times greater than ${}^tJ_z$, so we make the assumption

$$ {}^tJ = \text{diag}({}^tJ_x = {}^tJ_y, {}^tJ_y, {}^tJ_z) \tag{5.52}$$

to reduce the solution from Jacobi elliptic functions to trigonometric functions in the equations of motion (3.1). We have chosen to assign the two equal moments of inertia as ${}^tJ_y$ (instead of ${}^tJ_x$) so that it can be associated with the somersault axis (and ${}^tJ_z$ with the twist axis). The solution to the equations of motion (3.1) is then given by (2.50) using the initial condition $\boldsymbol{M}_3(0) = R_x^{-1}(\mathcal{P})\boldsymbol{L}_3(0)$, where $\boldsymbol{L}_3(0)$ is given by (5.47). Evaluating gives

$$ \boldsymbol{M}_3 = l \begin{pmatrix} -\cos(\mathcal{P}+\mathcal{X})\sin Wt \\ \cos(\mathcal{P}+\mathcal{X})\cos Wt \\ -\sin(\mathcal{P}+\mathcal{X}) \end{pmatrix}, \tag{5.53}$$

where W given by (2.46) is

$$ W = -({}^tJ_z^{-1} - {}^tJ_y^{-1})M_z = l({}^tJ_z^{-1} - {}^tJ_y^{-1})\sin(\mathcal{P}+\mathcal{X}). \tag{5.54}$$

Transforming back to $\boldsymbol{L}_3$ we have

$$ \boldsymbol{L}_3 = l \begin{pmatrix} -\cos(\mathcal{P}+\mathcal{X})\sin Wt \\ \cos\mathcal{P}\cos(\mathcal{P}+\mathcal{X})\cos Wt + \sin\mathcal{P}\sin(\mathcal{P}+\mathcal{X}) \\ \sin\mathcal{P}\cos(\mathcal{P}+\mathcal{X})\cos Wt - \cos\mathcal{P}\sin(\mathcal{P}+\mathcal{X}) \end{pmatrix}, \tag{5.55}$$

which is a circle with radius $l\cos(\mathcal{P}+\mathcal{X})$ on the L-sphere lying on the plane normal to the vector $R_x(\mathcal{P})\boldsymbol{e}_z$.

We can now compute the orientation using Euler angles as we already have the solution given by (2.86) when ${}^tJ_x = {}^tJ_y$. However, in order to do so, we must first setup the spatial frame so that the z-axis is pointing in the direction of the angular momentum vector, and the x-axis is aligned with the initial X-axis of the body frame. If we denote this spatial frame as $\mathcal{F}_T$, then the transformation of a vector $\boldsymbol{\mathcal{V}}_S$ in $\mathcal{F}_S$ to $\mathcal{F}_T$ is given by

$$ \boldsymbol{\mathcal{V}}_T = R_x^{-1}(-\pi/2)R_y^{-1}(\Omega_1\tau_1)\boldsymbol{\mathcal{V}}_S. \tag{5.56}$$

We now find the Euler angles between $\mathcal{F}_T$ and $\mathcal{F}_B$ for the twisting somersault phase $\mathcal{S}_3$. The initial condition is given by (2.81), where

$$ \theta_0 = \frac{\pi}{2} + \mathcal{P} + \mathcal{X}. \tag{5.57}$$

The angle $\mathcal{X}$ is generated by the fast-kick action which tilts the torso, while $\pi/2$ and $\mathcal{P}$ arise from switching frames and have no physical meaning. The solution to the Euler angles are thus

$$\phi = l\,{}^tJ_y^{-1}t \qquad \theta = \theta_0 \qquad \psi = -Wt. \tag{5.58}$$

The positive sign in the somersault rate $\dot{\phi}$ corresponds to a clockwise (forward) somersault, while the negative sign in $\dot{\psi}$ corresponds to a counterclockwise twist. Ignoring the signs we have

$$|\dot{\psi}| = \dot{\phi}\left(\frac{{}^tJ_y}{{}^tJ_z} - 1\right)\sin(\mathcal{P}+\mathcal{X}), \tag{5.59}$$

which is reminiscent of (2.87) and Yeadon's (25) in [66], although here we have an additional contribution from $\mathcal{P}$ that originates from the diagonalisation of ${}^tI$ in $\mathcal{F}_C$ to ${}^tJ$ in $\mathcal{F}_B$. As $\dot{\psi}$ is the twist rate, the period of twist ${}^tT$ is

$${}^tT = \frac{2\pi}{W} = \frac{2\pi}{l}\frac{{}^tJ_y\,{}^tJ_z}{{}^tJ_y - {}^tJ_z}\csc(\mathcal{P}+\mathcal{X}). \tag{5.60}$$

As the dynamics of $\mathcal{S}_1$ is pure somersault and $\mathcal{S}_2$ is a tilt, we then need n twists in $\mathcal{S}_3$, hence

$$\tau_3 = n\,{}^tT = \frac{2n\pi}{W} \text{ for } n \in \mathbb{N}, \tag{5.61}$$

and we can think of the case $n = 0$ as corresponding to the athlete performing two consecutive fast-kicks that result in no net effect.

The rotation matrix R_3 relating $\mathcal{F}_S$ and $\mathcal{F}_C$ in $\mathcal{S}_3$ is obtained by going through two intermediate frames, which can be summarised as

$$\underbrace{R_3}_{\mathcal{F}_S} = \underbrace{R_y(\Omega_1\tau_1)R_x(-\pi/2)}_{\to\ \mathcal{F}_T}\underbrace{R_z(\phi)R_x(\theta)R_z(\psi)}_{\to\ \mathcal{F}_B}\underbrace{R_x(-\mathcal{P})}_{\to\mathcal{F}_C}. \tag{5.62}$$

For completeness the quaternion $\boldsymbol{q}_3$ can be obtained by using (2.39) to transform R_3 into

$$\boldsymbol{q}_3 = \frac{1}{2r}\begin{pmatrix} r^2 \\ -s_\mathcal{P}s_\theta(c_\nu + c_\psi) - c_\mathcal{P}(c_\theta + c_\nu c_\theta c_\psi - s_\nu s_\psi) \\ c_\nu s_\psi(c_\theta - s_\mathcal{P}) + s_\nu(c_\mathcal{P}s_\theta - s_\mathcal{P}c_\theta c_\psi + c_\psi) \\ s_\psi(c_\mathcal{P}c_\nu + s_\theta) + s_\nu(c_\mathcal{P}c_\theta c_\psi + s_\mathcal{P}s_\theta) \end{pmatrix}, \tag{5.63}$$

where

$$\begin{aligned} \nu &= \Omega_1\tau_1 + \phi \\ r &= \pm\sqrt{1 - s_\mathcal{P}c_\theta + c_\mathcal{P}s_\theta c_\psi + c_\nu(c_\mathcal{P}s_\theta - s_\mathcal{P}c_\theta c_\psi + c_\psi) + s_\nu(s_\mathcal{P}s_\psi - c_\theta s_\psi)}, \end{aligned} \tag{5.64}$$

and cosines and sines are abbreviated as c and s (with arguments written as subscripts), respectively. The double cover results in two equivalent quaternions, which as explained in Chapter 2.7 yield the same continuous rotation matrix R_3.

However, in order for $\boldsymbol{q}_3$ to be continuous on $\mathcal{S}^3$, we need to switch between the two solutions whenever r crosses zero.

5.3.4 $\mathcal{S}_4$: Terminate Twist

The athlete finishes performing n twists after time τ_3 and uses the second transition stage to return to pure somersaulting motion. To find the initial conditions we substitute $t = \tau_3$ from (5.61) into $\boldsymbol{L}_3$ given by (5.55) and $\boldsymbol{q}_3$ given by (5.63). The parameters in (5.64) become

$$\nu = l\left(\frac{\tau_1}{{}^{s}I_y} + \frac{n\,{}^{t}T}{{}^{t}J_y}\right) \qquad r = \pm 2\cos(\mathcal{X}/2)\cos(\nu/2), \tag{5.65}$$

and by simplifying the trigonometric functions we have

$$\boldsymbol{L}_4(0) = l\begin{pmatrix} 0 \\ \cos\mathcal{X} \\ -\sin\mathcal{X} \end{pmatrix} \qquad \boldsymbol{q}_4(0) = \pm\begin{pmatrix} \cos(\mathcal{X}/2)\cos(\nu/2) \\ \sin(\mathcal{X}/2)\cos(\nu/2) \\ \cos(\mathcal{X}/2)\sin(\nu/2) \\ -\sin(\mathcal{X}/2)\sin(\nu/2) \end{pmatrix}, \tag{5.66}$$

noting that for convenience, we will take only the positive result for the quaternion $\boldsymbol{q}_4(0)$.

The tilt generated from the impulsive shape change $\alpha\colon 0 \to \pi$ is in the opposite direction to the one found in $\mathcal{S}_2$ for $\alpha\colon \pi \to 0$. Hence $\mathcal{X} \to -\mathcal{X}$ in (5.47) and (5.49), which gives

$$\boldsymbol{L}_5(0) = R_x(\mathcal{X})\boldsymbol{L}_4(0) = \begin{pmatrix} 0 \\ l \\ 0 \end{pmatrix} \tag{5.67}$$

$$\boldsymbol{q}_5(0) = \begin{pmatrix} R_2(-\mathcal{X}/2) & 0 \\ 0 & R_2(\mathcal{X}/2) \end{pmatrix}\boldsymbol{q}_4(0) = \begin{pmatrix} \cos(\nu/2) \\ 0 \\ \sin(\nu/2) \\ 0 \end{pmatrix}, \tag{5.68}$$

where ν is given by (5.65).

5.3.5 $\mathcal{S}_5$: Terminate Somersault

Prior to completing the dive, the athlete must return to pure somersaulting motion. We now want to find τ_5 to ensure the athlete enters the pool correctly with head-first entry. Upon comparison between $\boldsymbol{L}_5(0)$ and (2.35), we discover the athlete has somersaulted by ν. With the inclusion of the pure somersault phase in $\mathcal{S}_5$ we set

$$\nu + \frac{l}{{}^{s}I_y}\tau_5 = 2m\pi,$$

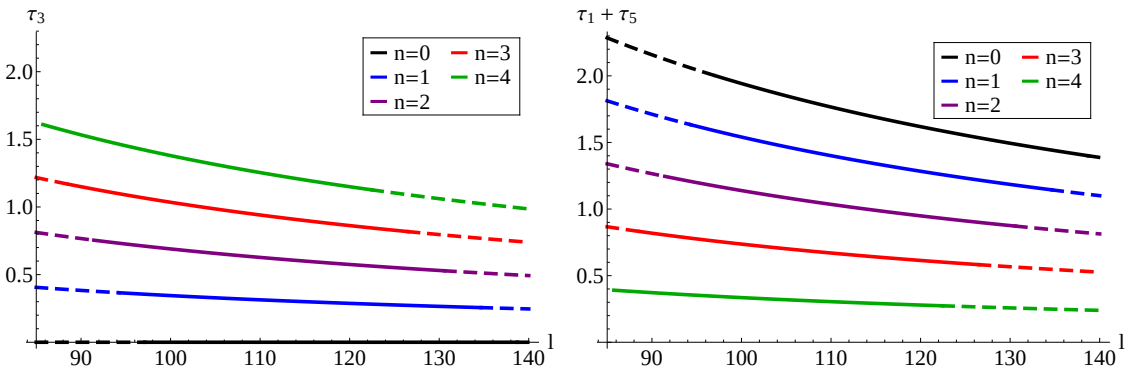

(A) Twisting somersault time. (B) Pure somersault time.

FIGURE 5.21. Time in τ_3 and $\tau_1 + \tau_5$ for $m = 1.5$ somersaults with n twists. The lines become dashed once T_{air} given by (5.70) moves outside the interval $[T_{min}, T_{max}]$ found in (5.5). Each curve shown here is higher than its corresponding numerical simulation counterpart in Figure 5.17 due to the absence of T_ψ and T_ϕ terms.

where m is a half-integer for a successful dive. Rearranging and using ${}^sT$ given by (5.34) we have

$$\tau_1 + \tau_5 = m\,{}^sT - n\,{}^tT\frac{{}^sI_y}{{}^tJ_y}, \tag{5.69}$$

where care must be taken in choosing m and n to ensure that $\tau_1 + \tau_5 \geq 0$. In the case of $m = 1.5$ somersaults with n twists the limit is four twists, and evaluating (5.69) for $\tau_1 + \tau_5$ and (5.61) for τ_3 produces the curves shown in Figure 5.21. The airborne time of the dive is given by (5.4), but since $\tau_2, \tau_4 \to 0$ in the fast-kick model we have

$$T_{air} = \tau_1 + \tau_3 + \tau_5. \tag{5.70}$$

The total time spent in pure somersault is given by $\tau_1 + \tau_5$, where τ_3 is the time spent in twisting somersault. It does not matter how τ_1 and τ_5 are distributed as long as the sum is the same, so we can set $\tau_1 = \tau_5$ to distribute the somersault time evenly. Substituting in the results of (5.61) and (5.69) for T_{air} gives

$$T_{air} = m\,{}^sT - n\left(\frac{{}^sI_y}{{}^tJ_y} - 1\right){}^tT, \tag{5.71}$$

and using the periods given by (5.34) and (5.60) we get

$$T_{air}(l) = \frac{2\pi}{l}\left(m\,{}^sI_y + n\,\frac{{}^tJ_z\,({}^tJ_y - {}^sI_y)}{{}^tJ_y - {}^tJ_z}\csc\left(\mathcal{P} + \mathcal{X}\right)\right). \tag{5.72}$$

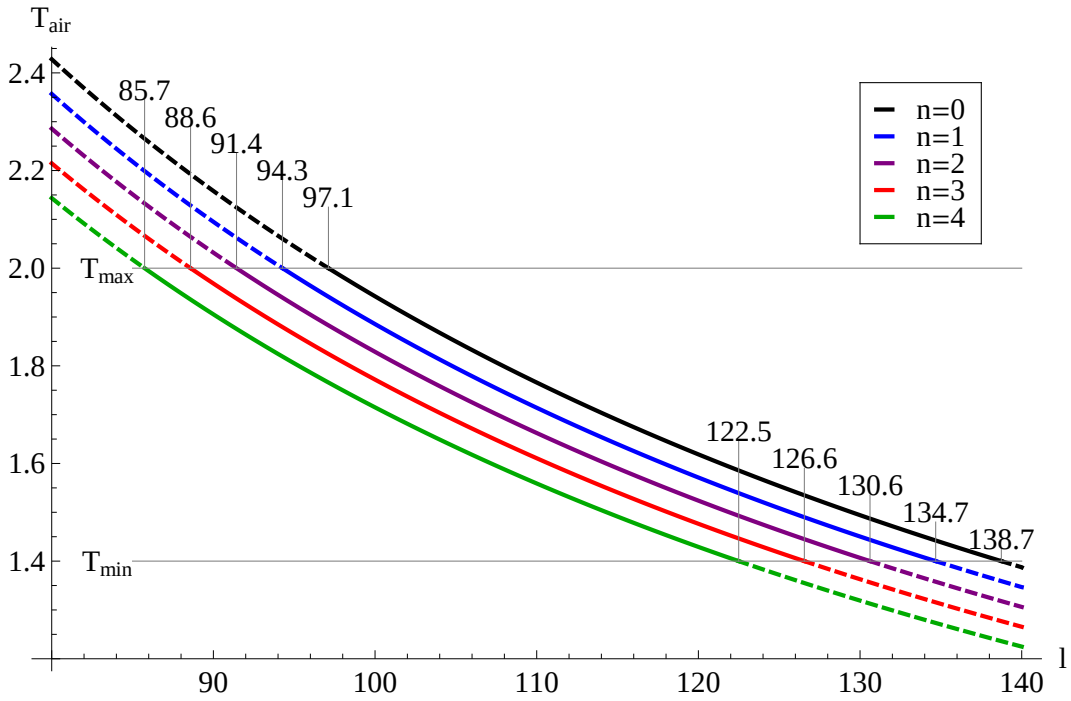

FIGURE 5.22. Relationship between the airborne time T_{air} and angular momentum l given by (5.72) in the case of $m = 1.5$ somersaults with $n = \{0, 1, 2, 3, 4\}$ twists. The bounds for airborne time T_{air} are shown in (5.5). The curves shown here are slightly lower than those shown in Figure 5.19 for the numerical simulation.

This reveals the relationship between the angular momentum and airborne time required for a successful dive, allowing us to express T_{air} as a function of l and plot the graph for $m = 1.5$ somersaults with n twists, as seen in Figure 5.22.

We now summarise the numerical simulation and analytical approximation using the fast-kick model in Table 5.3. It is important to note that ${}^{t}T$ is different in both models, unlike ${}^{s}T$ which remains the same. This is due to the different shape change mechanics producing different orbits on the L-sphere, as well as setting two moments of inertia equal in the fast-kick model. Hence we use left subscript n and f to distinguish the two models and depict the difference between the periods in Figure 5.23.

Substituting the numerical values listed in (5.1), (5.2), (5.3), and (5.46) for the parameters in ${}_{f}T_{air}(l)$ given by (5.72) we find

$$ {}_{f}T_{air}(l) = \frac{1}{l}(129.4905m - 5.6863n), \tag{5.73}$$

	numerical simulation	fast-kick model
τ_3	$n\ {}^{t}_{n}T - T_\psi$	$n\ {}^{t}_{f}T$
$\tau_1 + \tau_5$	$m\,{}^{s}T - n\mathfrak{T}\ {}^{t}_{n}T - T_\phi$	$m\,{}^{s}T - n\,\frac{{}^{s}I_y}{{}^{t}J_y}\ {}^{t}_{f}T$
τ_2, τ_4	0.25	0
T_{air}	$m\,{}^{s}T - n(\mathfrak{T}-1)\ {}^{t}_{n}T$	$m\,{}^{s}T - n\left(\frac{{}^{s}I_y}{{}^{t}J_y} - 1\right)\ {}^{t}_{f}T$

TABLE 5.3. The appearance of T_ψ and T_ϕ in the numerical simulation are the result of the twisting and somersaulting that occur in the transition stages, and since $\tau_2, \tau_4 \to 0$ in the fast-kick model there are no such terms there.

where the difference to ${}_{n}T_{air}(l)$ given by the numerical simulation found in (5.36) is

$$ {}_{f}T_{air}(l) - {}_{n}T_{air}(l) = -\frac{0.92265n}{l}, \tag{5.74}$$

which shows the airborne time is only slightly less with the fast-kick model, since n is small and l is large. The discrepancy in airborne time comes from two places, which can be seen in Table 5.3. There we see $\mathfrak{T} \approx {}^{s}I_y/{}^{t}J_y = 1.16152$, which can be compared to the numerical value of 1.14339 found in (5.28), while the other difference is the period of twist $\left({}^{t}_{n}T \text{ compared to } {}^{t}_{f}T\right)$. Now the fast-kick model was setup in approximation with equal moments of inertia, and repeating the computation with distinct moments of inertia (like in the numerical simulation) will reduce the difference shown in Figure 5.23. However, we will instead take a different approach that is related to the geometric phase in the next subsection.

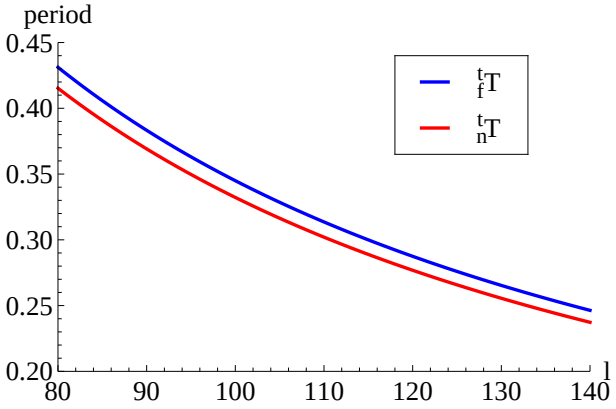

FIGURE 5.23. We have ${}^{t}_{f}T(l) - {}^{t}_{n}T(l) \approx 1.27219/l$. The difference is approximately 0.0159 when $l = 80$ and monotonically decreases to 0.009 when $l = 140$.

It is clear that performing additional somersaults requires additional time, but one interesting fact is that increasing the number of twists while maintaining the same number of somersaults and angular momentum actually requires less airborne time. While this may seem counter intuitive at first, it is in fact true because ${}^tJ_y - {}^sI_y < 0$, making the coefficient of n in $T_{air}(l)$ given by (5.72) negative.

While the layout position has a larger angular momentum component about the somersault axis (compared to the twist position), the athlete's arm position also results in a larger moment of inertia. Coincidentally, the angular velocity about the somersault axis is smaller in the layout position for our model, which overall results in more twists requiring less airborne time. Athletes typically take-off and complete the dive in the layout position, and for this reason we have chosen to adopt it in $\mathcal{S}_1$ and $\mathcal{S}_5$. Introducing additional stages to allow pure somersaults in pike or tuck position will result in ${}^tJ_y - {}^sI_y > 0$, giving the intuitive result that more time is taken to perform additional somersaults and/or twists.

5.4 Cabrera: Generalised Montgomery Formula

Montgomery [44] derived the well known formula

$$\Delta\phi = \frac{2ET}{l} - S \mod 2\pi, \tag{5.75}$$

which separates the change in orientation (given by $\Delta\phi$) of a rigid body into the dynamic phase (given by $2ET/l$) and geometric phase (given by S) after one period T of the angular momentum vector $\boldsymbol{L}$ (with magnitude l) in $\mathcal{F}_C$. In the formula, E is the kinetic energy and S is a signed solid angle, which is the angle swept out by the body's angular momentum vector.

While Montgomery's formula is only applicable to rigid bodies, Cabrera [9] gives

$$\Delta\phi = (\mp)\frac{A}{l^2} + \frac{1}{l}\int_0^T I^{-1}(\alpha)\boldsymbol{L} - I^{-1}(\alpha)\boldsymbol{A}(\alpha,\dot{\alpha})\cdot\boldsymbol{L}\,\mathrm{d}t \mod 2\pi \tag{5.76}$$

which generalises the result to self-deforming bodies, where $\boldsymbol{L}$, α, and $\dot{\alpha}$ are all functions of t. In the case of no shape change α is constant and $\dot{\alpha} = 0$, meaning $\boldsymbol{A}(\alpha, 0) = \boldsymbol{0}$ and $I^{-1}\boldsymbol{L}\cdot\boldsymbol{L} = 2E$, hence reducing (5.76) to Montgomery's formula (5.75). By keeping the surface area A lying to the left of the oriented curve we enforce $S > 0$, thus

$$S = \frac{A}{l^2}. \tag{5.77}$$

The mod 2π appearing in (5.76) can be removed by appropriately defining the surface area A, which is crucial for our application as we need to distinguish between the different number of m somersaults, and for our purposes the diver takes off in an upright position so that the initial orientation is always zero, allowing us to

write ϕ instead of $\Delta\phi$ for the orientation change. With these modifications and using $\boldsymbol{\Omega}$ given by (3.24), we can rewrite Cabrera's formula (5.76) as

$$\phi = -\frac{A}{l^2} + \frac{1}{l}\int_0^T \boldsymbol{L}\cdot\boldsymbol{\Omega}(\alpha,\dot{\alpha})\,\mathrm{d}t. \tag{5.78}$$

We will explain shortly that we want the surface area A to be the region bounded between the orbit $\boldsymbol{L}_3$ and the equator, which is verified by matching the result obtained using modified Cabrera's formula (5.78) with our analytical result found earlier. Any great circle can become the equator when viewed in the right frame, and provided it does not intersect with the orbit $\boldsymbol{L}_3$ then the bounded surface area will be the same. As $\boldsymbol{L}_3$ is tilted on the L-sphere, we will refer to the equator as the great circle lying on the M_xM_y-plane.

5.4.1 Fast-kick with ${}^tJ_x = {}^tJ_y > {}^tJ_z$

We are now going to apply the modified Cabrera formula (5.78) to the fast-kick model (from Chapter 5.3) to compute ϕ, justify our choice of A, and find τ_i, T_{air} to compare with the results found in Chapter 5.3.

The angular velocity vector $\boldsymbol{\Omega} = -I\boldsymbol{A}$ in fast-kick transition stages only has a non-zero x-component (verified by looking at the form of I in (3.45) and $\boldsymbol{A}$ in (3.37)), while the x-component in $\boldsymbol{L}$ remains zero because it is initially zero, and fast-kicks only induce a rotation about the x-axis of the body as shown in (5.47) and (5.67), hence

$$\int_0^{\tau_i} \boldsymbol{L}_i\cdot\boldsymbol{\Omega}_i\,\mathrm{d}t = 0 \qquad \text{for even } i. \tag{5.79}$$

Combining the fast-kick pair forms a closed curve that encloses zero area, so the geometric phase is also zero. Hence the transition stages play no part in the contribution to ϕ in (5.78), leaving only the rigid body stages. Since Montgomery's formula (5.75) is applicable in rigid body dynamics we have

$$\int_0^{\tau_i} \boldsymbol{L}_i\cdot\boldsymbol{\Omega}_i\,\mathrm{d}t = 2E_i\tau_i \qquad \text{for odd } i. \tag{5.80}$$

Computing the energies with (2.56), and using the angular momentums found in (5.40) and (5.53), we find

$$E_1 = E_5 = \frac{l^2}{2\,{}^sI_y} \qquad E_3 = \frac{l^2}{2}\left(\frac{\cos^2(\mathcal{P}+\mathcal{X})}{{}^tJ_y} + \frac{\sin^2(\mathcal{P}+\mathcal{X})}{{}^tJ_z}\right). \tag{5.81}$$

The athlete performs a fast-kick in $\mathcal{S}_2$ which tilts the torso by $\mathcal{X}$, causing $\mathcal{S}_3$ to have the orbit $\boldsymbol{L}_3$ shown in Figure 5.24. For the solid angle $S > 0$, we need the surface area to lie to the left of the oriented curve. It is clear that we expect more geometric phase with a larger tilt and less with a smaller tilt, so in the limiting case where there is an absence of tilt we expect no geometric phase at all, meaning

$A = 0$. So to remove $\mod 2\pi$ appearing in Cabrera's formula (5.76) we define A to be the surface area lying between the equator and orbit $\boldsymbol{L}_3$.

In the case ${}^tJ_x = {}^tJ_y$ the orbit $\boldsymbol{L}_3$ lies on a tilted plane with normal $R_x(\mathcal{P})\boldsymbol{e}_z$, but working in $\mathcal{F}_B$ straightens it. To compute the surface area A shown in Figure 5.24 we use spherical coordinates given by

$$\boldsymbol{x} = l \begin{pmatrix} \sin\tilde{\theta}\cos\tilde{\phi} \\ \sin\tilde{\theta}\sin\tilde{\phi} \\ \cos\tilde{\theta} \end{pmatrix}, \tag{5.82}$$

and use the surface integral

$$A = \int_0^{2\pi}\int_{\pi/2}^{\pi-\xi} \left| \frac{\partial \boldsymbol{x}}{\partial\tilde{\theta}} \times \frac{\partial \boldsymbol{x}}{\partial\tilde{\phi}} \right| \mathrm{d}\tilde{\theta}\,\mathrm{d}\tilde{\phi} = l^2 \int_0^{2\pi}\int_{\pi/2}^{\pi-\xi} \sin\tilde{\theta}\,\mathrm{d}\tilde{\theta}\,\mathrm{d}\tilde{\phi}, \tag{5.83}$$

whereby looking at the projection shown in Figure 5.25 we see

$$\xi = \arccos\left(\frac{|M_z|}{l}\right) = \arccos\Big(\sin\left(\mathcal{P} + \mathcal{X}\right)\Big).$$

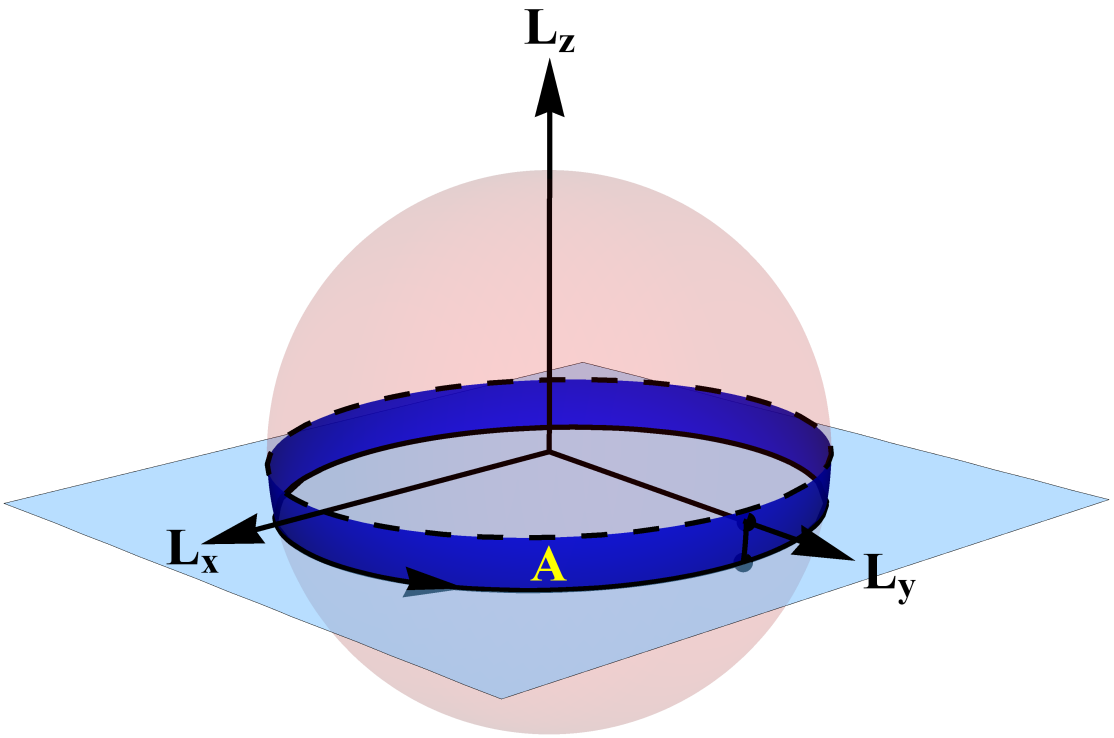

FIGURE 5.24. The surface area A bounded by $\boldsymbol{L}_3$ and the equator.

Evaluating the integral in (5.83) gives

$$ {}_2A = 2\pi l|M_z| = 2\pi l^2 \sin(\mathcal{P} + \mathcal{X}), \tag{5.84} $$

where we use left subscript 2 to indicate that the moments of inertia are equal. To compute ϕ in (5.78) for the dive consisting of n twists, we split the dynamic phase given by the integral into the five individual stages, and as the loop in $\mathcal{S}_3$ traverses around the L-sphere n times multiply the surface area A by n to yield the total geometric phase. Hence (5.78) becomes

$$ \phi = -\frac{n\,{}_2A}{l^2} + \frac{1}{l}\sum_{k=1}^{5}\int_0^{\tau_k} \boldsymbol{L}_k \cdot \boldsymbol{\Omega}_k \,\mathrm{d}t, \tag{5.85} $$

and substituting in (5.79) and (5.80) we obtain

$$ \phi = -\frac{n\,{}_2A}{l^2} + \frac{2}{l}\Big(E_1(\tau_1 + \tau_5) + E_3\tau_3\Big). \tag{5.86} $$

Since we want the athlete to complete m somersaults we set $\phi = 2m\pi$, and as τ_3 is determined by (5.61) for n twists, this leaves only $\tau_1 + \tau_5$, which can be rearranged to

$$ \tau_1 + \tau_5 = m\frac{\pi l}{E_1} - \frac{n}{E_1}\left[E_3\,{}^tT - \frac{{}_2A}{2l}\right]. \tag{5.87} $$

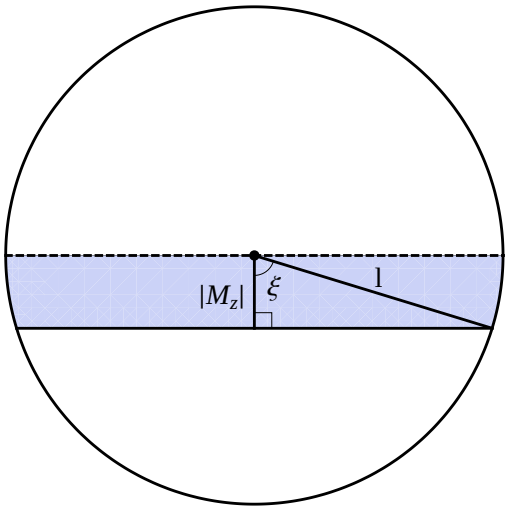

Figure 5.25. Projection of $\boldsymbol{M}_3$ onto the M_xM_z-plane. The perpendicular height h from the plane to the centre is $|M_z|$, where $M_z < 0$ is the third component of $\boldsymbol{M}_3$ given by (5.53).

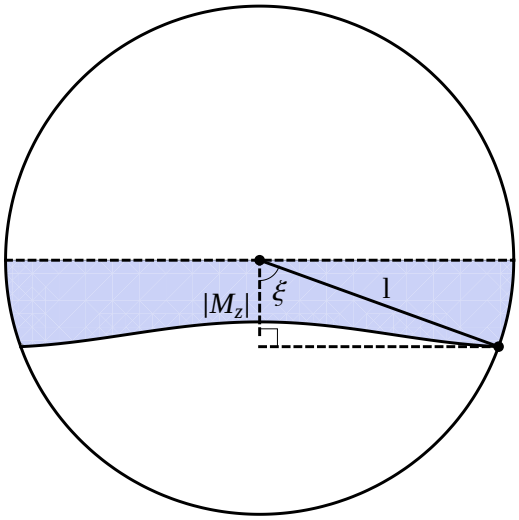

Figure 5.26. Projection of $\boldsymbol{M}_3$ onto the M_xM_z-plane; ξ is no longer constant.

The airborne time T_{air} is then found by summing (5.61) and (5.87) giving

$$T_{air} = m\frac{\pi l}{E_1} - \frac{n}{E_1}\left[(E_3 - E_1)\,{}^tT - \frac{{}_2A}{2l}\right]. \tag{5.88}$$

By substituting the energies given by (5.81), surface area ${}_2A$ given by (5.84), and period of twist ${}^tT$ given by (5.60) into the formulas (5.87) and (5.88), we find the results for $\tau_1 + \tau_5$ and T_{air} are the same as those found in (5.69) and (5.71), respectively, as expected. Thus we have successfully removed the $\bmod 2\pi$ appearing in Cabrera's original formula (5.76) and verified it works. The advantage of doing the computation this way is that we no longer need two moments of inertia being equal in order to obtain an analytical result. We now look at the fast-kick model with distinct moments of inertia, followed by the more general model with realistic arm motions.

5.4.2 Fast-kick with ${}^tJ_x > {}^tJ_y > {}^tJ_z$

Again we work in $\mathcal{F}_B$ to avoid the tilt $\mathcal{P}$ originating from the diagonalisation. With distinct moments of inertia the orbit $\boldsymbol{M}_3$ no longer lies on a plane, but wobbles as shown in Figure 5.26. The curve parametrisation of $\boldsymbol{M}_3$ is found with (2.61), where the energy E_3 needed remains unchanged from (5.81) even when ${}^tJ_x \neq {}^tJ_y$. The surface area integral (5.83) still holds, except ξ is no longer constant but a function of a. Rewriting the integral in terms of Cartesian coordinates we have

$$A = \iint_D \frac{l}{\sqrt{l^2 - x^2 - y^2}}\,\mathrm{d}y\,\mathrm{d}x, \tag{5.89}$$

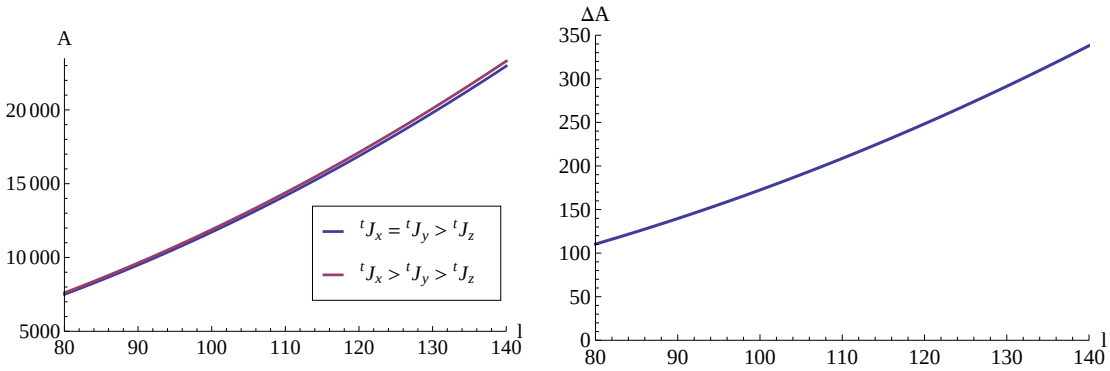

(A) ${}_2A$ on bottom and ${}_3A$ on top. (B) $\Delta A = {}_3A - {}_2A$.

FIGURE 5.27. Evaluating (5.84) and (5.93) for the surface areas we find ${}_2A = 1.1716l^2$ and ${}_3A = 1.1891^2$.

and if we find a vector field $\boldsymbol{F}(\boldsymbol{x})$ such that

$$\nabla \times \boldsymbol{F}(\boldsymbol{x}) \cdot \boldsymbol{n}(\boldsymbol{x}) = \frac{l}{\sqrt{l^2 - x^2 - y^2}}, \tag{5.90}$$

then we can use Stoke's theorem to convert the surface integral into a line integral to make the computation easier. One such $\boldsymbol{F}(\boldsymbol{x})$ that satisfies (5.90) is

$$\boldsymbol{F}(\boldsymbol{x}) = \frac{lz}{x^2 + y^2} \begin{pmatrix} y \\ -x \\ 0 \end{pmatrix}, \tag{5.91}$$

so by applying Stoke's theorem we get

$${}_3A = l \int_0^{2\pi} \frac{M_z(a)}{M_x^2(a) + M_y^2(a)} \Big(M_y(a)\dot{M}_x(a) - M_x(a)\dot{M}_y(a) \Big) \, \mathrm{d}a, \tag{5.92}$$

where left subscript 3 is used to denote distinct moments of inertia. The analytical solution is expressed in terms of complete elliptic integrals and is

$${}_3A = 4l^2 \sqrt{\frac{{}^tJ_y}{{}^tJ_x {}^tJ_z ({}^tJ_y - {}^tJ_z)\mathcal{H}_x}} \left(({}^tJ_x - {}^tJ_z)\Pi(\tilde{n}; \tilde{k}) - {}^tJ_x \mathcal{H}_z K(\tilde{k}) \right), \tag{5.93}$$

where

$$\mathcal{H}_x = 2\mathcal{E}_3 {}^tJ_x - 1 \qquad \tilde{n} = -\frac{{}^tJ_z({}^tJ_x - {}^tJ_y)}{{}^tJ_x({}^tJ_y - {}^tJ_z)}$$

$$\mathcal{H}_z = 1 - 2\mathcal{E}_3 {}^tJ_z \qquad \tilde{k} = \frac{({}^tJ_x - {}^tJ_y)\mathcal{H}_z}{({}^tJ_y - {}^tJ_z)\mathcal{H}_x}.$$

The approximation previously given for ${}^tT$ in (5.33) is usually sufficient, but since we are taking an analytical approach here we include the analytic form given by (2.65) to get

$$ {}^t_3T = T(\mathcal{E}_3, {}^tJ) = \frac{4K(\tilde{k})}{l}\sqrt{\frac{{}^tJ_x{}^tJ_y{}^tJ_z}{({}^tJ_y - {}^tJ_z)\mathcal{H}_x}}, \tag{5.94}$$

where again the left subscript is used to indicate distinct moments of inertia.

The formulas derived for τ_3, $\tau_1 + \tau_5$, and T_{air} given by (5.61), (5.87), (5.88), respectively, only need the slight modification of replacing ${}_2A$ with ${}_3A$ and ${}^tT$ with ${}^t_3T$ to hold true.

5.4.3 Realistic Arm Motion with ${}^tJ_x > {}^tJ_y > {}^tJ_z$

We now look at the realistic arm motion model described in Chapter 5.2. The geometric phase is given by (5.77), where the surface area for $n = 1$ twist is shown in Figure 5.28. For n twists the 'total' area A is

$$ A = n(A_+ + A_-) - A_- = nA_\pm - A_-, \tag{5.95}$$

where A_+, A_-, and $A_\pm = A_+ + A_-$ can be seen in Figure 5.29.

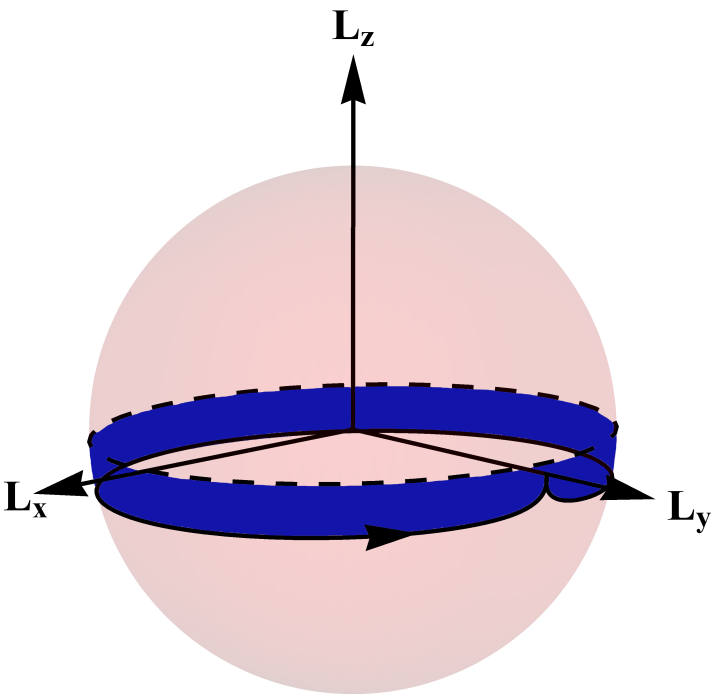

Figure 5.28. The blue region is the surface area for $n = 1$ twist.

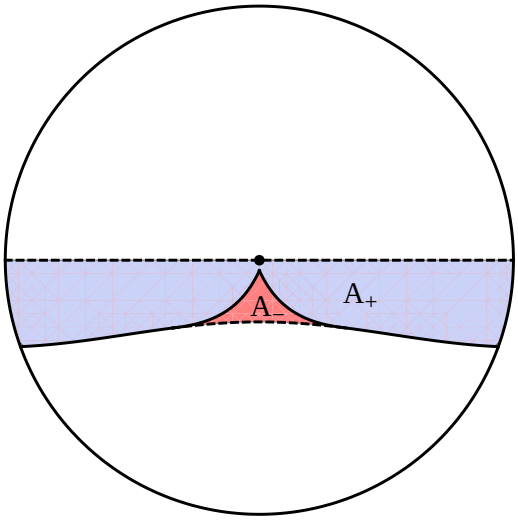

Figure 5.29. The larger blue region is A_+, the smaller red region is A_-, and the union of the two is denoted by $A_\pm$.

To evaluate $A_\pm$ we can use (5.93), where only the energy E_3 needs to be changed to the one shown in Figure 5.15A (the energies are different, so to avoid confusion we will refer to the fast-kick energy as ${}_fE_3$). The realistic arm motion has slightly more energy for any l compared to the fast-kick model, as can be seen in Figure 5.30. Performing the computation for each integer $l \in [80, 140]$ we obtain the results shown in Figure 5.31A.

The boundary of A_- is given by three piecewise smooth curves $\boldsymbol{L}_2, \boldsymbol{L}_3$ and $\boldsymbol{L}_4$, all of which can be obtained numerically (note that there is little point in using the analytical solution for $\boldsymbol{L}_3$ as the initial condition can only be found numerically).

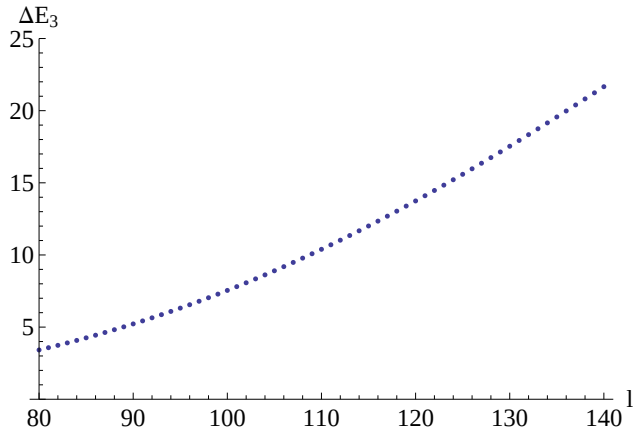

Figure 5.30. $\Delta E_3 = E_3 - {}_fE_3$.

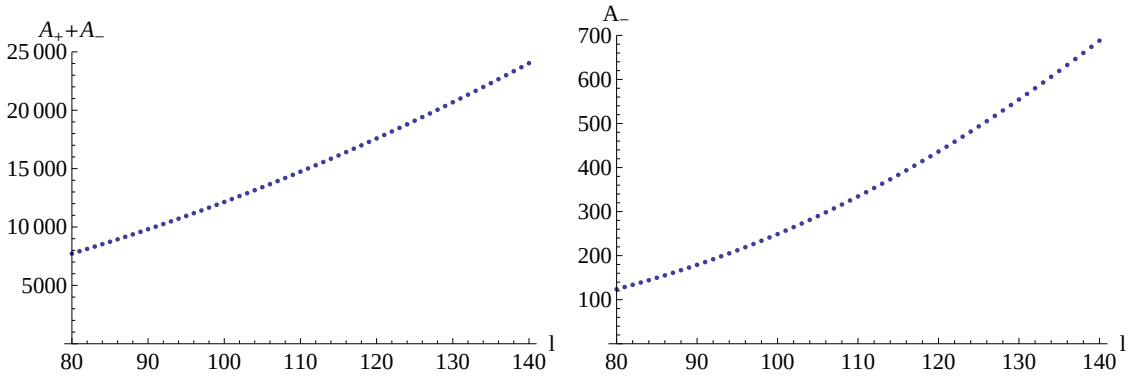

(A) Surface area of $A_{\pm} = A_{+} + A_{-}$. (B) Surface area of A_{-}.

FIGURE 5.31. The surface area of the two components that make up A given by (5.95).

So to obtain A_{-} indicated by the red region in Figure 5.29, we orient the line integral as follows

$$A_{-} = -\int_0^{\tau_2} \boldsymbol{F}(\boldsymbol{L}_2)\cdot\dot{\boldsymbol{L}}_2\,\mathrm{d}t + \int_{{}^tT-T_\psi}^{{}^tT} \boldsymbol{F}(\boldsymbol{L}_3)\cdot\dot{\boldsymbol{L}}_3\,\mathrm{d}t - \int_0^{\tau_4} \boldsymbol{F}(\boldsymbol{L}_4)\cdot\dot{\boldsymbol{L}}_4\,\mathrm{d}t, \tag{5.96}$$

where $\boldsymbol{F}(\boldsymbol{x})$ is defined in (5.91), the tabulated values of T_ψ are shown in Figure 5.13A, and evaluating for each integer $l \in [80, 140]$ we get result shown in Figure 5.31B.

While the integral shown in (5.80) is true, (5.79) is not, so for transition stages we instead have

$$\begin{aligned}\int_0^{\tau_k} \boldsymbol{L}_k\cdot\boldsymbol{\Omega}_k(\alpha_k,\dot\alpha_k)\,\mathrm{d}t &= \int_0^{\tau_k} \boldsymbol{L}_k^t I^{-1}(\alpha_k)\big(\boldsymbol{L}_k - \boldsymbol{A}(\alpha_k,\dot\alpha_k)\big)\,\mathrm{d}t \\ &= 2\bar{E}_k\tau_k \text{ for even } i,\end{aligned} \tag{5.97}$$

where $\boldsymbol{L}_k$, α_k, and $\dot\alpha_k$ are all functions of t. We interpret $\bar{E}_k$ as the average kinetic energy over time τ_k, which is obtained by evaluating the integral numerically. Due to the symmetry of shape change shown in (5.17), we have (5.22) and hence $\bar{E}_2 = \bar{E}_4$. The result for ϕ shown in (5.85) then becomes

$$\phi = -\frac{nA_{\pm} - A_{-}}{l^2} + \frac{2}{l}\Big(E_1(\tau_1+\tau_5) + E_3\tau_3 + 2\bar{E}_2\tau_2\Big). \tag{5.98}$$

Combining our empirically obtained result of $\tau_3 = n\,{}^tT - T_\psi$ from (5.29), the fact that $\tau_2 = \tau_4 = 0.25$, and our aim for the athlete to perform m somersaults (meaning $\phi = 2m\pi$) lets us solve $\tau_1 + \tau_5$ to obtain

$$\tau_1 + \tau_5 = m\frac{\pi l}{E_1} - n\frac{\phi_s\, l}{2E_1} - \frac{1}{E_1}\left(\hat{E} - E_3T_\psi\right), \tag{5.99}$$

where

$$\hat{E} = \frac{1}{2}\left(\frac{A_-}{l} + \bar{E}_2\right) \tag{5.100}$$

and

$$\phi_s = \frac{2E_3\,{}^tT}{l} - \frac{A_\pm}{l^2} \tag{5.101}$$

is the amount of somersault obtained after one period of twist ${}^tT$. Comparing the coefficients of (5.99) to (5.29) (recall that τ_1 was set to zero in the numerical simulation) we find

$${}^sT = \frac{\pi l}{E_1} \qquad \mathcal{T} = \frac{l}{2E_1}\frac{\phi_s}{{}^tT} \qquad T_\phi = \frac{1}{E_1}\left(\hat{E} - E_3 T_\psi\right). \tag{5.102}$$

While the equation for ${}^sT$ is nothing new, the remaining two reveal new discoveries, and unlike in (5.28) we now have a high precision equation for $\mathcal{T}$. Due to ϕ_s and t^T depending on E_3 (which is not exactly proportional to l^2 as shown in Figure 5.15C) this means l does not cancel and $\mathcal{T}$ has minute dependence on l. In fact, substituting in ${}^sT$ we see that

$$\mathcal{T} = \frac{\phi_s}{2\pi}\frac{{}^sT}{{}^tT},$$

and for $l = 100$ we have ϕ_s specified in (5.19) which reproduces the value of $\mathcal{T}$ shown in (5.28).

The connection between T_ψ and T_ϕ is finally linked, and by using the approximation (5.32) we can at last establish an analytical interpretation of the somersault and twist transitions. The result has nice symmetry and is

$$T_\psi \approx \hat{C}^{-1}\left(\hat{E}/E_1 - \tau_2 - \tau_4\right) \qquad T_\phi \approx \hat{C}^{-1}\left(\hat{E}/E_3 - \tau_2 - \tau_4\right), \tag{5.103}$$

where

$$\hat{C} = \frac{E_3}{E_1} - 1. \tag{5.104}$$

For completeness the airborne time T_{air} defined in (5.4) becomes

$$\begin{aligned} T_{air} &= m\frac{\pi l}{E_1} - n\left(\hat{C}\,{}^tT - \frac{A_\pm}{2lE_1}\right) - \frac{\hat{E}}{E_1} + \frac{1}{2} + \hat{C}T_\psi \\ &\approx m\frac{\pi l}{E_1} - n\left(\hat{C}\,{}^tT - \frac{A_\pm}{2lE_1}\right) && \text{substituting } T_\psi \\ &= m\,{}^sT - n(\mathcal{T}-1)\,{}^tT && \text{substituting } \mathcal{T}, \end{aligned}$$

which is precisely the result found in (5.35). In conclusion, we have discovered that we can modify Cabrera's formula (5.76) to obtain (5.78), which provides an elegant means of obtaining an analytical interpretation of the numerical quantities found in the numerical simulation, namely for $\mathcal{T}$, twist transition T_ψ, and somersault transition T_ϕ.

CHAPTER 6

New Dive: 513XD

In this chapter we want the athlete to use the second shape change to speed up the twisting somersault rather than stopping it, so that the diver can squeeze out additional twists without any additional cost of angular momentum or airborne time. This leads to the athlete performing a faster twisting somersault dive consisting of nine stages rather than five, where two pairs of transition stages are used instead of one. The formulas we derive are kept general for m somersaults and n twists, but the focus is on the 513XD dive (forward 1.5 somersaults with 5 twists).

Let us begin by first introducing a two letter arm code describing the actions of the athlete's arms, or more specifically, the motion or position of the left arm followed by the right arm. When the arm is moving, we use 'L' if the arm is being lowered or 'H' if the arm is being raised (H for higher). When the arm is not moving relative to the torso, we use 'U' for the up position (arm pointed straight up) or 'D' for the down position (arm down by the side).

In Chapter 5 we saw the dynamics of the one-armed diver, which is summarised in Figure 6.1. An important feature of that simulation was the precise timing of the arm reversal manoeuvre required to stop the twisting. Executing that manoeuvre arbitrarily will not stop the twisting motion, but instead leave the athlete continuing to perform twisting somersaults in the layout position with in

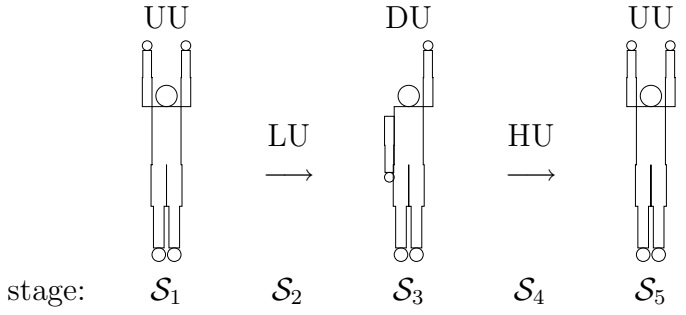

FIGURE 6.1. The diver takes off in pure somersault, performs a shape change mid-flight to transition into twisting somersault, before performing another shape change to revert into pure somersaulting motion to complete the dive.

general a new period of twist. This new period could become longer, shorter, or even stay the same depending on the precise timing of the arm reversal manoeuvre.

In Chapter 6.1 we explore the faster twisting somersault dive using the 2-body model described in Chapter 3.5.1 with impulsive shape changes. We examine the effect of performing the HU fast-kick of $\mathcal{S}_4$ after generic time τ_3 is spent in $\mathcal{S}_3$, and find the optimal time τ_3 which leads to $\mathcal{S}_5$ having the minimum period of twist in the twisting somersault. Two more additional fast-kicks in $\mathcal{S}_6$ and $\mathcal{S}_8$ will then be used to stop the twist and bring the athlete back into a pure somersaulting motion to finish off the dive in $\mathcal{S}_9$.

In Chapter 6.2 we move to the 3-body model described in Chapter 3.5.2 that allows the athlete to perform impulsive shape changes using both arms simultaneously, which we refer to as a 'dual fast-kick'. The tilt generated from a dual fast-kick is computed, and the results compared to the standard fast-kick of the one-armed diver.

In Chapter 6.3 we move away from impulsive shape changes and instead use realistic arm movements, and show how the 513XD dive (forward 1.5 somersaults with 5 twists) works using full numerical evaluation.

Finally, in Chapter 6.4 we go back to using impulsive shape changes where two consecutive single arm fast-kicks are compared to a dual fast-kick, and consider a theoretical study where multiple dual fast-kicks are used to transform a diver from a state of pure somersault into a state of pure twist, where all somersaulting motion is completely eliminated.

6.1 513XD - One-armed Diver

Let $\boldsymbol{L}_-$ be the instantaneous angular momentum of the athlete immediately before the fast-kick and $\boldsymbol{L}_+$ immediately after. Similarly, let $\boldsymbol{q}_-$ be the instantaneous orientation before the fast-kick and $\boldsymbol{q}_+$ immediately after. In Chapter 5 we saw the LU fast-kick initiate twist and the HU fast-kick terminate twist, but this only works when $\tau_3 = n\,{}^tT$. In general the fast-kicks shown in Figure 6.2 induce a jump in $\boldsymbol{L}(t)$ and $\boldsymbol{q}(t)$ governed by

$$\begin{aligned} \boldsymbol{L}_+ &= R_x(-\mathcal{X})\boldsymbol{L}_- \\ \boldsymbol{q}_+ &= \mathcal{R}(\mathcal{X})\boldsymbol{q}_- \end{aligned} \tag{6.1}$$

for the LU fast-kick, and

$$\begin{aligned} \boldsymbol{L}_+ &= R_x(\mathcal{X})\boldsymbol{L}_- \\ \boldsymbol{q}_+ &= \mathcal{R}(-\mathcal{X})\boldsymbol{q}_- \end{aligned} \tag{6.2}$$

for the HU fast-kick, where

$$\mathcal{R}(\theta) = \begin{pmatrix} R_2\left(\frac{1}{2}\theta\right) & 0 \\ 0 & R_2\left(-\frac{1}{2}\theta\right) \end{pmatrix}.$$

To obtain these results we use (5.47), (5.67) for $\boldsymbol{L}(t)$, and (5.49), (5.68) for $\boldsymbol{q}(t)$.

We now construct the faster twisting somersault dive using the one-armed diver shown in Figure 6.3. The idea is to use $\mathcal{S}_4$ to get the diver into a faster twisting state for $\mathcal{S}_5$, where the period of twist T_5 is reduced so that more twists can be

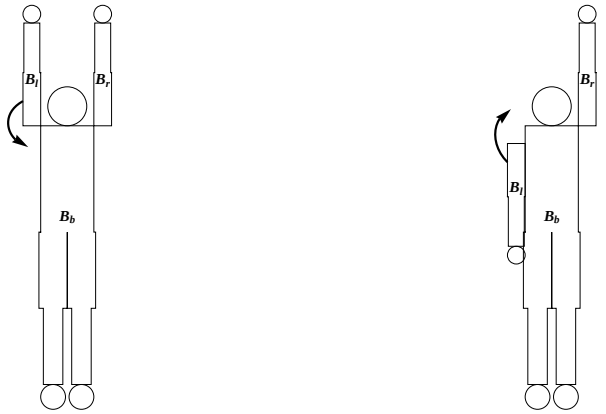

(A) LU fast-kick
$\boldsymbol{L}_+ = R_x(-\mathcal{X})\boldsymbol{L}_-$
$\boldsymbol{q}_+ = \mathcal{R}(\mathcal{X})\boldsymbol{q}_-$

(B) HU fast-kick
$\boldsymbol{L}_+ = R_x(\mathcal{X})\boldsymbol{L}_-$
$\boldsymbol{q}_+ = \mathcal{R}(-\mathcal{X})\boldsymbol{q}_-$

Figure 6.2. The change in angular momentum $\boldsymbol{L}$ and orientation $\boldsymbol{q}$ resulting from a fast-kick.

achieved within the same amount of time. The additional transition stages $\mathcal{S}_6$ will be used to bring the athlete back into the standard twisting somersaulting motion, and $\mathcal{S}_8$ to completely stop the twisting motion. The dive will start out the same as the standard twisting somersault shown in Figure 6.1, but begin to deviate from $\mathcal{S}_3$ onwards. The two key shapes are layout position (UU) and twist position (DU), which have inertia tensors ${}^sI$ and ${}^tJ$ given by (5.1) and (5.3), respectively.

$$\text{In } \mathcal{S}_1: \quad \text{Shape UU}$$
$$\mathcal{E}_1 = \frac{1}{2\ {}^sI_y} = 0.0243 \qquad \boldsymbol{L}_1(t) = (0, l, 0)^t$$

The angular momentum is given as initial condition, and the energy is computed with (2.56) using the scaling provided in (2.57). In $\mathcal{S}_2$ the athlete performs LU fast-kick so we use (6.1) to find the same initial condition given by (5.47), which can be rotated by $R_x^{-1}(\mathcal{P})$ to produce $\boldsymbol{M}_3(0)$. In this chapter we are using a more explicit notation for the rigid body solution given by (2.62). The constant s is a direction that is either ± 1 in general, but in our setup where the orbit is always below the equator we have $s = 1$. The constant c is a phase shift that depends on the initial condition, and as such we will include it as a parameter and write $\boldsymbol{\mathcal{M}}(t; \mathcal{E}, J, c)$. The constant s is omitted as it is always $s = 1$.

$$\text{In } \mathcal{S}_3: \quad \text{Shape DU}$$
$$\mathcal{E}_3 = \frac{1}{2}\left(\frac{\cos^2(\mathcal{P}+\mathcal{X})}{{}^tJ_y} + \frac{\sin^2(\mathcal{P}+\mathcal{X})}{{}^tJ_z}\right) = 0.0452$$
$$T_3 = T(\mathcal{E}_3, {}^tJ) = \frac{33.9610}{l}$$
$$\boldsymbol{L}_3(t) = l R_x(\mathcal{P}) \boldsymbol{\mathcal{M}}(t; \mathcal{E}_3, {}^tJ, T_3/4)$$

The (scaled) energy is found by substituting $\boldsymbol{M}_3(0)$ into (2.56), the period of twist T_3 computed with $T(\mathcal{E}, J)$ given by (2.65), and the (scaled) angular momentum in

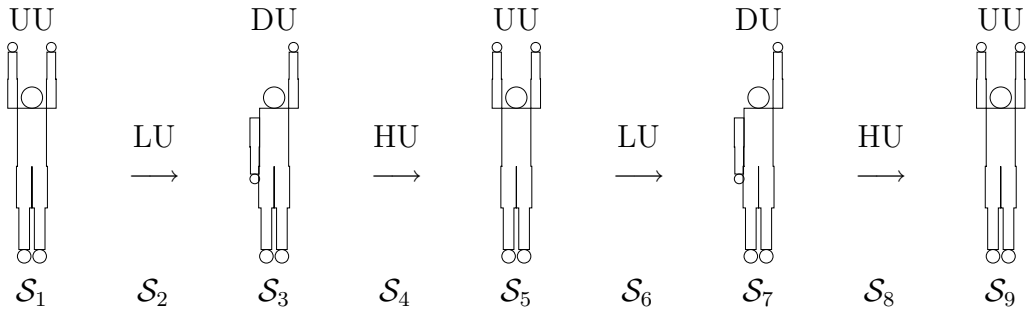

Figure 6.3. Stages of the faster twisting somersault.

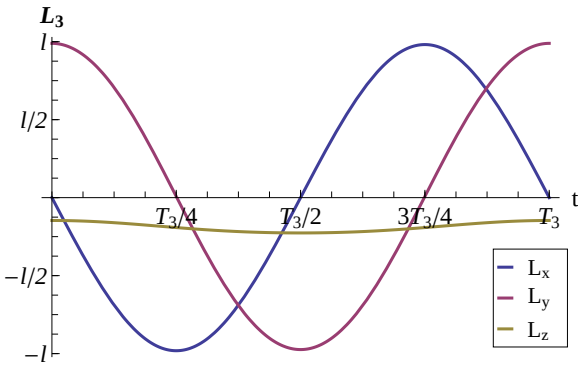

FIGURE 6.4. The components of $\boldsymbol{L}_3(t)$ for one period T_3.

$\mathcal{F}_B$ obtained with (2.62). The angular momentum can then be transformed into $\mathcal{F}_C$ by either applying the identity rotation when the shape is UU (layout position), or $R_x(\mathcal{P})$ when the shape is DU (twist position) to the angular momentum found in $\mathcal{F}_B$. We show the periodic orbit $\boldsymbol{L}_3(t)$ for one period T_3 in Figure 6.4. At some time τ_3 during the orbit $\boldsymbol{L}_3(t)$, the HU fast-kick of $\mathcal{S}_4$ is performed, bringing the athlete's shape back to UU in $\mathcal{S}_5$. The change in $\boldsymbol{L}$ is given by (6.2), so that the initial angular momentum in $\mathcal{S}_5$ is

$$\boldsymbol{L}_5(0;\tau_3) = R_x(\mathcal{X})\boldsymbol{L}_3(\tau_3) = lR_x(\mathcal{P}+\mathcal{X})\boldsymbol{\mathcal{M}}(\tau_3;\mathcal{E}_3,{}^tJ,T_3/4), \tag{6.3}$$

which is dependent on the time τ_3 spent in $\mathcal{S}_3$. In the case of $\tau_3 = nT_3$ for $n \in \mathbb{N}$ the diver reverts to pure somersaulting motion (which was used in Chapter 5 and corresponds to the point where the blue dashed loop of Figure 6.5 crosses the point $\boldsymbol{L}_1(t)$), but for any other τ_3 the twisting motion will not stop because the L_z component is non-zero. The period of twist T_5 will in general be different to T_3, and the case we are interested in is the time τ_3 which minimises T_5, so that we get the fastest possible twist in the twisting somersault in $\mathcal{S}_5$. To find this we look at the scaled energy given by

$$\mathcal{E}_5(\tau_3) = \frac{1}{2}\boldsymbol{\mathcal{M}}^t R_x^t(\mathcal{P}+\mathcal{X})\,{}^sI^{-1}R_x(\mathcal{P}+\mathcal{X})\boldsymbol{\mathcal{M}}, \tag{6.4}$$

where the arguments are $\boldsymbol{\mathcal{M}}(\tau_3;\mathcal{E}_3,{}^tJ,T_3/4)$. The time τ_3 spent in $\mathcal{S}_3$ affects both the initial angular momentum $\boldsymbol{L}_5(0;\tau_3)$ and energy $E_5(\tau_3)$ in $\mathcal{S}_5$, which are plotted in Figure 6.6. Since both of these quantities are periodic in τ_3 with period T_3 we only plot the results for the interval $\tau_3 \in [0,T_3)$. The dashed horizontal lines in Figure 6.6B show it is possible to pick τ_3 so that $\mathcal{E}_5(0) = \mathcal{E}_1 = 0.0243l^2$, $\mathcal{E}_5(0.2713T_3) = \mathcal{E}_3 = 0.0452l^2$, or have the maximum of $\mathcal{E}_5(T_3/2) = 0.0885l^2$. To find the minimum period of twist in the twisting somersault we use (2.65) with the scaled energy given by (6.4). For the formula to be applicable we require $\mathcal{E}_5 > 1/(2\,{}^sI_y)$, but this is always the case for the twisting somersault. Whenever

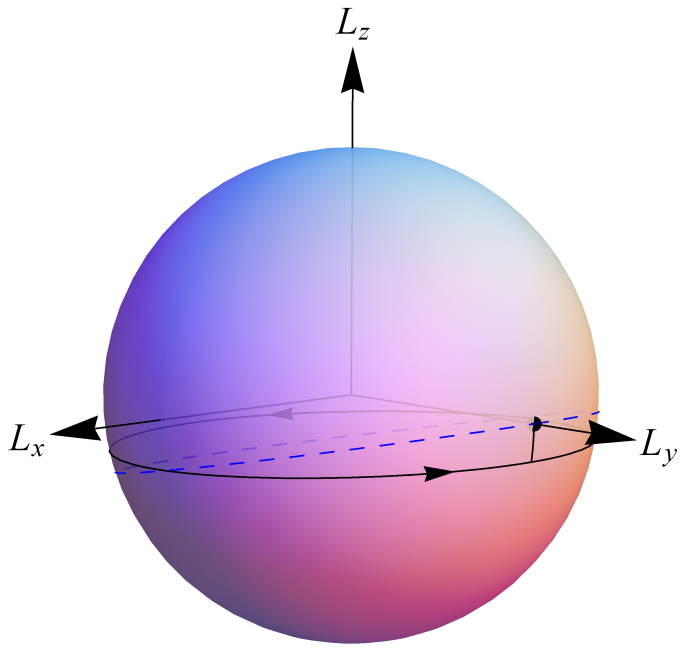

FIGURE 6.5. The point shown on the L_y-axis is the steady (somersault) rotation corresponding to $\boldsymbol{L}_1(t)$ in $\mathcal{S}_1$, the black solid vertical arc stemming from that point illustrates the LU fast-kick of $\mathcal{S}_2$, the black solid loop shows the orbit $\boldsymbol{L}_3(t)$ in $\mathcal{S}_3$, and the blue dashed loop represents the family of initial conditions $\boldsymbol{L}_5(0;\tau_3)$ in $\mathcal{S}_5$.

$\mathcal{E}_5 < 1/(2\,{}^sI_y)$ we have a different set of dynamics known as the wobbling somersault, which is discussed in Appendix I. We show the period of twist $T_5(\tau_3)$ in Figure 6.7, where we can see and numerically verify that

$$\tau_3 = T_3/2 \tag{6.5}$$

yields the minimum period of twist, which is of no surprise as it corresponds to the maximal obtainable energy in $\mathcal{S}_5$. This means that the second shape change that speeds up the twisting the most occurs exactly a half twist after the first shape change. So when we evaluate the initial angular momentum at (6.5) we get

$$\boldsymbol{L}_5(0;T_3/2) = -lR_x(\mathcal{P}+\mathcal{X})\begin{pmatrix} 0 \\ \cos(\mathcal{P}+\mathcal{X}) \\ \sin(\mathcal{P}+\mathcal{X}) \end{pmatrix} = -l\begin{pmatrix} 0 \\ \cos[2(\mathcal{P}+\mathcal{X})] \\ \sin[2(\mathcal{P}+\mathcal{X})] \end{pmatrix}. \tag{6.6}$$

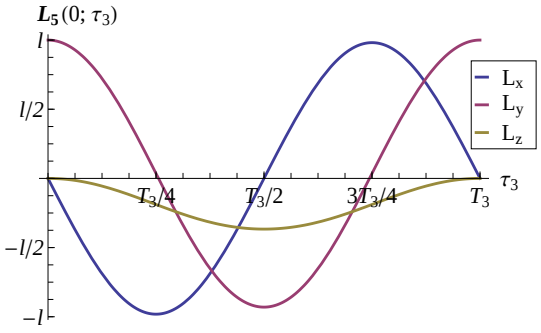

(A) Family of initial conditions given by $\boldsymbol{L}_5(0;\tau_3)$.

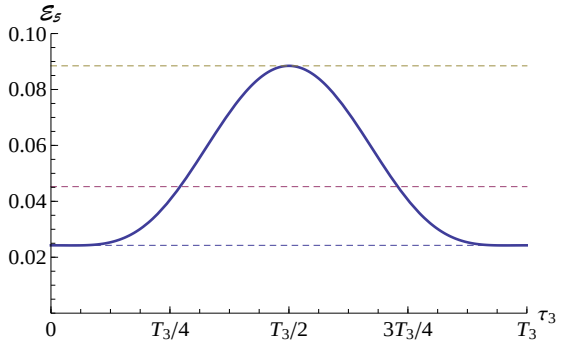

(B) All possible values of $E_5(\tau_3)$.

FIGURE 6.6. The left pane shows the initial angular momentum $\boldsymbol{L}_5(0;\tau_3)$ given by (6.3), and corresponds to the blue dashed loop of Figure 6.5. On the right pane we have the scaled energy $\mathcal{E}_5(\tau_3)$ given by (6.4), which has an additional symmetry being that it is symmetric about $T_3/2$ on the interval $[0, T_3)$.

In $\mathcal{S}_5$: Shape UU

$$\mathcal{E}_5 = \frac{1}{2}\left(\frac{\cos^2\left[2(\mathcal{P}+\mathcal{X})\right]}{{}^sI_y} + \frac{\sin^2\left[2(\mathcal{P}+\mathcal{X})\right]}{{}^sI_z}\right) = 0.0885$$

$$T_5 = T(\mathcal{E}_5, {}^sI) = \frac{17.8720}{l}$$

$$\boldsymbol{L}_5(t) = l\boldsymbol{\mathcal{M}}(t;\mathcal{E}_5, {}^sI, 3T_5/4)$$

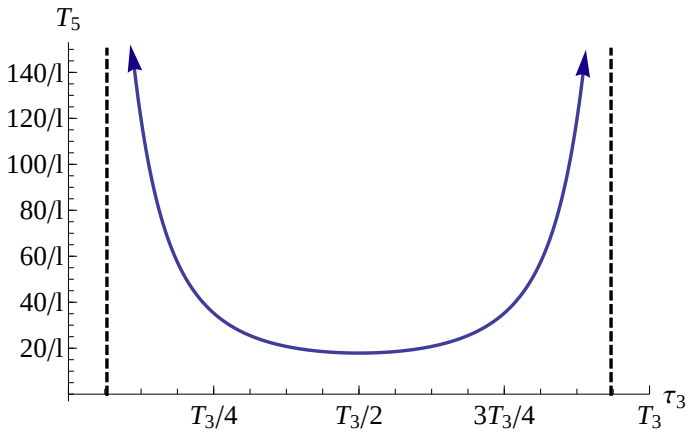

FIGURE 6.7. The period of twist in $\mathcal{S}_5$ when the HU fast-kick of $\mathcal{S}_4$ occurs after time τ_3.

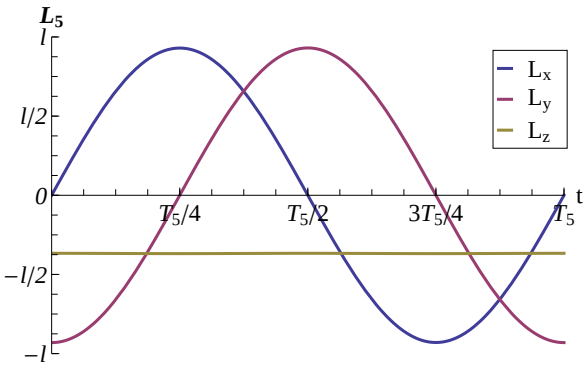

FIGURE 6.8. The L_z component may appear constant but in fact is not as the Jacobi elliptic function dn is oscillatory.

As the optimal τ_3 has been found in (6.5), we now suppress this parameter in $\mathcal{E}_5$ and $\boldsymbol{L}_5(t)$. We see that the period of twist T_5 in $\mathcal{S}_5$ is nearly half the period of twist T_3 found in $\mathcal{S}_3$, hence the athlete has entered a faster twisting somersault state where more twists can be performed in the same amount of time without any additional cost. We show the angular momentum components of this orbit for one period T_5 in Figure 6.8. For n twists to be completed in the faster twisting somersault state we require

$$\tau_5 = nT_5, \tag{6.7}$$

where $n \in \mathbb{N}$ before the LU fast-kick of $\mathcal{S}_6$ brings the athlete's orbit back to the standard twisting somersault state in $\mathcal{S}_7$. We know this is true because $\boldsymbol{L}_5(t)$ is periodic with period T_5, which means $\boldsymbol{L}_5(nT_5) = \boldsymbol{L}_5(0)$, and using (6.1) we can show

$$\boldsymbol{L}_7(0) = \boldsymbol{L}_3(T_3/2) = -l \begin{pmatrix} 0 \\ \cos(2\mathcal{P} + \mathcal{X}) \\ \sin(2\mathcal{P} + \mathcal{X}) \end{pmatrix}. \tag{6.8}$$

In $\mathcal{S}_7$:	Shape DU	$T_7 = T_3 = \dfrac{33.9610}{l}$
	$\boldsymbol{L}_7(t) = \boldsymbol{L}_3(t + T_3/2)$	$\mathcal{E}_7 = \mathcal{E}_3 = 0.0452$

the orbit $\boldsymbol{L}_7(t)$ is a continuation of $\boldsymbol{L}_3(t)$. The final HU fast-kick in $\mathcal{S}_8$ is used to revert the twisting somersaulting motion to pure somersaulting motion. For this we need

$$\tau_7 = \tau_3 = T_3/2, \tag{6.9}$$

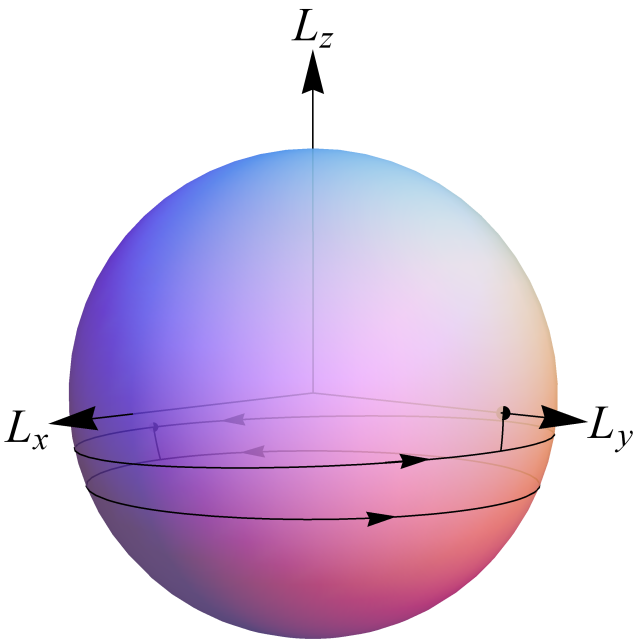

FIGURE 6.9. The athlete takes off and finishes the dive in pure somersaulting motion indicated by the point on the L_y-axis. The upper black loop corresponds to the standard twisting somersault comprising $\boldsymbol{L}_3(t)$ and $\boldsymbol{L}_7(t)$, and the lower black loop corresponds to the faster twisting somersault given by $\boldsymbol{L}_5(t)$.

since

$$\begin{aligned}\boldsymbol{L}_9(0) &= R_x(\mathcal{X})\boldsymbol{L}_7(T_3/2) = R_x(\mathcal{X})\boldsymbol{L}_3(T_3) = R_x(\mathcal{X})\boldsymbol{L}_3(0)\\ &= R_x(\mathcal{X})R_x(-\mathcal{X})\boldsymbol{L}_1 = (0,l,0)^t.\end{aligned}$$

In $\mathcal{S}_9$:	Shape UU	
	$\mathcal{E}_9 = \mathcal{E}_1 = 0.0243$	$\boldsymbol{L}_9(t) = \boldsymbol{L}_1(t)$

In this dive, the diver performs a half-twist in $\mathcal{S}_3$, n twists in $\mathcal{S}_5$, and another half-twist in $\mathcal{S}_7$, resulting in a total of $n+1$ twists being performed. We show the orbit of the complete dive on the L-sphere in Figure 6.9.

Due to the nature of the fast-kick model, the transition stages $\mathcal{S}_i$ for even i take zero time, so to find T_{air} we only need to sum τ_i for odd i. Using (6.5), (6.7), and (6.9) we get

$$T_{air} = nT_5 + T_3 + \tau_1 + \tau_9, \tag{6.10}$$

where the only parameter yet to be determined is the sum

$$T_{som} = \tau_1 + \tau_9, \tag{6.11}$$

which represents the total time spent in pure somersault. To find T_{som} we use the condition that the athlete completes the dive after performing m somersaults with $n+1$ twists, allowing Cabrera's formula (5.78) (with the mod 2π removed by appropriately defining the surface area A) to work.

We showed in (5.79) that $\int_0^{\tau_i} \boldsymbol{L}_i \cdot \boldsymbol{\Omega}_i \, \mathrm{d}t = 0$ for all transition stages, and grouping the fast-kick pairs together, i.e. $\mathcal{S}_2$ with $\mathcal{S}_8$ and $\mathcal{S}_4$ with $\mathcal{S}_6$, gives two closed curves that enclose zero area. Hence the transition stages play no part in the contribution to ϕ in Cabrera's formula (5.78), thereby leaving only the rigid body stages in which we can use (5.80) to obtain

$$\phi = -\frac{A_s + nA_f}{l^2} + l\Big[{}^{s}I_y^{-1} T_{som} + 2\mathcal{E}_3 T_3 + 2n\mathcal{E}_5 T_5\Big], \tag{6.12}$$

where A_s is the area bounded between the equator and $\boldsymbol{L}_3(t), \boldsymbol{L}_7(t)$, and A_f is the area between the equator and $\boldsymbol{L}_5(t)$, both of which can be computed with (5.93). As we want $\phi = 2m\pi$ for m somersaults, we rearrange (6.12) to get

$$T_{som} = {}^{s}I_y \left[\frac{1}{l}\left(2m\pi + \frac{A_s + nA_f}{l^2}\right) - 2\big(\mathcal{E}_3 T_3 + n\mathcal{E}_5 T_5\big)\right]. \tag{6.13}$$

Since both A_s and A_f are quadratic in l according to (5.93), and both T_3 and T_5 are inversely proportional to l, this also means $\tau_1 + \tau_9$ is inversely proportional to l. Evaluating the constants numerically in (6.13) gives

$$A_s/l^2 = 1.1891 \qquad \mathcal{E}_3 = 0.0452 \qquad {}^{s}I_y = 20.6091$$
$$A_f/l^2 = 2.3088 \qquad \mathcal{E}_5 = 0.0885,$$

so plugging these numbers in (6.13) yields

$$T_{som} = \frac{1}{l}\Big(129.4905m - 17.5751n - 38.8309\Big). \tag{6.14}$$

The other rigid body stages have a twist component so we denote that total time as T_{twi}, where

$$T_{twi} = \tau_3 + \tau_5 + \tau_7 = T_3 + nT_5 = \frac{1}{l}\Big(17.8720n + 33.9610\Big). \tag{6.15}$$

These equations are for a dive consisting of m somersaults and $n+1$ twists. The airborne time T_{air} is given by (6.10), so substituting in all the values found we get

$$T_{air} = T_{som} + T_{twi} = \frac{1}{l}\Big(129.4905m + 0.2970n - 4.8699\Big). \tag{6.16}$$

The times T_{som}, T_{twi}, and T_{air} for the previous fast-kick dive explored in Chapter 5 can be found in (5.87), (5.61), and (5.88). To avoid confusion with the new formulas we will explicitly write $(ch\ 5)$ as left superscript to indicate that these

are obtained from Chapter 5. The equations were given for the case ${}^tJ_x = {}^tJ_y > {}^tJ_z$ but hold true for the more general ${}^tJ_x > {}^tJ_y > {}^tJ_z$, provided we use A given by (5.93) and ${}^tT$ given by (5.94) instead of the original formulas. The equations for the previous fast-kick dive are for the dive consisting of m somersaults and n twists, so before we can make a comparison we set $n \to n+1$, ${}^tT \to T_3$, $A \to A_s$, $E_1 \to l^2/(2\,{}^sI_y)$, $E_3 \to \mathcal{E}_3 l^2$, and evaluating gives:

$$ {}^{(ch\,5)}T_{som} = \frac{1}{l}\Big(129.4905m - 38.8309n - 38.8309\Big) \tag{6.17}$$

$$ {}^{(ch\,5)}T_{twi} = \frac{1}{l}\Big(33.9610n + 33.9610\Big) \tag{6.18}$$

$$ {}^{(ch\,5)}T_{air} = \frac{1}{l}\Big(129.4905m - 4.8699n - 4.8699\Big). \tag{6.19}$$

Comparing these results to (6.14), (6.15), and (6.16) we see that for a dive consisting of the same number of somersaults and twists, the new dive spends significantly less time in motion involving twist and more time in pure somersault. In the faster twisting somersault state there is more angular momentum about the twist axis resulting in faster twist, which therefore also means the somersaulting motion is slower. The airborne time required for the new dive is longer, but that is due to the nature of the 2-body model where ${}^tJ_y < {}^sI_y$. With more movable segments so that pure somersaults may be performed in pike or tuck as opposed to the layout position, we would expect T_{air} to be less with the faster twisting somersault dive.

We require T_{som} to be positive in (6.14) and (6.17), so with the standard twisting somersault dive of Chapter 5 shown in Figure 6.1 the maximum number of twists with m somersaults is $\lfloor 3.3347m \rfloor$, while for the faster twisting somersault dive shown in Figure 6.3 it is $\lfloor 7.3679m - 1.2094 \rfloor$ (recall that the formulas were for $n+1$ twists). For $m = 1.5$ somersaults we find maximum number of twists for the standard twisting somersault dive is[1] 5, while for the faster twisting somersault dive it is 9. Note that these numbers are only valid for the fast-kick model, and with realistic arm motions the numbers will be lower. We are now going to use the 3-body model described in Chapter 3.5.2 to allow the athlete to use both arms when performing impulsive shape changes, and later in Chapter 6.3 we will repeat the computation using realistic arm motions to demonstrate the 513XD dive simulation.

6.2 513XD - Two-armed Diver

So far we have covered the one-armed diver performing LU and HU fast-kicks, where its effect is given by (6.1) and (6.2), respectively. From a symmetry perspective, if the diver instead uses their right arm to perform UL and UH fast-kicks,

[1] In Chapter 5.3 we showed this number was 4, but that is due to the assumption ${}^tJ_x = {}^tJ_y$ making the period of twist slightly longer, by about $0.5329/l$.

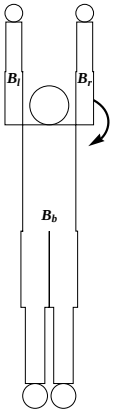

(A) UL fast-kick
$\boldsymbol{L}_+ = R_x(\mathcal{X})\boldsymbol{L}_-$
$\boldsymbol{q}_+ = \mathcal{R}(-\mathcal{X})\boldsymbol{q}_-$

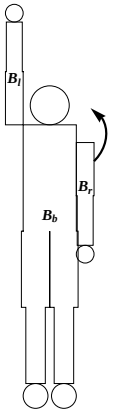

(B) UH fast-kick
$\boldsymbol{L}_+ = R_x(-\mathcal{X})\boldsymbol{L}_-$
$\boldsymbol{q}_+ = \mathcal{R}(\mathcal{X})\boldsymbol{q}_-$

FIGURE 6.10. Impulsive shape changes using the right arm.

then the only modifications would be $\mathcal{X} \to -\mathcal{X}$, $\mathcal{P} \to -\mathcal{P}$, and the direction of twist would change from counterclockwise to clockwise.

We now study the dual fast-kick which involves using both arms in the impulsive shape change shown in Figure 6.11. To compute the tilt $\mathcal{Y}$ generated by the

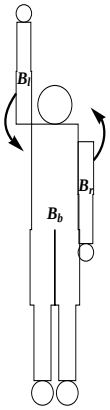

(A) LH fast-kick
$\boldsymbol{L}_+ = R_x(-\mathcal{Y})\boldsymbol{L}_-$
$\boldsymbol{q}_+ = \mathcal{R}(\mathcal{Y})\boldsymbol{q}_-$

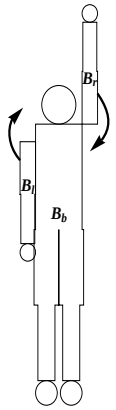

(B) HL fast-kick
$\boldsymbol{L}_+ = R_x(\mathcal{Y})\boldsymbol{L}_-$
$\boldsymbol{q}_+ = \mathcal{R}(-\mathcal{Y})\boldsymbol{q}_-$

FIGURE 6.11. Impulsive shape changes involving both arms. In the case of the LL fast-kick and HH fast-kick, both arms move symmetrically resulting in no net tilt, so we are not interested in those cases.

dual fast-kick, we start with the reduced equations of motion given by (5.38), and follow the same process used in (5.44) which determined $\mathcal{X} = 0.147$, allowing for comparison to be made later on. In the computation we need to use the tensor of inertia I and angular momentum shift $\boldsymbol{A}$ derived for the 3-body model, which are given by (3.53) and (3.54), respectively. The integrand in (5.44) then becomes

$$-I_{xx}^{-1}(\alpha_l, \alpha_r)(A_l(\alpha_l, \alpha_r)\dot{\alpha}_l + A_r(\alpha_l, \alpha_r)\dot{\alpha}_r),$$

where $A_l(\alpha_l, \alpha_r), A_r(\alpha_l, \alpha_r)$ are given in (3.56), and

$$I_{xx}(\alpha_l, \alpha_r) = b_4 - 2b_1(\cos\alpha_l + \cos\alpha_r) + 2b_2(\sin\alpha_l + \sin\alpha_r) - 2b_3\cos(\alpha_l + \alpha_r).$$

For our shape change of interest we can parametrise the angles as

$$\alpha_l = \alpha \qquad \alpha_r = \pi - \alpha \qquad \text{for } \alpha \in [0, \pi].$$

In this parametrisation the DU position corresponds to $\alpha = 0$, and UD position when $\alpha = \pi$. The parametrisation simplifies the integrand, and thus the integral (5.44) becomes

$$\begin{aligned} \mathcal{Y} &= -\int_{\pi}^{0} I_{xx}^{-1}(\alpha_l, \alpha_r)(A_l(\alpha_l, \alpha_r)\dot{\alpha}_l + A_r(\alpha_l, \alpha_r)\dot{\alpha}_r)\,\mathrm{d}\alpha \\ &= 2\int_{0}^{\pi} \frac{b_0 + b_3 + b_2\sin\alpha}{b_4 + 2b_3 + 4b_2\sin\alpha}\,\mathrm{d}\alpha \\ &= \frac{\pi}{2}\left(1 - \frac{b_\Sigma}{b_R}\right) - \frac{b_\Sigma}{b_R}\arctan\left(\frac{4b_2}{b_R}\right) = 0.330, \end{aligned} \tag{6.20}$$

where

$$\begin{aligned} b_\Sigma &= b_4 - 2b_3 - 4b_0 = 15.191 \\ b_R &= \sqrt{(2b_3 + b_4)^2 - 16b_2^2} = 18.324. \end{aligned}$$

The integral (6.20) is evaluated using Weierstrass' substitution, and because the derivation uses the same techniques provided in Appendix H for computing $\mathcal{X}$, we omit it here and provide the end result only. The result shows that the tilt produced by using a dual fast-kick is more than twice the tilt generated from a single arm, so the minimum period of twist in $\mathcal{S}_5$ is reduced much more compared to the one-armed diver.

Repeating the simulation in Chapter 6.1 for the dive shown in Figure 6.12 changes the the tilt generated in the transition stages $\mathcal{S}_4$ and $\mathcal{S}_6$, which affects the rigid body stage $\mathcal{S}_5$, but leaves the remaining stages intact.

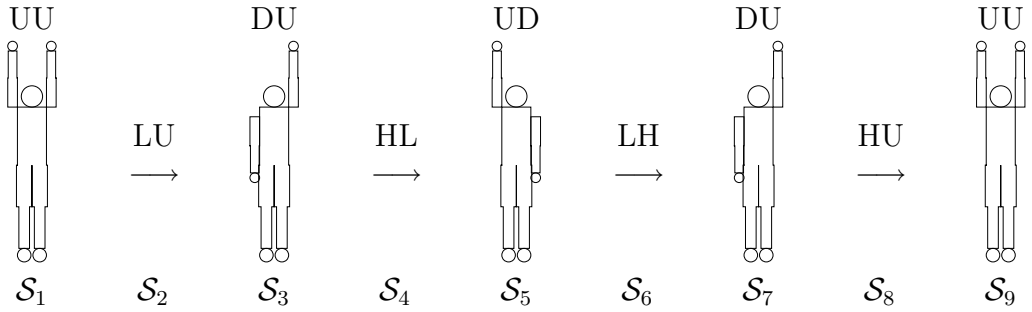

FIGURE 6.12. Stages of the faster twisting somersault using dual fast-kicks.

In $\mathcal{S}_5$: Shape UD

$$
\begin{aligned}
{}^{d}\mathcal{E}_5 &= \frac{1}{2}\widetilde{\boldsymbol{\mathcal{M}}}^{t}\,{}^{t}J^{-1}\widetilde{\boldsymbol{\mathcal{M}}} = 0.1835\\
\text{where } \widetilde{\boldsymbol{\mathcal{M}}} &= R_x(\mathcal{P}+\mathcal{Y})\boldsymbol{L}_3(T_3/2)/l\\
{}^{d}T_5 &= T\Big({}^{d}\mathcal{E}_5, {}^{t}J\Big) = \frac{11.3854}{l}\\
{}^{d}\boldsymbol{L}_5(t) &= lR_x(-\mathcal{P})\boldsymbol{\mathcal{M}}(t; {}^{d}\mathcal{E}_5, {}^{t}J, 3\,{}^{d}T_5/4)
\end{aligned}
$$

We use left superscript d to represent quantities obtained with the dual fast-kick. The area ${}^{d}A_f$ bounded between the equator and ${}^{d}\boldsymbol{L}_5(t)$ is ${}^{d}A_f = 3.5465l^2$, and re-evaluating (6.13), (6.15), and (6.10) with the new parameters ${}^{d}\mathcal{E}_5$, ${}^{d}T_5$, ${}^{d}A_f$, while keeping everything else unchanged, we find:

$$
{}^{d}T_{som} = \frac{1}{l}\Big(129.4905m - 13.0164n - 38.8309\Big) \tag{6.21}
$$

$$
{}^{d}T_{twi} = \frac{1}{l}\Big(11.3854n + 33.9610\Big) \tag{6.22}
$$

$$
{}^{d}T_{air} = \frac{1}{l}\Big(129.4905m - 1.6310n - 4.8699\Big). \tag{6.23}
$$

When compared to (6.14) and (6.15), we see that ${}^{d}T_{som}$ is a little longer than T_{som}, but ${}^{d}T_{twi}$ is a little shorter than T_{twi}, which is expected. For m somersaults we find the new maximum number of twists to be $\lfloor 9.9483m - 1.9832 \rfloor$. So for $m = 1.5$ somersaults it increases the maximum number twists to 12, compared to 5 for the dive shown in Figure 6.1, and 9 for the dive shown in Figure 6.3.

6.3 The Realistic 513XD Dive

We now repeat the dive shown in Figure 6.12 using realistic shape changes to simulate the 513XD dive, i.e. the dive consisting of one and a half forward somersaults with five twists. Unlike in Chapter 6.2, we will now do full numerical evaluation with realistic arm velocities. The arm movements will take a quarter second each to complete and follow the shape change path of a cubic spline as done in Chapter 5. So for each $\mathcal{S}_{2k}$ with integer $k \geq 1$ we have

$$\tau_{2k} = 1/4, \tag{6.24}$$

since every even stage is a transition stage. In order to obtain the numerical solutions in the 513XD dive, we choose to fix $l = 100$ as that is the angular momentum used in Chapter 5.

In $\mathcal{S}_1$:	Shape UU
energy	$E_1 = \frac{1}{2} l^2 \, {}^s I_y^{-1} = 243.61$
orbit	$\boldsymbol{L}_1(t) = (0, l, 0)^t$

The athlete takes off in pure somersaulting motion and remains in steady rotation for duration τ_1 before moving on to $\mathcal{S}_2$.

In $\mathcal{S}_2$:	Shape change LU
average energy	$\bar{E}_2 = \frac{1}{2\tau_2} \int_0^{\tau_2} \boldsymbol{L}_2(t) \cdot \boldsymbol{\Omega}_2(t) \, \mathrm{d}t = 314.71$
end point	$\boldsymbol{L}_2(\tau_2) = (-97.957, 5.328, -19.393)^t$

We compute $\boldsymbol{L}_2(t)$ numerically by solving the equations of motion (3.25), and show the evolution on the L-sphere in Figure 6.15B.

In $\mathcal{S}_3$:	Shape DU
energy	$E_3 = \frac{1}{2} \tilde{\boldsymbol{M}}^t \, {}^t J^{-1} \tilde{\boldsymbol{M}} = 460.012$
	where $\tilde{\boldsymbol{M}} = R_x(-\mathcal{P}) \boldsymbol{L}_2(\tau_2)$
period of twist	$T_3 = T(E_3/l^2, {}^t J) = 0.3325$
orbit	$\boldsymbol{L}_3(t) = l R_x(\mathcal{P}) \boldsymbol{\mathcal{M}}(t; E_3/l^2, {}^t J, 0.1638)$

In order to determine how long the athlete should remain in $\mathcal{S}_3$, we look for the maximal obtainable energy in $\mathcal{S}_5$ after the HL shape change of $\mathcal{S}_4$. The energy $E_5(\tau_3)$ therefore depends on the time τ_3 spent in $\mathcal{S}_3$, which we plot in Figure 6.13A

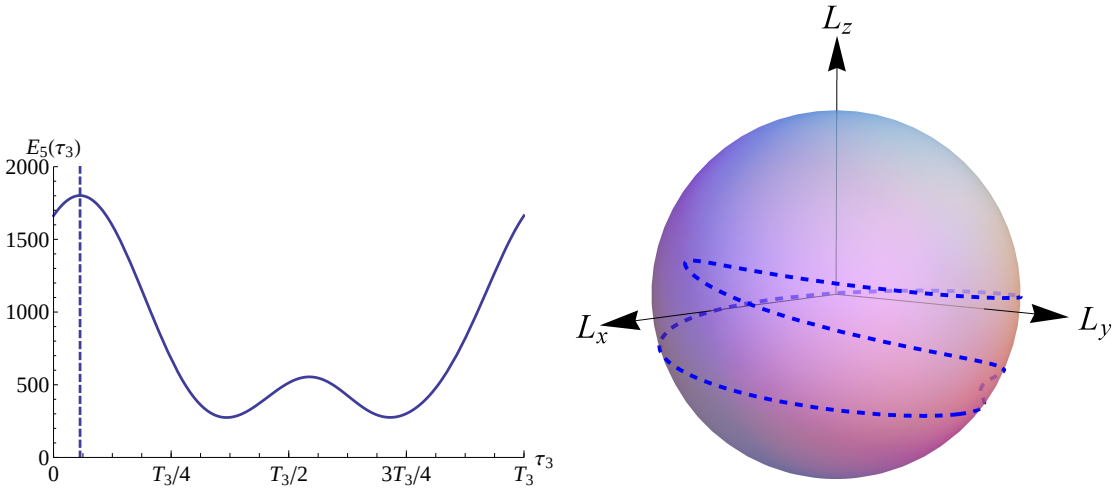

(A) The energy depends on τ_3.

(B) The family of $\boldsymbol{L}_5(0, \tau_3)$.

FIGURE 6.13. The left pane shows the energy where the maximum is $E_5(0.0564T_3) = 1801.23$. The right pane shows the family of possible initial angular momentum for $\mathcal{S}_5$ depending on the time τ_3.

to find the optimal

$$\tau_3 = 0.0564T_3 = 0.0187. \tag{6.25}$$

The evolution of $\boldsymbol{L}_3(t)$ is shown in Figure 6.15C, where the end point is

$$\boldsymbol{L}_3(\tau_3) = (-93.3061, -29.3789, -20.7569)^t.$$

In $\mathcal{S}_4$:	Shape change HL
average energy	$\bar{E}_4 = \dfrac{1}{2\tau_4}\displaystyle\int_0^{\tau_4} \boldsymbol{L}_4(t) \cdot \boldsymbol{\Omega}_4(t)\, \mathrm{d}t = 732.51$
end point	$\boldsymbol{L}_4(\tau_4) = (-49.041, 64.607, -58.489)^t$

We show the evolution of $\boldsymbol{L}_4(t)$ in Figure 6.15D.

In $\mathcal{S}_5$:	Shape UD
energy	$E_5 = \dfrac{1}{2}\tilde{\boldsymbol{M}}^t\, {}^tJ^{-1}\tilde{\boldsymbol{M}} = 1801.23$
	where $\tilde{\boldsymbol{M}} = R_x(\mathcal{P})\boldsymbol{L}_4(\tau_4)$
period of twist	$T_5 = T(E_5/l^2, {}^tJ) = 0.1151$
orbit	$\boldsymbol{L}_5(t) = lR_x(-\mathcal{P})\boldsymbol{\mathcal{M}}(t; E_5/l^2, {}^tJ, 0.0404)$

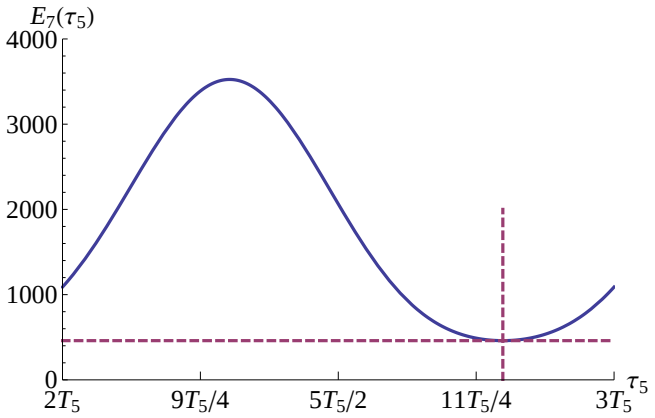

FIGURE 6.14. The energy $E_7(\tau_5)$ in $\mathcal{S}_7$ when initiating the LH shape change of $\mathcal{S}_6$ at arbitrary τ_5 in $\mathcal{S}_5$. The minimum energy is $E_7(0.0919 + 2T_5) = 460.012$ indicated by the intersection of the two dashed lines.

The athlete is in the faster twisting somersault state and remains in $\mathcal{S}_5$ for nearly three periods of twist, as a total of five loops around the L-sphere (corresponding to the five twists) is required. In order to reach the faster twisting somersault state from pure somersault the diver will have completed slightly more than one twist, which can be seen in the evolution of $\boldsymbol{L}_2(t)$ to $\boldsymbol{L}_4(t)$ given by Figures 6.15B to 6.15D. By symmetry, a bit more than one twist will also be required when the athlete returns to pure somersault from here, hence τ_5 is between $2T_5$ and $3T_5$. To determine the precise time τ_5 we look at the resulting energy after the LH shape change, which we plot in Figure 6.14. The graph shows that it is possible for the diver to obtain even more energy resulting in a shorter period of twist, which corresponds to traversing further down towards the south pole on the L-sphere. However, here we want the diver to return to the orbit $\boldsymbol{L}_3(t)$ specified in $\mathcal{S}_3$ so that the dive can be completed. To achieve this, it turns out the diver needs to enter the state of minimum energy, which occurs at

$$\tau_5 = \tilde{\tau}_5 + 2T_5 = 0.0919 + 2T_5 = 0.3221, \tag{6.26}$$

where the $2T_5$ phase shift is needed to enforce the number of twists to be between two and three in $\mathcal{S}_5$. The evolution of $\boldsymbol{L}_5(t)$ is shown in Figure 6.15E, where the end point is

$$\boldsymbol{L}_5(\tau_5) = (49.0409, 64.6069, -58.4888)^t.$$

In $\mathcal{S}_6$:	Shape change LH
average energy	$\bar{E}_6 = \dfrac{1}{2\tau_6}\displaystyle\int_0^{\tau_6} \boldsymbol{L}_6(t)\cdot\boldsymbol{\Omega}_6(t)\,\mathrm{d}t = 732.51$
	is the same as $\bar{E}_4$
end point	$\boldsymbol{L}_6(\tau_6) = (93.306, -29.379, -20.757)^t$

The evolution of $\boldsymbol{L}_6(t)$ is shown in Figure 6.15F, which brings the athlete back to the standard twisting somersaulting orbit.

In $\mathcal{S}_7$:	Shape DU	
	$E_7 = E_3 = 460.012$	$T_7 = T_3 = 0.3325$
orbit	$\boldsymbol{L}_7(t) = \boldsymbol{L}_3(t + 0.1523)$,	

which can alternatively be written as

$$\boldsymbol{L}_7 = lR_x(\mathcal{P})\boldsymbol{\mathcal{M}}\big(t; E_7/l^2, {}^tJ, c_7\big),$$

where $c_7 = T_3/2 - \tau_3 - c_3$, and $c_3 = 3.1390$ is the constant that appears in $\boldsymbol{L}_3(t)$.

Again the athlete only stays in $\mathcal{S}_7$ for a brief period of time before moving onto the last transition stage $\mathcal{S}_8$. By symmetry and numerical verification we can show

$$\tau_7 = \tau_3, \tag{6.27}$$

which makes the HU shape change of $\mathcal{S}_8$ bring the athlete back into pure somersaulting motion for $\mathcal{S}_9$.

In $\mathcal{S}_8$:	Shape change HU
average energy	$\bar{E}_8 = \dfrac{1}{2\tau_2}\displaystyle\int_0^{\tau_8} \boldsymbol{L}_8(t)\cdot\boldsymbol{\Omega}_8(t)\,\mathrm{d}t = 314.71$
	is the same as $\bar{E}_2$
end point	$\boldsymbol{L}_8(\tau_8) = (0, 100, 0)^t$

In $\mathcal{S}_9$:	Shape UU
energy	$E_9 = E_1 = \dfrac{1}{2} l^2\, {}^sI_y^{-1} = 243.61$
orbit	$\boldsymbol{L}_9(t) = \boldsymbol{L}_1(t) = (0, 100, 0)^t$

The diver returns to pure somersaulting motion in $\mathcal{S}_9$, ready to complete the dive. Combining the trajectories of $\boldsymbol{L}_i(t)$ shown in Figures 6.15B to 6.15H we get the complete trajectory shown in Figure 6.15I for the 513XD dive. The time τ_9 spent

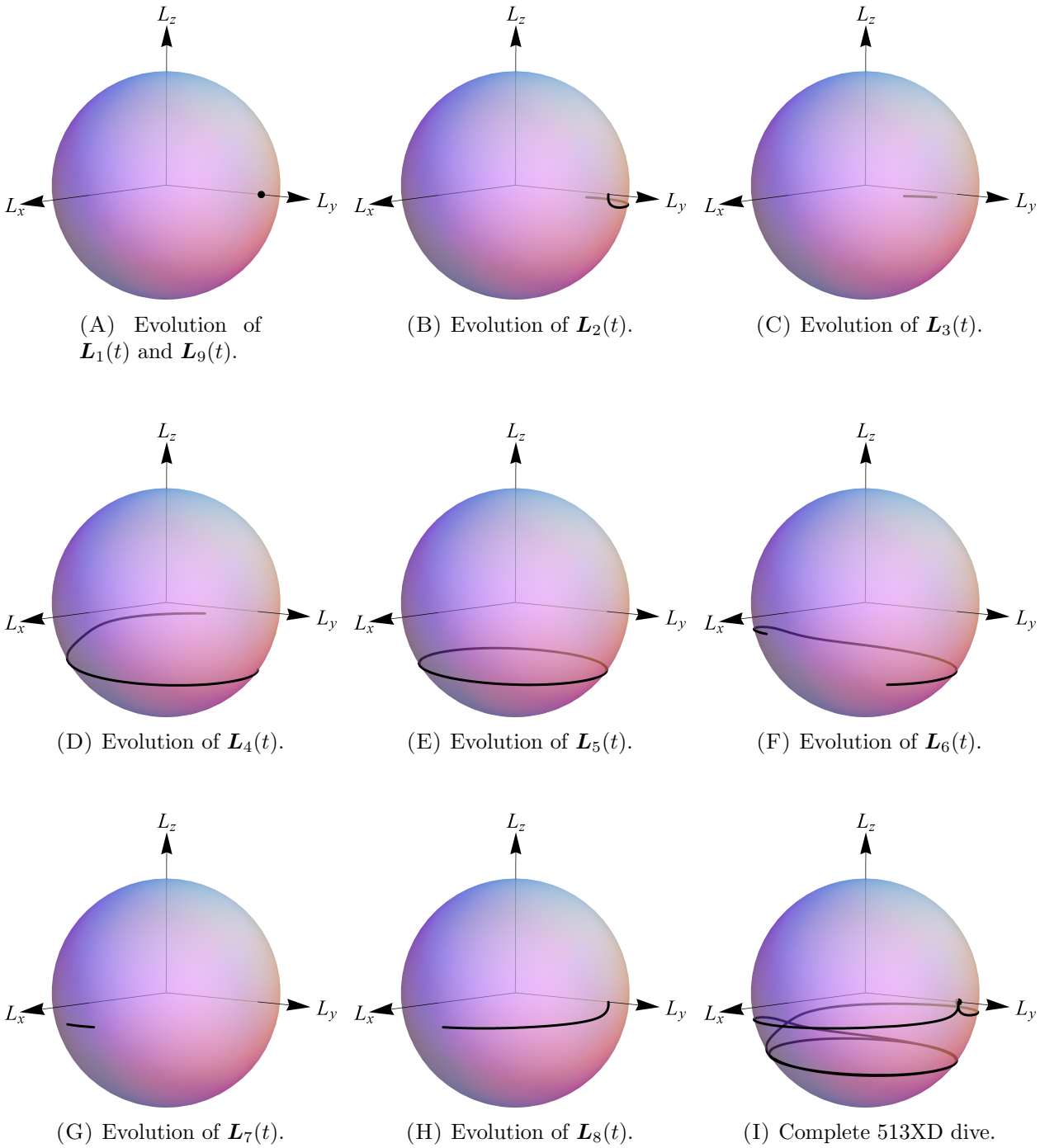

(A) Evolution of $\boldsymbol{L}_1(t)$ and $\boldsymbol{L}_9(t)$.

(B) Evolution of $\boldsymbol{L}_2(t)$.

(C) Evolution of $\boldsymbol{L}_3(t)$.

(D) Evolution of $\boldsymbol{L}_4(t)$.

(E) Evolution of $\boldsymbol{L}_5(t)$.

(F) Evolution of $\boldsymbol{L}_6(t)$.

(G) Evolution of $\boldsymbol{L}_7(t)$.

(H) Evolution of $\boldsymbol{L}_8(t)$.

(I) Complete 513XD dive.

Figure 6.15. The evolution of $\boldsymbol{L}_i(t)$ in each stage. The pure somersaulting stages $\mathcal{S}_1$ and $\mathcal{S}_9$ have the same dynamics so they are only illustrated once, and the last figure shows the complete trajectory on the L-sphere for the 513XD dive.

in $\mathcal{S}_9$ is chosen to ensure the athlete enters the water correctly, with head-first entry into the water. To determine the total time $T_{som} = \tau_1 + \tau_9$ spent in pure somersault we use Cabrera's formula (5.78), where the result becomes

$$\phi = \phi_{som} + \sum_{i=2}^{8} \left[\frac{1}{l} \int_0^{\tau_i} \boldsymbol{L}_i(t) \cdot \boldsymbol{\Omega}_i(t) \, \mathrm{d}t - \frac{A_i}{l^2} \right]. \tag{6.28}$$

We want $\phi = 3\pi$ for one and a half somersaults and need to find ϕ_{som}, which is the total somersault angle obtained from the pure somersaulting stages $\mathcal{S}_1$ and $\mathcal{S}_9$. The integral yields the product of (average) energy and time, and from using the (average) energies found we get

$$\sum_{i=2}^{8} \int_0^{\tau_i} \boldsymbol{L}_i(t) \cdot \boldsymbol{\Omega}_i(t) \, \mathrm{d}t = \bar{E}_2 + \bar{E}_4 + 4E_3\tau_3 + 2E_5\tau_5 = 2242.07. \tag{6.29}$$

The total area A needed in the computation of the geometric phase is partitioned into sub-areas denoted by A_i, where $A = \sum_{i=2}^{8} A_i$. Each A_i is enclosed by $\boldsymbol{L}_i(t)$, either one or two vertical arcs on the sphere, and the equator. We show the first three sub-areas in Figure 6.16, and to compute each sub-area A_i we use the line integral

$$A_i = \oint_{\boldsymbol{C}_i} \boldsymbol{F}(\boldsymbol{x}(s)) \cdot \dot{\boldsymbol{x}}(s) \, \mathrm{d}s, \tag{6.30}$$

which comes from (5.92) with $\boldsymbol{F}$ defined in (5.91). Each loop $\boldsymbol{C}_i$ will consist of a segment from the equator, one or two vertical arcs and $\boldsymbol{L}_i(t)$. Now the equator has $L_z = 0$ so $\boldsymbol{F} = \boldsymbol{0}$, hence this part of the line integral is zero. The vertical arcs

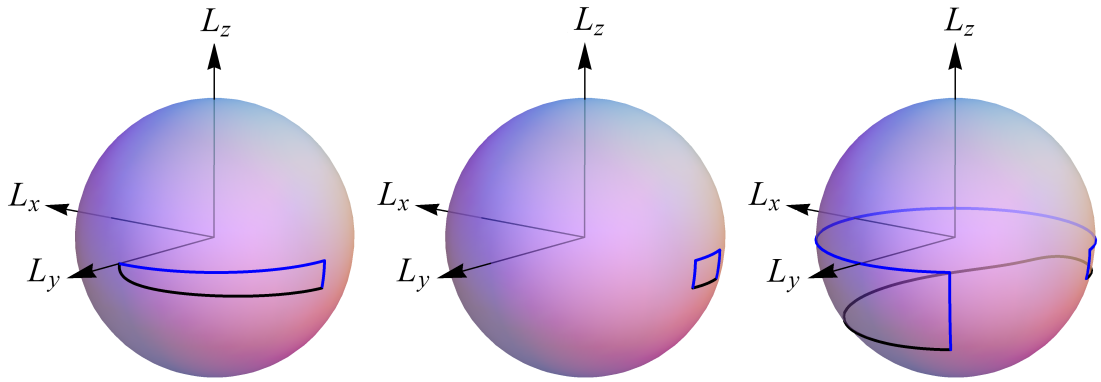

(A) $A_2 = 2406.62$. (B) $A_3 = 722.037$. (C) $A_4 = 23770.8$.

Figure 6.16. Due to symmetry $A_6 = A_4, A_7 = A_3$, and $A_8 = A_2$. The sub-area $A_5 = 97593.3$ is not shown here.

have parametric form given by (5.82), so

$$\boldsymbol{F}(\boldsymbol{x}(s)) = l \begin{pmatrix} \cot\theta\sin\phi \\ -\cot\theta\cos\phi \\ 0 \end{pmatrix} \text{ and } \dot{\boldsymbol{x}} = l \begin{pmatrix} \sin\theta\cos\phi \\ \sin\theta\sin\phi \\ \cos\theta \end{pmatrix},$$

hence the dot product is zero and this too yields no contribution to the line integral (6.30). The only contribution must therefore come from the line segment $\boldsymbol{L}_i(t)$, meaning

$$A_i = \int_0^{\tau_i} \boldsymbol{F}\big(\boldsymbol{L}_i(t)\big) \cdot \dot{\boldsymbol{L}}_i(t)\,\mathrm{d}t. \tag{6.31}$$

Evaluating the integral yields results shown in Figure 6.16 and we therefore have

$$A = \sum_{i=2}^{8} A_i = 151392. \tag{6.32}$$

Using this result along with (6.29) we find that (6.28) becomes

$$\phi_{som} = 3\pi - 22.4207 + 15.1392 = 2.1433, \tag{6.33}$$

where $\phi_{som} = 2E_1T_{som}/l = 2.1433$, and so $T_{som} = 0.4417$. Distributing this time evenly between $\mathcal{S}_1$ and $\mathcal{S}_9$ for aesthetic reasons gives

$$\tau_1 = \tau_9 = 0.2209. \tag{6.34}$$

Finally, we plot the components of $\boldsymbol{L}(t)$ and $\boldsymbol{q}(t)$ using τ_1 and τ_9 given by (6.34) to ensure proper entry into the water. In Figure 6.17A we find L_x is anti-symmetric, while L_y and L_z are symmetric about $T_{air}/2$. The athlete takes off in pure somersault and uses shape change to get into twisting somersault orbit, so it makes sense that the dynamics allowing the athlete to leave steady rotation are the same dynamics which bring the athlete back, hence the symmetry. We solve the equations of orientation (3.2) numerically and plot the result in Figure 6.17B, which shows

$$q_0(t) = q_2(T_{air} - t) \qquad\qquad q_1(t) = -q_3(T_{air} - t).$$

This symmetry is a result of (6.34), and would not exist had any other choice of distributing τ_1 and τ_9 been made.

6.4 From Pure Somersault to Pure Twist

The 513XD dive uses the concept of the athlete entering and exiting a faster twist state by performing an additional pair of shape changes. For impulsive shape changes, we showed that the optimal time to fast-kick is after a half period of twist, so complexity of the dive aside, there is no reason why this procedure cannot be repeated to enter even faster twisting somersault states. In this final section

we are going to show it is possible to take off in pure somersault and reach a state of pure twist using only appropriately timed fast-kicks.

So far we have used standard (slower) twisting somersault and faster twisting somersault to distinguish between the different speeds of twist, but with additional twist speeds it is easier to simply define the term twist-level $\mathcal{T}_i$ to represent the different speeds of twist. The standard (slower) twisting somersault has twist-level $\mathcal{T}_1$, and the faster twisting somersault has twist-level $\mathcal{T}_2$ or $\mathcal{T}_3$, depending on whether one arm or two arms is used for the second fast-kick. Essentially the index is the total number of times the arms have moved in favour of speeding up the twist, where dual fast-kicks increment the index by two. Impulsive shape changes that slow down the twist lower the index, and by convention the pure somersault will have twist-level $\mathcal{T}_0$.

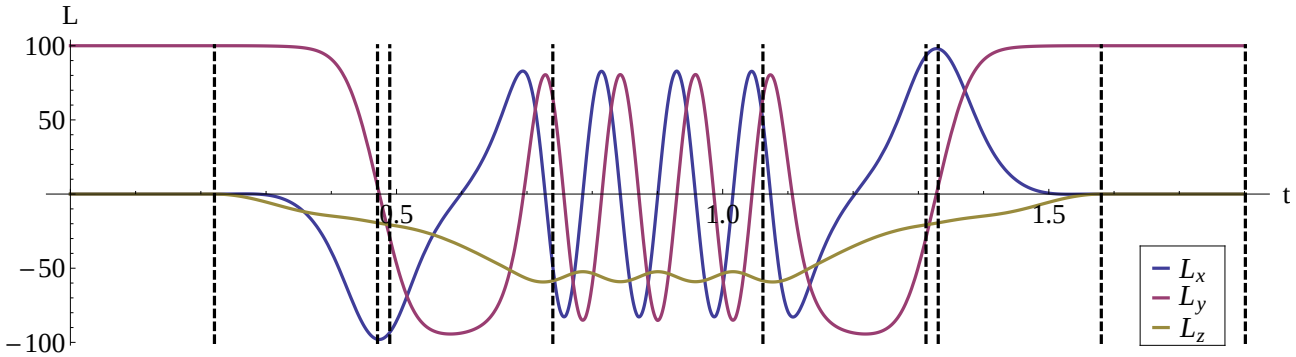

(A) Trajectory of $\boldsymbol{L}$.

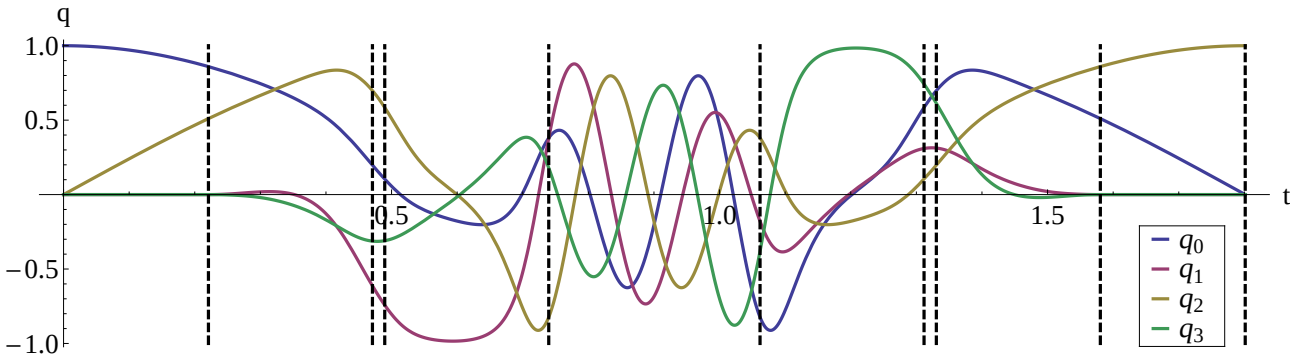

(B) Trajectory of $\boldsymbol{q}$.

Figure 6.17. The evolution of the angular momentum $\boldsymbol{L}(t)$ and quaternion $\boldsymbol{q}(t)$ for the 513XD dive. The vertical dashed lines separate the different stages of the dive, from $\mathcal{S}_1$ to $\mathcal{S}_9$. The airborne time for this simulation with $l = 100$ is 1.8 seconds.

In the dive given by Figure 6.3 for the one-armed diver, we have $\mathcal{S}_5$ corresponding to twist-level $\mathcal{T}_2$. Now if the diver instead remained in $\mathcal{S}_5$ for $T_5/2$ duration (as opposed to nT_5) before executing the LU fast-kick in $\mathcal{S}_6$, then the diver would reach twist-level $\mathcal{T}_3$ rather than revert back to twist-level $\mathcal{T}_1$.

Alternate $\mathcal{S}_7$:	Shape DU
scaled energy	$\mathcal{E}_7 = \frac{1}{2}\widetilde{\boldsymbol{\mathcal{M}}}^t\, {}^tJ^{-1}\widetilde{\boldsymbol{\mathcal{M}}} = 0.1673$
	where $\widetilde{\boldsymbol{\mathcal{M}}} = R_x(-\mathcal{P}-\mathcal{X})\boldsymbol{L}_5(T_5/2)$
period of twist	$T_7 = T(\mathcal{E}_7, {}^tJ) = \dfrac{12.0281}{l}$
orbit	$\boldsymbol{L}_7(t) = lR_x(\mathcal{P})\boldsymbol{\mathcal{M}}(t; \mathcal{E}_7, {}^tJ, T_7/4)$

We now show how the diver can take off in pure somersault with twist-level $\mathcal{T}_0$, and achieve twist-level $\mathcal{T}_3$ by simply using only the left arm in Figure 6.18. For such a dive to then finish without twist, three more additional fast-kicks will be required, raising the dive to a total of thirteen stages. When n twists are performed for the complete dive, the twisting somersault time T_{twi} accumulates to

$$T_{twi} = T_3 + T_5 + (n-2)T_7. \tag{6.35}$$

As we can see, a considerable amount of time and effort is needed for the athlete to reach $\mathcal{T}_3$. One way to reduce T_{twi} is to incorporate the use of the right arm as shown in Figure 6.19. The reason this reduces T_{twi} is because both the HU fast-kick and UL fast-kick provide the same tilt in the same direction, and so the two can be performed consecutively without pause. Hence the time wasted in

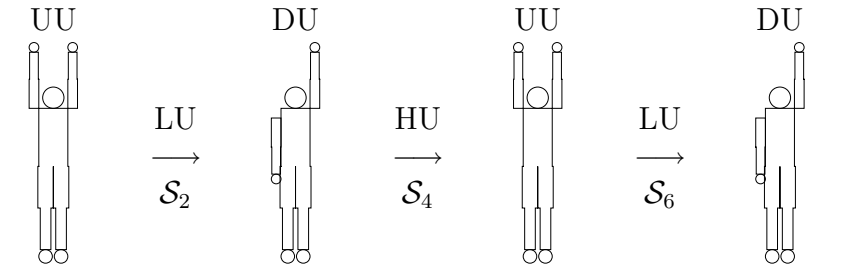

Figure 6.18. Transition from twist-level $\mathcal{T}_0$ to twist-level $\mathcal{T}_3$ using only the left arm. Underneath each diagram we list the stage, twist-level, scaled energy, and period of twist.

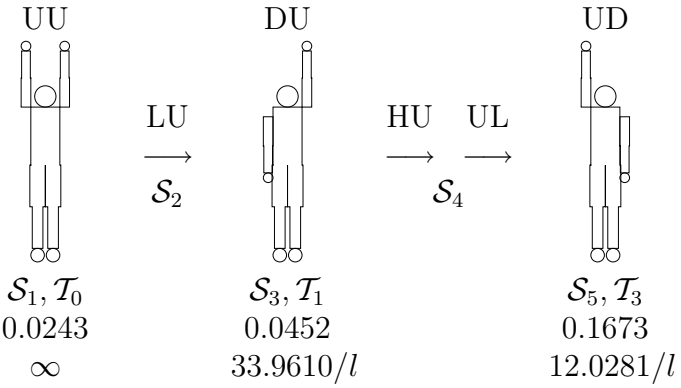

FIGURE 6.19. A faster way to reach twist-level $\mathcal{T}_3$ by incorporating the right arm for impulsive shape changes.

twist-level $\mathcal{T}_2$ can be avoided and we have

$$^cT_{twi} = T_3 + (n-1)T_7. \tag{6.36}$$

We use left superscript c to differentiate quantities obtained with the consecutive fast-kick dive. Comparing the two dives we have the scaled energy $^c\mathcal{E}_5 = \mathcal{E}_7$, period of twist $^cT_5 = T_7$, and orbit

$$^c\boldsymbol{L}_5(t) = R_x(-2\mathcal{P})\boldsymbol{L}_7(t + T_7/2).$$

The difference in orbit comes from the diver being in UD shape as opposed to DU shape in twist-level $\mathcal{T}_3$.

Finally, the alternative to performing consecutive fast-kicks is to simply perform a dual fast-kick, which we covered in Chapter 6.2. The quantities obtained with dual fast-kick will have left superscript d to distinguish them from the other shape changing techniques. As we can see in $\mathcal{S}_5$ of Chapter 6.2 the period of twist $^dT_5$ is even shorter, a result due to $\mathcal{Y} > 2\mathcal{X}$. So the accumulated time in twisting

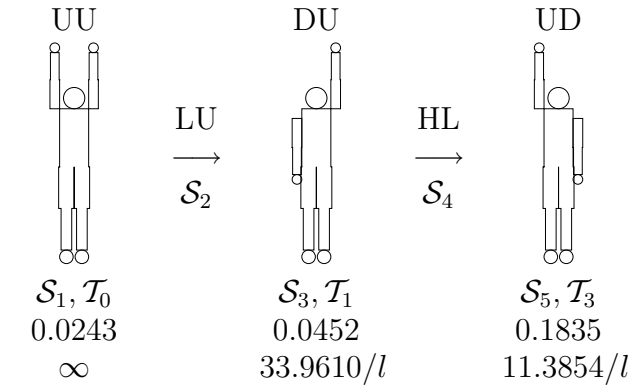

FIGURE 6.20. Achieving $\mathcal{T}_3$ with dual fast-kick.

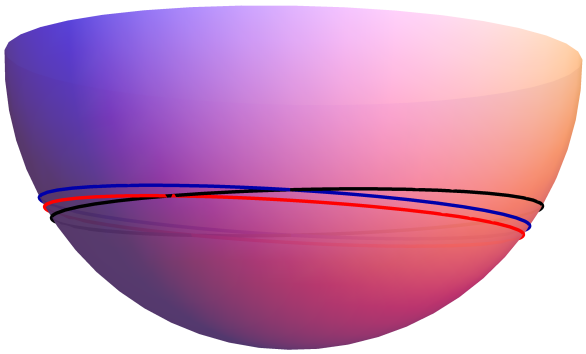

FIGURE 6.21. The black, blue, and red loops correspond to $\boldsymbol{L}_7$, ${}^c\boldsymbol{L}_7$, and ${}^d\boldsymbol{L}_5$, respectively.

motion is further reduced and we have

$$ {}^dT_{twi} = T_3 + (n-1)\,{}^dT_5. \tag{6.37}$$

Comparing all three orbits $\boldsymbol{L}_7$, ${}^c\boldsymbol{L}_5$, and ${}^d\boldsymbol{L}_5$ in Figure 6.21, the dual fast-kick brings the diver closest to the south pole corresponding to a state of pure twist, where all somersaulting motion is abandoned and the diver only twists. The pure somersault and pure twist states are shown in Figure 6.22. The energy E_T is maximised in

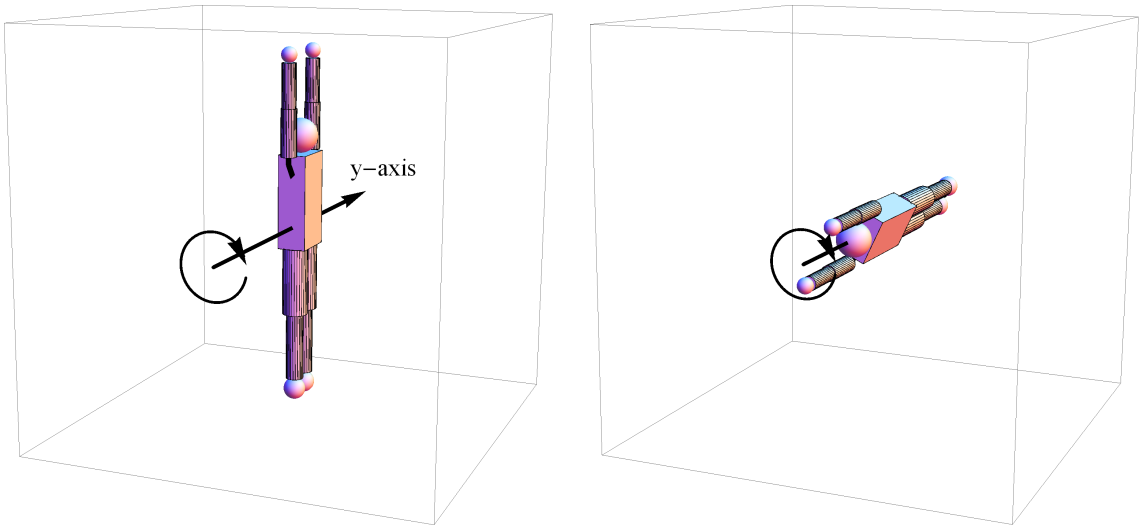

(A) Pure somersault. (B) Pure twist.

FIGURE 6.22. The pure somersault and pure twist states.

the state of pure twist, and with (2.56) we can show that

$$E_T = \frac{l^2}{2\,{}^sI_z} = 0.5022l^2. \tag{6.38}$$

As this is a steady rotation the period of twist is

$$T_T = \frac{2\pi\,{}^sI_z}{l} = \frac{6.2553}{l}. \tag{6.39}$$

We now show how the athlete can take-off in a state of pure somersault and reach the state of pure twist by only using appropriately timed fast-kicks. For consistency we want the athlete to be in layout position (UU shape) for both the pure somersault and pure twist states. In order to maximise the effects of the impulsive shape changes we use dual fast-kicks whenever possible, and only use single arm fast-kick when exiting or entering the pure somersault or pure twist states. Using blue curves to denote rigid body stages with DU shape, red curves for UD shape, and black curves for the transition stages, we get the L-sphere projection shown in Figure 6.23 when the fast-kick timings are after half periods of twist. The energy and period of twist from the pure somersault to the most inner red loop shown in Figure 6.23 are

shape:	UU	DU	UD	DU	UD
curve:	black point	outer blue	outer red	inner blue	inner red
energy:	$0.0243l^2$	$0.0452l^2$	$0.1835l^2$	$0.3786l^2$	$0.5058l^2$
period:	-	$33.9610/l$	$11.3854/l$	$7.5855/l$	$6.4984/l$

Initially we see an increase in energy, the period of twist becomes shorter and the diver approaches the pure twist state. However, continuing the strategy beyond this point provides no further improvement, in fact it becomes worse, so a new strategy needs to be adopted.

We realise there are two ways of entering the pure twist state, either the athlete is in DU shape and performs the HU fast-kick, or the athlete is in UD shape and performs the UH fast-kick, where both of these rigid body orbits are shown in Figure 6.24. So the idea is to find a fast-kick that brings the athlete into one of these two orbits. In Figure 6.23 the outer blue loop corresponds to $\boldsymbol{L}_3(t)$ found in Chapter 6.1, the outer red loop corresponds to ${}^d\boldsymbol{L}_5(t)$ found in Chapter 6.2, and the first new loop is the inner blue loop.

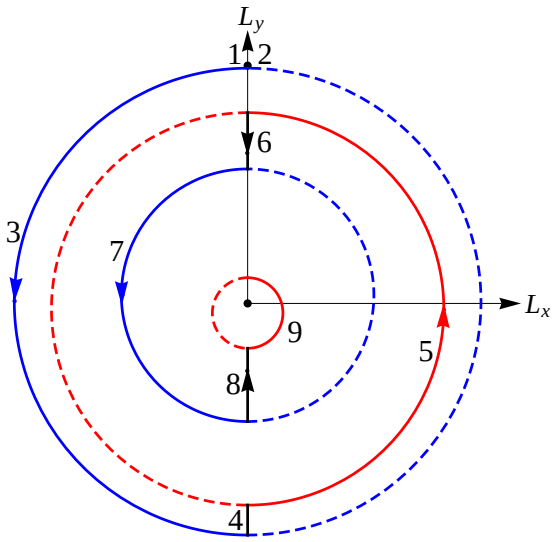

Figure 6.23. The athlete takes off in pure somersault state indicated by the black point on the L_y axis, performs the LU fast-kick to enter the rigid body orbit indicated by the outer blue loop, and performs dual fast-kicks at half periods of twist in order to approach the pure twist state indicated by the black point at the origin, which corresponds to point $(0, 0, -l)$ on the L-sphere. Each dual fast-kick interchanges the arm positions between DU and UD, hence the changes in colour. The numbers labelled help distinguish the different stages, as the LU fast-kick of $\mathcal{S}_2$ cannot be seen due to the projection of the L-sphere.

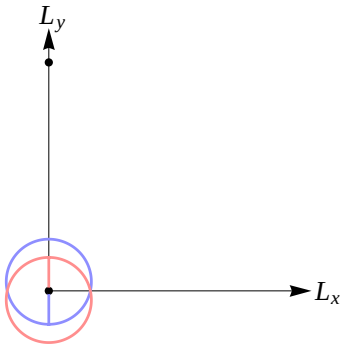

Figure 6.24. Both of the rigid body orbits shown have a fast-kick timing that reaches the pure twist state. The light blue orbit corresponds to shape DU and light red shape UD.

inner blue loop	Shape DU
scaled energy	${}^d\mathcal{E}_7 = \frac{1}{2}\widetilde{\boldsymbol{\mathcal{M}}}^t\, {}^tJ^{-1}\widetilde{\boldsymbol{\mathcal{M}}} = 0.3786$
	where $\widetilde{\boldsymbol{\mathcal{M}}} = R_x(-\mathcal{P}-\mathcal{Y})\, {}^d\boldsymbol{L}_5({}^dT_5/2)$
period of twist	${}^dT_7 = T({}^d\mathcal{E}_7, {}^tJ) = \dfrac{7.5855}{l}$
orbit	${}^d\boldsymbol{L}_7(t) = lR_x(\mathcal{P})\boldsymbol{\mathcal{M}}(t; {}^d\mathcal{E}_7, {}^tJ, {}^dT_7/4)$

The goal now is to see if there exists a τ_7 in $\mathcal{S}_7$ that lets the HL fast-kick of $\mathcal{S}_8$ land on a point laying on the light red loop shown in Figure 6.24.

The family of possible initial conditions of $\mathcal{S}_9$ is given by

$$ {}^d\boldsymbol{L}_9(0;\tau_7) = R_x(\mathcal{Y})\, {}^d\boldsymbol{L}_7(\tau_7), \tag{6.40}$$

so we plot this as the red dashed loop in Figure 6.25. There are two solutions for τ_7 corresponding to the two intersections shown in Figure 6.25, but the desired solution is

$$ \tau_7 = 0.4607\ {}^dT_7 = 3.4946/l, \tag{6.41}$$

because it allows the athlete to move into the pure twisting state earlier (the other solution being $\tau_7 = 0.5393\, {}^dT_7$ will be ignored). The orbit in $\mathcal{S}_9$ is then

$$ {}^d\boldsymbol{L}_9(t) = lR_x(-\mathcal{P})\boldsymbol{\mathcal{M}}(t; 0.4996, {}^tJ, 4.1028), \tag{6.42}$$

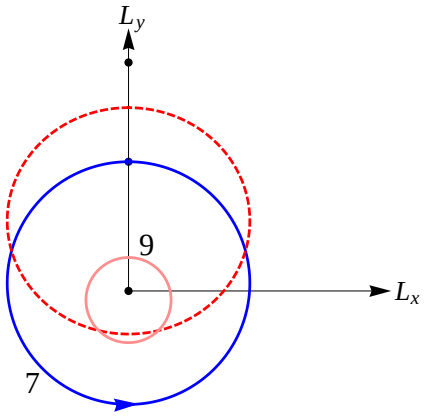

Figure 6.25. The blue loop is the orbit ${}^d\boldsymbol{L}_7(t)$ (labelled as 7), the light red solid loop is the desired orbit in $\mathcal{S}_9$ (labelled as 9) which is one fast-kick away from the pure twist state, and the red dashed loop is the family of initial conditions for $\mathcal{S}_9$ given by (6.40).

where one last UH fast-kick after

$$\tau_9 = 0.6228\ {}^{d}T_9 = 4.0735/l \tag{6.43}$$

time in $\mathcal{S}_9$ brings the athlete to the state of pure twist. Thus the goal of transitioning from a state of pure somersault to a state of pure twist has been obtained through the use of five fast-kicks. The dive sequence needed in order to achieve this is shown in Figure 6.26, and the corresponding L-sphere projection is shown in Figure 6.27. Although the same effect can be found in Yeadon's thesis [**60**] (page 323), both the model and arm movement presented here are different. Yeadon uses three complete cycles of arm movement initiating from pretwist layout (similar to layout position except with arms outstretched horizontally) whereas we use five impulsive shape changes as indicated in Figure 6.26.

The minimum time required to reach the state of pure twist from take-off is $30.2413/l$, so in theory the fast-kick model allows the athlete to take off in pure somersault, reach pure twist, and return to pure somersault with sufficient time to

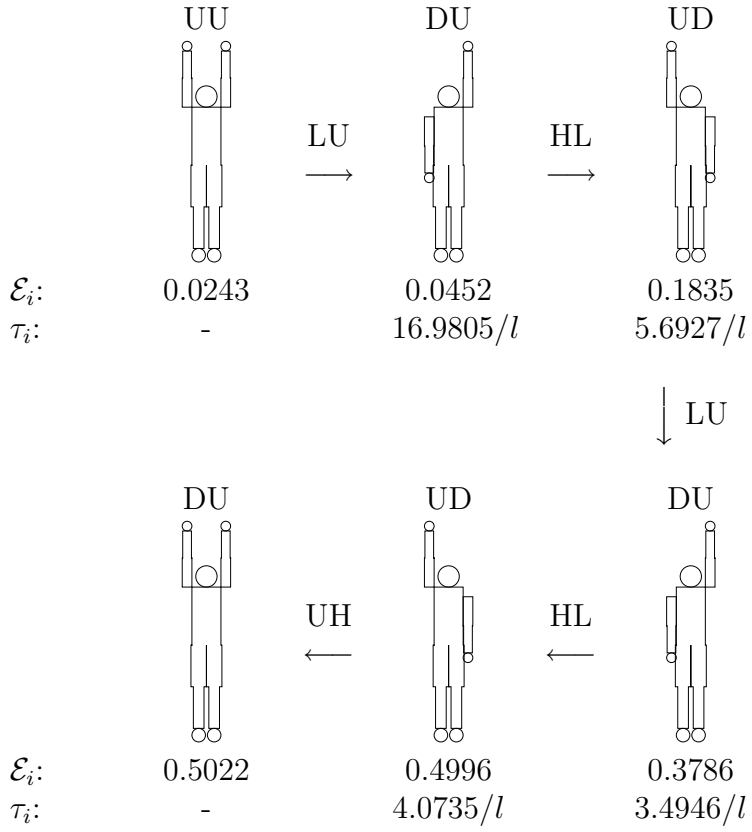

Figure 6.26. Sequence of impulsive shape changes to transition from a state of pure somersault to state of pure twist, where $i = 1, 2, 3$ for top and 11, 9, 7 for bottom.

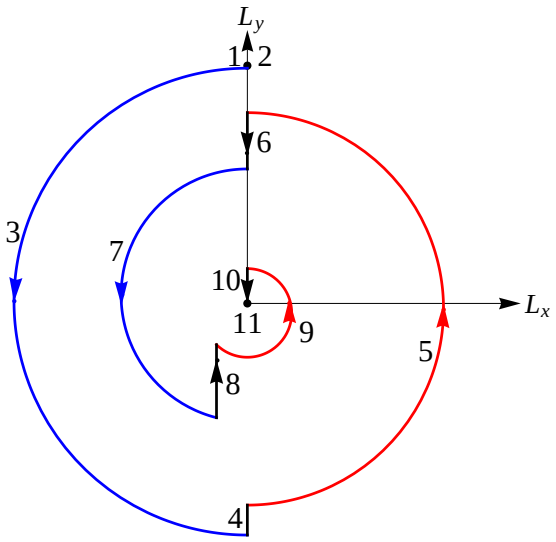

FIGURE 6.27. L-sphere projection of the dive taking off in pure somersault and transitioning into pure twist. The dive takes 10 stages to reach pure twist, where each stage is labelled accordingly.

complete the dive. However, with realistic arm motions taking a quarter second each, this makes it impossible in Olympic diving as $T_{air} < 2$, but in sports (possibly in for example, high diving or aerial skiing) where T_{air} is large enough, a realistic version of this dive could in principle be performed.

Appendices

APPENDIX A

Diving Accidents and Common Injuries

All pools with a diving board and stand must meet the minimum water depths set forth by the International Swimming Federation (FINA) for safety purposes. The FINA facility rule FR 5.3.1 states that the minimum depth of water at plummet is 3.7m for the 3m springboard and 4.5m for the 10m platform. However, these numbers are only minimum requirements and pools may in fact have greater water depths. Now if a diver trains in a pool with FINA's preferred depth of 5m (instead of the 4.5m minimum) but competes in a pool with shallower water depth, then he or she will approach the bottom of the pool much quicker than they are accustomed to. The reduced time may be enough to cause injury if the diver does not make the necessary adjustments upon entry into the water.

Some of the worst diving accidents recorded involve the athlete hitting their head at the bottom of the pool and sustaining a life changing injury of paralysis (e.g. Dr Charles Krauthammer). It is therefore imperative for all divers (both recreational and competitive alike) to always check the pool depth, which is either specified on the pool deck or the side of the pool. The diver should be prepared to readily make the necessary adjustments based on pool depth to ensure safe diving. Although recreational diving injuries are often severe and catastrophic, they are mostly preventable. Of all spinal cord injuries, up to 75% are due to diving mishaps [**32**] and 10% to 20% of all hospital spinal cord admissions the direct result of diving accidents [**4**], [**32**] and [**53**].

However, at the other end of the spectrum competitive diving is a relatively safe sport that is rarely associated with catastrophic injury. A case study in 2004 by Badman and Rechtine [**3**] found that only two deaths have been reported worldwide, both of which involved the diver hitting their head during a reverse somersaulting platform dive.

The acrobatic manoeuvres used in diving resemble those found in gymnastics, so it is not surprising that divers often have a gymnastics background. Most of the athletes who transitioned from gymnastics to diving feel safer diving head-first into water than feet-first onto a mat. Coaches generally also agree that diving is a safer alternative to gymnastics (provided that safety precautions are taken) due to the lower injury rate resulting from reduced stress on knee and elbow joints. While sporting accidents are always expected (even at the elite level), some are not actually related to diving at all, e.g. slipping on the platform stairs. However,

the most horrific diving stories involve the athlete taking off incorrectly and hitting their head on the springboard or platform. Although rare at elite levels it does happen occasionally, e.g. at the 1988 Seoul Olympics, Greg Louganis hit his head on the springboard after take-off, and Monique Gladding struck her head on the diving platform during a synchronised dive at the 2011 World Cup in Penza, Russia. Fortunately, neither athlete sustained life changing injuries. Accidents like these occur because athletes often push the physical boundaries of what can be achieved, increasing the number of somersaults and thus angular momentum requirements. However, the trade off between horizontal velocity and angular momentum at take-off means that if athletes were to generate more horizontal velocity (to have a larger safety margin of clearing the board or platform), the resulting reduction in angular momentum may prevent the athlete from successfully completing the dive.

Diving accidents involving athletes hitting the platform or springboard after take-off, or hitting their head at the bottom of the pool, generally occur at the recreational level of diving and are uncommon at the competitive level. Instead, competitive divers are typically more prone to overuse injuries and those sustained from 'dry land' training, the latter of which normally incorporates weight training, the use of spotting belts, trampolines, and/or springboards.

Common diving injuries involve the shoulder, neck, elbow, knee, wrist, and lower back pain. Most of these injuries are due to overuse and are usually sustained during entry into the pool, where the force of impact between the athlete and water is exhibited.

We now briefly summarise these injuries. Shoulder injuries typically occur when the athlete's arms are extended overhead and get pushed back upon impact, occasionally causing an immediate dislocation of the shoulder joint from the socket, and can be prevented with the help of strength training exercises. A neck injury is usually associated with repetitive extension of the neck upon entry into the water, which can cause irritation on the neck joints. Elbow injuries are usually sustained due to the elbow being hyperextended upon entry into the pool, but can be prevented with proper technique. Wrist and hand injuries are the result of overuse; each time the athlete enters the water they essentially punch a hole in the surface with their hands open placed atop one another with palms facing down, causing the wrist to bend backwards upon impact with the water. Doing this repetitively causes pain, swelling, stiffness, and irritation of the wrist joint, but can be usually managed by taping or bracing the wrist as well as rest, ice and non-steroidal anti-inflammatory drugs. Back pain is mostly an overuse injury, usually associated with arching or extending the back too much, and can be managed or reduced by improving one's flexibility, core strength and the use of a back brace. Knee injuries often result from jumping, which puts pressure on the kneecap and can lead to pain in the front of the knee; however, these injuries can also be sustained from 'dry land' training.

APPENDIX B

Dive Number

A dive number is an alphanumeric code that describes precisely the dive that is to be performed by the athlete. If there is ever any doubt as to what dive is to be executed by the diver, then the dive number will always take precedence. For example, if an athlete specifies on the dive sheet forward 2.5 somersault in pike for the description and 105C (forward 2.5 somersault in tuck) for the dive number, then the athlete must perform the forward 2.5 somersault in tuck or incur a penalty. A dive number always begins with three or four numerals followed by a letter, which will now be explained for various dives.

The first digit in a dive number describes the group of the dive and will always be:

Forward dives - 1
Back dives - 2
Reverse dives - 3
Inward dives - 4
Twisting dives - 5
Armstand dives - 6.

The dive numbers for the forward, back, reverse and inward groups always contain three numerals followed by a letter, while twisting dives have four numerals followed by a letter. The only exception is the armstand dive, which could have either three or four numerals (depending on whether twists are present) followed by a letter.

The second digit for the first four dive groups (forward, back, reverse and inward) is:

Somersault - 0
Flying Somersault - 1.

Continuing on, the third digit describes the number of half somersaults, that is:

0.5 (a dive)	-	1
1 Somersault	-	2
1.5 Somersaults	-	3
2 Somersaults	-	4
2.5 Somersaults	-	5
3 Somersaults	-	6
3.5 Somersaults	-	7
4 Somersaults	-	8
4.5 Somersaults	-	9.

Finally, the letter denotes flight position. The letters are:

Straight	-	A
Pike	-	B
Tuck	-	C
Free	-	D.

Note that the free (D) position can only be adopted for twisting somersaults, and is only listed here for completeness (it does not actually appear in the first four dive groups).

Now if the first number is either a five or six (to denote twisting or armstand dives), then the second number describes the type of somersault. That is,

Forward somersaults	-	1
Backward somersaults	-	2
Reverse somersaults	-	3
Inward somersaults	-	4.

The third number counts the number of half somersaults, and if applicable, the fourth number counts the number of half twists.

Here are some examples of dive numbers with their corresponding dive description:

- 105A is a forward 2.5 somersaults in straight position
- 313C is a reverse flying 1.5 somersaults in tuck position
- 5434D is an inward 1.5 somersaults with 2 twists, the D indicates the dive is in the free position
- 631B is an armstand reverse 0.5 somersault in pike
- 6261C is an armstand backward triple somersault with 0.5 twist in tuck

APPENDIX C

Dive Score

A dive score consists of two components multiplied together - the judges score and the degree-of-difficulty.

Judges Score

For the individual event a panel of seven judges preside over major international events (including the Olympic Games); however, panels of five judges are usually used in smaller competitive events. Each judge scores the dive out of 10, awarding up to 3 points in each of the following categories: quality of take-off, execution (flight through the air), and entry into the water. The remaining point serves as a bonus which may be awarded in any of the three categories. It should be noted that these points are awarded without regard for the dive's degree-of-difficulty, which is considered separately.

The highest and lowest scores from the judges are discarded, leaving five scores to be added together and then multiplied by 3/5 to yield the judges score. The system of discarding the extreme scores promotes fairness by making it difficult for a single judge to manipulate the dive scores, while the ratio of 3/5 is used to ensure consistent comparison with other events using a five judge panel. The seven judge procedure was recently modified in the 2012 London Olympic Games by discarding the two highest and lowest scores (instead of the single highest and lowest) to leave only three scores to be summed, thereby evading the need for the 3/5 factor.

For the synchronised event the preferred number of judges is eleven, although smaller competitions may use a panel of only seven or nine. In an eleven judge panel, three are assigned to each diver to score the dive like the individual event, and the remaining five judges are used to score the synchronisation. The highest and lowest execution scores are discarded, leaving one execution score per diver. The highest and lowest synchronisation scores are also discarded, leaving three synchronisation scores for the duo. These five scores are then summed and multiplied by $\frac{3}{5}$ to provide consistency with other events that may use the seven judge

panel. The judges score is then multiplied by the degree-of-difficulty to obtain the dive score, much like the individual event.

If a nine judge panel is used instead of eleven, then only two judges (instead of three) are assigned to score each diver on execution. From a pool of four execution scores, the highest and lowest scores are discarded to leave only two remaining scores, while the synchronisation component remains the same. The seven judge panel functions much like the nine judge panel but with 2 exceptions - only 3 judges score the synchronisation (instead of 3), and the 3/5 factor is not needed.

Degree-of-Difficulty

Completing a backward 3.5 somersault in pike (207B) is clearly more difficult than a forward 2.5 somersault in tuck (105C), but the difference in difficulty is hard to evaluate. Such problems led to the development of the degree-of-difficulty, which helps to rank dives according to their difficulty. FINA defines degree-of-difficulty to incorporate all the elements of a dive that influence its difficulty, such as the number of somersaults and/or twists performed, the dive group (e.g. forward), flight position (e.g. pike), and natural (head-first) or unnatural (feet-first) type of entry into the pool. The formula is calculated by summing

$$A + B + C + D + E,$$

where each letter corresponds to the value given in the following tables which are updated on a regular basis every few years. For simplicity the standard degree-of-difficulty tables sourced from http://www.fina.org/content/diving-rules are included for both springboard and platform diving, accurate as of 2015.

FINA DEGREE OF DIFFICULTY - FORMULA AND COMPONENTS
SPRINGBOARD

Note: Degree of Difficulty (DD) is calculated by adding: A + B + C + D + E = DD

A. Somersaults

Level / Somersault	0	½	1	1½	2	2½	3	3½	4	4½
1m	0.9	1.1	1.2	1.6	2.0	2.4	2.7	3.0	3.3	3.8
3m	1.0	1.3	1.3	1.5	1.8	2.2	2.3	2.8	2.9	3.5

B. Flight Position For flying dives add fly position (E) to either (B) or (C) Position

	0 - 1 Somersault				1½ - 2 Somersaults				2½ Somersaults				3 - 3½ Somersaults				4 - 4½ Somersaults			
	Fwd	Back	Rev	Inw	Fwd	Back	Rev	Inw	Fwd	Back	Rev	Inw	Fwd	Back	Rev	Inw	Fwd	Back	Rev	Inw
C =Tuck	0.1	0.1	0.1	-0.3	0	0	0	0.1	0	0.1	0	0.2	0	0	0	0.3	0	0.1	0.2	0.4
B = Pike	0.2	0.2	0.2	-0.2	0.1	0.3	0.3	0.3	0.2	0.3	0.2	0.5	0.3	0.3	0.3	0.6	0.4	0.4	0.5	0.8
A = Str	0.3	0.3	0.3	0.1	0.4	0.5	0.6	0.8	0.6	0.7	0.6	-	-	-	-	-	-	-	-	-
D = Free	0.1	0.1	0.1	-0.1	0	-0.1	-0.1	0.2	0	-0.1	-0.2	0.4	0	0	0	-	-	-	-	-
E = Fly	0.2	0.1	0.1	0.4	0.2	0.2	0.2	0.5	0.3	0.3	0.3	0.7	0.4	-	-	-	-	-	-	-

Seven of the above components have negative values. Dashes indicate dives that currently are not possible.

C. Twists

Group	½ Twist ½ - 1 Som.	½ Twist 1 ½ - 2 Som.	½ Twist 2 ½ Som.	½ Twist 3 - 3 ½ Som.	1 Twist	1 ½ Twists ½ - 2 Som.	1 ½ Twists 2½-3½ Som.	2 Twists	2 ½ Twist ½ - 2 Som.	2 ½ Twists 2½-3½ Som.	3 Twists	3 ½ Twists	4 Twists	4 ½ Twists
Fwd.	0.4	0.4	0.4	0.4	0.6	0.8	0.8	1.0	1.2	1.2	1.5	1.6	1.9	2.0
Back	0.2	0.4	0	0	0.4	0.8	0.7	0.8	1.2	1.1	1.4	1.7	1.8	2.1
Rev.	0.2	0.4	0	0	0.4	0.8	0.6	0.8	1.2	1.0	1.4	1.8	1.8	2.1
Inw.	0.2	0.4	0.2	0.4	0.4	0.8	0.8	0.8	1.2	1.2	1.5	1.6	1.9	2.0

(1) Dives with ½ somersault and twists can only be executed in positions A, B, or C,
(2) Dives with 1 or 1 ½ somersaults and twists can only be executed in position D,
(3) Dives with 2 or more somersaults and twists can only be executed in positions B or C

D. Approach

Level	Forward ½ - 3½ Som.	Forward 4 – 4 ½ Som.	Back ½ - 3 Som.	Back 3½ - 4½ Som.	Reverse ½ - 3 Som.	Reverse 3½ - 4½ Som.	Inward ½ - 1 Som.	Inward 1½ - 4½ Som.
1m	0	0.5	0.2	0.6	0.3	0.5	0.6	0.5
3m	0	0.3	0.2	0.4	0.3	0.3	0.3	0.3

E. Unnatural Entry (does not apply to twisting dives)

Group	½ Som.	1 Som.	1½ Som.	2 Som.	2½ Som.	3 Som.	3½ Som.	4 Som.	4½ Som.
Forward / Inward	-	0.1	-	0.2	-	0.2	-	0.2	-
Back / Reverse	0.1	-	0.2	-	0.3	-	0.4	-	0.4

A value indicates the diver does not see the water before the entry. The component is the same at all levels.
(-) indicates the diver does see the water before the entry. The component is the same at all levels.

Examples

Dive	Pos	Height	A	B	C	D	E	DD
207	B	3	2.8	0.3	0.0	0.4	0.4	3.9
207	C	3	2.8	0.0	0.0	0.4	0.4	3.6
5253	B	3	2.2	0.3	0.7	0.2	0	3.4
5355	B	3	2.2	0.2	1.0	0.3	0	3.7

Dive	Pos	Height	A	B	C	D	E	DD
309	B	3	3.5	0.5	0.0	0.3	0.4	4.7
309	C	3	3.5	0.2	0.0	0.3	0.4	4.4
5255	B	3	2.2	0.3	1.1	0.2	0	3.8
313	C	3	1.5	0.2	0	0.3	0.2	2.2

FINA TABLE OF DEGREES OF DIFFICULTY
SPRINGBOARD

In the following table, a dive with (-) is not possible and dives with empty spaces have not been calculated

SPRINGBOARD		1 METER				3 METER			
		STR	PIKE	TUCK	FREE	STR	PIKE	TUCK	FREE
Forward Group		**A**	**B**	**C**	**D**	**A**	**B**	**C**	**D**
101	Forward Dive	1.4	1.3	1.2	-	1.6	1.5	1.4	-
102	Forward Somersault	1.6	1.5	1.4	-	1.7	1.6	1.5	-
103	Forward 1½ Somersaults	2.0	1.7	1.6	-	1.9	1.6	1.5	-
104	Forward 2 Somersaults	2.6	2.3	2.2	-	2.4	2.1	2.0	-
105	Forward 2½ Somersaults		2.6	2.4	-	2.8	2.4	2.2	-
106	Forward 3 Somersaults		3.2	2.9	-		2.8	2.5	-
107	Forward 3½ Somersaults		3.3	3.0	-		3.1	2.8	-
108	Forward 4 Somersaults			4.0	-		3.8	3.4	-
109	Forward 4½ Somersaults			4.3	-		4.2	3.8	-
112	Forward Flying Somersault	-	1.7	1.6	-	-	1.8	1.7	-
113	Forward Flying 1½ Somersaults	-	1.9	1.8	-	-	1.8	1.7	-
115	Forward Flying 2½ Somersaults	-			-	-	2.7	2.5	-
Back Group		**A**	**B**	**C**	**D**	**A**	**B**	**C**	**D**
201	Back Dive	1.7	1.6	1.5	-	1.9	1.8	1.7	-
202	Back Somersault	1.7	1.6	1.5	-	1.8	1.7	1.6	-
203	Back 1½ Somersaults	2.5	2.3	2.0	-	2.4	2.2	1.9	-
204	Back 2 Somersaults		2.5	2.2	-	2.5	2.3	2.0	-
205	Back 2½ Somersaults		3.2	3.0	-		3.0	2.8	-
206	Back 3 Somersaults		3.2	2.9	-		2.8	2.5	-
207	Back 3½ Somersaults				-		3.9	3.6	-
208	Back 4 Somersaults				-		3.7	3.4	-
209	Back 4½ Somersaults				-		4.7	4.4	-
212	Back Flying Somersault	-	1.7	1.6	-	-	1.8	1.7	-
213	Back Flying 1½ Somersaults	-			-	-	2.4	2.1	-
215	Back Flying 2½ Somersaults	-			-	-	3.3	3.1	-
Reverse Group		**A**	**B**	**C**	**D**	**A**	**B**	**C**	**D**
301	Reverse Dive	1.8	1.7	1.6	-	2.0	1.9	1.8	-
302	Reverse Somersault	1.8	1.7	1.6	-	1.9	1.8	1.7	-
303	Reverse 1½ Somersaults	2.7	2.4	2.1	-	2.6	2.3	2.0	-
304	Reverse 2 Somersaults	2.9	2.6	2.3	-	2.7	2.4	2.1	-
305	Reverse 2½ Somersaults		3.2	3.0	-	3.4	3.0	2.8	-
306	Reverse 3 Somersaults		3.3	3.0	-		2.9	2.6	-
307	Reverse 3½ Somersaults				-		3.8	3.5	-
308	Reverse 4 Somersaults				-		3.7	3.4	-
309	Reverse 4½ Somersaults				-		4.7	4.4	-
312	Reverse Flying Somersault	-	1.8	1.7	-	-	1.9	1.8	-
313	Reverse Flying 1½ Somersaults	-	2.6	2.3	-	-	2.5	2.2	-
Inward Group		**A**	**B**	**C**	**D**	**A**	**B**	**C**	**D**
401	Inward Dive	1.8	1.5	1.4	-	1.7	1.4	1.3	-
402	Inward Somersault	2.0	1.7	1.6	-	1.8	1.5	1.4	-
403	Inward 1½ Somersaults		2.4	2.2	-		2.1	1.9	-
404	Inward 2 Somersaults		3.0	2.8	-		2.6	2.4	-
405	Inward 2½ Somersaults		3.4	3.1	-		3.0	2.7	-
407	Inward 3½ Somersaults				-		3.7	3.4	-
409	Inward 4½ Somersaults				-		4.6	4.2	--
412	Inward Flying Somersault	-	2.1	2.0	-	-	1.9	1.8	-
413	Inward Flying 1½ Somersaults	-	2.9	2.7	-	-	2.6	2.4	-

		1 METER				3 METER			
	Twisting Group	**A**	**B**	**C**	**D**	**A**	**B**	**C**	**D**
5111	Forward Dive ½ Twist	1.8	1.7	1.6	-	2.0	1.9	1.8	-
5112	Forward Dive 1 Twist	2.0	1.9		-	2.2	2.1		-
5121	Forward Somersault ½ Twist	-	-	-	1.7	-	-	-	1.8
5122	Forward Somersault 1 Twist	-	-	-	1.9	-	-	-	2.0
5124	Forward Somersault 2 Twists	-	-	-	2.3	-	-	-	2.4
5126	Forward Somersault 3 Twists	-	-	-	2.8	-	-	-	2.9
5131	Forward 1½ Somersaults ½ Twist	-	-	-	2.0	-	-	-	1.9
5132	Forward 1½ Somersaults 1 Twist	-	-	-	2.2	-	-	-	2.1
5134	Forward 1½ Somersaults 2 Twists	-	-	-	2.6	-	-	-	2.5
5136	Forward 1½ Somersaults 3 Twists	-	-	-	3.1	-	-	-	3.0
5138	Forward 1½ Somersaults 4 Twists	-	-	-	3.5	-	-	-	3.4
5151	Forward 2½ Somersaults ½ Twist	-	3.0	2.8	-	-	2.8	2.6	-
5152	Forward 2½ Somersaults 1 Twist	-	3.2	3.0	-	-	3.0	2.8	-
5154	Forward 2½ Somersaults 2 Twists	-	3.6	3.4	-	-	3.4	3.2	-
5156	Forward 2½ Somersaults 3 Twists	-			-	-	3.9	3.7	-
5172	Forward 3½ Somersaults 1 Twist	-			-	-	3.7	3.4	-
5211	Back Dive ½ Twist	1.8	1.7	1.6	-	2.0	1.9	1.8	-
5212	Back Dive 1 Twist	2.0			-	2.2			-
5221	Back Somersault ½ Twist	-	-	-	1.7	-	-	-	1.8
5222	Back Somersault 1 Twist	-	-	-	1.9	-	-	-	2.0
5223	Back Somersault 1½ Twists	-	-	-	2.3	-	-	-	2.4
5225	Back Somersault 2½ Twists	-	-	-	2.7	-	-	-	2.8
5227	Back Somersault 3½ Twists	-	-	-	3.2	-	-	-	3.3
5231	Back 1½ Somersaults ½ Twist	-	-	-	2.1	-	-	-	2.0
5233	Back 1½ Somersaults 1½ Twists	-	-	-	2.5	-	-	-	2.4
5235	Back 1½ Somersaults 2½ Twists	-	-	-	2.9	-	-	-	2.8
5237	Back 1½ Somersaults 3½ Twists	-	-	-	-	-	-	-	3.3
5239	Back 1½ Somersaults 4½ Twists	-	-	-	-	-	-	-	3.7
5251	Back 2½ Somersaults ½ Twist	-	2.9	2.7	-	-	2.7	2.5	-
5253	Back 2½ Somersaults 1½ Twists	-			-	-	3.4	3.2	-
5255	Back 2½ Somersaults 2½ Twists	-			-	-	3.8	3.6	-
5311	Reverse Dive ½ Twist	1.9	1.8	1.7	-	2.1	2.0	1.9	-
5312	Reverse Dive 1 Twist	2.1			-	2.3			-
5321	Reverse Somersault ½ Twist	-	-	-	1.8	-	-	-	1.9
5322	Reverse Somersault 1Twist	-	-	-	2.0	-	-	-	2.1
5323	Reverse Somersault 1½ Twists	-	-	-	2.4	-	-	-	2.5
5325	Reverse Somersault 2½ Twists	-	-	-	2.8	-	-	-	2.9
5331	Reverse 1½ Somersaults ½ Twist	-	-	-	2.2	-	-	-	2.1
5333	Reverse 1½ Somersaults 1½ Twists	-	-	-	2.6	-	-	-	2.5
5335	Reverse 1½ Somersaults 2½ Twists	-	-	-	3.0	-	-	-	2.9
5337	Reverse 1½ Somersaults 3½ Twists	-	-	-	3.6	-	-	-	3.5
5339	Reverse 1½ Somersaults 4½ Twists	-	-	-	-	-	-	-	3.8
5351	Reverse 2½ Somersaults ½ Twist	-	2.9	2.7	-	-	2.7	2.5	-
5353	Reverse 2½ Somersaults 1½ Twists	-	3.5	3.3	-	-	3.3	3.1	-
5355	Reverse 2½ Somersaults 2½ Twists	-	3.9	3.7	-	-	3.7	3.5	-
5371	Reverse 3½ Somersaults ½ Twist	-			-	-	3.4	3.1	-
5373	Reverse 3½ Somersaults 1½ Twists	-			-	-		3.7	-
5375	Reverse 3½ Somersaults 2 ½ Twists	-			-	-		4.1	-
5411	Inward Dive ½ Twist	2.0	1.7	1.6	-	1.9	1.6	1.5	-
5412	Inward Dive 1 Twist	2.2	1.9	1.8	-	2.1	1.8	1.7	-
5421	Inward Somersault ½ Twist	-	-	-	1.9	-	-	-	1.7
5422	Inward Somersault 1 Twist	-	-	-	2.1	-	-	-	1.9
5432	Inward 1½ Somersaults 1 Twist	-	-	-	2.7	-	-	-	2.4
5434	Inward 1½ Somersaults 2 Twists	-	-	-	3.1	-	-	-	2.8
5436	Inward 1½ Somersaults 3 Twists	-	-	-		-	-	-	3.5

FINA DEGREE OF DIFFICULTY - FORMULA AND COMPONENTS
PLATFORM

Note: Degree of Difficulty (DD) is calculated by adding: A + B + C + D + E = DD

A. Somersaults

Level	0	½	1	1½	2	2½	3	3½	4	4½	5½
5m	0.9	1.1	1.2	1.6	2.0	2.4	2.7	3.0	-	-	-
7½m	1.0	1.3	1.3	1.5	1.8	2.2	2.3	2.8	3.5	3.5	-
10m	1.0	1.3	1.4	1.5	1.9	2.1	2.5	2.7	3.5	3.5	4.5

B. Flight Position For flying dives add fly position (E) to either (B) or (C) Position

	0 - 1 Somersault					1½ - 2 Somersaults					2½ Somersaults					3 - 3½ Somersaults					4 - 4½ Somersaults					5½ Som
	Fwd	Back	Rev	Inw	Arm	Fwd	Back	Rev	Inw	Arm	Fwd	Back	Rev	Inw	Arm	Fwd	Back	Rev	Inw	Arm	Fwd	Back	Rev	Inw	Arm	Fwd
C = Tuck	0.1	0.1	0.1	-0.3	0.1	0	0	0	0.1	0	0	0.1	0	0.2	0.1	0	0	0	0.3	0.2	0	0.1	0.3	0.4	0.3	0
B = Pike	0.2	0.2	0.2	-0.2	0.3	0.1	0.3	0.3	0.3	0.3	0.2	0.3	0.2	0.5	0	0.3	0.3	0.3	0.6	0.4	0.4	0.4	0.6	0.7	0.5	-
A = Strait	0.3	0.3	0.3	0.1	0.4	0.4	0.5	0.6	0.8	0.5	0.6	0.7	0.6	-	-	-	-	-	-	-	-	-	-	-	-	-
D = Free	0.1	0.1	0.1	-0.1	0	0	-0.1	-0.1	0.2	0	0	-0.1	-0.2	0.4	0	0	0	0	-	-	-	-	-	-	-	-
E = Fly	0.2	0.1	0.1	0.4	-	0.2	0.2	0.2	0.5	-	0.3	0.3	0.3	0.7	-	0.4	-	-	-	-	-	-	-	-	-	-

Seven of the above components have negative values. Dashes indicate dives that currently are not possible.

C. Twists

Group	½ Twist ½ - 1 Som.	½ Twist 1½ - 2 Som.	½ Twist 2½ Som.	½ Twist 3 - 3½ Som.	1 Twist	1½ Twists ½ - 2 Som.	1½ Twists 2½ - 3½ Som.	2 Twists	2½ Twists ½ - 2 Som.	2½ Twists 2½ - 3½ Som.	3 Twists	3½ Twists ½ - 2 Som.	3½ Twists 2½ - 3½ Som.	4 Twists	4½ Twists ½ - 2 Som.	4½ Twists 2½ - 3½ Som.
Forward	0.4	0.4	0.4	0.4	0.6	0.8	0.8	1.0	1.2	1.2	1.5	1.6	1.6	1.9	2.0	2.0
Back	0.2	0.4	0	0	0.4	0.8	0.6	0.8	1.2	1.0	1.4	1.7	1.5	1.8	2.1	1.9
Reverse	0.2	0.4	0	0	0.4	0.8	0.6	0.8	1.2	1.0	1.4	1.7	1.5	1.8	2.1	1.9
Inward	0.2	0.4	0.2	0.4	0.4	0.8	0.8	0.8	1.2	1.2	1.5	1.6	1.6	1.9	2.0	2.0
Arm. Forw.	0.4	0.5	0.5	0.4	1.2	1.3	1.3	1.5	1.7	1.7	1.9	2.1	2.1	2.3	2.5	2.5
Arm. Back / Rev	0.4	0.5	0.5	0.5	1.2	1.3	1.3	1.3	1.7	1.7	1.9	2.1	2.1	2.3	2.5	2.5

(1) Dives with ½ somersault and twists can only be executed in positions A, B, or C,
(2) Dives with 1 or 1½ somersaults and twists can only be executed in position D,
(3) Dives with 2 or more somersaults and twists can only be executed in positions B or C,
(4) Armstand dives with 1, 1½, or 2 somersaults and one or more twists can only be executed in position D, and
(5) Armstand dives with 2½ or more somersaults and twist can only be executed in positions B or C

D. Approach Forward-, Back-, Reverse-, Inward-, and Twisting Groups

Level	Forward ½ - 3½ Soms.	Forward 4 - 5½ Soms.	Back ½ - 3 Soms.	Back 3½ - 4½ Soms.	Reverse ½ - 2 Soms.	Reverse 2½ - 3 Soms.	Reverse 3½ - 4½ Soms.	Inward ½ - 1 Soms.	Inward 1½ - 4½ Soms.
5m	0	0.5	0.2	0.5	0.3	0.4	0.6	0.6	0.5
7.5m	0	0.3	0.2	0.3	0.3	0.4	0.4	0.3	0.3
10m	0	0.2	0.2	0.2	0.3	0.4	0.3	0.3	0.2

D. Approach Armstand Group (Does not apply to armstand dives with twists)

Level	Armstand Forward with 0 - 2 Soms.	Armstand Forward with more than 2 Soms	Armstand Back with 0 - ½ Soms.	Armstand Back with 1 - 4 Soms.	Armstand Reverse with 0 - ½ Som.	Armstand Reverse with 1 - 4 Soms.
5m / 7.5m / 10m	0.2	0.4	0.2	0.4	0.3	0.5

E. Unnatural Entry (does not apply to twisting dives)

Group	½ Som.	1 Som.	1½ Som.	2 Som.	2½ Som.	3 Som.	3½ Som.	4 Som.	4½ Som.	5½ Som.
Forward / Inward	-	0.1	-	0.2	-	0.2	-	0.0	-	-
Back / Reverse	0.1	-	0.2	-	0.3	-	0.4	-	0.4	0.0
Armstand Back / Reverse	-	0.1	-	0.2	-	0.2	-	0.3	-	-
Armstand Forward	0.1	-	0.2	-	0.3	-	0.4	-	0.4	0.0

A value indicates the diver does not see the water before the entry. The component is the same at all levels.
(-) indicates the diver does see the water before the entry. The component is the same at all levels.

Examples

Dive	Pos	Hght	A	B	C	D	E	DD
307	B	10	2.7	0.3	0.0	0.3	0.4	**3.7**
307	C	10	2.7	0.0	0.0	0.3	0.4	**3.4**
5371	B	10	2.7	0.3	0.0	0.3	0.0	**3.3**
5257	B	10	2.1	0.3	1.5	0.2	0.0	**4.1**

Dive	Pos	Hght	A	B	C	D	E	DD
309	B	10	3.5	0.6	0.0	0.3	0.4	**4.8**
309	C	10	3.5	0.3	0.0	0.3	0.4	**4.5**
5371	C	10	2.7	0.0	0.0	0.3	0.0	**3.0**
6247	D	10	1.9	0.0	2.1	0.0	0.0	**4.0**

FINA TABLE OF DEGREES OF DIFFICULTY
PLATFORM

In the following table, a dive with (-) is not possible and dives with empty spaces have not been calculated.

PLATFORM		10 METER				7.5 METER				5 METER			
		STR	PIKE	TUCK	FREE	STR	PIKE	TUCK	FREE	STR	PIKE	TUCK	FREE
Forward Group		**A**	**B**	**C**	**D**	**A**	**B**	**C**	**D**	**A**	**B**	**C**	**D**
101	Forward Dive	1.6	1.5	1.4	-	1.6	1.5	1.4	-	1.4	1.3	1.2	-
102	Forward 1 Somersault	1.8	1.7	1.6	-	1.7	1.6	1.5	-	1.6	1.5	1.4	-
103	Forward 1 ½ Somersaults	1.9	1.6	1.5	-	1.9	1.6	1.5	-	2.0	1.7	1.6	-
104	Forward 2 Somersaults	2.5	2.2	2.1	-	2.4	2.1	2.0	-	2.6	2.3	2.2	-
105	Forward 2½ Somersaults	2.7	2.3	2.1	-		2.4	2.2	-		2.6	2.4	-
106	Forward 3 Somersaults		3.0	2.7	-		2.8	2.5	-		3.2	2.9	-
107	Forward 3½ Somersaults		3.0	2.7	-		3.1	2.8	-			3.0	-
108	Forward 4 Somersaults		4.1	3.7	-				-				-
109	Forward 4½ Somersaults		4.1	3.7	-				-				-
1011	Forward 5½ Somersaults			4.7	-				-				-
112	Forward Flying Somersaults	-	1.9	1.8	-	-	1.8	1.7	-	-	1.7	1.6	-
113	Forward Flying 1½ Somersaults	-	1.8	1.7	-	-	1.8	1.7	-	-	1.9	1.8	-
114	Forward Flying 2 Somersaults	-	2.4	2.3	-	-	2.3	2.2	-	-	2.5	2.4	-
115	Forward Flying 2½ Somersaults	-	2.6	2.4	-	-		2.5	-	-			-
Back Group		**A**	**B**	**C**	**D**	**A**	**B**	**C**	**D**	**A**	**B**	**C**	**D**
201	Back Dive	1.9	1.8	1.7	-	1.9	1.8	1.7	-	1.7	1.6	1.5	-
202	Back 1 Somersault	1.9	1.8	1.7	-	1.8	1.7	1.6	-	1.7	1.6	1.5	-
203	Back 1½ Somersaults	2.4	2.2	1.9	-	2.4	2.2	1.9	-	2.5	2.3	2.0	-
204	Back 2 Soms Somersaults	2.6	2.4	2.1	-	2.5	2.3	2.0	-		2.5	2.2	-
205	Back 2½ Somersaults	3.3	2.9	2.7	-		3.0	2.8	-		3.2	3.0	-
206	Back 3 Somersaults		3.0	2.7	-		2.8	2.5	-		3.2	2.9	-
207	Back 3½ Somersaults		3.6	3.3	-			3.5	-				-
208	Back 4 Somersaults		4.1	3.8	-		4.2	3.9	-		4.4	4.1	-
209	Back 4½ Somersaults		4.5	4.2	-				-				-
212	Back Flying Somersaults	-	1.9	1.8	-	-	1.8	1.7	-	-	1.7	1.6	-
213	Back Flying 1½ Somersaults	-	2.4	2.1	-	-	2.4	2.1	-	-	2.5	2.2	-
215	Back Flying 2 ½ Somersaults	-	3.2	3.0	-	-			-	-			-
Reverse Group		**A**	**B**	**C**	**D**	**A**	**B**	**C**	**D**	**A**	**B**	**C**	**D**
301	Reverse Dive	2.0	1.9	1.8	-	2.0	1.9	1.8	-	1.8	1.7	1.6	-
302	Reverse 1 Somersault	2.0	1.9	1.8	-	1.9	1.8	1.7	-	1.8	1.7	1.6	-
303	Reverse 1½ Somersaults	2.6	2.3	2.0	-	2.6	2.3	2.0	-	2.7	2.4	2.1	-
304	Reverse 2 Somersaults	2.8	2.5	2.2	-	2.7	2.4	2.1	-	2.9	2.6	2.3	-
305	Reverse 2½ Somersaults	3.4	3.0	2.8	-	3.5	3.1	2.9	-		3.3	3.1	-
306	Reverse 3 Somersaults		3.2	2.9	-		3.0	2.7	-		3.4	3.1	-
307	Reverse 3½ Somersaults		3.7	3.4	-				-				-
308	Reverse 4 Somersaults		4.4	4.1	-		4.5	4.2	-				-
309	Reverse 4½ Somersaults		4.8	4.5	-				-				-
312	Reverse Flying Somersaults	-	2.0	1.9	-	-	1.9	1.8	-	-	1.8	1.7	-
313	Reverse Flying 1½ Somersaults	-	2.5	2.2	-	-	2.5	2.2	-	-	2.6	2.3	-
Inward Group		**A**	**B**	**C**	**D**	**A**	**B**	**C**	**D**	**A**	**B**	**C**	**D**
401	Inward Dive	1.7	1.4	1.3	-	1.7	1.4	1.3	-	1.8	1.5	1.4	-
402	Inward 1 Somersault	1.9	1.6	1.5	-	1.8	1.5	1.4	-	2.0	1.7	1.6	-
403	Inward 1½ Somersault		2.0	1.8	-		2.1	1.9	-		2.4	2.2	-

		10 METER				7.5 METER				5 METER			
	Inward Group	**A**	**B**	**C**	**D**	**A**	**B**	**C**	**D**	**A**	**B**	**C**	**D**
404	Inward 2 Somersaults		2.6	2.4	-		2.6	2.4	-		3.0	2.8	-
405	Inward 2½ Somersaults		2.8	2.5	-		3.0	2.7	-		3.4	3.1	-
406	Inward 3 Somersaults		3.5	3.2	-		3.4	3.1	-		4.0	3.7	-
407	Inward 3½ Somersaults		3.5	3.2	-			3.4	-				-
408	Inward 4 Somersaults		4.4	4.1	-				-				-
409	Inward 4½ Somersaults		4.4	4.1	-				-				-
412	Inward Flying Somersaults	-	2.0	1.9	-	-	1.9	1.8	-	-	2.1	2.0	-
413	Inward Flying 1½ Somersaults	-	2.5	2.3	-	-	2.6	2.4	-	-	2.9	2.7	-
	Twisting Group	**A**	**B**	**C**	**D**	**A**	**B**	**C**	**D**	**A**	**B**	**C**	**D**
5111	Fwd Dive ½ Twist	2.0	1.9	1.8	-	2.0	1.9	1.8	-	1.8	1.7	1.6	-
5112	Fwd Dive 1 Twist	2.2	2.1		-	2.2	2.1		-	2.0	1.9		-
5121	Fwd Somersault ½ Twist	-	-	-	1.9	-	-	-	1.8	-	-	-	1.7
5122	Fwd Somersault 1 Twist	-	-	-	2.1	-	-	-	2.0	-	-	-	1.9
5124	Fwd Somersault 2 Twists	-	-	-	2.5	-	-	-	2.4	-	-	-	2.3
5131	Fwd 1½ Somersaults ½ Twist	-	-	-	1.9	-	-	-	1.9	-	-	-	2.0
5132	Fwd 1½ Somersaults 1 Twist	-	-	-	2.1	-	-	-	2.1	-	-	-	2.2
5134	Fwd 1½ Somersaults 2 Twists	-	-	-	2.5	-	-	-	2.5	-	-	-	2.6
5136	Fwd 1½ Somersaults 3 Twists	-	-	-	3.0	-	-	-	3.0	-	-	-	3.1
5138	Fwd 1½ Somersaults 4 Twists	-	-	-	3.4	-	-	-	3.4	-	-	-	3.5
5152	Fwd 2½ Somersaults 1 Twist	-	2.9	2.7	-	-	3.0	2.8	-	-	3.2	3.0	-
5154	Fwd 2½ Somersaults 2 Twists	-	3.3	3.1	-	-	3.4	3.2	-	-	3.6	3.4	-
5156	Fwd 2½ Somersaults 3 Twists	-	3.8	3.6	-	-			-	-			-
5172	Fwd 3½ Somersaults 1 Twist	-	3.6	3.3	-	-	3.7	3.4	-	-	-	-	-
5211	Back Dive ½ Twist	2.0	1.9	1.8	-	2.0	1.9	1.8	-	1.8	1.7	1.6	-
5212	Back Dive 1 Twist	2.2			-	2.2			-	2.0			-
5221	Back Somersault ½ Twist	-	-	-	1.9	-	-	-	1.8	-	-	-	1.7
5222	Back Somersault 1 Twist	-	-	-	2.1	-	-	-	2.0	-	-	-	1.9
5223	Back Somersault 1½ Twists	-	-	-	2.5	-	-	-	2.4	-	-	-	2.3
5225	Back Somersault 2½ Twists	-	-	-	2.9	-	-	-	2.8	-	-	-	2.7
5231	Back 1½ Somersaults ½ Twist	-	-	-	2.0	-	--	-	2.0	-	-	-	2.1
5233	Back 1½ Somersaults 1½ Twists	-	-	-	2.4	-	-	-	2.4	-	-	-	2.5
5235	Back 1½ Somersaults 2½ Twists	-	-	-	2.8	-	-	-	2.8	-	-	-	2.9
5237	Back 1½ Somersaults 3½ Twists	-	-	-	3.3	-	-	-	3.3	-	-	-	3.4
5239	Back 1½ Somersaults 4½ Twists	-	-	-	3.7	-	-	-	3.7	-	-	-	3.8
5251	Back 2½ Somersaults ½ Twist	-	2.6	2.4	-	-	2.7	2.5	-	-	2.9	2.7	-
5253	Back 2½ Somersaults 1½ Twists	-	3.2	3.0	-	-	3.3	3.1	-	-			-
5255	Back 2½ Somersaults 2½ Twists	-	3.6	3.4	-	-			-	-			-
5257	Back 2½ Somersaults 3½ Twists	-	4.1	3.9	-	-			-	-			-
5271	Back 3½ Somersaults ½ Twist	-	3.2	2.9	-	-			-	-			-
5273	Back 3½ Somersaults 1½ Twist	-	3.8	3.5	-	-			-	-			-
5275	Back 3½ Somersaults 2½ Twist	-	4.2	3.9	-	-			-	-			-
5311	Reverse Dive ½ Twist	2.1	2.0	1.9	-	2.1	2.0	1.9	-	1.9	1.8	1.7	-
5312	Reverse Dive 1 Twist	2.3			-	2.3			-	2.1			-
5321	Reverse Somersault ½ Twist	-	-	-	2.0	-	-	-	1.9	-	-	-	1.8
5322	Reverse Somersault 1 Twist	-	-	-	2.2	-	-	-	2.1	-	-	-	2.0
5323	Reverse Somersault 1½ Twists	-	-	-	2.6	-	-	-	2.5	-	-	-	2.4
5325	Reverse Somersault 2½ Twists	-	-	-	3.0	-	-	-	2.9	-	-	-	2.8
5331	Reverse 1½ Soms. ½ Twists	-	-	-	2.1	-	-	-	2.1	-	-	-	2.2
5333	Reverse 1½ Soms. 1½ Twists	-	-	-	2.5	-	-	-	2.5	-	-	-	2.6
5335	Reverse 1½ Soms. 2½ Twists	-	-	-	2.9	-	-	-	2.9	-	-	-	3.0
5337	Reverse 1½ Soms. 3½ Twists	-	-	-	3.4	-	-	-	3.4	-	-	-	3.5
5339	Reverse 1½ Soms. 4½ Twists	-	-	-	3.8	-	-	-	3.8	-	-	-	-
5351	Reverse 2½ Soms. ½ Twists	-	2.7	2.5	-	-	2.8	2.6	-	-	3.0	2.8	-

		10 METER				7.5 METER				5 METER			
Twisting Group		**A**	**B**	**C**	**D**	**A**	**B**	**C**	**D**	**A**	**B**	**C**	**D**
5353	Reverse 2½ Soms. 1½ Twists	-	3.3	3.1	-	-	3.4	3.2	-	-		3.4	-
5355	Reverse 2½ Soms. 2½ Twists	-	3.7	3.5	-	-	3.8	3.6	-	-		3.8	-
5371	Reverse 3½ Soms. ½ Twists	-	3.3	3.0	-	-			-	-			-
5373	Reverse 3½ Soms. 1½ Twist	-		3.6	-	-			-	-			-
5375	Reverse 3½ Soms. 2½ Twist	-		4.0	-	-			-	-			-
5411	Inward Dive ½ Twist	1.9	1.6	1.5	-	1.9	1.6	1.5	-	2.0	1.7	1.6	-
5412	Inward Dive 1 Twist	2.1	1.8	1.7	-	2.1	1.8	1.7	-	2.2	1.9	1.8	-
5421	Inward Somersault ½ Twist	-	-	-	1.8	-	-	-	1.7	-	-	-	1.9
5422	Inward Somersault 1 Twist	-	-	-	2.0	-	-	-	1.9	-	-	-	2.1
5432	Inward 1½ Somersaults 1 Twist	-	-	-	2.3	-	-	-	2.4	-	-	-	2.7
5434	Inward 1½ Somersaults 2 Twists	-	-	-	2.7	-	-	-	2.8	-	-	-	3.1
5436	Inward 1½ Somersaults 3 Twists	-	-	-	3.4	-	-	-		-	-	-	
Armstand Group													
600	Armstand Dive	1.6	-	-	-	1.6	-	-	-	1.5	-	-	-
611	Armstand Forward ½ Somersault	2.0	1.9	1.7	-	2.0	1.9	1.7	-	1.8	1.7	1.5	-
612	Armstand Forward 1 Somersault	2.0	1.9	1.7	-	1.9	1.8	1.6	-	1.8	1.7	1.5	-
614	Armstand Forward 2 Somersaults		2.4	2.1	-		2.3	2.0	-		2.5	2.2	-
616	Armstand Forward 3 Somersaults		3.3	3.1	-				-				-
621	Armstand Back ½ Somersault	1.9	1.8	1.6	-	1.9	1.8	1.6	-	1.7	1.6	1.4	-
622	Armstand Back Somersault	2.3	2.2	2.0	-	2.2	2.1	1.9	-	2.1	2.0	1.8	-
623	Armstand Back 1½ Somersaults		2.2	1.9	-		2.2	1.9	-		2.3	2.0	-
624	Armstand Back 2 Somersaults	3.0	2.8	2.5	-	2.9	2.7	2.4	-	3.1	2.9	2.6	-
626	Armstand Back 3 Somersaults		3.5	3.3	-		3.3	3.1	-			3.5	-
628	Armstand Back 4 Somersaults		4.7	4.5	-				-				-
631	Armstand Reverse ½ Somersault	2.0	1.9	1.7	-	2.0	1.9	1.7	-	1.8	1.7	1.5	-
632	Armstand Reverse 1 Somersault		2.3	2.1	-		2.2	2.0	-		2.1	1.9	-
633	Armstand Reverse 1½ Soms.		2.3	2.0	-		2.3	2.0	-		2.4	2.1	-
634	Armstand Reverse 2 Soms.		2.9	2.6	-		2.8	2.5	-		3.0	2.7	-
636	Armstand Reverse 3 Soms.		3.6	3.4	-			3.2	-				-
638	Armstand Reverse 4 Soms.		4.8	4.6	-				-				-
6122	Armstand Fwd Som. 1 Twist	-	-	-	2.6	-	-	-	2.5	-	-	-	2.4
6124	Armstand Fwd Som. 2 Twists	-	-	-	2.9	-	-	-	2.8	-	-	-	2.7
6142	Armstand Fwd 2 Soms. 1 Twist	-	-	-	3.1	-	-	-	3.0	-	-	-	3.2
6144	Armstand Fwd 2 Soms. 2 Twists	-	-	-	3.4	-	-	-	3.3	-	-	-	3.5
6162	Armstand Fwd 3 Soms. 1 Twist	-		3.9	-	-			-	-			-
6221	Armstand Back Som. ½ Twist	-	-	-	1.8	-	-	-	1.7	-	-	-	1.6
6241	Armstand Back 2 Soms. ½ Twist	-	2.7	2.4	-	-	2.6	2.3	-	-	2.8	2.5	-
6243	Armstand Back 2 Soms 1½ Twists	-	-	-	3.2	-	-	-	3.1	-	-	-	3.3
6245	Armstand Back 2 Soms 2½ Twists	-	-	-	3.6	-	-	-	3.5	-	-	-	3.7
6247	Armstand Back 2 Soms 3½ Twists	-	-	-	4.0	-	-	-		-	-	-	
6261	Armstand Back 3 Soms. ½ Twist	-	3.4	3.2	-	-	3.2	3.0	-	-	3.6	3.4	-
6263	Armstand Back 3 Soms 1½ Twists	-	4.2	4.0	-	-			-	-			-
6265	Armstand Back 3 Soms 2½ Twists	-	4.6	4.4	-	-			-	-			-

APPENDIX D

Magnus Expansion

For a system of linear differential equations of the form

$$\dot{\boldsymbol{L}} = M(t)\boldsymbol{L}$$

the solution is

$$\boldsymbol{L} = e^{\Omega(t)}\boldsymbol{L}(0),$$

where

$$\Omega(t) = \sum_{n=1}^{\infty} \Omega_n(t).$$

The Magnus terms Ω_n of the Magnus series $\Omega(t)$ can be generated recursively with the matrix S_n^j, defined as

$$\begin{aligned} S_n^1(\tau) &= [\Omega_{n-1}(\tau), M(\tau)] \\ S_n^j(\tau) &= \sum_{m=1}^{n-j} [\Omega_m(\tau), S_{n-m}^{j-1}(\tau)] \quad \text{for } 2 \leq j \leq n-1, \end{aligned}$$

where $[.,.]$ is the matrix commutator. The Magnus terms Ω_n are then

$$\begin{aligned} \Omega_1(t) &= \int_0^t M(\tau)\,\mathrm{d}\tau \\ \Omega_n(t) &= \sum_{j=1}^{n-1} \frac{B_j}{j!} \int_0^t S_n^j(\tau)\,\mathrm{d}\tau \quad \text{for } n \geq 2, \end{aligned}$$

where B_j is the jth Bernoulli number. We now derive the first three terms of the Magnus expansion. Clearly,

$$\Omega_1(t) = \int_0^t M(t_1)\,\mathrm{d}t_1,$$

and

$$\begin{aligned}\Omega_2(t) &= \frac{B_1}{1!}\int_0^t S_2^1(t_1)\,\mathrm{d}t_1 \\ &= -\frac{1}{2}\int_0^t [\Omega_1(t_1), M(t_1)]\,\mathrm{d}t_1 \\ &= -\frac{1}{2}\int_0^t \left[\int_0^{t_1} M(t_2)\,\mathrm{d}t_2, M(t_1)\right]\,\mathrm{d}t_1 \\ &= \frac{1}{2}\int_0^t\int_0^{t1} [M(t_1), M(t_2)]\;\mathrm{d}t_2\mathrm{d}t_1.\end{aligned}$$

Now

$$\begin{aligned}\Omega_3(t) &= \frac{B_1}{1!}\int_0^t S_3^1(t_1)\,\mathrm{d}t_1 + \frac{B_2}{2!}\int_0^t S_3^2(t_1)\,\mathrm{d}t_1 \\ &= -\frac{1}{2}\int_0^t [\Omega_2(t_1), M(t_1)]\,\mathrm{d}t_1 + \frac{1}{12}\int_0^t [\Omega_1(t_1), [\Omega_1(t_1), M(t_1)]]\,\mathrm{d}t_1,\end{aligned}$$

and writing M_i to denote $M(t_i)$ for simplicity, the first integral becomes

$$-\frac{1}{2}\int_0^t [\Omega_2(t_1), M_1]\,\mathrm{d}t_1 = \frac{1}{4}\int_0^t\int_0^{t_1}\int_0^{t_2} [M_1, [M_2, M_3]]\,\mathrm{d}t_3\mathrm{d}t_2\mathrm{d}t_1,$$

where we substituted in $\Omega_2(t_1)$ and swapped the order of the commutator. The second integral is more complicated. Looking firstly at the integrand

$$\begin{aligned}\Big[\Omega_1(t_1), [\Omega_1(t_1), M_1)]\Big] &= \left[\int_0^{t_1} M_3\,\mathrm{d}t_3, \left[\int_0^{t_1} M_2\,\mathrm{d}t_2, M_1\right]\right] \\ &= \int_0^{t_1}\int_0^{t_1} \Big[M_3, [M_2, M_1]\Big]\,\mathrm{d}t_3\,\mathrm{d}t_2,\end{aligned}$$

we now split up the inner interval so that $\int_0^{t_1}\int_0^{t_1} = \int_0^{t_1}\int_0^{t_2} + \int_0^{t_1}\int_{t_2}^{t_1}$, and apply the transformation

$$\int_0^{t_1}\int_{t_2}^{t_1} f(t_2, t_3)\,\mathrm{d}t_3\mathrm{d}t_2 = \int_0^{t_1}\int_0^{t_3} f(t_2, t_3)\,\mathrm{d}t_2\mathrm{d}t_3.$$

Following the transformation, we swap the dummy variables $t_2 \leftrightarrow t_3$ to obtain

$$\Big[\Omega_1(t_1), [\Omega_1(t_1), M_1]\Big] = \int_0^{t_1}\int_0^{t_2} \Big[M_3, [M_2, M_1]\Big] + \Big[M_2, [M_3, M_1]\Big]\,\mathrm{d}t_3\,\mathrm{d}t_2.$$

Substituting this result back into $\Omega_3(t)$, we arrive at

$$\Omega_3(t) = \int_0^t\int_0^{t_1}\int_0^{t_2} \left(\frac{1}{4}[M_1, [M_2, M_3]] + \frac{1}{12}[M_3, [M_2, M_1]] + \frac{1}{12}[M_2, [M_3, M_1]]\right)\,\mathrm{d}t_3\mathrm{d}t_2\mathrm{d}t_1.$$

The last step is to use the Jacobi identity to show that

$$\begin{aligned}[M_2,[M_3,M_1]] &= -[M_3,[M_1,M_2]] - [M_1,[M_2,M_3]] \\ &= [M_3,[M_2,M_1]] - [M_1,[M_2,M_3]],\end{aligned}$$

thus we have

$$\Omega_3(t) = \frac{1}{6}\int_0^t\int_0^{t_1}\int_0^{t_2} \Big([M_1,[M_2,M_3]] - [M_3,[M_2,M_1]]\Big)\,\mathrm{d}t_3\mathrm{d}t_2\mathrm{d}t_1.$$

APPENDIX E

Digitised Dataset

Frame	v_{ref}	v_{hd}	v_{up}	v_{ud}	v_{lp}	v_{ld}
0	0.647832	0.720361	-2.06629	-1.94748	0.0341072	0.359781
1	0.660258	0.722664	-2.04806	-1.92977	0.0374983	0.354845
2	0.684925	0.727475	-2.01089	-1.89374	0.0441458	0.345205
3	0.721438	0.735205	-1.95339	-1.83824	0.0537881	0.331326
4	0.769137	0.746453	-1.87372	-1.76182	0.0660538	0.313898
5	0.827053	0.762001	-1.77003	-1.66313	0.0804853	0.293821
6	0.893879	0.782802	-1.64135	-1.54174	0.0965708	0.27218
7	0.96801	0.809977	-1.48896	-1.39927	0.113781	0.250198
8	1.04764	0.84481	-1.31768	-1.24025	0.131608	0.22918
9	1.13093	0.88875	-1.13599	-1.0721	0.149608	0.21045
10	1.21619	0.943391	-0.953924	-0.903405	0.167431	0.195289
11	1.30205	1.01042	-0.779847	-0.741423	0.184856	0.184884
12	1.38757	1.09151	-0.618298	-0.590325	0.201807	0.180292
13	1.47228	1.18803	-0.469959	-0.45107	0.218371	0.182428
14	1.55613	1.30071	-0.332918	-0.322296	0.234795	0.192057
15	1.63949	1.42906	-0.204007	-0.201379	0.251488	0.209802
16	1.72299	1.57094	-0.079668	-0.0851889	0.269011	0.23615
17	1.8075	1.72242	0.0436073	0.0295079	0.28806	0.271447
18	1.89406	1.87841	0.169101	0.14587	0.309455	0.315889
19	1.98378	2.0338	0.299772	0.266896	0.334114	0.369494
20	2.0778	2.18465	0.438124	0.395328	0.363037	0.432075
21	2.1772	2.32887	0.585961	0.533439	0.397279	0.503198
22	2.28288	2.46621	0.744026	0.682672	0.437913	0.58217
23	2.39544	2.59774	0.911589	0.843124	0.485984	0.668041
24	2.51499	2.72539	1.08623	1.01307	0.542448	0.759658
25	2.64107	2.85142	1.26407	1.18885	0.608074	0.855751
26	2.7725	2.97813	1.44058	1.36546	0.683327	0.955052
27	2.90752	3.10764	1.61165	1.53773	0.768237	1.05643
28	3.04399	-3.04159	1.77444	1.70162	0.862272	1.15898
29	-3.10344	-2.90219	1.92773	1.85489	0.964282	1.26211

#	υ_{ref}	υ_{hd}	υ_{up}	υ_{ud}	υ_{lp}	υ_{ld}
30	-2.97019	-2.75723	2.0717	1.99707	1.07255	1.36555
31	-2.84065	-2.60768	2.20746	2.12901	1.18501	1.46933
32	-2.7153	-2.45553	2.33673	2.25227	1.29951	1.57376
33	-2.59396	-2.30347	2.46142	2.36871	1.41419	1.67931
34	-2.47591	-2.15435	2.5835	2.48016	1.52771	1.78662
35	-2.36008	-2.01061	2.70489	2.58826	1.63938	1.89634
36	-2.2452	-1.87381	2.82741	2.69436	1.74914	2.00916
37	-2.12992	-1.74448	2.95274	2.79946	1.85745	2.12563
38	-2.01296	-1.6222	3.08233	2.90417	1.96514	2.24617
39	-1.89321	-1.50579	-3.0658	3.00872	2.07329	2.37094
40	-1.76985	-1.39345	-2.9245	3.11291	2.18305	2.4998
41	-1.64248	-1.28294	-2.77675	-3.06691	2.29559	2.63225
42	-1.51122	-1.17159	-2.62309	-2.96511	2.41188	2.76748
43	-1.37672	-1.05623	-2.46486	-2.86564	2.53267	2.90441
44	-1.2402	-0.933152	-2.30415	-2.76917	2.6583	3.04181
45	-1.10318	-0.797983	-2.14354	-2.67616	2.7886	-3.10471
46	-0.967331	-0.645859	-1.98569	-2.58666	2.92286	-2.96985
47	-0.834116	-0.472064	-1.83288	-2.50033	3.05988	-2.83759
48	-0.704618	-0.273743	-1.68676	-2.41638	-3.08511	-2.70843
49	-0.579395	-0.0527986	-1.54818	-2.33357	-2.94742	-2.58255
50	-0.458464	0.181595	-1.41727	-2.25028	-2.81176	-2.45989
51	-0.341368	0.414381	-1.29362	-2.16451	-2.67926	-2.34017
52	-0.227276	0.630859	-1.17638	-2.07401	-2.55053	-2.22303
53	-0.115091	0.822623	-1.06449	-1.97634	-2.42567	-2.10801
54	-0.0035469	0.988459	-0.956682	-1.86918	-2.30431	-1.99465
55	0.108713	1.13168	-0.851616	-1.75066	-2.18574	-1.88252
56	0.223058	1.25732	-0.747842	-1.62002	-2.06905	-1.77122
57	0.340783	1.37062	-0.643819	-1.47819	-1.9532	-1.66044
58	0.463011	1.47646	-0.537902	-1.32827	-1.83719	-1.5499
59	0.590552	1.57936	-0.428333	-1.17524	-1.7201	-1.4394
60	0.723748	1.68365	-0.31327	-1.02478	-1.60116	-1.32878
61	0.862316	1.79366	-0.190864	-0.881794	-1.47991	-1.21794
62	1.00525	1.9138	-0.0594543	-0.749322	-1.35617	-1.10676
63	1.15086	2.0484	0.0820959	-0.628332	-1.23011	-0.995169
64	1.29695	2.20105	0.233908	-0.518135	-1.10223	-0.883053
65	1.4412	2.37309	0.394558	-0.417017	-0.973312	-0.770292
66	1.58154	2.56178	0.560787	-0.322743	-0.844263	-0.656737
67	1.71645	2.75914	0.727803	-0.232863	-0.715984	-0.542208
68	1.84514	2.9537	0.890258	-0.144827	-0.589214	-0.426507
69	1.96749	3.13471	1.04352	-0.0559718	-0.464417	-0.309419

#	υ_{ref}	υ_{hd}	υ_{up}	υ_{ud}	υ_{lp}	υ_{ld}
70	2.08395	-2.98736	1.18457	0.036576	-0.341719	-0.190738
71	2.19542	-2.8475	1.31223	0.136067	-0.220908	-0.070278
72	2.30303	-2.72685	1.42683	0.246324	-0.101474	0.0520982
73	2.40811	-2.62188	1.52964	0.371914	0.0173191	0.176463
74	2.5121	-2.52882	1.62246	0.51813	0.136348	0.302805
75	2.61645	-2.44417	1.70725	0.690378	0.256536	0.43102
76	2.72271	-2.36494	1.78602	0.892276	0.378753	0.560914
77	2.83237	-2.28861	1.86074	1.12207	0.503714	0.692219
78	2.94694	-2.21308	1.9334	1.36913	0.631878	0.824613
79	3.06781	-2.13657	2.00598	1.61545	0.763359	0.957763
80	-3.08706	-2.05761	2.08062	1.84372	0.897878	1.09136
81	-2.95054	-1.97492	2.15966	2.04466	1.03477	1.22515
82	-2.80567	-1.88746	2.24572	2.21753	1.17305	1.35898
83	-2.65316	-1.79433	2.34182	2.36636	1.31161	1.49276
84	-2.49465	-1.69483	2.45131	2.49654	1.44937	1.62653
85	-2.33263	-1.58834	2.57768	2.61316	1.58548	1.76035
86	-2.17002	-1.47437	2.72387	2.72049	1.71947	1.89437
87	-2.0097	-1.35246	2.891	2.82197	1.8513	2.02867
88	-1.85395	-1.22211	3.07664	2.92039	1.98133	2.16334
89	-1.70415	-1.08274	-3.00948	3.01796	2.11028	2.29833
90	-1.56081	-0.933605	-2.8115	3.11647	2.23913	2.4335
91	-1.42365	-0.7738	-2.62297	-3.06589	2.36899	2.56858
92	-1.29186	-0.602403	-2.45053	-2.96181	2.50081	2.70319
93	-1.16434	-0.418769	-2.29619	-2.85402	2.63622	2.83687
94	-1.03988	-0.223064	-2.15842	-2.74266	2.77538	2.96913
95	-0.917269	-0.0169174	-2.03395	-2.62851	2.91885	3.09954
96	-0.795387	0.196108	-1.919	-2.513	3.06645	-3.05541
97	-0.673259	0.410688	-1.80989	-2.39804	-3.06578	-2.92952
98	-0.550088	0.620767	-1.70333	-2.28579	-2.91283	-2.80596
99	-0.42528	0.821048	-1.59645	-2.17835	-2.75962	-2.6845
100	-0.298452	1.00812	-1.48685	-2.07743	-2.60797	-2.56472
101	-0.169436	1.18072	-1.37259	-1.98416	-2.4595	-2.44599
102	-0.0382567	1.33937	-1.25234	-1.89905	-2.31536	-2.32753
103	0.094893	1.48566	-1.12548	-1.82197	-2.17612	-2.20842
104	0.229704	1.62175	-0.9922	-1.75224	-2.04181	-2.0876
105	0.365805	1.74995	-0.853569	-1.68867	-1.91198	-1.96395
106	0.502821	1.87259	-0.711362	-1.62964	-1.78585	-1.83632
107	0.640421	1.99192	-0.567748	-1.57302	-1.66247	-1.70363
108	0.778352	2.11012	-0.424833	-1.51612	-1.5408	-1.56496
109	0.916454	2.22934	-0.28423	-1.4556	-1.41981	-1.41972

#	υ_{ref}	υ_{hd}	υ_{up}	υ_{ud}	υ_{lp}	υ_{ld}
110	1.05465	2.35177	-0.146783	-1.38732	-1.29857	-1.26787
111	1.19293	2.47961	-0.0124966	-1.3063	-1.1763	-1.11
112	1.33133	2.61508	0.119368	-1.20704	-1.05239	-0.947527
113	1.46986	2.7603	0.250107	-1.0844	-0.926464	-0.782499
114	1.60854	2.91702	0.381367	-0.935845	-0.798363	-0.617388
115	1.74734	3.08619	0.514925	-0.764531	-0.668135	-0.454648
116	1.8862	-3.01584	0.65246	-0.581163	-0.535989	-0.296306
117	2.02503	-2.82511	0.795297	-0.400982	-0.402222	-0.143693
118	2.16371	-2.62922	0.944104	-0.236856	-0.26713	0.0026348
119	2.30216	-2.43386	1.09861	-0.0945835	-0.130923	0.142811
120	2.44035	-2.24464	1.25742	0.0265706	0.0063504	0.277494
121	2.57833	-2.06578	1.4181	0.130894	0.144834	0.407682
122	2.71621	-1.89955	1.57753	0.223821	0.284861	0.534566
123	2.85425	-1.74636	1.73262	0.310845	0.426903	0.659417
124	2.99276	-1.6054	1.88085	0.397362	0.571475	0.783506
125	3.13215	-1.47518	2.02072	0.48903	0.719009	0.908054
126	-3.0103	-1.354	2.1518	0.592456	0.869706	1.03419
127	-2.86778	-1.24019	2.27458	0.716192	1.0234	1.1629
128	-2.72304	-1.13219	2.39015	0.871883	1.17945	1.29501
129	-2.57578	-1.02864	2.50005	1.07453	1.33676	1.43108
130	-2.42584	-0.92832	2.60603	1.33775	1.49388	1.57141
131	-2.27329	-0.830146	2.70999	1.65709	1.64923	1.71595
132	-2.11842	-0.733114	2.81392	1.99218	1.80139	1.86429
133	-1.9618	-0.636262	2.9199	2.28929	1.9493	2.01568
134	-1.80422	-0.538617	3.03013	2.52469	2.09245	2.1691
135	-1.64659	-0.439145	-3.13632	2.7048	2.23087	2.32336
136	-1.48988	-0.3367	-3.01079	2.84469	2.36508	2.4773
137	-1.33496	-0.229968	-2.87437	2.95746	2.49599	2.62986
138	-1.18256	-0.117424	-2.72552	3.05244	2.62474	2.78026
139	-1.03316	0.0026958	-2.56384	3.13606	2.7526	2.92798
140	-0.887005	0.132366	-2.39071	-3.0703	2.88088	3.07279
141	-0.744107	0.273631	-2.2097	-2.99683	3.01076	-3.06846
142	-0.604278	0.428268	-2.02623	-2.92387	-3.13996	-2.9292
143	-0.467193	0.597165	-1.84635	-2.8488	-3.00424	-2.79227
144	-0.33243	0.77945	-1.67517	-2.7689	-2.86503	-2.65726
145	-0.199524	0.971683	-1.51588	-2.68106	-2.72258	-2.52373
146	-0.0680029	1.1678	-1.36956	-2.58143	-2.57765	-2.39122
147	0.0625854	1.36028	-1.23568	-2.46506	-2.4314	-2.25931
148	0.192644	1.54225	-1.11281	-2.3256	-2.28523	-2.12757
149	0.322511	1.70911	-0.999167	-2.15554	-2.14049	-1.99558

#	υ_{ref}	υ_{hd}	υ_{up}	υ_{ud}	υ_{lp}	υ_{ld}
150	0.452439	1.85906	-0.892967	-1.94802	-1.9983	-1.86295
151	0.582585	1.99246	-0.792638	-1.70195	-1.85933	-1.7293
152	0.712991	2.11099	-0.696912	-1.4293	-1.72373	-1.59426
153	0.843575	2.21685	-0.604865	-1.15559	-1.59119	-1.45753
154	0.974114	2.31236	-0.515924	-0.906592	-1.46099	-1.31884
155	1.10424	2.39968	-0.42986	-0.694767	-1.33215	-1.17803
156	1.23344	2.48079	-0.346759	-0.519406	-1.20349	-1.03512
157	1.36107	2.55748	-0.266975	-0.3739	-1.07385	-0.890272
158	1.48636	2.63138	-0.191058	-0.25097	-0.942121	-0.743918
159	1.60847	2.70398	-0.119669	-0.144605	-0.807452	-0.596709
160	1.72655	2.77672	-0.0534857	-0.0503514	-0.66935	-0.449504
161	1.83976	2.85091	0.0068923	0.0349221	-0.52781	-0.303302
162	1.94732	2.92776	0.0610157	0.113321	-0.383374	-0.159129
163	2.04858	3.00832	0.108638	0.186162	-0.237109	-0.0179223
164	2.14301	3.09329	0.149744	0.254149	-0.0904482	0.119577
165	2.23024	-3.10028	0.184548	0.317488	0.0550539	0.252897
166	2.31004	-3.00655	0.213482	0.37598	0.198021	0.381871
167	2.3823	-2.91019	0.237162	0.429096	0.3375	0.506622
168	2.44703	-2.81369	0.256351	0.476056	0.473109	0.627522
169	2.50432	-2.72037	0.271908	0.515903	0.605055	0.745136
170	2.55437	-2.63397	0.284735	0.547593	0.734057	0.860146
171	2.5974	-2.55804	0.295726	0.570093	0.861202	0.973273
172	2.63372	-2.49544	0.305714	0.58249	0.987765	1.08519
173	2.6637	-2.44804	0.31542	0.584119	1.11499	1.19641
174	2.68772	-2.41665	0.325422	0.574705	1.24384	1.30721
175	2.70626	-2.40115	0.336119	0.554517	1.37468	1.41748
176	2.71983	-2.40055	0.347721	0.524492	1.50703	1.52666
177	2.729	-2.41315	0.360249	0.486296	1.63931	1.63369
178	2.73441	-2.43658	0.373542	0.442263	1.76892	1.73706
179	2.73674	-2.46798	0.38728	0.395179	1.89248	1.83487
180	2.73668	-2.50413	0.401023	0.347966	2.00646	1.92511
181	2.73495	-2.54175	0.414246	0.303332	2.10772	2.00584
182	2.73224	-2.57778	0.426387	0.263525	2.19393	2.07534
183	2.7292	-2.6096	0.436893	0.230213	2.26361	2.13227
184	2.72638	-2.63513	0.445263	0.204512	2.31604	2.17567
185	2.72423	-2.65291	0.451087	0.187091	2.35099	2.2049
186	2.72308	-2.66202	0.454074	0.178306	2.36844	2.2196

APPENDIX F

Segment Reduction

Interlaying α_{up} with α_{ud} in Figure F.1A we see that the arm segments overall have similar shape angles, as do the leg segments α_{lp} and α_{ld} as shown in Figure F.1B. Assuming the elbows and knees are kept straight and the head is fixed relative to the torso, we have the assumptions made in (4.21) which essentially reduce the six segment model requiring five shape angles $\{\alpha_{up}, \alpha_{ud}, \alpha_{lp}, \alpha_{ld}, \alpha_{hd}\}$ to just three segments requiring two shape angles $\{\alpha_u, \alpha_l\}$. This reduction affects the dynamics, but not by very much as shown in Figure F.2.

At the end of the 107B dive the dynamic phase in the reduced three segment model is smaller by $0.0012L$, but the geometric phase is greater by 0.0284, resulting in an overall difference of $0.0284 - 0.0012L$. For $L = 120$, this means the athlete rotates less 0.1140 radians or 6.53°, which is small considering the athlete performs 3.5 somersaults. Finally, we plot the evolution of the dynamic and geometric phases during the complete dive in Figure F.3 for the reduced three segment model.

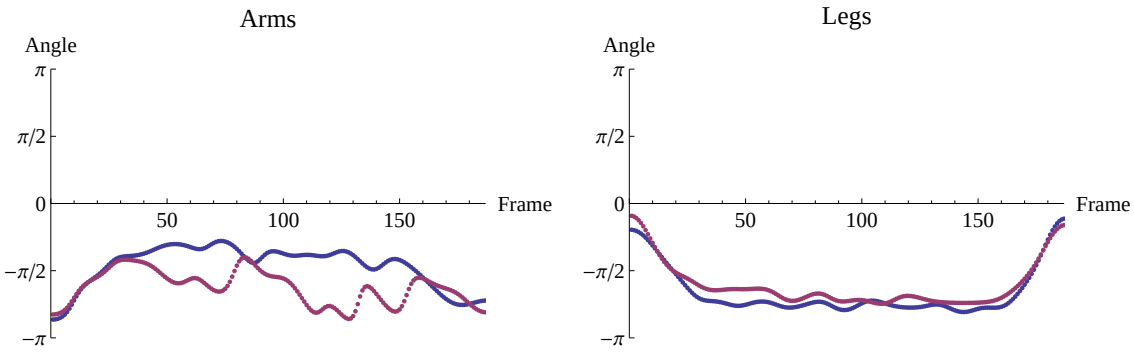

(A) α_{up} in blue, α_{ud} in magenta.

(B) α_{lp} in blue, α_{ld} in magenta.

FIGURE F.1. Plot shows the arm and leg segments move similarly in time.

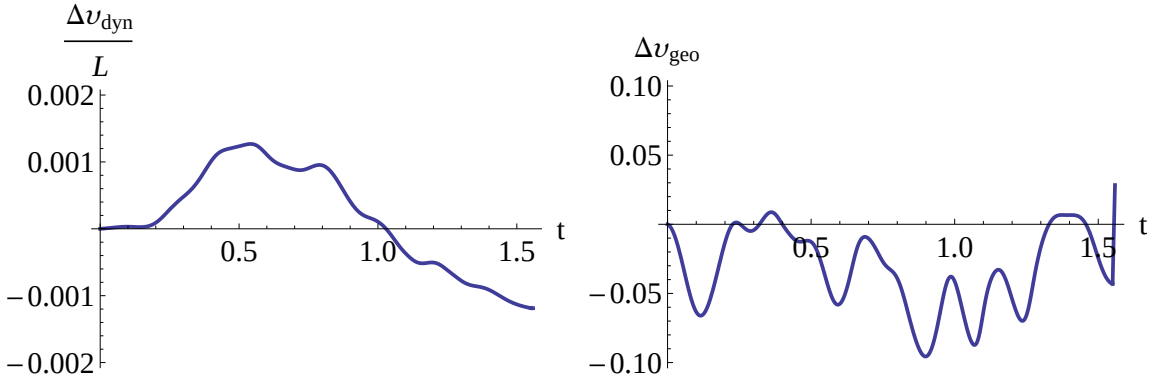

(A) Difference in dynamic phase.

(B) Difference in geometric phase.

FIGURE F.2. The differences Δv_{dyn} and Δv_{geo} are obtained by taking the result from the reduced three segment model and subtracting the corresponding result from the six segment model.

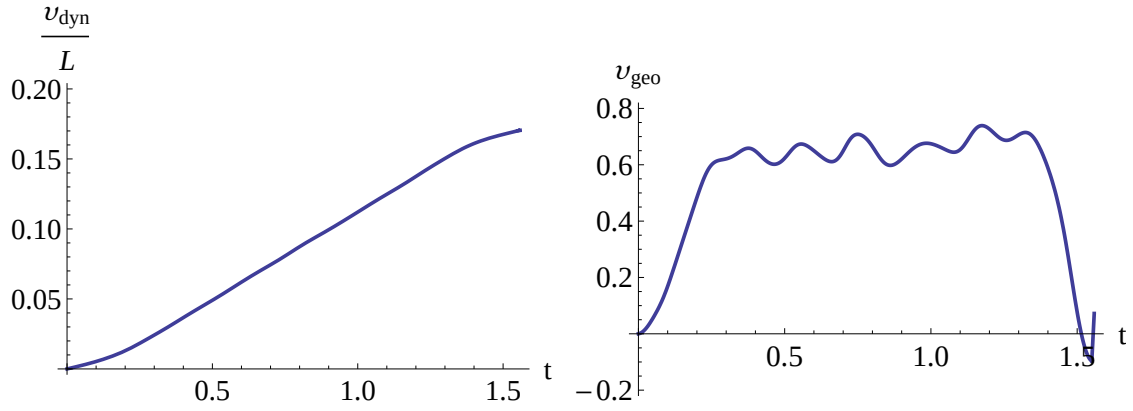

(A) Dynamic phase divided by L.

(B) Geometric phase.

FIGURE F.3. At the end of the dive the dynamic phase is $0.1705L$ and the geometric phase is 0.0721 radians.

APPENDIX G

Geometric Phase

The loop $\boldsymbol{C}$ obtained from letting $\boldsymbol{\alpha}(t)$ run from 0 to T_e is divided into ten pieces denoted by $\boldsymbol{C}_i$ for $i \in \{1, \ldots, 10\}$, where the intervals are specified in Table G.1. In Figure 4.8 we labelled the longer pieces $\boldsymbol{C}_1$, $\boldsymbol{C}_2$, $\boldsymbol{C}_8$, $\boldsymbol{C}_9$ and $\boldsymbol{C}_{10}$, but the

	t_s	t_e	$\alpha_u(t_s)$	$\alpha_l(t_s)$	$\alpha_u(t_e)$	$\alpha_l(t_e)$
$\boldsymbol{C}_1$	0	0.0674	−2.7141	−0.6137	−2.3571	−0.9215
$\boldsymbol{C}_2$	0.0674	0.2947	−2.3571	−0.9215	−1.2157	−2.2854
$\boldsymbol{C}_3$	0.2947	0.8811	−1.2157	−2.2854	−1.2157	−2.2854
$\boldsymbol{C}_4$	0.8811	0.9259	−1.2157	−2.2854	−1.2061	−2.3709
$\boldsymbol{C}_5$	0.9259	1.0747	−1.2061	−2.3709	−1.2061	−2.3709
$\boldsymbol{C}_6$	1.0747	1.1361	−1.2061	−2.3709	−1.5287	−2.4362
$\boldsymbol{C}_7$	1.1361	1.2907	−1.5287	−2.4362	−1.5287	−2.4362
$\boldsymbol{C}_8$	1.2907	1.4863	−1.5287	−2.4362	−2.3571	−0.9215
$\boldsymbol{C}_9$	1.4863	1.55	−2.3571	−0.9215	−2.2690	−0.3546
$\boldsymbol{C}_{10}$	1.55	T_e	−2.2690	−0.3546	−2.7141	−0.6137

TABLE G.1. Each $\boldsymbol{C}_i$ is extracted from $\boldsymbol{\alpha}(t)$ by letting t run from t_s to t_e, and we give the shape angles at the end points.

remaining pieces around the yellow loops were either too small or hard to label clearly, so we zoom in on this portion of the diagram in Figure G.1. There are five smaller loops within the main loop $\boldsymbol{C}$, which consist of the black loop made up of $\boldsymbol{C}_2$, $\boldsymbol{C}_4$, $\boldsymbol{C}_6$ and $\boldsymbol{C}_8$, the red loop made up of $\boldsymbol{C}_1$, $\boldsymbol{C}_9$ and $\boldsymbol{C}_{10}$, and the three yellow loops $\boldsymbol{C}_3$, $\boldsymbol{C}_5$ and $\boldsymbol{C}_7$. Now the yellow loop $\boldsymbol{C}_3$ contains even smaller sub-loops, but as the orientation does not change within $\boldsymbol{C}_3$ we will not sub-divide further. Currently the contribution towards the geometric phase from each loop is as follows:

loop color	pieces	contribution
Black loop	$\boldsymbol{C}_2, \boldsymbol{C}_4, \boldsymbol{C}_6, \boldsymbol{C}_8$	0.0953
Red loop	$\boldsymbol{C}_1, \boldsymbol{C}_9, \boldsymbol{C}_{10}$	-0.0023
Yellow loop	$\boldsymbol{C}_3$	-0.0149
Yellow loop	$\boldsymbol{C}_5$	-0.0012
Yellow loop	$\boldsymbol{C}_7$	-0.0048

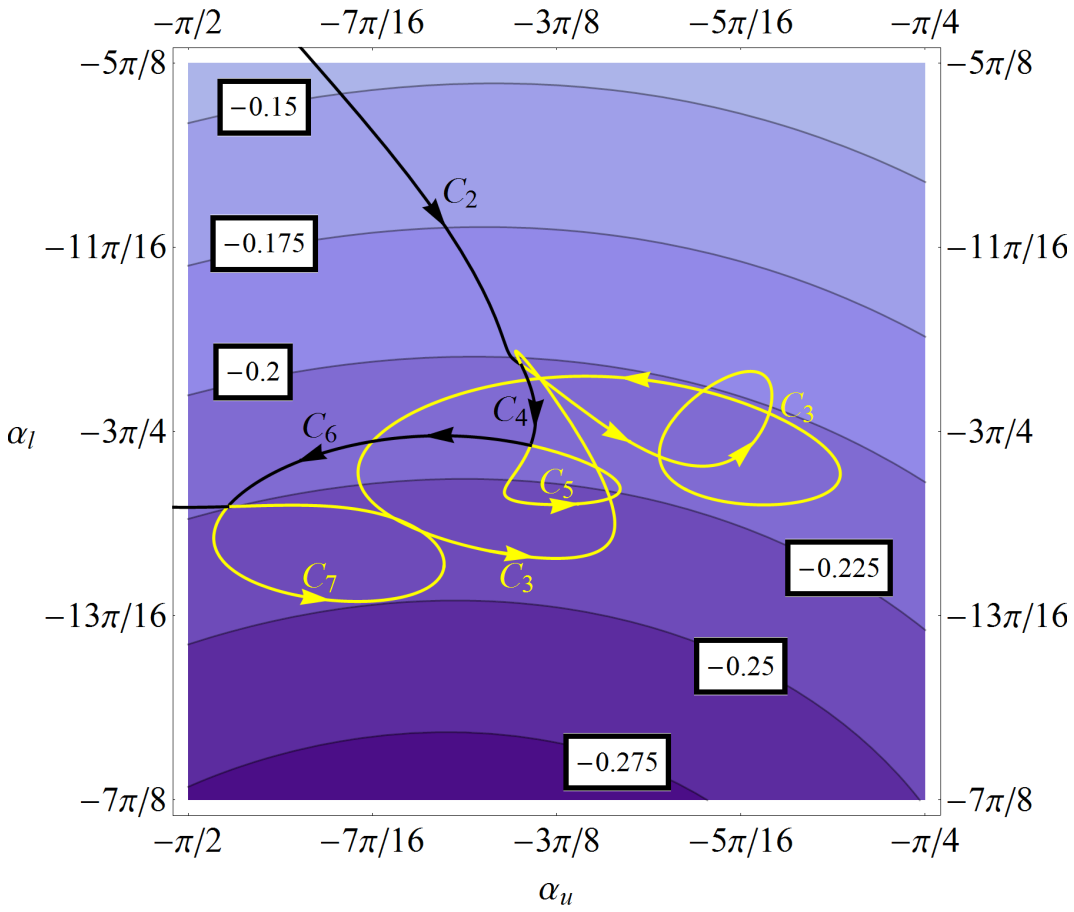

FIGURE G.1. The path of the digitised dive is from $\boldsymbol{C}_1$ to $\boldsymbol{C}_{10}$ in ascending order. The three yellow loops $\boldsymbol{C}_3$, $\boldsymbol{C}_5$ and $\boldsymbol{C}_7$ are orientated counterclockwise so they provide a negative contribution towards the geometric phase.

Now by reversing the orientation of the red and three yellow loops we can improve the geometric phase without affecting the dynamic phase. This improvement amounts to 0.0464 and brings the new result to $\upsilon_{geo} = 0.1186$. We conclude by showing the shape angles of the original dive in Figure G.2 followed by the modified shape angles in Figure G.3.

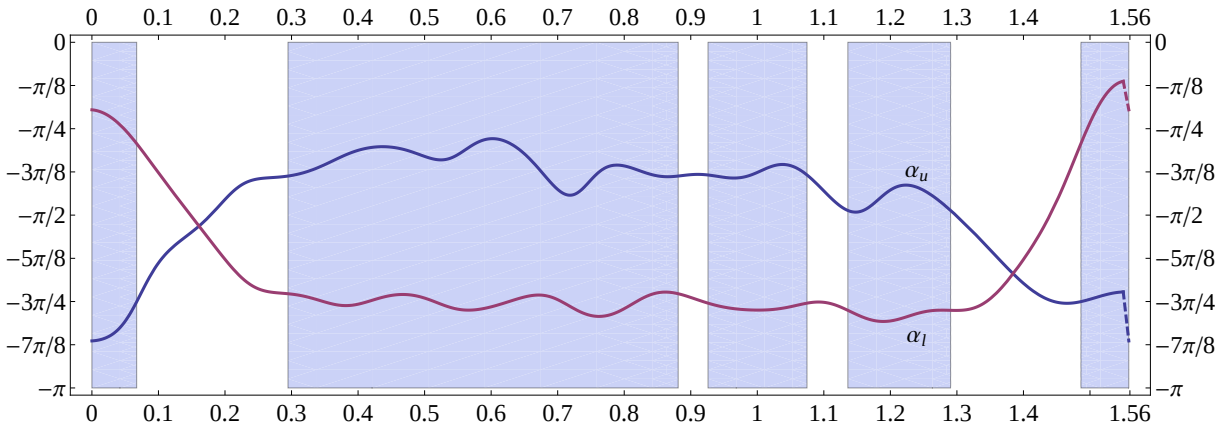

FIGURE G.2. Shape angles of the digitised dive. The regions shaded in blue correspond to the loops oriented in the counterclockwise direction that needs reversing in order to optimise the geometric phase. Towards the very end, the dashed portion of the shape angles correspond to the linear interpolation we added to close the curve on shape space.

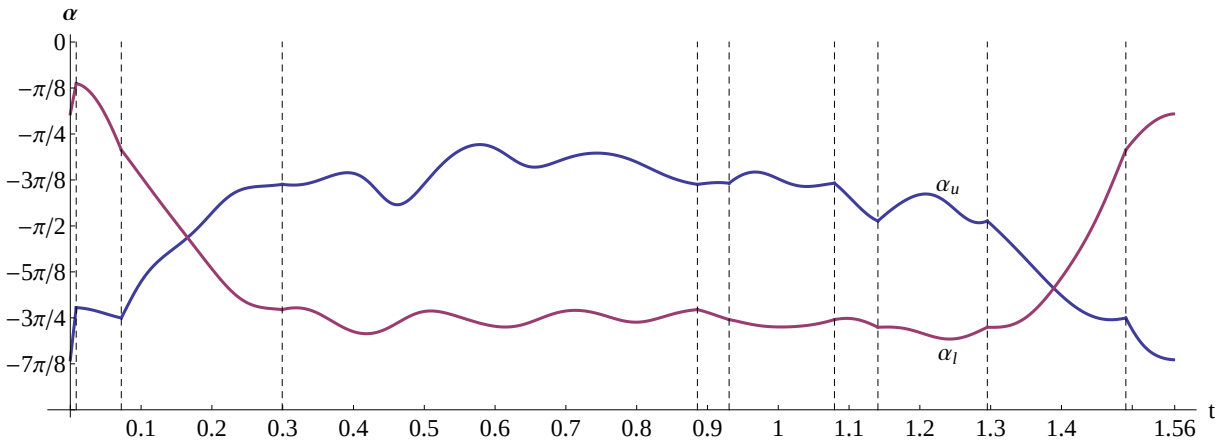

FIGURE G.3. The shape angles after orientating all loops in the clockwise direction. The vertical dashed lines indicate where the pieces are connected. The ordering now becomes $-\boldsymbol{C}_{10} \to -\boldsymbol{C}_9 \to \boldsymbol{C}_2 \to -\boldsymbol{C}_3 \to \boldsymbol{C}_4 \to -\boldsymbol{C}_5 \to \boldsymbol{C}_6 \to -\boldsymbol{C}_7 \to \boldsymbol{C}_8 \to -\boldsymbol{C}_1$, where a negative means we traverse along the piece in the opposite direction.

APPENDIX H

The Fast-kick Integral

The integral of the form

$$\mathcal{X} = \int_0^\pi \frac{1}{2} - \frac{a_0}{a_1 - a_2\cos\alpha + a_3\sin\alpha}\,\mathrm{d}\alpha$$

can be evaluated using the Weierstrass substitution $t = \tan(\alpha/2)$, and in doing so we find that

$$\begin{aligned}\mathcal{X} &= \int_0^\pi \frac{1}{2}\,\mathrm{d}\alpha - \int_0^\infty \frac{a_0}{a_1 - a_2\frac{1-t^2}{1+t^2} + a_3\frac{2t}{1+t^2}}\cdot\frac{2}{1+t^2}\,\mathrm{d}t \\ &= \frac{\pi}{2} - \int_0^\infty \frac{2a_0}{a_1(1+t^2) - a_2(1-t^2) + a_3(2t)}\,\mathrm{d}t \\ &= \frac{\pi}{2} - \frac{2a_0}{a_1+a_2}\int_0^\infty \frac{1}{t^2 + \frac{2a_3}{a_1+a_2}t + \frac{a_1-a_2}{a_1+a_2}}\,\mathrm{d}t.\end{aligned}$$

Factorising the denominator with the quadratic formula we find that

$$t^2 + \frac{2a_3}{a_1+a_2}t + \frac{a_1-a_2}{a_1+a_2} = \left(t + \frac{a_3}{a_+} + \frac{a_r}{a_+}i\right)\left(t + \frac{a_3}{a_+} - \frac{a_r}{a_+}i\right),$$

where

$$\begin{aligned}a_r &= \sqrt{a_1^2 - a_2^2 - a_3^2} \\ a_+ &= a_1 + a_2,\end{aligned}$$

and by using partial fractions we obtain

$$\mathcal{X} = \frac{\pi}{2} - \frac{a_0 i}{a_r}\int_0^\infty \left(t + \frac{a_3}{a_+} + \frac{a_r}{a_+}i\right)^{-1} - \left(t + \frac{a_3}{a_+} - \frac{a_r}{a_+}i\right)^{-1}\mathrm{d}t. \tag{H.1}$$

This integral can now be integrated using complex logarithms, and looking solely at the integral component we get

$$\left[\ln\left|t + \tfrac{a_3}{a_+} + \tfrac{a_r}{a_+}i\right| + i\,\mathrm{Arg}\left(t + \tfrac{a_3}{a_+} + \tfrac{a_r}{a_+}i\right) - \ln\left|t + \tfrac{a_3}{a_+} - \tfrac{a_r}{a_+}i\right| - i\,\mathrm{Arg}\left(t + \tfrac{a_3}{a_+} - \tfrac{a_r}{a_+}i\right)\right]_0^\infty.$$

Notice how the logarithmic terms completely cancel due to the two moduli being equal. The upper bound of both principal arguments are zero because $t \to \infty$ means the imaginary components inside Arg become insignificant, and Arg of a

positive number is zero. This means the lower bound of the principal arguments are the only non-zero terms, which simplify to

$$-i\operatorname{Arg}\left(\frac{a_3}{a_+}+\frac{a_r}{a_+}i\right)+i\operatorname{Arg}\left(\frac{a_3}{a_+}-\frac{a_r}{a_+}i\right)=-2i\operatorname{Arg}\left(\frac{a_3}{a_+}+\frac{a_r}{a_+}i\right),$$

since $-\operatorname{Arg} z=\operatorname{Arg}\bar{z}$ for any $z\in\mathbb{C}$. Also, as the complex number $\frac{a_3}{a_+}+\frac{a_r}{a_+}i$ is in the first quadrant of the complex plane, we can use arctan to rewrite (H.1) as

$$\begin{aligned}\mathfrak{X}&=\frac{\pi}{2}-\frac{2a_0}{a_r}\arctan\left(\frac{a_r}{a_3}\right)\\&=\frac{\pi}{2}-\frac{2a_0}{\sqrt{a_1^2-a_2^2-a_3^2}}\arctan\left(\frac{\sqrt{a_1^2-a_2^2-a_3^2}}{a_3}\right),\end{aligned}$$

which is the result shown in (5.46).

APPENDIX I

Energies and Wobbling Somersault

An additional point to note about Figure 6.6B is that the minimum (scaled) energy does not occur at $\tau_3 = 0$ (or $\tau_3 = T_3$), but instead has a slightly lower value of $\mathcal{E}_5\big((0.5 \pm 0.434)T_3\big) = 0.0242$ (as opposed to $\mathcal{E}_5(0) = 0.0243$), as seen in Figure I.1. In the case of $\mathcal{E}_5(0.2713T_3) = \mathcal{E}_3 = 0.0452$, the period of twist is not the same as T_3, but is

$$T(\mathcal{E}_3, {}^sI) = \frac{31.0595}{l} < T(\mathcal{E}_3, {}^tJ) = \frac{33.9610}{l} \quad \Big(= T_3\Big).$$

The discrepancy is a consequence of the athlete being in different diving positions, i.e. layout position (Figure 5.1A) in $\mathcal{S}_5$ compared to twist position (Figure 5.1F) in $\mathcal{S}_3$, which results in different energy-inertia ellipsoids.

When $\mathcal{E}_5(\tau_3) \to 1/(2\,{}^sI_y)$ as $\tau_3 \to (0.5 \pm 0.434)T_3$ the dynamics approach the separatrix given by two plane curves with scaled equation (2.66). As the diver is in layout position for $\mathcal{S}_5$ we have $\boldsymbol{L} = \boldsymbol{M}$, and the tensor of inertia is ${}^sI$. The orbit on the separatrix is given by (2.67) and due to the hyperbolic functions the dynamics slow down when approaching the unstable equilibrium points $(0, \pm l, 0)^t$. On one side of the separatrix where $\mathcal{E}_5 > 1/(2\,{}^sI_y)$, we have loops around the L_z-axis (twist axis) that produce the familiar twisting somersaulting motion, but on the other side where $\mathcal{E}_5 < 1/(2\,{}^sI_y)$ we instead have loops around the L_x-axis, which is the

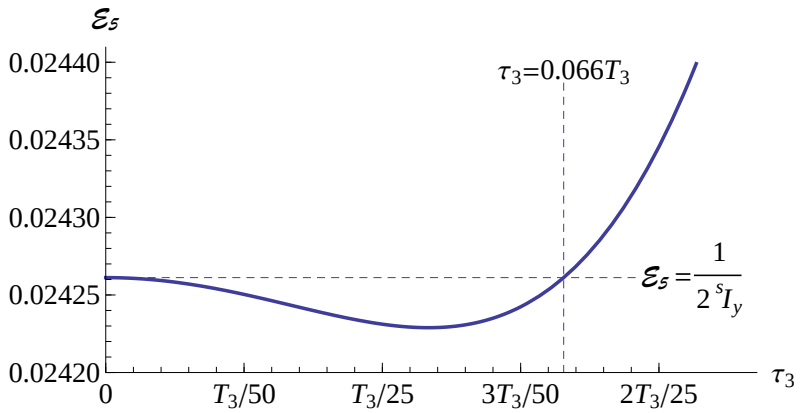

FIGURE I.1. Magnification of Figure 6.6B to show when $E_5 < l^2/(2\,{}^sI_y)$.

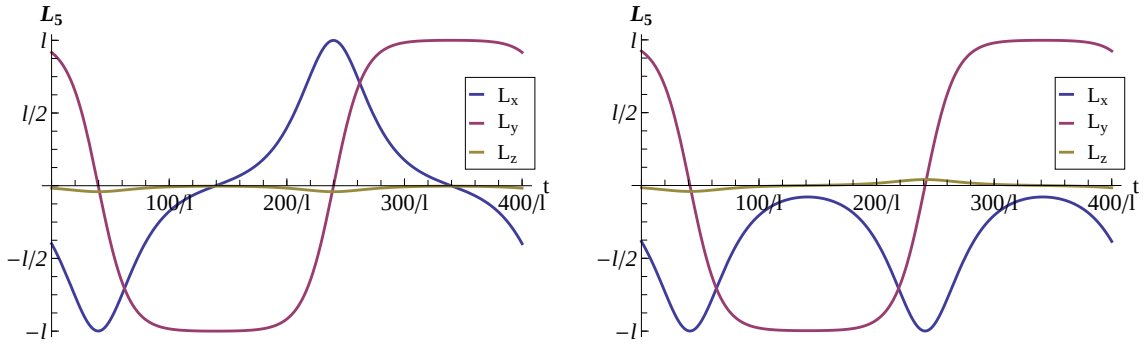

(A) Twisting somersault with initial condition $\boldsymbol{L}_5(0) = l(-0.3987, 0.9169, -0.0167)^t$.

(B) Wobbling somersault with initial condition $\boldsymbol{L}_5(0) = l(-0.3842, 0.9231, -0.0155)^t$.

Figure I.2. A comparison between the dynamics of the twisting somersault and wobbling somersault. Both initial conditions are chosen to be close to the point $l(-0.3919, 0.9199, -0.0161)^t$ on the separatrix, be part of the loop $\boldsymbol{L}_5(0; \tau_3)$ given by (6.6), and have period $400/l$.

tilt axis and this produces a different type of motion. Yeadon [**70**] refers to this motion as the wobbling somersault, because the body experiences an oscillating twist motion that goes one way and then the other, which is essentially a wobble where no twist is actually completed by the diver. We show a comparison between the two dynamics in Figure I.2.

References

[1] S. L. Altmann, *Rotations, Quaternions, and Double Groups*, Courier Corporation, illustrated, reprint ed., 2005.

[2] M. S. Ashbaugh, C. C. Chicone, and R. H. Cushman, *The twisting tennis racket*, Journal of Dynamics and Differential Equations, 3 (1991), pp. 67–85.

[3] B. L. Badman and G. R. Rechtine, *Spinal injury considerations in the competitive diver: a case report and review of the literature*, The Spine Journal, 4 (2004), pp. 584–590.

[4] J. E. Bailes, J. M. Herman, M. R. Quigley, et al., *Analysis of 139 spinal cord injuries due to accidents in water sports*, Surgical Neurology, 34 (1990), pp. 155–158.

[5] C. Batterman, *The Techniques of Springboard Diving*, MIT Press, 2003.

[6] S. Bharadwaj, N. Duignan, H. R. Dullin, K. Leung, and W. Tong, *The diver with a rotor*, eprint arXiv:1510.02978, (2015).

[7] I. Bialynicki-Birula, B. Mielnik, and J. Plebański, *Explicit solution of the continuous baker-campbell-hausdorff problem and a new expression for the phase operator*, Annals of Physics, 51 (1969), pp. 187–200.

[8] S. Blanes, F. Casas, J. A. Oteo, and J. Ros, *The magnus expansion and some of its applications*, Physics Reports, 470 (2009), pp. 151–238.

[9] A. Cabrera, *A generalized montgomery phase formula for rotating self-deforming bodies*, Journal of Geometry and Physics, 57 (2007), pp. 1405–1420.

[10] R. V. Chacon and A. T. Fomenko, *Recursion formulas for the lie integral*, Advances in Mathematics, 88 (1991), pp. 200–257.

[11] K. B. Cheng and M. Hubbard, *Role of arms in somersaulting from compliant surfaces: A simulation study of springboard standing dives*, Human Movement Science, 27 (2008), pp. 80–95.

[12] T. L. Chow, *Classical Mechanics*, Wiley, 1995.

[13] C. E. Clauser, J. T. McConville, and J. Young, *Weight, volume and center of mass of segments of the human body*, AMRL Technical Report 69-70, Wright-Patterson Air Force Base, Ohio, 1969.

[14] J. Dapena, *A method to determine the angular momentum of a human body about three orthogonal axes passing through its center of gravity*, Journal of Biomechanics, 11 (1978), pp. 251–256.

[15] W. T. DEMPSTER, *Space requirements of the seated operator*, WADC-55-159, AD-087-892, Wright-Patterson Air Force Base, Ohio, 1955.

[16] H. R. Dullin and W. Tong, *Twisting somersault*, eprint arXiv:1510.08046, (2015).

[17] G. H. G. Dyson, *The mechanics of athletes*, University of London, 3rd ed., 1964.
[18] H.-D. Ebbinghaus, *Numbers*, Springer-Verlag, 2nd ed., 1990.
[19] A. R. Fairbanks, *Teaching Springboard Diving*, Prentice-Hall Inc., Englewood Cliffs, N.J., 1963.
[20] C. Frohlich, *Do springboard divers violate angular momentum?*, American Journal of Physics, 47 (1979), pp. 583–592.
[21] H. Goldstein, J. L. Safko, and C. P. Poole, *Classical Mechanics*, Addison-Wesley, 3rd ed., 2001.
[22] I. Gradshteyn and I. Ryzhik, *Table of Integrals, Series and Products, Corrected and Enlarged Edition*, Academic Press, New York, 1980.
[23] J. Hamill, M. D. Ricard, and D. M. Golden, *Angular momentum in multiple rotation nontwisting platform dives*, International Journal of Sport Biomechanics, 2 (1986), pp. 78–87.
[24] E. P. Hanavan, *A mathematical model of the human body*, AMRL-TR-64-102, AD-608-463, Aerospace Medical Research Laboratories, Wright-Patterson Air Force Base, Ohio, 1964.
[25] H. Hatze, *A mathematical model for the computational determination of parameter values of anthropomorphic segments*, Journal of Biomechanics, 13 (1980), pp. 833–843.
[26] J. G. Hay, B. D. Wilson, J. Dapena, et al., *A computational technique to determine the angular momentum of a human body*, Journal of Biomechanics, 10 (1977), pp. 269–277.
[27] J. Huber, *Springboard and Platform Diving*, Human Kinetics, 2015.
[28] A. Iserles and S. Nørsett, *On the solution of linear differential equations in lie groups*, Philosophical Transactions of The Royal Society, 357 (1999), pp. 983–1019.
[29] R. K. Jensen, *Model for body segment parameters*, In Biomechanics V-B, ed. P.V. Komi, University Park Press. Baltimore, (1976), pp. 380–386.
[30] ——, *Estimation of biomechanical properties of three body types using a photogrammetry method*, Journal of Biomechanics, 11 (1978), pp. 349–358.
[31] T. R. Kane and M. P. Scher, *a dynamical explanation of the falling cat phenomenon*, Int. J. Solids Structures, 5 (1969), pp. 663–670.
[32] L. S. Kewalramani and R. G. Taylor, *Injuries to the cervical spine from diving accidents*, The Journal of Trauma, 15 (1975), pp. 130–142.
[33] J. Koschorreck and K. Mombaur, *Modeling and optimal control of human platform diving with somersaults and twists*, Optimization and Engineering, 13 (2009), pp. 29–56.
[34] ——, *Optimisation of somersaults and twists in platform diving*, Computer Methods in Biomechanics and Biomedical Engineering, 12 (2009), pp. 157–159.

[35] L. D. LANDAU AND E. M. LIFSHITZ, *Mechanics*, vol. 1, Butterworth-Heinemann, 3rd ed., 1976.

[36] R. G. LITTLEJOHN AND M. REINSCH, *Gauge fields in the separation of rotations and internal motions in the n-body problem*, Rev. Mod. Phys., 69 (1997), pp. 213–275.

[37] G. LOUGANIS AND E. MARCUS, *Breaking the Surface*, Plume, 1996.

[38] W. MAGNUS, *On the exponential solution of differential equations for a linear operator*, Communications on Pure and Applied Mathematics, 7 (1954), pp. 649–673.

[39] D. I. MILLER, G. S. GEORGE, M. R. YEADON, AND A. ZECEVIC, *Biomechanics of Competitive Diving: A U.S. Diving Reference Manual*, U.S. Diving Publications, 2000.

[40] D. I. MILLER AND C. F. MUNRO, *Greg louganis' springboard takeoff: I. temporal and joint position analysis*, Journal of Applied Biomechanics, 1 (1985), pp. 209–220.

[41] ——, *Greg louganis' springboard takeoff: II. linear and angular momentum considerations*, Journal of Applied Biomechanics, 1 (1985), pp. 288–307.

[42] D. I. MILLER AND E. J. SPRIGINGS, *Factors influencing the performance of springboard dives of increasing difficulty*, Journal of Applied Biomechanics, 17 (2001), pp. 217–231.

[43] P. C. MOAN AND J. NIESEN, *Convergence of the magnus series*, Foundations of Computational Mathematics, 8 (2008), pp. 291–301.

[44] R. MONTGOMERY, *How much does the rigid body rotate? a berrys phase from the 18th century*, American Journal of Physics, 59 (1991), pp. 394–398.

[45] R. MONTGOMERY, *Gauge theory of the falling cat*, in Dynamics and control of mechanical systems (Waterloo, ON, 1992), vol. 1 of Fields Inst. Commun., Amer. Math. Soc., Providence, RI, 1993, pp. 193–218.

[46] P. MORIARTY, *Springboard Diving*, Ronald Press Company, 1959.

[47] R. O'BRIEN, *Springboard and Platform Diving*, Human Kinetics, 2nd ed., 2002.

[48] D. PRATO AND P. W. LAMBERTI, *A note on magnus formula*, The Journal of Chemical Physics, 106 (1997), pp. 4640–4643.

[49] E. PUTTERMAN AND O. RAZ, *The square cat*, American Journal of Physics, 76 (2008), pp. 1040–1044.

[50] H. E. RAUCH AND A. LEBOWITZ, *Elliptic functions, theta functions, and Riemann surfaces*, Williams and Wilkins, Baltimore, 1973.

[51] R. H. SANDERS AND B. D. WILSON, *Angular momentum requirements of the twisting and nontwisting forward 1-somersault dive*, International Journal of Sport Biomechanics, 3 (1987), pp. 47–62.

[52] E. J. SPRIGINGS AND D. I. MILLER, *Optimal knee extension timing in springboard and platform dives from the reverse group*, Journal of Applied Biomechanics, 20 (2004), pp. 275–290.

[53] K. Steinbruck and V. Paelslack, *Analysis of 139 spinal cord injuries due to accidents in water sports*, Paraplegia, 18 (1980), pp. 86–93.
[54] S. Still and C. A. Carter, *Springboard and Highboard Diving: Training, Techniques and Competition*, Pelham pictorial sports instruction series, Pelham Books, London, illustrated ed., 1979.
[55] W. Tong and H. R. Dullin, *The equilateral pentagon at zero angular momentum: Maximal rotation through optimal deformation*, SIAM Journal on Applied Dynamical Systems, 11 (2012), pp. 963–987.
[56] ——, *Geometric phase in diving*, in Diving Research Worldwide: 1st Symposium for Researchers in Diving, T. Köthe and O. Stoll, eds., 2013, pp. 24–29.
[57] Video4coach, *Skillspector*. http://video4coach.com, version 1.2.4.
[58] D. Wallechinsky and J. Loucky, *The Book of Olympic Lists: A Treasure-Trove of 116 Years of Olympic Trivia*, Aurum Press, 2012.
[59] A. P. Weinbach, *Contour maps, center of gravity, moment of inertia and surface area of the human body*, Human Biology, 10 (1938), pp. 356–371.
[60] M. R. YEADON, *The Mechanics of Twisting Somersaults*, PhD thesis, Loughborough University, 1984.
[61] ——, *Twisting techniques used in springboard diving*, Proceedings of the First IOC World Congress on Sport Sciences, (1989), pp. 307–308.
[62] ——, *The simulation of aerial movement - I. the determination of orientation angles from film data*, Journal of Biomechanics, 23 (1990), pp. 59–66.
[63] ——, *The simulation of aerial movement - II. A mathematical inertia model of the human body*, Journal of Biomechanics, 23 (1990), pp. 67–74.
[64] ——, *The simulation of aerial movement - III. the determination of the angular momentum of the human body*, Journal of Biomechanics, 23 (1990), pp. 75–83.
[65] ——, *The simulation of aerial movement - IV. A computer simulation model*, Journal of Biomechanics, 23 (1990), pp. 85–89.
[66] ——, *The biomechanics of twisting somersaults: Part I. rigid body motions*, Journal of Sports Sciences, 11 (1993), pp. 187–198.
[67] ——, *The biomechanics of twisting somersaults: Part II. contact twist*, Journal of Sports Sciences, 11 (1993), pp. 199–208.
[68] ——, *The biomechanics of twisting somersaults: Part III. aerial twist*, Journal of Sports Sciences, 11 (1993), pp. 209–218.
[69] ——, *The biomechanics of twisting somersaults: Part IV. partitioning performances using the tilt angle*, Journal of Sports Sciences, 11 (1993), pp. 219–225.
[70] ——, *Learning how to twist fast*, In Proceedings XVII International Symposium of Biomechanics in Sports, (1999).
[71] ——, *The physics of twisting somersaults*, Physics World, 13 (2000), pp. 33–37.
[72] M. R. YEADON and D. G. Kerwin, *Contributions of twisting techniques used in backward somersaults with one twist*, Journal of Applied Biomechanics, 15 (1999), pp. 152–165.